Title	Studies on Improvement of Mechanical Properties by Microstructural Control for MoSi2 Based Composites
Author(s)	鈴木, 義和
Citation	大阪大学, 1998, 博士論文
Version Type	VoR
URL	https://doi.org/10.11501/3143983
rights	
Note	

Studies on
Improvement of Mechanical Properties by
Microstructural Control for MoSi$_2$
Based Composites

(微構造制御によるMoSi$_2$基複合材料の機械的特性改善に関する研究)
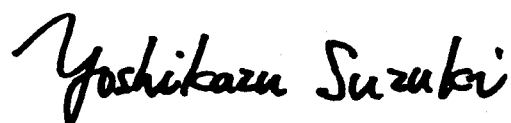
1998

Yoshikazu Suzuki

Department of Materials Chemistry
Faculty of Engineering
Osaka University

Preface

The studies presented in this thesis were carried out under the guidance of Professor Koichi Niihara at Department of Materials Chemistry, Faculty of Engineering, Osaka University.

Molybdenum disilicide, $MoSi_2$, is a promising material for various applications such as aerospace exposed to temperatures more than 1500 °C, mainly because of its high melting point (2030°C) and fairly good oxidation resistance. However, its fracture toughness and strength are not sufficiently high for high-temperature structural applications. Furthermore, glassy SiO_2 which is present in metallurgically-produced $MoSi_2$ strongly degrades the high-temperature mechanical properties.

The thesis concerned with a new material design concept for $MoSi_2$ based materials, "simultaneous strengthening and toughening both of $MoSi_2$ matrix and SiO_2 grain boundary phase," to overcome above mentioned problems. Strong and tough $MoSi_2$ based composites up to high temperatures were successfully developed along with the proposed concept; the mechanisms of the strengthening and toughening were also clarified, and the relationship between microstructure and mechanical properties of $MoSi_2$ based composites was studied in detail. The strategy to fabricate excellent and promising $MoSi_2$ based materials was established via this study. The author hopes that the concepts, findings, and strategies obtained in this study will contribute to the progress in science and engineering.

Yoshikazu Suzuki

Yoshikazu Suzuki

Department of Materials Chemistry
Faculty of Engineering
Osaka University
2-1, Yamada-oka, Suita, Osaka 565
Japan

January, 1998

Contents

1

Introduction

1.1 Introduction

Molybdenum disilicide, $MoSi_2$, has been recognized as a potential material for high-temperature structural applications since the early study conducted by Maxwell in 1949 [1]. It realized that $MoSi_2$ has excellent high-temperature oxidation resistance, high thermal conductivity and ductility at elevated temperatures, which are desirable for a high-temperature structural material.

Studies on $MoSi_2$ intermetallic compound began in 1907; $MoSi_2$ was first obtained in a pure form by aluminothermy (i.e. thermit process) by Hönigschmid [2]. At the time, $MoSi_2$ was considered as a high temperature corrosion-protective coating material for ductile metals. Forty years later, in 1947, $MoSi_2$ came to receive much attention due to its possibility as a heating element material. Hägglund and Rehnquist [3] proposed heating elements composed of a Mo-50wt%Si alloy, which now corresponds to a $MoSi_2$-Si alloy. Fitzer et al. [4] actively investigated $MoSi_2$ based materials in 1950's to 1970's. Kanthal [5] first patented commercial heating elements in 1956.

It was Maxwell [1] who first pointed out the use of $MoSi_2$ as a high-temperature structural material, and performed an initial study of $MoSi_2/Al_2O_3$ composites. Nowotny et al. [6-10] carried out very informative study on the disilicide-disilicide pseudo binary and ternary alloys, the Mo-Si-C phase diagram, and so on. In 1971, Erdoes [11] considered silicides as coating materials for gas turbine engines. In 1973, Fitzer et al. [12] reported that $MoSi_2/Al_2O_3$ and $MoSi_2/SiC$ composites showed improved high-temperature strength. They also investigated $MoSi_2/Nb$ wire composites. Their works are summarized in Schlichiting's review [13].

After Gac and Petrovic [14] showed in 1985 that SiC whisker reinforced $MoSi_2$ matrix composites have improved strength and toughness at room temperature, $MoSi_2$ based materials came to attract a great deal of interests, not only of metallurgists but also of wide fields of materials scientists and engineers. The history of $MoSi_2$ intermetallic compound was well reviewed by Schlichiting in 1978 [13], and Vasudévan and Petrovic in 1992 (Table 1.1) [15]. It has been ninety years since the first synthesis of $MoSi_2$, but $MoSi_2$ as an ultra-high temperature material in future has just started.

1

Table 1.1 An abbreviated history of $MoSi_2$ depicting a number of important events and milestones [15].

HISTORY OF MoSi₂

ONR First High Temperature Structural Silicide Conference

Los Alamos Labs. US - PATENTS (Petrovic)
Los Alamos Labs. IR-100 Award

Los Alamos Labs / ONR MoSi₂ Composites developmental studies
DARPA-PRATT & WHITNEY Intermetallics Review Meeting

CARTER (LANL-MIT) Thesis on vapor solid whiskers in MoSi₂

Los Alamos Labs./DOE-ECUT
MoSi₂ developmental Studies(Petrovic)

UMAKOSHI & HIRANO
(Japan)
Single Crystal MoSi₂,WSi₂
Studies

KEY PAPERS ON MoSi₂
FITZER & REMMELE (Germany)
GAC & PETROVIC (USA)

ERDOS (USA) Silicide coatings
for gas turbine applications

FITZER (Germany) High temperature study of MoSi₂

KANTHAL (Sweden) Patent on MoSi₂ for Commercial heating element

MAXWELL (USA) First suggested the use of MoSi₂ as a structural material

NOWOTNY (Germany) Mo-Si-C Phase diagram

KIEFFER et al (Austria) Patent on MoSi₂ heat conductor by P/M methods

BEIDLER & CAMPBELL (USA) Patent on MoSi₂ composition

HAEGGLUND & REHNQUIST (Sweden) Suggested 50Mo/50Si Alloys for furnace heating elements

HOENIGSCHMID
WEDEKIND & PINTSCH
(Germany) Suggested high melting silicides for use in heat conductor material

HOENIGSCHMID (Germany) Protective coating for Ductile metal

1991, 1990, 1989, 1988, 1985, 1984, 1973, 1971, 1956, 1954, 1951, 1950, 1949, 1947, 1914, 1913, 1907

1.2 Characteristics of $MoSi_2$ Intermetallic Compound

1.2.1 Crystal Structure and Interatomic Bonds of $MoSi_2$

$MoSi_2$ crystallizes in the body-centered tetragonal (BCT) $C11_b$ structure. It is well described by Andersen et al. [16]. It may exist in a hexagonal C40-type crystal form above $1860°C$ (as is claimed by Svechnikov et al.[17,18]) or $1900°C$ (reported by Inoue [19]), but Boettinger et al. [20] have insisted that such polymorphic transformation from tetragonal $C11_b$ to hexagonal C40 does not occur in pure $MoSi_2$. (C40 form is often observed by high-energy processing such as CVD and mechanical alloying.) The BCT unit cell containing two formula units is shown in Fig. 1.1. The black and white spheres correspond to Mo and Si atoms, respectively. Each Mo belongs to a planar square sublattice with lattice constant a in the x-y plane. Such a Mo (001) plane is a mirror plane and is sandwiched between two Si planar square sublattices. The primitive translation vectors are

$$T_1 = \begin{pmatrix} a \\ 0 \\ 0 \end{pmatrix} \quad T_2 = \begin{pmatrix} 0 \\ a \\ 0 \end{pmatrix} \quad T_3 = \begin{pmatrix} -a/2 \\ -a/2 \\ c/2 \end{pmatrix} \tag{1.1}$$

expressed in Cartesian xyz-coordinates. The distance between Mo planes is $c/2$, rather than c. The space group of $MoSi_2$ is I4/mmm (No. 139) with Mo at the 2a positions and Si at the 4e positions (Table 1.2). In terms of the Si z-parameter, the vertical nearest-neighbor Si-Si distance is $D_{Si-Si} \cong c\ (1-\ 2z)$. Several sets of lattice parameters have been reported [21-28] (Table 1.3). All of them are identical to each others within 0.2%. Since the c axis of $MoSi_2$ elongates with increase in solid solution atoms as will be shown in Chap. 6, it seems reasonable to assume $a = 0.3204$-5, $c = 0.7845$-6. The Si-Si distance D_{Si-Si} is thus 11% larger than in elemental diamond-structured silicon, and the Mo-Mo distance a is close to the second-nearest distance in elemental body centered cubic (BCC) molybdenum [16].

It may be seen that, to an accuracy better than 0.005 nm, $D_{Si-Si} = c/3 = (2/3)^{1/2}a$ [29]. This means that each Mo has ten (rather than eight) nearest Si neighbors and that each Si has five nearest neighbors at the same distance. The Si atoms in the (110)-planes form hexagonal, graphite-like sheets with Mo at the centers of the regular hexagons and $C11_b$ structure may be described as an ABAB... stacking in the [110]-direction of hexagonal sheets. This will be discussed in Chap. 6. $MoSi_2$ has relatively complex structure, compared with cubic disilicides
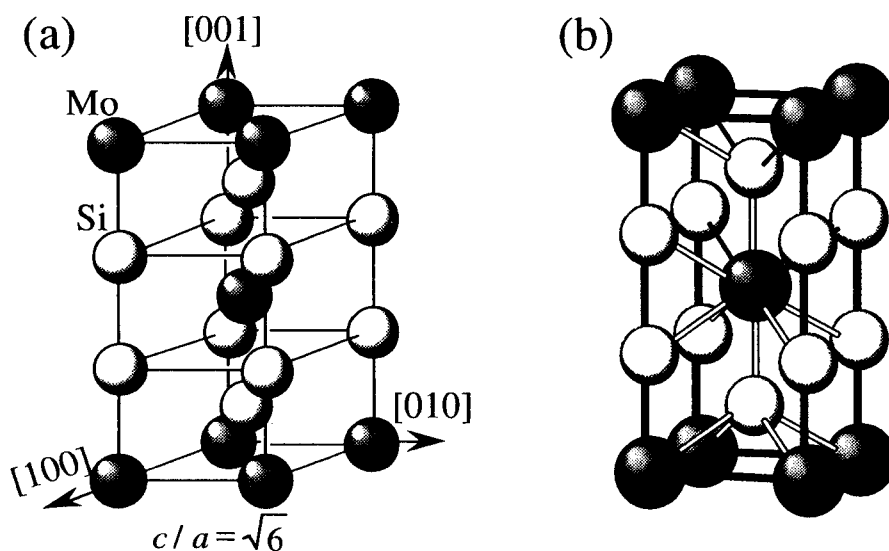
Fig. 1.1 The crystal structure of $MoSi_2$ $(C11_b)$; (a) normal expression, (b) the coordination number to Mo atoms is ten, rather than eight.

Table 1.2 Crystallographical data of $MoSi_2$ $(C11_b)$.

Formula	$MoSi_2$	
Space group	I4/mmm (No.139)	
Strukturberichte	$C11_b$	
Atom position	2 Mo in a	0, 0, 0; 1/2, 1/2, 1/2
	4 Si in e	0, 0, z; 0, 0, -z; 1/2, 1/2, 1/2+z; 1/2, 1/2, 1/2-z (ideal z = 1/3)

Table 1.3 Lattice parameters of $MoSi_2$.

a (nm)	c (nm)	z	Reference
0.3200	0.7861	0.333 ± 0.015	Experimental [21]
0.3202	0.7843		Experimental [17]
0.3202[a]	0.7852[a]	0.3374[b]	[a]Experimental [22] &[b]Band calculation [23]
0.3205	0.7845		Experimental (Single crystal) [24]
0.32040	0.78481	1/3	Experimental (Powder&Si Internal Standard) [25]
0.32047(2)	0.78449(8)		Experimental (Powder&Si Internal Standard) [26]
0.3204(3)	0.7845(5)	0.3371	Experimental (Powder&Rietveld Analysis) [27,28]

such as $CoSi_2$. Such a complex crystal structure results in the poor deformability and brittle nature. Deformation mechanism of single crystal and polycrystal $MoSi_2$ will be shown later.

According to band calculations [23], there are strong covalent bonds between constituent atoms in $MoSi_2$. Harada et al. [30] have reported that $MoSi_2$ has strong bonds between Si atoms and also between Mo and Si. McMahan et al. [31] have showed that there is a hierarchy in bond strength, ordered from strongest to weakest: Mo-Mo, Mo-Si, and Si-Si. However, the Mo-Mo bond in $C11_b$ structure is longer than that in the BCC molybdenum as mentioned before, and the Mo-Si bonds, in particular $Mo(4d)$-$Si(3p)$ hybridization, are dominant in the $MoSi_2$ structure. The electronic configuration is approximately $Mo\ 4d^5\ Si_2\ 3s^2 3p^{2.5}$ [16].

1.2.2 Some Physical and Chemical Properties of $MoSi_2$

$MoSi_2$ has very high melting point of 2030°C, which allows to operate $MoSi_2$ around 1900°C [32]. Some physical properties of various high-temperature structural materials are summarized in Table 1.4 [15,26,33,34]. $MoSi_2$ has moderate density, relatively small coefficient of thermal expansion (CTE) and fairly good oxidation resistance. Since brittle-to-ductile transition temperature (BDTT) of $MoSi_2$ is about 1000°C; $MoSi_2$ shows ductile deformation above this temperature, and should be a more reliable material without sudden fracture. Other properties of $MoSi_2$ are summarized in Table 1.5 [35-44]. A good review on the physical properties of transition-metal silicides was presented by Nicolet and Lau [45]. Mechanical properties will be mentioned latter.

$MoSi_2$ is non-toxic and environmentally benign [15]. The constituent elements, molybdenum and silicon, are also non-toxic for living bodies [46]. This is a very important feature of this material for future applications.

1.2.3 Deformation Mechanism of Single Crystal $MoSi_2$

The plastic deformation mechanism of single crystal $MoSi_2$ has been studied by Umakoshi et al. [47-49], Hirano et al. [50-51], Maloy et al. [52-53], Ito et al. [54-56] and Evans et al.[57].

Table 1.4 Comparison of some physical properties of various high-temperature structural materials.

Materials	Density g/cm^3	$T_{melting}$ (°C)	$T_{oxidation}$ (°C)	BDTT (°C)	CTE ($\times 10^{-6}K^{-1}$)
MoSi$_2$	6.27*	2030	1600	1000	8.1
Ti$_5$Si$_3$	4.32	2130	–	–	–
FeAl	5.56	1337	1027	430	16.5
Fe$_3$Al	6.70	1540	–	550	16.5
NiAl	5.86	1647	1227	527	15
Ni$_3$Al	7.56	1390	–	700	12.5
TiAl	3.91	1462	827	700	11
Ti$_3$Al	4.20	1602	652	–	10
TiAl$_3$	3.30	1352	1027	527	13
NbAl$_3$	4.50	1577	1027	727	9
Nb$_2$Be$_{17}$	3.28	1702	–	> 727	16
SiC Ceramic	3.21[b]	2830[b] (decompose, 2200)	1600	NA	5
Si$_3$N$_4$ Ceramic	3.19	decompose, 1900[c]	–	NA	3.4
MAR M-246*	8.44	1317	927	NA	16

Data without any symbols were referred from Ref.15; [a]Ref. 26; [b]Ref. 31; [c]Ref. 32.
*a nickel-base superalloy

Table 1.5 Thermal, Electrical and Chemical Properties of MoSi$_2$.

Thermal			
Linear expansion	$6.8 \times 10^{-6} K^{-1}$	at 293 K	[35]
Isobaric specific heat	426.2 J kg^{-1} K^{-1}	at 303 K	[36]
Conductivity	0.63 W cm^{-1}K^{-1}	at R.T.	[37]
Debye temperature	759 K		[38]
Electrical			
Resistivity:	18.9×10^{-6} Ωcm	at 193 K	[39]
	21.5×10^{-6} Ωcm	at 295 K	[39]
	22.7×10^{-6} Ωcm	at 338 K	[39]
	145×10^{-6} Ωcm	at 1100 K	[40]
	198×10^{-6} Ωcm	at 1400 K	[40]
	Superconductive	< 1.3 K	[41]
Hall Constant R	12.7×10^{-4} cm^3/Coul (in bulk)		[42]
	$-5 \sim -15 \times 10^{-4}$ cm^3/Coul (in thin film)		[43]
Work Function ϕ	4.73 eV		[44]
Chemical			
Insoluble	All mineral acids, hot gases, fused metals, aqueous HF		[41]
Soluble	HF + HNO$_3$, fused alkali		[41]

Although their works are not fully consistent with each other's, it is clear that $MoSi_2$ has basically poor deformability below 1000°C. However, Ito et al. [54-56] have recently reported that some slip systems away from the [100] orientation can be operative even at room temperature. Fig. 1.2 shows the five operative slip systems which have relatively low critical resolved shear stress (CRSS) [54-56].

In order to deform polycrystalline materials, five independent slip systems are required to operate (von Mises yield criterion [58]). The CRSS for the [013)<331] slip*, however, strongly depends on the crystal orientation and exhibits a quite large value along with the [001] orientation (*the mixed notations {hkl} and <hkl] are used to differentiate the first two indices from third one which does not play the same role as the first two because of the tetragonality of structure; e.g. [013) means the group of (013), (103), ($0\bar{1}3$) and ($\bar{1}03$), and <331] shows the possible orientations on [013) planes [55]). Hence, single crystals with the exact [001] orientation cannot be plastically deformed below 900°C and therefore ductility is quite limited in polycrystalline $MoSi_2$.

A trace of substitute elements dramatically change the yield stress of single crystal $MoSi_2$ [57], and it may partially explain the different results proposed by several groups [47-57].

1.2.4 Deformation Mechanism of Polycrystalline $MoSi_2$

Polycrystalline $MoSi_2$ exhibits brittle fracture below the brittle-to-ductile transition temperature (BDTT) about 1000°C (actually 900 to 1300°C, depending on the grain size and impurities).
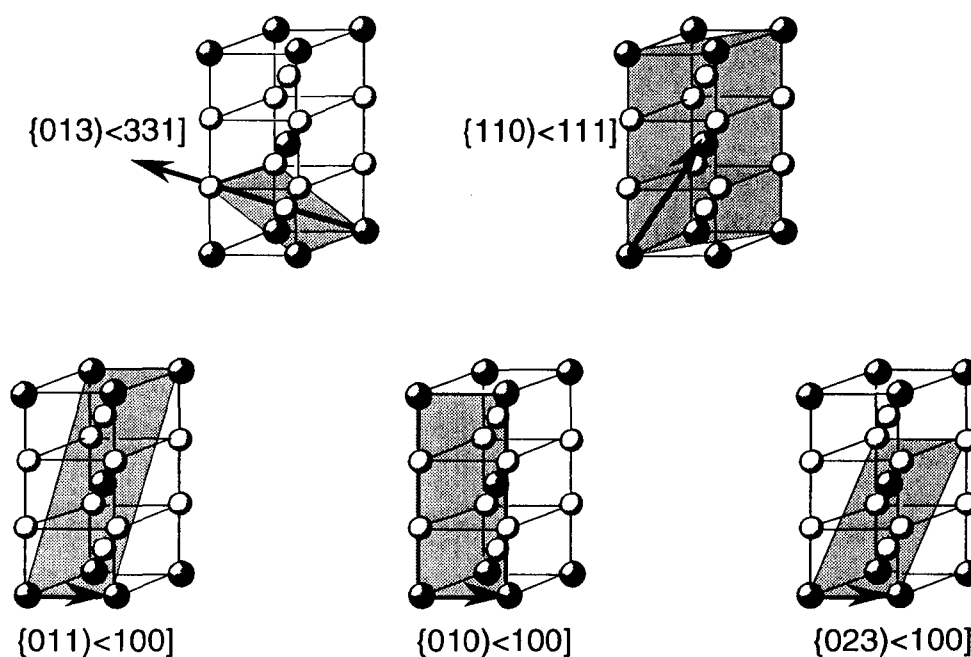

{013)<331]   {110)<111]

{011)<100]   {010)<100]   {023)<100]

Fig. 1.2 Operative slip systems in $MoSi_2$ [55].

Thus, MoSi$_2$ is sometimes categorized as a non-oxide ceramic material. In fact, processing, machining and evaluation methods for ceramic materials are almost applicable for MoSi$_2$. At high temperatures above the BDTT, MoSi$_2$ shows plastic deformation and ductility like conventional metallic systems. The deformation mechanism at high temperatures is strongly affected by the microstructure (e.g. grain size) and impurities such as glassy SiO$_2$ at the grain boundary and Mo$_5$Si$_3$ precipitates. Thus, the high-temperature deformation behavior depends on the processing route of polycrystalline MoSi$_2$. Although high-purity polycrystalline MoSi$_2$ can be fabricated by, for example, chemical vapor deposition (CVD) technique, such processing requires enormous costs for mass production, and such high-purity (and usually thin film) MoSi$_2$ will be limited to electrical applications [45]. For structural applications, thus, powder metallurgical techniques are generally used for preparing polycrystalline MoSi$_2$ with bulk form. Hence, three types of typical polycrystalline MoSi$_2$ produced by powder metallurgical processes are discussed here.

(i) Coarse grained MoSi$_2$ with less impurities

MoSi$_2$ compacts, fabricated by hot-pressing or hot-isostatically-pressing coarse MoSi$_2$ powders (e.g. 10 to 50 μm) with less oxygen content at 1700-1800°C, are typically composed of several tens to hundreds μm of MoSi$_2$ grains and less than 1wt% of glassy SiO$_2$. Such a kind of MoSi$_2$ compacts has been used for basic researches to understanding the deformation mechanism of polycrystalline MoSi$_2$ [59-63]. Evans et al. [62,63] reported that at 1200°C, plastic deformation is provided by dislocation glide on expected slip planes; at 1400 and 1600°C, there is an increasing tendency for unexpected slip planes (e.g. {112), {123} and {257}) to be operative with decreasing strain rate and increasing temperature, and the contribution of dislocation climb increases. Although each research group has proposed different combinations of operative slip systems [59-63], the consensus is that the dislocation glide and climb (so called 'glimb') are the major deformation mechanism at high temperatures more than 1200°C in this kind of polycrystalline MoSi$_2$. Fig. 1.3 shows a schematic illustration of dislocation motion [64]. At about 1000° C and under low stress, grain boundary sliding partially contributes to the deformation [65].

(ii) Coarse grained MoSi$_2$ with much impurities

MoSi$_2$ compacts, obtained by pressureless sintering coarse MoSi$_2$ powders (e.g. 10 to 50 μm) with intentional silica additive at 1700-1800°C, are typically composed of fifty to hundreds μm of MoSi$_2$ grains and ~15 vol% of glassy SiO$_2$, for example, in a commercial heating element produced by Kanthal. Gibala et al. [66] have assessed microstructure and mechanical properties of a commercial *Kanthal Super* (a popular MoSi$_2$ based heating element). Although SiO$_2$ exists as discrete particles in sintered MoSi$_2$ regardless of its high content, such too much SiO$_2$ tends to connect each other under deformation process, and weakens high-temperature mechani-
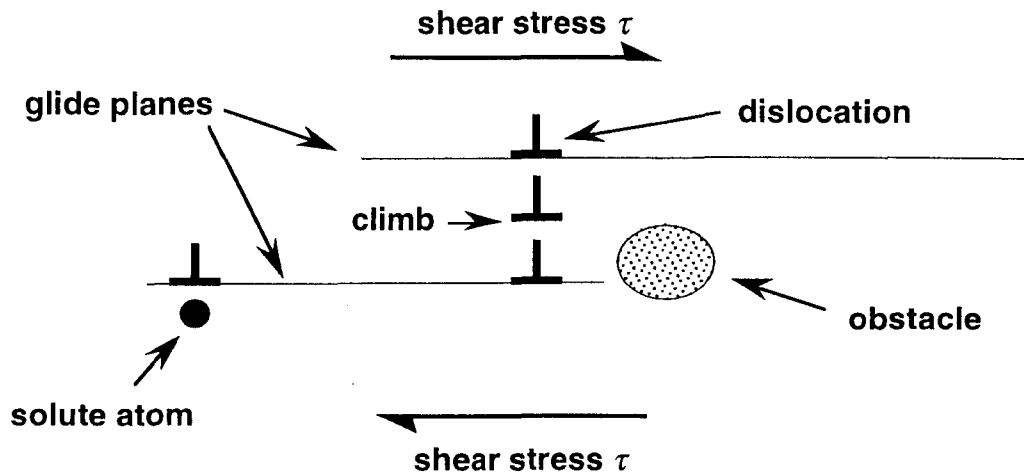
Fig. 1.3 Schematic illustration of dislocation motion. Dislocation slip involves both glide on slip planes and climb over physical obstacles [64].

cal properties. Hence, the high-temperature deformation mechanism of coarse grained $MoSi_2$ with much SiO_2 impurities is presumably the combination of viscous flow of SiO_2 and grain boundary sliding of $MoSi_2$ assisted by glassy SiO_2.

(iii) Fine grained MoSi₂ with some impurities

$MoSi_2$ compacts, fabricated by hot-pressing or hot-isostatically-pressing fine $MoSi_2$ powders (~several μm) with about 0.5-1 wt% oxygen at 1500-1700°C, are typically composed of 5 to 20 μm of $MoSi_2$ grains and about 1-2 wt% (2-4 mol%, or 2.5-5 vol%) of glassy SiO_2. Even if deformation temperetures are below the intrinsic BDTT, the glassy SiO_2 mainly at the triple junctions is softened and acts as a kind of lubricant for grain boundary sliding of $MoSi_2$. Associated with its small grain size, hot-pressed $MoSi_2$ shows substantial plasticity through the grain boundary sliding accommodated by glassy SiO_2. Figs. 1.4 (a) and (b) show a deformed $MoSi_2$ specimen after three point bending test at 1200°C and a corresponding load-displacement curve, respectively. Plastic deformation can be clearly seen from Figs. 1.4 (a) and (b).

Although such plastic deformability at high temperatures provides the more reliability (i.e. without sudden brittle fracture) and the possibility of hot-working like conventional metallic alloys, it also results in poor yield strength and creep resistance.

1.2.5 Mechanical Properties of Conventional MoSi₂ Based Materials

Recently, Jeng et al. [67] reviewed mechanical properties of $MoSi_2$ based materials as shown in Table 1.6 [68-79]. Various research groups have thought to improve the poor fracture toughness at room temperature and low strength at both room and high temperatures, which are typically associated with $MoSi_2$. In general, ductile reinforcements, i.e. metallic particles and

8
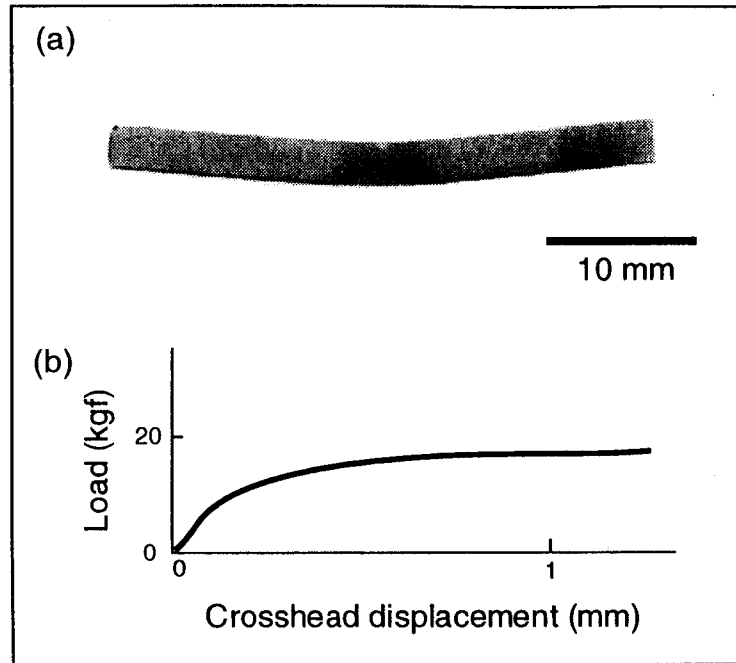
Fig. 1.4   (a) Appearance of deformed $MoSi_2$ specimen (hot-pressed at 1500℃, mean grain size is about 5 μm, 2 wt.% SiO_2) after three point bending test at 1200°C in air. Crosshead speed = 0.5 mm/min, and span = 30mm. (b) Corresponding load- displacement curve.

fibers, are effective to improve the low-temperature fracture toughness of $MoSi_2$. Such ductile materials, however, tend to undergo extensive oxidation and chemical reactions at elevated temperatures. Although coating the ductile phase reinforcement can inhibit the oxida- tion and reactions, oxidation resistant and chemically inert dispersoids are intrinsically desirable; SiC and some oxide ceramics are possible candidate dispersoids. In contrast to moderate or substantial improvement in fracture toughness for $MoSi_2$ based composites, strength values of the materials are still small. Further improvement in mechanical properties is indispensable to practical structural components.

1.3   Objective of This Study

As is mentioned above, conventional $MoSi_2$ based materials show poor fracture strength as structural materials. Needless to say, it is important to improve fracture toughness, but $MoSi_2$ has intrinsically ductile nature at its intended operating temperatures. Thus, to enhance strength is now essentially required in order that $MoSi_2$ becomes an alternative structural material at ultra-high temperatures. Grain-size refinement is needed to improve the fracture strength, and it can be achieved in some extent by simply incorporating second phases to conventional $MoSi_2$ powders. Note that the final grain size in sintered $MoSi_2$ is basically governed by the initial

Table 1.6 Mechanical Properties of $MoSi_2$-Based Composites by Various Processings [67].

Composition	Processing condition	Flexure strength (MPa)	Vickers hardness (GPa)	Fracture toughness $(MPa \cdot m^{1/2})$	Reference
$MoSi_2$	Hot press	~250	8 - 10	2.5 - 3	[14]
$MoSi_2$/10 vol% Nb	Hot press, 1700°C, 30 MPa 40 min	–	–	5	[68]
$MoSi_2$/10 vol% W	Hot press, 1700°C, 30 MPa 40 min	–	–	~5	[68]
$MoSi_2$/20 vol% Ta	Low pressure plasma deposition	–	8.65±0.28	6.9(SD), 4.4(PSD)	[69]
$MoSi_2$/20 vol% Ta	LPPD+HIP	–	7.86±0.12	5.9(SD), 4.9(PSD)	[69]
$MoSi_2$/2 wt% C	Hot press, 1830°C, in Ar	–	12.74	5.5 (800°C) 11.5 (1400°C)	[70]
$MoSi_2$/25 vol% Al_2O_3	Vacuum hot press, 1500-1600°C, 46 MPa	550 (at 1100°C)	–	4.8 (R.T.) 6.5 (1100°C)	[71]
$MoSi_2$/20 vol% ZrO_2	Hot press, 1700°C, 32 MPa	–	–	7.8	[72]
$MoSi_2$/30 vol% PSZ	Hot press, 1700°C, 30 MPa	–	8.49	6.56	[73]
$MoSi_2$/20 vol% $SiC_{w(VLS)}$	Hot press, 1625-1640°C, 41.4 MPa, in CO-CO_2	310	-	8.20	[14]
$MoSi_2$/20 vol% $SiC_{w(VS)}$	Hot press, 1800-1900°C, in Ar	~280	-	6.59	[74]
$MoSi_2$/20 vol% SiC	Hot press, 1700°C, 35 MPa in an inert atmosphere	263	-	6.37	[75]
$MoSi_2$/30 vol% SiC	Displacement reaction, at 1350°C, at 10^{-4} MPa	-	12.8	-	[76]
$MoSi_2$/30 vol% SiC	Hot press & solid state reaction, at 1350 and 1700°C	-	14.2	8.70	[76]
50$MoSi_2$-50WSi_2/ 20 vol% SiC	Hot press, 1900°C, 30 MPa in Ar	80 (at 1500°C)	-	-	[77]
$MoSi_2$/20 vol% TiC	Hot press, 1700°C, 35 MPa in an inert atmosphere	125.3	-	5.00	[78]
$MoSi_2$/20 vol% TiB_2	Plasma spray	380	10.36±0.26	6.10	[79]

particle size of $MoSi_2$ powders. Unfortunately, an ultra fine $MoSi_2$ powder includes much oxygen, and using such a powder will decrease high-temperature strength and creep resistance, in contrast to the expected increase in room temperature strength. Although more expensive processes, of course, enable to decrease oxygen content, the presence of glassy SiO_2 phase is generally unavoidable in $MoSi_2$, as a result of the thermodynamic stability of this phase.

In this study, the author proposes a new material design concept for $MoSi_2$ based materials, "simultaneous strengthening and toughening both of $MoSi_2$ matrix and SiO_2 grain boundary phase."

The objects of this study are as follows: first is to develop very strong and tough $MoSi_2$ based composite up to high temperatures based on the new material design, and to clarify the mechanisms of the strengthening and toughening. Second is to reveal the relationship between

microstructure and mechanical properties of $MoSi_2$ based composites, and to establish the strategy to fabricate excellent and promising $MoSi_2$ based materials.

In the concrete, the author has preferred to adopt a fine $MoSi_2$ powder (about 1 μ m) with rather high oxygen content (about 1 wt%) as a starting material, and applied composite and alloying techniques for improving the properties of matrix and grain boundary phase.

This thesis consists of following chapters.

In Chapter 2, the formation mechanism of discrete glassy SiO_2 in $MoSi_2$, and sintering mechanism of a $MoSi_2$ powder were discussed on the basis of observation from an $in situ$ (i.e. direct and dynamic) SEM. Furthermore, the glassy SiO_2 in sintered $MoSi_2$ was quantitatively evaluated by the cryogenic specific heat measurements, which has been recently developed for Si_3N_4 based materials. Combination of these two methods enabled more precise evaluation of sintered $MoSi_2$ based material.

In Chapter 3, the fabrication processes and the relationship between microstructure and mechanical properties of $MoSi_2$/nano-sized SiC composites were revealed. Simultaneous strengthening and toughening both of $MoSi_2$ and glassy SiO_2 were observed by SEM and TEM observations. The mechanisms of improvement in mechanical properties were discussed.

In Chapter 4, the improvement in mechanical properties of powder processed $MoSi_2$ by the additions of Sc_2O_3 and Y_2O_3 was discussed. These two rare earth oxides have small ionic radii of cations, so that they have higher atomic bond strength and elastic modulus than other oxides. A new approach, $in situ$ crystallization of grain boundary glassy SiO_2, was given.

In Chapter 5, the improvement in mechanical properties of powder processed $MoSi_2$ by the additions of ZrO_2 and HfO_2 was argued. The combination effects of $in situ$ crystallization and transformation toughening were pointed out.

In Chapter 6, the combination effects of Al-alloying and nano-sized SiC dispersions were discussed. Mo-Si-Al alloys and Mo-Si-Al/nano-sized SiC composites were prepared by the powder metallurgical process from novel Mo-Si-Al pre-alloyed powders, and their microstructure and mechanical properties were evaluated.

In Chapter 7, the first systematic study of $Mo_{\leq 5}Si_3C_{\leq 1}$, closely relating to sintered $MoSi_2$, and $Mo_{\leq 5}Si_3C_{\leq 1}$-based composites was conducted. Single phase $Mo_{\leq 5}Si_3C_{\leq 1}$ was successfully synthesized by the reactive hot-pressing (RHP) from elemental molybdenum, silicon, and carbon powders. Feasibility of $Mo_{\leq 5}Si_3C_{\leq 1}$-$MoSi_2$ pseudo-binary system was indicated.

In Chapter 8, the present results were summarized, and strategies to fabricate excellent and promising $MoSi_2$ based materials were shown.

Additionally, in Appendix 1, preliminary results of molecular dynamics simulation of single crystal $MoSi_2$ were shown, and possibility of computer simulation of this material was discussed. To the best of the author's knowledge, this is the first application of molecular dynamic method for $MoSi_2$.

References

1. W. A. Maxwell, "Properties of Certain Intermetallics as Related to Elevated-Temperature Applications 1 -Molybdenum Disilicide," *Rep. RM E9G01*, NACA, Washington, DC, (1949).

2. O. Hönigschmid, *Monatsh. Chem.*, **2 8**, 1017 (1907).

3. E. H. M. Hägglund and N. G. Rehnquist, *Swed Patent 153,961*, (1947).

4. E. Fitzer, K. Reinmuth and H. Schnabel., "Compacting and Sintering of Molybdenum Disilicide," *Arch. Eisenhüttenwesen*, **4 0** [11] 895 - 900 (1969).

5. Kanthal, *Swed Patent 155,836*, (1956, applied in 1953).

6. H. Nowotny, E. Parthé, R. Kieffer and F. Benesovsky, "Das Dreistoffsystem: Molybdän -Silizium-Kohlenstoff," *Monatsh. Chem*, **8 5**, 255-272 (1954).

7. H. Kudielka and H. Nowotny, "Disilizidsysteme," *Monatsh. Chem.*, **8 7** [3] 471-482(1956).

8. H. Nowotny and H. Huschka, "Untersuchungen der Teilsysteme Aluminium-TiSi$_2$, -ZrSi$_2$, -MoSi$_2$ und -WSi$_2$," *Monatsh. Chem.*, **8 8** [4] 494-501 (1957).

9. H. Nowotny and C. Brukl, "Ein Beitrag zum Dreistoff: Molybdän -Aluminium-Silizium," *Monatsh. Chem.*, **9 1** [2] 313-318 (1960).

10. C. Brukl, H. Nowotny and F. Benesovsky, "Untersuchungen in den Dreistoffsystemen: V-Al-Si, Nb-Al-Si, Mo-Al-Si bsw. Cr(Mo)-Al-Si," *Mh. Chem.*, **9 2** [5] 967-980 (1961).

11. E. Erdoes, "Investigation of surface layers of gas turbine alloys," *Internal Rep.*, Dec. 1971

12. E. Fitzer, O. Rubisch, J. Schlichiting and I. Sewdas, *Spec. Ceram.*, 6 (1973).

13. J. Schlichting, "Molybdändisilizid als Komponente moderner Hochtemperaturverbundwerkstoffe, *High Temp. -High Press.*, **1 0**, 241-269 (1978).

14. F. D. Gac and J. J. Petrovic, "Feasibility of a Composite of SiC Whiskers in an MoSi$_2$ Matrix," *J. Am. Ceram. Soc.*, **6 8** [8] C200-C201 (1985).

15. A. K. Vasudévan and J. J. Petrovic, "A Comparative Overview of Molybdenum Disilicide Composites," *Mater. Sci. Eng.*, **A 1 5 5**, 1-17 (1992).

16. O. K. Andersen, O. Jepsen, Vl. N. Antonov, V. N. Antonov, B. Yu. Yavorsky, A. Ya. Perlov and A. P. Shpak, "Fermi surface, bonding, and peudogap in MoSi$_2$," *Physica*, **B 2 0 4**, 65-82 (1995).

17. V. N. Svechnikov, Yu. A. Kocherzhinskii and L. M. Yupko, "Polymorphism of Molybdenum Disilicide," *Dokl. Akad. Nauk SSSR*, **1 8 2** [6] 1313-1314 (1968).

18. V. N. Svechnikov, Yu. A. Kocherzhinskii and L. M. Yupko, "Phase Diagram of the Molybdenum-Silicon System" (in Russian), *Diagrammy Sostoyaniya Metal Sist. Nauka*, 116-119 (1971).

19. S. Inoue, N. Toyokura, T. Nakamura, M. Maeda and M. Takagi, "Properties of Molybdenum Silicide Film Deposited by CVD," *J. Electrochem. Soc.*, **1 3 0** [7] 1603-1607 (1983).

20. W. J. Boettinger, J. H. Perepezko and P. S. Frankwicz, "Application of Ternary Phase Diagrams to the Development of MoSi$_2$-Based Materials," *Mater. Sci. Eng.*, **A 1 5 5**, 33-44 (1992).

21. W. Zachariasen, "Crystal Structure of MoSi$_2$ and WSi$_2$," *Z. Phys. Chem. (Leipzig)*, **1 2 8**, 39-48 (1927).

22. H. J. Goldschmidt, *Interstitial Compounds* (Plenum, New York), 1967.

23. B. K. Bhattacharyya, D. M. Bylander and Leonard Kleinman, "Comparison of fully relativistic energy bands and cohesive energies of MoSi$_2$ and WSi$_2$," *Phys. Rev. B*, **3 2**, 7973-7978 (1985).

24. F. W. Vahldiek and S. A. Mersol, "Phase Relations and Substructure in Single-Crystal MoSi$_2$," *J. Less-Common Met.*, **1 5**, 165-71 (1968).

25. T. A. Adler and C. R. Houska, "Integrated Intensities and Lattice Parameters for MoSi$_2$," *J. Am. Ceram. Soc.*, **6 1** [3-4] 182-183 (1978).

26. JCPDS Powder Diffraction File No. 41-612

27. Y. Suzuki, T. Sekino and K. Niihara, "Effects of Al Substitution and Nano-Sized SiC Dispersion on Microstructure and Mechanical Properties of MoSi$_2$," *Proc. 6th Tohwa University Int'l Symp.*, Fukuoka, October 1996, ed. by Y. Nagano (Tohwa University Press, 1996) pp.189-194.

28. Y. Suzuki and K. Niihara, "Microstructure and Mechanical Properties of SiC Particulate Reinforced Mo-Si-Al Alloy Matrix Composites," *unpublished work*.

29. L. F. Mattheiss, "Calculated structural properties of $CrSi_2$, $MoSi_2$, and WSi_2," *Phys. Rev. B*, **4 5** [7] 3252-3259 (1992).

30. Y. Harada, M. Morinaga, A. Ito and Y. Sugita, "Electronic states of alloying elements in $MoSi_2$ compound," *J. Alloys and Comp.*, **2 3 6**, 92-101 (1996).

31. A. K. McMahan, J. E. Klepeis, M. van Schilfgaarde and M. Methfessel, "Bonding in the Molybdenum Silicides," *Phys. Rev. B*, **5 0** [15] 10742-60 (1994).

32. *Kanthal Super 1900 Heating Element, Advertisement.*

33. H. Yanagida et al. (Eds), *Cyclopedia of Fine Ceramics*, Gihodo Press, Tokyo, (1987).

34. R. Kubo et al. (Eds), *Cyclopedia of Sience and Chemistry*, 4 th Edition, Iwanami Press, Tokyo, (1987).

35. Y. S. Touloukian, R. K. Kirby, R. E. Taylor and T. Y. R. Lee, *Thermophysical properties of matter vol.13: Thermal expansion- Nonmetallic solids*, Plenum, New York (1977).

36. Y. S. Touloukian and E. H. Buyco, *Thermophysical properties of matter vol.5: Specific heat - Nonmetallic solids*, Plenum, New York (1970).

37. S. Bose and R. J. Hecht, "Thermal Properties of $MoSi_2$ and SiC Whisker-Reinforced $MoSi_2$," *J. Mater. Sci.*, **2 7**, 2749-2752 (1992).

38. M. Nakamura, S. Matsumoto and T. Hirano, "Elastic Constants of $MoSi_2$ and WSi_2 Single Crystals," *J. Mater. Sci.*, **2 5**, 3309-3313 (1990).

39. F. W. Glaser, "A note on the metallic behavior of $MoSi_2$," *J. App. Phys.*, **2 2** [1] 103 (1951).

40. Y. S. Touloukian, Intermetallics, Cermets, Polymers, and Composite Systems, Part 1,*Thermophysical properties of High Temperature Solid Materials,"* Vol.6. MacMillian, New York, 1967.

41 P. T. B. Shaffer, *Plenum Press Handbooks of High-Temperature Materials, No.1, Materials Index*, Plenum Press, New York (1964).

42. V. S. Neshpor and G. V. Samsonov, *Dokl. Akad. Nauk. SSSR.*, **1 3 4** [6] 1337-1339 (1960).

43. R. E. Weinmeister and J. E. Mahan, "Electronic Transport and Microstructure in Molybdenum Silicide Thin Films," *Appl. Phys. Lett.*, **3 9** [12] 977-9 (1981).

44. G. V. Samsonov and I. M. Vinitskii, *Handbook of Refractory Compounds*, IFI/Plenum Press, New York, 1980.

45. M. A. Nicolet, S. S. Lau, "Formation and Characterization of Transition-Metal Silicides," *VLSI Electronics: Microstructure Science, Vol.6 Materials and Process characterization*, eds. N. G. Einsprush & G. B. Larrabee, pp.329-464 (1983).

46. Y. Okazaki, K. Kyo, Y. Ito, E. Nishimura and T. Tateishi, "Development of New Ti Alloy for Medical Implant and Standardization of Biomaterials," *Materia Japan*, **3 6** [11] 1092-1099 (1997).

47. Y. Umakoshi, T. Hirano, T. Sakagami and T. Yamane, "Silp Systems and Hardness in $MoSi_2$ Single Crystals," *Scripta Metall.*, **2 3** [1] 87-90 (1989).

48. Y. Umakoshi, T. Sakagami. T. Yamane and T. Hirano, "Planar Faults in $MoSi_2$ Single Crystals Deformed at High Temperatures," *Phil. Mag. Lett.*, **5 9** [4] 159-164 (1989).

49. Y. Umakoshi, T. Hirano, T. Sakagami and T. Yamane, "High Temperature Deformation of $MoSi_2$ Single Crystals with the $C11_b$ Structure," *Acta Metall. Mater.*, **3 8** [6] 909-915 (1990).

50. K. Kimura, M. Nakamura and T. Hirano, "High Temperature Deformation Behabior of $MoSi_2$ and WSi_2 Single Crystals," *J. Mater. Sci.*, **2 5**, 2487-2492 (1990).

51. T. Hirano, M. Nakamura, K. Kimura and Y. Umakoshi, "Single Crystal Growth and Mechanical Properties of $MoSi_2$ and WSi_2," *Ceram. Eng. Sci. Proc.*, **1 2** [9-10] 1619-1632 (1991).

52 S. A. Maloy, T. E. Mitchell, J. J. Petrovic, A. H. Heuer and J. J.Lewandowski, "The Temperature and Strain Rate Dependence of the Flow Stress in $MoSi_2$ Single Crystals," *Proc. High Temperature Silicides and Refractory Alloys*, MRS, Pittsburgh, USA, 1994.

53. S. A. Maloy, T. E. Mitchell and A. H. Heuer, "High Temperature Plastic Anisotropy in $MoSi_2$ Single Crystals," *Acta Metall. Mater.*, **4 3** [2] 657-668 (1995).

54. K. Ito, H. Inui, Y. Shirai and M. Yamaguchi, "Plastic Deformation of MoSi$_2$ Single Crystals," *Phil. Mag. A*, **7 2** [4] 1075-1097 (1995).

55. K. Ito, T. Yano, T. Nakamoto, H. Inui and M. Yamaguchi, "Plastic Deformation of MoSi$_2$ and WSi$_2$ Single Crystals and Directionally Solified MoSi$_2$-Based Alloys," *Intermetallics*, **4**, S119-S131 (1996).

56. K. Ito, "Plastic Deformation of Single Crystals of MoSi$_2$ and Related Transition Metal Disilicides," *Materia Japan*, **3 5** [10] 1102-1107 (1996).

57. D. J. Evans, F. J. Scheltens, J. B. Woodhouse and H. L. Fraser, "Deformation Mechanisms in MoSi$_2$ at Temperatures above the Brittle-to-Ductile Transition Temperature. II. Single-Crystal MoSi$_2$," *Phil. Mag. A*, **7 5** [1] 17-30 (1997).

58. R. C. Bradt and R. E. Tressler, *Deformation of Ceramic Materials*, Prenum Press, New York (1975).

59. O. Unal, J, J. Petrovic. D. H. Carter and T. E. Mitchell, "Dislocations and Plastic Deformation in Molybdenum Disilicide," *J. Am. Ceram. Soc.* **7 3** [6] 1752-1757 (1990).

60. K. Sadananda, C. R. Feng, H. Jones and J. J. Petrovic, "Creep of Molybdenum Disilicide Composites," *Mater. Sci. Eng.*, **A 1 5 5**, 227-239 (1992).

61. T. E. Mitchell, R. G. Castro, J. J. Petrovic, S. A. Maloy, O. Unal and M. M. Chadwick, "Dislocations, Twins, Grain Boundaries and Precipitates in MoSi$_2$," *Mater. Sci. Eng.*, **A 1 5 5**, 241-249 (1992).

62. D. J. Evans, S. A. Court, P. M. Hazzledine and H. L. Fraser, "Deformation Mechanisms in the Intermetallic Compound MoSi$_2$," *MRS Symp. Proc.*, **2 8 8**, 567-572 (1993).

63. D. J. Evans, F. J. Scheltens, J. B. Woodhouse and H. L. Fraser, "Deformation Mechanisms in MoSi$_2$ at Temperatures above the Brittle-to-Ductile Transition Temperature. I. Polycrystalline MoSi$_2$," *Philos. Mag. A*, **7 5** [1] 1-15 (1997).

64. T. G. Nieh, J. Wadsworth and O. D. Sherby, Superplasticity in Metals and Ceramics, Cambridge University Press, UK, 1997.

65. K. Sadananda, H. Jones, J. Feng, J. J. Petrovic and A. K. Vasudevan, "Creep of Monolithic and SiC Whisker-Reinforced MoSi$_2$," *Ceram. Eng. Sci. Proc.*, **1 2** [9-10] 1671-1678 (1991).

66. R. Gibala, A. K. Ghosh, D. C. Van Aken, D. J. Srolovitz, A. Basu, H. Chang, D. P. Mason and W. Yang, "Mechanical Behavior and Interface Design of MoSi$_2$-Based Alloys and Composites," *Mater. Sci. Eng.*, **A 1 5 5**, 147-158 (1992).

67. Y. L. Jeng and E. J. Lavernia, "Processing of Molybdenum Disilicide," J. Mater. Sci., **2 9**, 2557-2571 (1994).

68. L, Xiao, Y. S. Kim and R. Abbaschian, *MRS Symp. Proc.*, **1 9 4**, 399 (1990).

69. R. G. Castro, R. W. Smith, A. D. Rollett and P. W. Stanec, "Toughness of Dense MoSi$_2$ and MoSi$_2$/ Tantalum Composites Produced by Low Pressure Plasma Deposition," *Scripta. Metall. Mater.*, **2 6** [2] 207-212 (1992).

70. S. A. Maloy, A. H. Heuer, J. J. Lewandowski, and J. J. Petrovic, "Carbon Addtions to Molybdenum Disilicide: Improved High-Temperature Mechanical Properties," *J. Am. Ceram. Soc.*, **7 4** [10] 2704-2706 (1991).

71. S. C. Tuffe, K. P. Plucknett and D. S. Wilkinson., *Ceram. Engng. Sci. Proc.*, **1 4**, 1199 (1993).

72. J. J. Petrovic, R. E. Honnell, T. E. Mitchell, R. K. Wade and K. J. McClellan, "ZrO$_2$- Reinforced MoSi$_2$ Matrix Composites," *Ceram. Eng. Sci. Proc.*, **1 2** [9-10] 1633-1642 (1991).

73. J. J. Petrovic and R. E. Honnell, "Partially Stabilized ZrO$_2$ Particle-MoSi$_2$ Matrix Composites," *J. Mater. Sci.*, **2 5**, 4453-4456 (1990).

74. W. S. Gibbs, J. J. Petrovic and R. E. Honnell, *Ceram. Engng Sci. Proc.*, **8**, 645 (1987).

75. J.-M. Yang and S. M. Jeng, *MRS Symp. Proc.*, **1 9 4**, 138 (1990).

76. C. H. Henager, Jr., J. L. Brimhall and J. P. Hirth. "Synthesis of a MoSi$_2$/SiC Composite in Situ Using a Solid State Displasement Reaction Between Mo$_2$C and Si," *Scripta. Metall. Mater.* **2 6** [4] 585-589 (1992).

77. J. J. Petrovic and R. E. Honnell, *Ceram. Eng. Sci. Proc.*, **1 1**, 734 (1990).

78. J.-M. Yang, W. Kai and S. M. Jeng, *Scripta. Metall.*, **2 3**, 1953 (1989).

79. R. Tiwari, H, Herman and S. Sampath, "Vacuum Plasma Spraying of MoSi$_2$ and Its Composites," *Mater. Sci. Eng.*, **A 1 5 5**, 95-100 (1992).

In Situ Observation of Discrete Glassy SiO$_2$ Formation and Quantitative Evaluation of Glassy SiO$_2$ in MoSi$_2$ Compacts

Properties, distribution and quantity of grain boundary glassy SiO$_2$ are very important factors to determine the mechanical properties of MoSi$_2$ sintered bodies. It is indispensable for developing MoSi$_2$ based materials to clarify the formation mechanism and the distribution state of glassy SiO$_2$. The formation mechanism of discrete glassy SiO$_2$ in MoSi$_2$, and sintering mechanism of a MoSi$_2$ powder were clarified by *in situ* scanning electron microscopic (SEM) observation method using a new type of direct heating stage with less thermal drift. Furthermore, the glassy SiO$_2$ in sintered MoSi$_2$ was quantitatively evaluated by the cryogenic specific heat measurements, which have been recently developed for Si$_3$N$_4$ based materials.

2.1 Introduction

As discussed before, mechanical properties of MoSi$_2$ are strongly affected by the grain boundary phases. Intergranular glassy SiO$_2$ in MoSi$_2$ compacts degrades mechanical properties, especially for high-temperature strength and creep resistance. The glassy SiO$_2$ phase in MoSi$_2$ sintered bodies forms discrete regions [1-4]; glassy SiO$_2$ in MoSi$_2$ sintered bodies has spherical or irregular shape, as opposed to Si$_3$N$_4$ where glassy SiO$_2$ wets two-grain boundaries and triple points as layers. Fig. 2.1 shows a typical micrograph of hot-pressed MoSi$_2$ taken by optical microscope with polarized light; bright and transparent particles are glassy SiO$_2$. The glassy SiO$_2$ in MoSi$_2$ promotes grain boundary sliding, as in Si$_3$N$_4$, because it softens at high temperatures. Although there are such similarities between the two-types of glassy phases, the different morphology of glassy phase results in various different characteristics between MoSi$_2$ and Si$_3$N$_4$, for example, on the sintering mechanism, bonding state and so on (Table 2.1). The formation mechanism of discrete glassy SiO$_2$ phase in MoSi$_2$ can be assumed by the wettability between MoSi$_2$ and glassy SiO$_2$, but it is actually still unclear. Thus, to make it clear is essential for future development of MoSi$_2$ based materials with excellent properties.
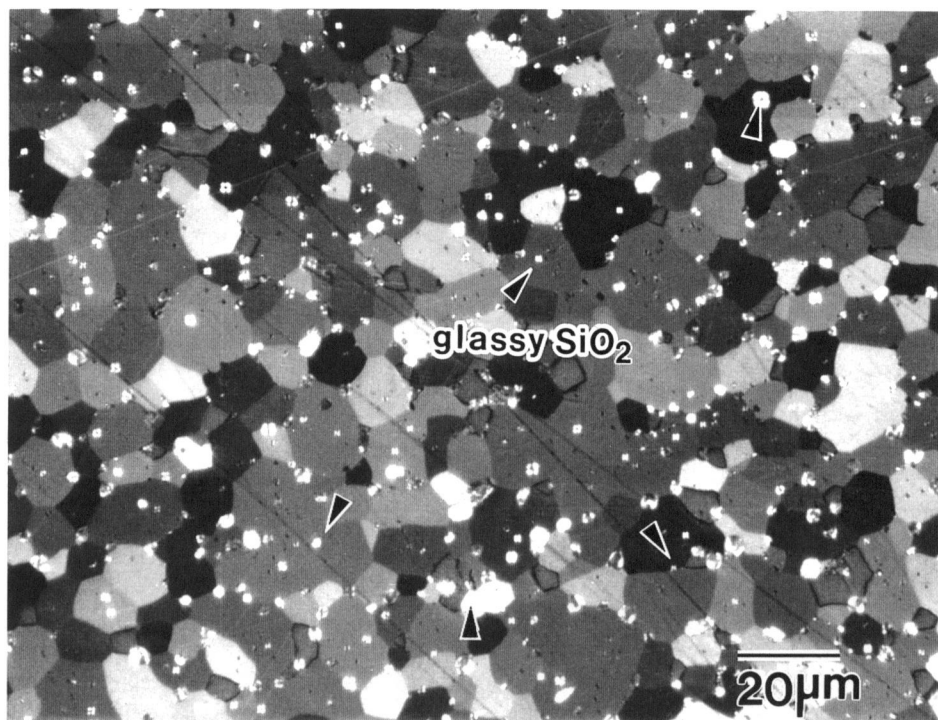
Fig. 2.1 Polarized optical micrograph for a $MoSi_2$ compact hot-pressed at 1700°C, 1 h; average matrix grain size was 13.9 μm.

Table 2.1 Comparison between $MoSi_2$ and Si_3N_4 related to glassy SiO_2 phase.

	$MoSi_2$	Si_3N_4
Morphology of SiO_2	Discrete particles	Films between two-grain boundaries
Bonding at grain boundaries	Direct bonding	Indirect bonding
Sintering mechanism	Solid state sintering	Liquid phase sintering

Moreover, to clarify the influences of glassy phase in sintered $MoSi_2$, quantitative evaluation of the glassy phase is indispensable. Watari et al. [5,6] reported that the glassy SiO_2 phase in Si_3N_4 sintered bodies can be quantitatively analyzed by cryogenic specific heat measurement. Hamasaki et al. [7,8,9] extended the cryogenic specific heat measurement method so as to distinguish the glassy and crystalline SiO_2 in Si_3N_4. Although the morphology of glassy SiO_2 in $MoSi_2$ and Si_3N_4 sintered bodies are quite different each other, it is expected that the quantitative evaluation by specific heat measurements can be applicable for $MoSi_2$ because specific heat is a structure-insensitive physical parameter.

In this chapter, the formation mechanism of discrete glassy SiO_2 phase in $MoSi_2$ was studied by *in situ* scanning electron microscopic (SEM) observation using a new type of direct heating stage with less thermal drift. Moreover, the glassy SiO_2 in $MoSi_2$ sintered bodies was

quantitatively evaluated by the cryogenic specific heat measurements. The effects of glassy phase on $MoSi_2$ sintered bodies will be discussed.

2.2 Outlines of Adopted Evaluation Methods

2.2.1 Background and Benefits of *In Situ* SEM Observation

In situ experiments in transmission electron microscopes (TEM) have been well established and applied to wide fields of materials science [10]. Recently, Kamino et al. [11,12] developed a heating stage for TEM, in which a fine tungsten wire (25 μ m in diameter) was used as a heating element. The heating stage was more stable (with less thermal drift) and suitable for high-temperature observation up to $1400°C$. Niihara and Sekino collaborated with Kamino et al. on this [13]. They also developed this type of heating stage for a field emission scanning electron microscope (FE-SEM), and this was put into practical use in 1994 [14]. The SEM hot-stage is also very stable (i.e. less thermal drift) up to high temperatures, so it enables dynamic high-temperature observation with nanometer scale [15]. Since the *in situ* SEM method is more sensitive for surface and 3-dimensional structure and less radioactive than the *in situ* TEM method, the *in situ* SEM method is suitable for studying surface diffusion, sintering behavior and so on.

Shaw et al. [16] reported that exposure of clean $MoSi_2$ surface (sputter-etched, i.e. without SiO_2 film) to the air resulted in rapid oxidation of $MoSi_2$ surface. Hence, a conventional technique, that is, heat-treatment and following SEM observation, may result in further oxidation of $MoSi_2$ surface. On the other hand, environmental effects, such as oxygen and moisture, can be minimized for the *in situ* SEM experiment. That is a distinct advantage of this method.

2.2.2 Theory of Quantitative Evaluation of Glassy SiO_2 by Cryogenic Specific Heat Measurements

Debye Specific Heat Model

In the Debye approximation for crystalline materials [17,18], the total phonon energy is written as,

$$U = 9Nk_BT\left(\frac{T}{\theta_D}\right)^3 \int_0^{\theta_D/T} \frac{x^3}{e^x-1}dx \tag{2.1}$$

where N is the number of atoms, k_B is the Boltzmann constant, θ_D ($= h\nu_{max}/k_B$) is the Debye temperature, and $x \equiv \theta/T = (h\nu/k_B)/T < \theta_D/T = (h\nu_{max}/k_B)/T$.

The specific heat at constant volume (isochoric specific heat,C_V) is found easily by differentiating Eq. 2.1 with respect to temperature. Then,

$$\left(\frac{\partial U}{\partial T}\right)_V \equiv C_V = 9Nk_B\left(\frac{T}{\theta_D}\right)^3 \int_0^{\theta_D/T} \frac{e^x x^4}{(e^x-1)^2}dx \qquad (2.2)$$

Eq. 2.2 is called as Debye's specific heat formula. At $T \gg \theta_D$, the integral part of Eq. 2.1 becomes

$$\int_0^{\theta_D/T} \frac{x^3}{e^x-1}dx \approx \int_0^{\theta_D/T} x^2 dx = \frac{1}{3}\left(\frac{\theta_D}{T}\right)^3 \qquad (2.3)$$

The total phonon energy U approaches $3Nk_B T$, and the heat capacity C_V becomes $3Nk_B$, equivalent to the classical Dupong-Petit law. On the other hand, at very low temperatures, the integral part of Eq. 2.1 can be approximate by letting the upper limit go to infinity. Then

$$\int_0^{\theta_D/T} \frac{x^3}{e^x-1}dx \approx \int_0^\infty \frac{x^3}{e^x-1}dx = \frac{\pi^4}{15} \qquad (2.4)$$

Thus the total phonon energy U and the isochoric specific heat C_V are

$$U = \frac{3\pi^4}{5}Nk_B T\left(\frac{T}{\theta_D}\right)^3 \qquad (2.5)$$

$$C_V = \frac{12\pi^4}{5}Nk_B\left(\frac{T}{\theta_D}\right)^3 = 234Nk_B\left(\frac{T}{\theta_D}\right)^3 \qquad (2.6)$$

which is the Debye T^3 approximation. In 1 mole of elemental solid, for example, there are Avogadoro's number of atoms ($N = N_A$), so that Nk_B becomes R; the molar heat is

$$C_V = 234Nk_B\left(\frac{T}{\theta_D}\right)^3 = 1944\left(\frac{T}{\theta_D}\right)^3 [\text{Jmol}^{-1}\text{K}^{-1}] \qquad (2.7)$$

At sufficiently low temperatures, the T^3 approximation is quite good [5-9,18], and the difference between the isochoric specific heat and the isobaric one can be negligible at the cryogenic temperatures.

Abnormal Specific Heat in Noncrystalline Materials

Contrary to the excellent agreement between observed and theoretical specific heat at cryogenic temperatures for crystalline materials, Zeller and Pohl [19] reported that noncrystalline solids do not obey the Debye T^3 law; the observed specific heat for noncrystalline materials was extremely larger than the theoretical one, and this was attributed to the scattering of phonons. Although the real crystals have excess specific heat due to the lattice imperfection, such excess specific heat is much smaller than the abnormal specific heat for noncrystalline solids [19].

Hence, the amount of glassy phase in crystalline solids can be determined by the theoretical specific heat of crystalline materials calculated from the Debye T^3 law and the experimental specific heat of pure glass [5-9]. In this study, this technique was first applied for sintered $MoSi_2$.

2.3 Experimental Procedure

2.3.1 *In Situ* Observation by FE-SEM with Hot-Stages

The vacuum of the specimen chamber, in the field emission scanning electron microscope (Hitachi, S-5000) was kept between 1×10^{-6} and 2×10^{-6} Pa during the *in situ* heating experiment. Elemental analysis had to be carried out at room temperature (i.e. before and after heating), using an energy dispersive X-ray spectrometer (EDS, HORIBA EMAX-5770), in order to protect the Si semiconductor detector of EDS from thermal radiation.

The heating element was a fine tungsten wire (25 μm in diameter), heated by direct electric current supplied by dry batteries [11,14]. Fig. 2.2 shows the direct heating holder and its circuit. The $MoSi_2$ powder (mean particle size: 1.01 μm, Japan New Metal Co. Ltd.) was mounted on a tungsten heater using a paint-brush. Less than about 1 μm particles became attached to the heater by the surface energy. The specimens were then blown by a blower to remove the particles not attached firmly to the heating element. The temperature of the heating element was estimated by the heating current [11,14], and calibrated with a pyrometer.
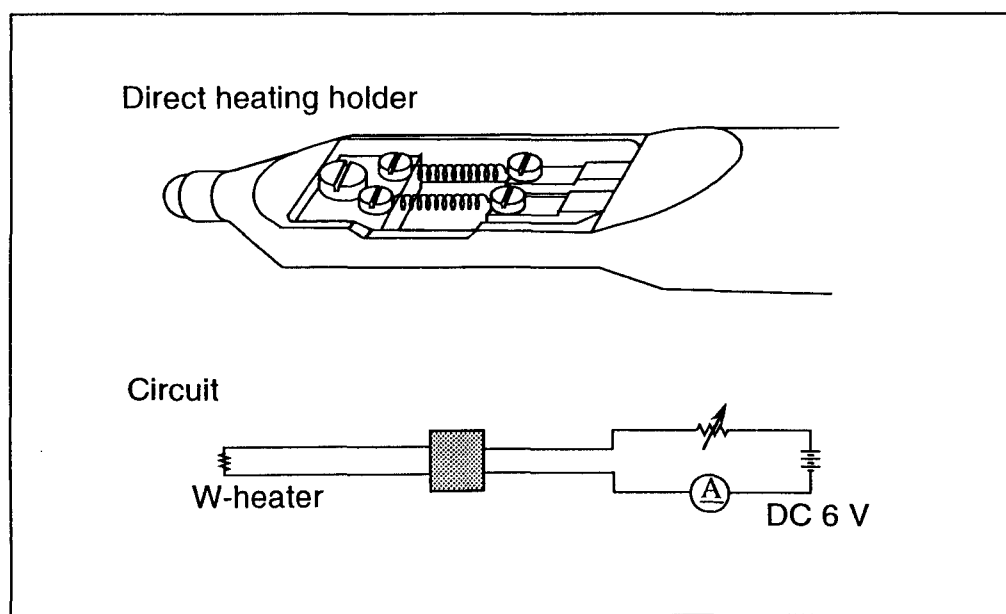

Fig. 2.2 Structure of a direct heating holder for FE-SEM; the holder is a side-entry type. Two tungsten heaters are attached and can be controlled independently.

19

2.3.2 Cryogenic Specific Heat Measurements

Two types of hot-pressed $MoSi_2$ were investigated in this study. Sample A was hot-pressed from an ultra fine $MoSi_2$ powder (special order grade, Japan New Metals Co., Ltd.; powder A) with a mean particle size of 1.01 μm, identical with the powder used for the *in situ* SEM observation. Sample B was also hot-pressed from a usual fine $MoSi_2$ powder (fine grade, Japan New Metals Co., Ltd.; powder B) with a mean particle size of 2.49 μm. The results of chemical analysis of powders are shown in Table 2.2. The major impurities of the powders were oxygen, carbon and iron. It is clear that there are more impurities in the powder A than in the powder B. The higher impurities level of the powder A is attributed to the longer crushing treatment and more oxidation of fresh surfaces. Table 2.3 shows the calculated composition of starting powders. The calculation was made assuming that most oxygen existed as amorphous SiO_2 on $MoSi_2$ surfaces and a little as iron oxide.

Starting powders were packed into carbon dies coated with BN and then hot-pressed at 1500°C under an applied pressure of 30 MPa for 1 h in an argon atmosphere. The sintered disks were 44 mm in diameter and 5.0 mm in thickness. Hot-pressed samples were machined into rectangular prisms with the size of 15 mm× 15 mm× 3 mm for cryogenic specific heat measurement using diamond saw.

The cryogenic specific heat was evaluated at temperatures from 10 to 30 K using an adiabatic calorimeter at Nagaoka University of Technology. The details of the cryogenic specific heat measurement has been described elsewhere [9].

Table 2.2 Results of Chemical Analyses of $MoSi_2$ starting powders.

	Mo*	Si	O	C	Fe (wt%)
Powder A (~ 1.01 μm)	62.71	35.68	1.14	0.23	0.24
Powder B (~ 2.49 μm)	62.93	36.53	0.39	0.02	0.13

*The content of Mo was calculated so that the total content was 100%.

Table 2.3 Calculated composition of $MoSi_2$ starting powders.

	$MoSi_2$	Mo_5Si_3	glassy SiO_2	Free-C	Fe_2O_3 (wt%)
Powder A (~ 1.01 μm)	91.90	5.58	1.95	0.23	0.34
Powder B (~ 2.49 μm)	97.43	1.74	0.63	0.02	0.18

2.4 Results and Discussion

2.4.1 *In Situ* Observation of Discrete Glassy SiO_2 Formation

Figs. 2.3 (a)-(c) show a sequence of SEM micrographs for the sintering behavior of the $MoSi_2$ powder attached on the tungsten heater. Fig. 2.3 (a) was taken before heating; the $MoSi_2$ powder used was produced by crushing processes, it had angular shapes. The particles became roundish with an increase in temperature in order to decrease the surface energy, and started to connect each other (Fig. 2.3 (b)). In the upper half of Fig. 2.3 (b), white particles appeared on the surface of the $MoSi_2$ particles. These white particles were glassy SiO_2, confirmed by EDS analysis after cooling. Since SiO_2 is an insulator material, the SiO_2 particles took an electrical charge by the SEM electron beam, resulting in the white contrast. Surface-edge effect also emphasized the particles. The formation mechanism of such discrete glassy SiO_2 can be explained as follows: the starting $MoSi_2$ powder had the oxidized layer (i.e. glassy SiO_2) on the surfaces. Glassy SiO_2 was softened with an increase in temperature, it easily diffused on the surface of $MoSi_2$. Since glassy SiO_2 does not wet $MoSi_2$, glassy SiO_2 condense to form discrete particles.

Due to the condensation of glassy SiO_2 at the surface of the $MoSi_2$ powder, $MoSi_2$ fresh surfaces of different particles directly connected and sintered each other. Hence, the sintering mechanism of $MoSi_2$ can be categorized as solid state sintering, unlike to the Si_3N_4 whose sintering mechanism is categorized as liquid phase sintering. The progress of sintering was observed in Fig.2.3 (c); the bonding area and the radius of curvature between particles increased. Rearrangement of particles were also observed. The necking was initiated around 1000°C, which was calibrated against the heating current. It was in good agreement with that for the hot-press sintering.

Although the vaporization of the glassy phase was observed during the *in situ* SEM experiments due to its high level vacuum condition (7×10^{-7}Pa), it will not be so severe under hot-pressing conditions; the vacuum level for normal vacuum hot-pressing is the order of 10^{-2}Pa -10^{-1}Pa. Thus, the vaporization of glassy SiO_2 in $MoSi_2$ powder compacts seems to be difficult under actual hot-pressing conditions. Even if it vaporizes, it will easily consolidate on the $MoSi_2$ powder surface due to the high green density. That is why $MoSi_2$ sintered bodies include glassy SiO_2.

2.4.2 Quantitative Evaluation of Glassy SiO_2 in $MoSi_2$ Compacts

For electric conducting materials, it is important to consider the contribution of electronic specific heat. However, it is small when temperatures above liquid helium temperature [20], and can be negligible in this experiment (10 - 30 K). The difference between isobaric and isochoric specific heats (C_p and C_V) is also negligible at such low temperatures. Thus, the C_p from experiments and the C_V from Debye theory were directly compared.
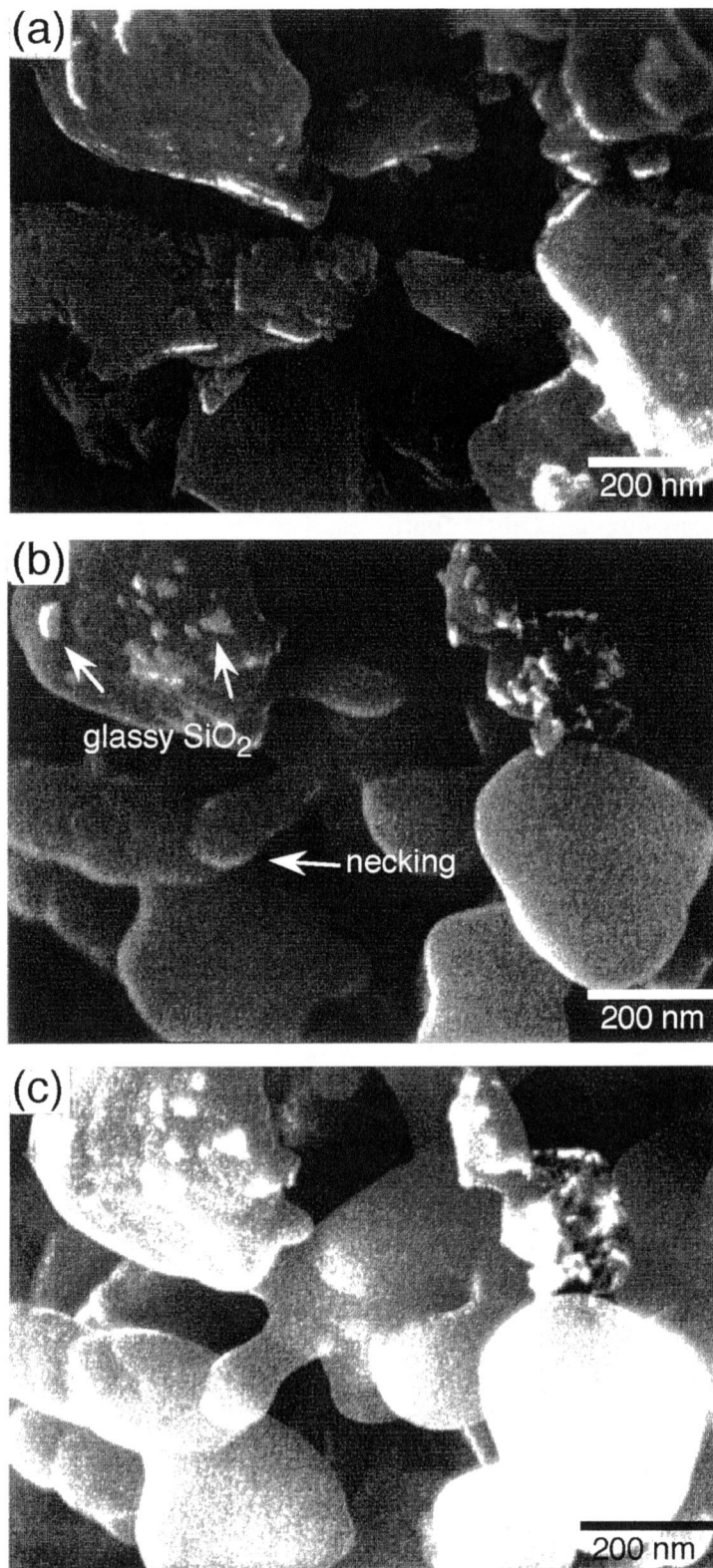
Fig. 2.3 Series of the *in situ* SEM observation for MoSi$_2$ powder; (a) before heating, (b) formation of discrete glassy SiO$_2$ and (c) progress of sintering.

The difference between crystalline and noncrystalline states is observable by a deviation of specific heat from the Debye T^3 law. Fig. 2.4 shows the measured specific heat and calculated specific heat with reported Debye temperature for $MoSi_2$ ($\theta_D = 759$ K[21]). With applying the Debye theory, different atoms (i.e. molybdenum and silicon) were considered lattice dynamically equivalent [5-9]. Specific heat was calculated per 1 mol of $MoSi_2$ (i.e. 3 mol of atoms) from Eq. 2.6, and then it divided by 0.15211 kg (1 mol of $MoSi_2$) for calibrating per a 1 kg. Measured specific heat was in good agreement with calculated one ranging from about 20 K to 30 K for both samples, however, the measured values were larger than calculated ones at lower temperatures. Thus, the result shown in Fig. 2.4 indicates the existence of glassy phase in $MoSi_2$ sintered bodies. Fig. 2.4 also suggests that the content of glassy phase in sample A was larger than that in sample B.

The specific heat of a sintered body can be represented by following equation,

$$C = (1-x)\ C_1 + x\ C_2 \tag{2.7}$$

where C, C_1, C_2, and x are the total specific heat of the sample, the lattice specific heat of $MoSi_2$ calculated from the Debye theory, the specific heat of the grain boundary glassy SiO_2, and the weight fraction of grain boundary glassy phase, respectively.

TEM-EDS analysis strongly suggested that the grain boundary glassy phase in $MoSi_2$ was mainly composed of SiO_2. Thus, the literature value of the specific heat for glassy SiO_2 [19] was applied to the following calculation. $Mo_{\leq 5}Si_3C_{\leq 1}$ phase was ignored in the calculation, because physical properties of $Mo_{\leq 5}Si_3C_{\leq 1}$ is much closer to those of $MoSi_2$ than those of glassy SiO_2 as is shown in Chap. 7 [22], and because the amount of $Mo_{\leq 5}Si_3C_{\leq 1}$ was not so much. Hence, it was approximated that the hot-pressed bodies were composed of only $MoSi_2$ and glassy SiO_2. At 15 K, where abnormal specific heat was clearly observed, the measured specific heat for sample A (C_A) and B (C_B) were 0.536 and 0.369 J kg^{-1} K^{-1}, respectively. C_A and C_B were interpolated values around 15 K. The calculated specific heat from the Debye theory for $MoSi_2$ (C_1) and the reported specific heat for glassy SiO_2 (C_2) were 0.296 and 10.98 J kg^{-1} K^{-1} at 15 K, respectively.

The weight fractions of glassy phase (x) were calculated by Eq. 2.7 as $x = 0.022$ (2.2 wt%) for sample A and 0.007 (0.7wt%) for sample B. These values were in fair agreement with the calculated contents in raw powder shown in Table 2.3 and the calculated contents from SEM image analysis. Combining these method enables more precise evaluation of sintered $MoSi_2$ based material. The quantitative analysis of glassy SiO_2 by using cryogenic specific heat measurement can be principally applicable to other complex $MoSi_2$ based systems, when Debye temperature of a dispersoid is available. In addition, the cryogenic specific heat measurement is a non-destructive evaluation method, and thus it will enable to evaluate whole complex parts made by $MoSi_2$ based materials without preparing any testing specimens.
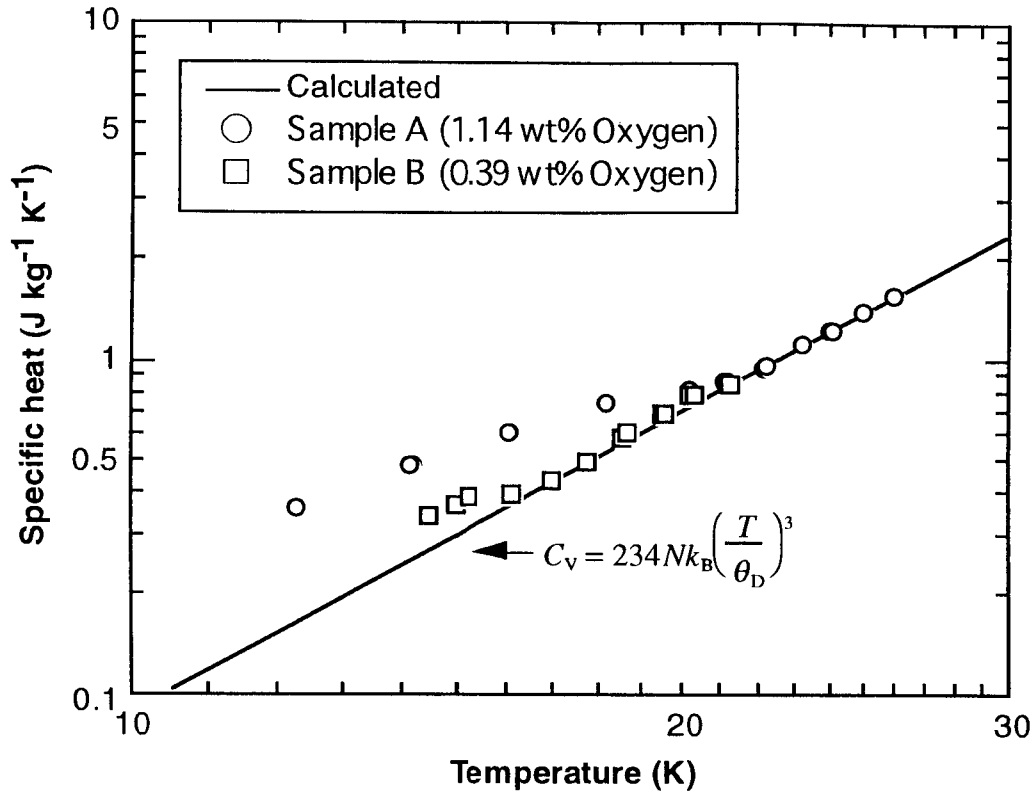
Fig. 2.4 Specific heat dependence with temperature for hot-pressed $MoSi_2$ at cryogenic temperatures. Dotted line shows the specific heat calculated from Debye theory, using the Debye temperature of 759 K for $MoSi_2$; sample A and B were made by hot-pressing $MoSi_2$ powders with the particle size of 1.01 and 2.4 μm, respectively.

2.5 Conclusions

In this chapter, the formation mechanism of discrete glassy SiO_2 phase in $MoSi_2$ was studied by *in situ* SEM observation, and the glassy SiO_2 in $MoSi_2$ sintered bodies was quantitatively evaluated by the cryogenic specific heat measurements. The results are summarized as follows;

1. The *in situ* SEM observation indicated that the discrete glassy SiO_2 in $MoSi_2$ sintered bodies was formed by softening of surface oxide layer of a $MoSi_2$ powder, and following condensation due to the poor wettability between $MoSi_2$ and glassy SiO_2. The *in situ* observation also exhibited that the sintering mechanism of a $MoSi_2$ powder was solid state sintering.

2. The cryogenic specific heat measurement was first applied to the quantitative evaluation of glassy phase in $MoSi_2$. The contents of glassy SiO_2 phase obtained by the cryogenic specific heat measurement agreed with the calculated contents in raw powder.

24

References

1. Y. Suzuki, T. Sekino and K. Niihara, "Effects of ZrO_2 Addition on Microstructure and Mechanical Properties of $MoSi_2$," *Scripta Metall. et Mater.*, **3 3** [1] 69-74 (1995).

2. Y. Suzuki, A. Nakahira, T. Sekino and K. Niihara, "Microstructure and Mechanical Properties of Mo-Si-Al Alloy and Mo-Si-Al/SiC Composite," *J. Jap. Soc. Pow. & Pow. Metall.*, **4 3** [3] 272-277 (1996).

3. R. Gibala, A. K. Ghosh, D. C. Van Aken, D. J. Srolovitz, A. Basu, H. Chang, D. P. Mason and W. Yang, "Mechanical Behavior and Interface Design of $MoSi_2$-Based Alloys and Composites," *Mater. Sci. Eng.*, **A 1 5 5**, 147-158 (1992).

4. K. Shobu, T. Watanabe and K. Tsuji, "Effects of Mo_2B_5 Addition to $MoSi_2$ Ceramics", *J. Ceram. Soc. Jap.*, **9 7** [10] 1311-14 (1989).

5. K. Watari, Y. Seki and K. Ishizaki, "Temperature Dependence of Thermal Coefficients for HIPped Silicon Nitride," *J. Ceram. Soc. Jpn.*, **9 7** [2] 174-81 (1989); *J. Ceram. Soc. Jpn. Int. Ed.*, **9 7** [2] 170-78 (1989).

6. K. Watari, K. Ishizaki and K. Mori, "Evaluation of Glassy Phase in Sintered Silicon Nitride by Low-Temperature Specific Heat Measurements," *J. Am. Ceram. Soc.*, **7 4** [1] 244-246 (1991).

7. T. Hamasaki and K. Ishizaki, "The Quantitative Evaluation of Grain Boundary Phases by Cryogenic Specific Heat Measurements," in *Grain Boundary Controlled Properties of Fine Ceramics*, eds. K. Ishizaki, K. Niihara, M. Isotani and R. G. Ford, Elsevier Applied Science, London and New York, (1992) pp. 53-61.

8. T. Hamasaki and K. Ishizaki, "Qualitative and Quantitative Evaluation of Silicon Nitride Grain-Boundary Phase by Cryogenic Specific Heat Measurements," *J. Am. Ceram. Soc.*, **7 7** [4] 1101-1103 (1994).

9. T. Hamasaki, "Evaluation of Grain Boundary Glassy and Crystalline Phases of Silicon Nitride – Properties of New Non-Destructive Analysis Method –," Ph. D thesis, Dep. Mater. Sci. & Eng., Nagaoka University of Technology, Japan, (1994).

10. H. Fujita (Ed.), *In situ experiments with high voltage electron microscopes*, Research Center for Ultra-High Voltage Electron Microscopy, Osaka University, (1985).

11. T. Kamino, T. Yaguchi and H. Saka, "*In Situ* Study of Chemical Reaction between Silicon and Graphite at 1400°C in a High Resolution/Analytical Electron Microscope," *J. Elec.Microscopy*, **43**, 104-110 (1994).

12. T. Kamino and Ukiana, "High Temperature HREM Image Observation by using Direct Heating Hot Stage," *Denshi-Kenbikyou (in Jpn.)*, **2 8** [3] 202-5 (1994).

13. K. Niihara, T. Sekino, A. Nakahira, T. Kamino and T. Yaguchi, "*In-situ* Fabrication of Tungsten Nanocrystal Encapsulated Carbon Ball in TEM," *Materials Letters*, **2 7** [3] 121-4 (1996).

14. M. Nakagawa, T. Kamino, M. Yamada and M. Sato, "High-temperature/high-resolution SEM observation by a direct heating holder," *Hitachi Technical Data (in Jpn.)*, **7 9**, 1-4 (1995).

15. Y. Suzuki, P. E. D. Morgan, T. Sekino and K. Niihara, "Manufacturing Nano-Diphasic Materials from Natural Dolomite: *In Situ* Observation of Nanophase Formation Behavior," *J. Am. Ceram. Soc.*, **8 0** [11] 2949-2953 (1997).

16. L. Shaw and R. Abbaschian, "Chemical State of the Molydbenum Disilicide ($MoSi_2$) Surface," *J. Mater. Sci.*, **3 0**, 5272-5280 (1995).

17. P. Debye, *Annalen der Physik*, **3 9**, 789-839 (1912).

18. C. Kittel, *Introduction to Solid State Physics*, 6th Ed., John Wiley & Sons, Inc., NY, (1986) chap.5.

19. R. C. Zeller and R. O. Pohl, "Thermal Conductivity and Specific Heat of Noncrystalline Solids," *Phys. Rev. B*, **4** [6] 2029-2041 (1971).

20. J. C. Lasjaunias, M. Saint-Paul, O. Laborde, O. Thomas, J. P. Senateur and R. Madar, "Low-Temperature Specific Heat of $MoSi_2$," *Phys. Rev. B*, **3 7** [17] 10364-10366 (1988).

21. M. Nakamura, S. Matsumoto and T. Hirano, "Elastic constants of $MoSi_2$ and WSi_2 single crystals," *J. Mater. Sci.*, **2 5**, 3309-3313 (1990).

22. Y. Suzuki and K. Niihara, "Synthesis and Mechanical Properties of $Mo_{\leq 5}Si_3C_{\leq 1}$ and $Mo_{\leq 5}Si_3C_{\leq 1}$-Based Composites," *Intermetallics*, **6** [1] 7-13 (1998).

2 5

3

Microstructural Control by Nanocomposite Technology

$MoSi_2$ matrix composites reinforced by nano-sized β-SiC particles were fabricated by hot-pressing, and the relationship between microstructure and mechanical properties was investigated both for monolithic $MoSi_2$ and $MoSi_2$/SiC composites. In the composite system, SiC particles were dispersed mainly at the grain boundaries and partially within the $MoSi_2$ matrix grains. TEM observation showed that the interface between $MoSi_2$ and SiC within $MoSi_2$ matrix grain was directly bonded without any reaction phases. It was found that 15 vol% SiC, added to the $MoSi_2$ matrix, significantly improved the strength to 1215 MPa at room temperature. The enhancement of fracture strength in this system was attributed to the grain growth inhibition mainly by SiC dispersoid. High temperature mechanical properties such as strength and hardness were also improved by homogeneous SiC dispersoids. Added SiC (15 vol%) also improved the high-temperature strength to 1030 MPa at 1000°C.

3.1 Introduction

Advanced structural material systems are being extensively investigated for the applications under severe circumstances such as high temperatures more than 1500° C. Molybdenum disilicide, $MoSi_2$, is an excellent material mainly because of its high melting point of 2030° C and excellent oxidation resistance. In addition, $MoSi_2$ has electroconductivity (resistivity: 40-100 × 10^{-6} Ωcm at 1600°C [1]) and relatively high emissivity [2]. Thus, $MoSi_2$ is expected to be a high-temperature structural material. However, its mechanical properties such as fracture strength and toughness are not sufficiently high for practical uses. Thus, many efforts have focused on improving mechanical properties of this material [3]. SiC is a candidate material as a dispersoid to improve mechanical properties of $MoSi_2$ because of its good oxidation resistance and fairly less reactivity with $MoSi_2$. $MoSi_2$/SiC composite system have been widely investigated; for example, $MoSi_2$/SiC whisker [4-6], $MoSi_2$/SiC platelet [7] and $MoSi_2$/SiC particle systems [8,9]. These studies have dealt with "micro-composites" where micrometer-sized SiC reinforcements were dispersed. These approaches give the potential to

increase the fracture toughness effectively. However, the fracture strength was not so much improved by the micro-sized SiC addition , for instance, 310 MPa with 20 vol% SiC whiskers [4], which is indicated in Chap. 1.

Recently, it has been reported that mechanical properties are significantly improved by the addition of nano-sized second phases in ceramic/ceramic composites [10-16]. Nanocomposite is a new type of materials in which "nano-sized" particles are dispersed within the matrix grains or at the grain boundaries [11]. The microstructure of nanocomposites is schematically shown in Fig. 3.1. Mechanical properties such as fracture strength and toughness are expected to be simultaneously improved by the nanocomposite technology for $MoSi_2/SiC$ system.

In this chapter, $MoSi_2/SiC$ composites were fabricated from a fine $MoSi_2$ powder and a nano-sized SiC powder to obtain good mechanical properties. Effect of SiC reinforcement on microstructure and mechanical properties was evaluated.

3.2 Experimental Procedure

3.2.1 Sample Preparation

A fine $MoSi_2$ powder was supplied by Japan New Metals Co., Ltd. It was fabricated from elemental powders of molybdenum (>99.9 wt.%), and silicon (>99.75 wt.%). The elemental powders (nominal composition; $MoSi_2$) were mixed, heated for solid state reaction, crushed and then sieved. The result of chemical analysis of the $MoSi_2$ powder is shown in Table 3.1. Spectrochemical analysis revealed that the major impurities were 1.22 wt% oxygen, 0.28 wt% carbon and 0.28 wt% iron. The high oxygen content was attributed to the fine particle size (0.98 μm) of the powder. Results of the chemical analyses for a β-SiC powder (Ibiden Co., Ltd.) are also listed in Table 3.1. The primary and average particle sizes of the SiC powder were 0.07 μm and 0.27 μm, respectively.

The experimental procedure is schematically summarized in Fig. 3.2. The SiC content was up to 15 vol% in this experiment. The $MoSi_2$ and SiC powders were mixed by wet ball-milling in 1-butanol with ZrO_2 balls for 24 h, and then the dried mixture was dry ball-milled for 12 h to crush the agglomeration. Monolithic $MoSi_2$ and $MoSi_2/SiC$ mixed powders were packed into carbon dies which were coated with BN and then hot-pressed at 1300 to 1800° C under an applied pressure of 30 MPa for 1 h in an argon atmosphere. The sintered disks were 44 mm in diameter and 5.0 mm in thickness. The hot-pressed bodies were cut, ground and polished into rectangular bars with 4 × 3 × 36 mm in size for bending test and 4 × 2 × 43 mm for shear modulus measurement.

The minimum hot-pressing temperature for densification was 1300°C for the materials with the SiC content up to 10 vol% and 1400°C for 15 vol%. These hot-pressing temperatures were lower than those in previous works (around 1700°C [4-7]). In general, using raw powders with
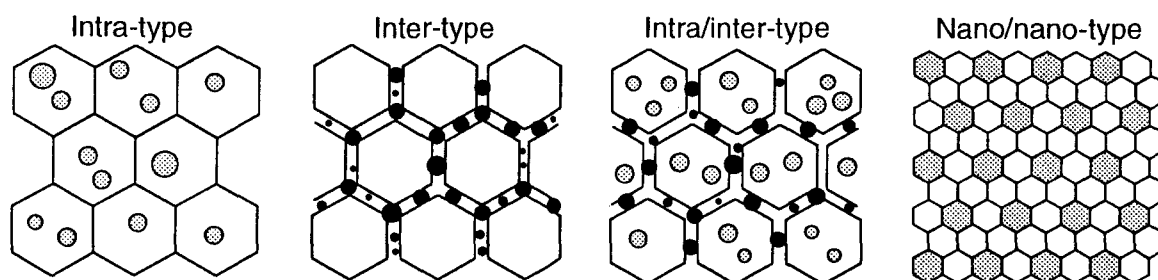
Intra-type   Inter-type   Intra/inter-type   Nano/nano-type

Fig. 3.1 The classification of ceramic nanocomposites [11].

| Matrix Material MoSi₂ powder | Second Phase Material β-SiC powder |

Wet ball-milling in n-BuOH, 24 h

Drying

Dry ball-milling,12 h

Hot-Press Sintering
Temperature: 1300~1800°C
Pressure: 30 MPa
Keep time: 1 h
Atmosphere: Ar

Grinding/Polishing

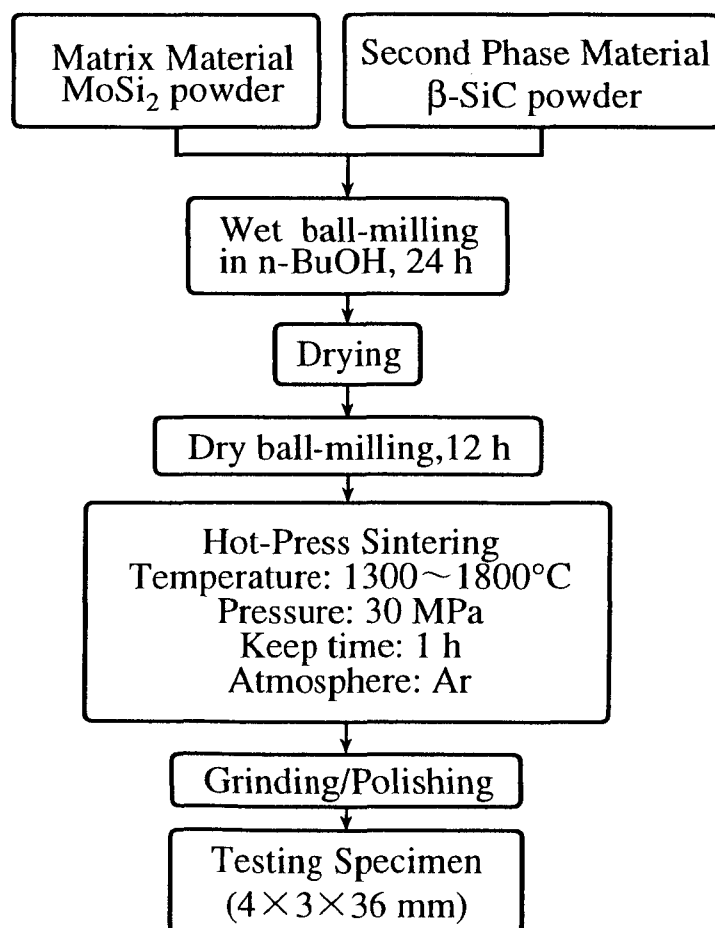Testing Specimen
(4×3×36 mm)

Fig. 3.2 Schematic illustration of experimental procedure.

28

Table 3.1 Chemical analyses of MoSi₂(left) and SiC (right) powders.

	Content			Content (wt.%)
	(wt.%)	(at.%)		
Mo	62.70	32.31	SiC	>99
Si	35.32	62.52	SiO2	0.3
			free-C	0.4
O	1.22	3.77	Fe	0.04
C	0.28	1.15	Al	0.03
Fe	0.28	0.28	H2O*	<0.35

*(110°C,2 h)

finer particle size enable to decrease sintering temperatures owing to their faster transport rate when there is no hard agglomeration [17]. The decrement of the hot-pressing temperatures for densification were attributed to the smallness of the $MoSi_2$ powder (0.98 µm) compared with that in the literatures (typically about 400 mesh [4-7]).

3.2.2 Evaluation Methods

Phase identification was carried out by the X-ray diffraction (XRD) analysis using a *RIGAKU* Rotaflex diffractometer using a Cu target operated at 50 kV and 150 mA. The instrument was equipped with a computer-controlled goniometer, a graphite diffracted-beam monochromator, a scintillation counter, and a workstation with analytical software (*RINT*, by *RIGAKU*).

Bulk densities were measured by the Archimedes method in toluene at room temperature; temperature corrections were always carried out for the density measurements. Microstructure was characterized by scanning electron microscopy (SEM, HITACHI S-5000) with an energy dispersive X-ray spectrometer (EDS, HORIBA EMAX- 5770). Samples for SEM observations were pre-coated with Au. Transmission electron microscopy (TEM, HITACHI H-8100) with EDS (Phillips PV9900) was also applied to the microstructural characterization. Average grain size was calculated by the linear intercept method for polarized optical micrographs. Young's modulus (*E* [GPa]) was determined by the resonance vibration method adjusted to the thickness correction by using Eq. 3.1,

$$E = 0.9465 \times 10^{-9} \frac{m \cdot f_{res}^2 \cdot L^3}{w \cdot t^3} \left\{ 1 + 6.585 \left(\frac{t}{L} \right)^2 \right\}$$

(3.1)

where *m* [g] is the sample mass, f_{res} [Hz] is the resonance frequency, *L* [mm] is the sample length, *w* [mm] is the sample width and *t* [mm] is the sample thickness.

Five or six specimens were subjected to three-point bending test (span: 30 mm) to determine

the fracture strength up to 1200°C. Bending load was applied parallel to hot-pressing axis with a crosshead speed of 0.5 mm/min. Fracture strength (σ_f [MPa]) was calculated from Eq.3.2,

$$\sigma_f = 3PL_s / 3wt^2 \tag{3.2}$$

where P [N] is the applied fracture load, L_s [mm] is the bending span.

The hardness (H_v) was evaluated by Vickers indentation under a conditions of 98 N load with loading duration of 15 s in air for room-temperature measurements, and 4.9 N load in vacuum for high-temperature measurements. The fracture toughness (K_{IC}) was determined simultaneously by the indentation fracture (IF) method using an empirical equation for a median crack [18]. H_v [GPa] and K_{IC} [MPa·m$^{1/2}$] were calculated by the Eqs. 3.3 and 3.4,

$$Hv = \frac{2P\sin(\alpha / 2)}{d^2} \tag{3.3}$$

$$K_{IC} = 0.203(c / a)^{-3/2} H_v \cdot a^{1/2} \tag{3.4}$$

where α (=136°) is the angle comprised between the two opposite faces of the pyramidal indenter, d [μm] is the diagonal of the indentation measured by an optical microscope, c and a (=$d/2$) are the lengths of a median crack and half of a diagonal of a indentation, respectively.

The internal friction and the shear modulus were concurrently measured by the shear resonance vibration method in an argon atmosphere in order to clarify the plastic deformation mechanism at elevated temperatures.

3.3 Results

3.3.1 Phase Identification

XRD analysis indicated that hot-pressed $MoSi_2$ was composed of $MoSi_2$ (tetragonal, C11$_b$) and a small amount of $Mo_{\leq 5}Si_3C_{\leq 1}$(hexagonal, D8$_8$). $Mo_{\leq 5}Si_3C_{\leq 1}$ is the only stable Mo-Si-C ternary phase; called as Nowotny phase [19]). For the composite, β-SiC was identified in addition to above mentioned phases. The formation of $Mo_{\leq 5}Si_3C_{\leq 1}$ phase was ascribed to (1) the deviation from the stoichiometric composition of the $MoSi_2$ powder and (2) the presence of carbon arising from the impurity of powders as well as that from ball milling and hot-pressing processes. Both for $MoSi_2$ and $MoSi_2$/SiC, crystalline SiO_2 peaks were scarcely seen by usual resolution of the X-ray diffraction profiles, while a trace of cristobalite, spontaneously crystallized from glassy SiO_2, was identified by more precise experiments as will be discussed in Chap. 4. These results were consistent with the supposition that most SiO_2 existed as glassy

phase.

From Table 3.1, the composition of the starting $MoSi_2$ powder was calculated (Table 3.2). The calculation was made assuming that phases in the powder were $MoSi_2$, Mo_5Si_3, glassy SiO_2, free carbon and Fe_2O_3, because $MoSi_2$ is a line compound in the Mo-Si binary system and silicon-lean $MoSi_2$ is usually accompanied by Mo_5Si_3 phase as indicated in Fig. 3.3 [20]. During hot-pressing, carbon dissolved in Mo_5Si_3 to form $Mo_{\leq 5}Si_3C_{\leq 1}$. Suppose the $MoSi_2$ starting powder should be fully-densified without changing the initial compositions, the theoretical density (d) would be 6.09 g/cm^3 calculated by using the values in Table 3.2 and the following equation,

$$d = \frac{1}{W_{MoSi_2} / D_{MoSi_2} + W_{Mo_5Si_3} / D_{Mo_5Si_3} + W_{SiO_2} / D_{SiO_2+}...} \tag{3.5}$$

where W_i and D_i are the weight fraction and the density of each phase, respectively. By using the X-ray density value of SiC (3.21 g/cm^3), the theoretical densities of $MoSi_2$/5, 10 and 15 vol% SiC composites are also calculated to be 5.95, 5.81 and 5.61 g/cm^3, respectively; relative densities were calculated using these values. The relative density of monolithic $MoSi_2$ hot-pressed at 1500°C was 98.7%. The relative densities of $MoSi_2$/ 5-15 vol % SiC composites hot-pressed at same temperature were about 96%. Although relative densities would be actually higher (~1%) than these calculated values owing to the change of compositions during processing, calculated ones indicated the tendency that added SiC inhibited densification.

3.3.2 Microstructure

Figs. 3.4(a) and 4(b) show the representative SEM images of microstructure for the $MoSi_2$ and the $MoSi_2$/15 vol% SiC composite hot-pressed at 1500°C, respectively. As seen from Fig. 3.4(a), three phases were identified in the hot-pressed $MoSi_2$; SEM-EDS analysis and selected area diffraction (SAD) by TEM revealed that phases which appear dark, relatively bright and bright were glassy SiO_2, $MoSi_2$ and $Mo_{\leq 5}Si_3C_{\leq 1}$, respectively. In combination with polarized optical microscopic observations, it was revealed that the smaller glassy SiO_2 phase (less than about 1 μm) had a nearly round shape and located within matrix grains and at grain boundaries, especially at triple points. On the other hand, the larger SiO_2 phase (about 1-5 μm) had an irregular shape and dominantly located at grain boundaries, especially at triple points. Most of the $Mo_{\leq 5}Si_3C_{\leq 1}$ phase neighbored with glassy SiO_2. In the composite system (Fig. 3.4(b)), $MoSi_2$ and $Mo_{\leq 5}Si_3C_{\leq 1}$ were similarly identified. However, it was revealed by EDS and SAD analyses that dark regions were composed of not only glassy SiO_2 but also β-SiC. A part of added SiC particles were trapped in glassy SiO_2.

Further SEM observation on fracture surfaces was performed to make clear the fracture mode for $MoSi_2$ and $MoSi_2$/15 vol% SiC composite hot-pressed at 1500°C, and corresponding SEM micrographs are shown in Figs.3.4 (c) and (d), respectively. Comparing Figs.3.4 (c) and (d),

Table 3.2 Phases in the $MoSi_2$ powder.

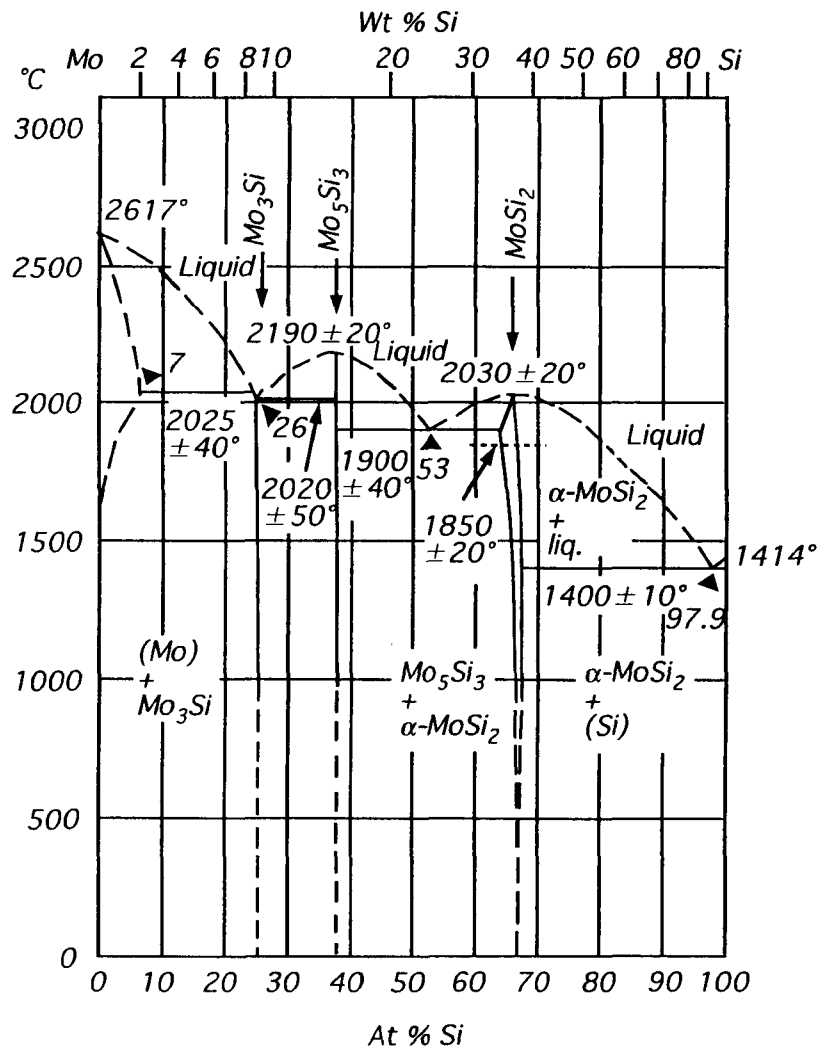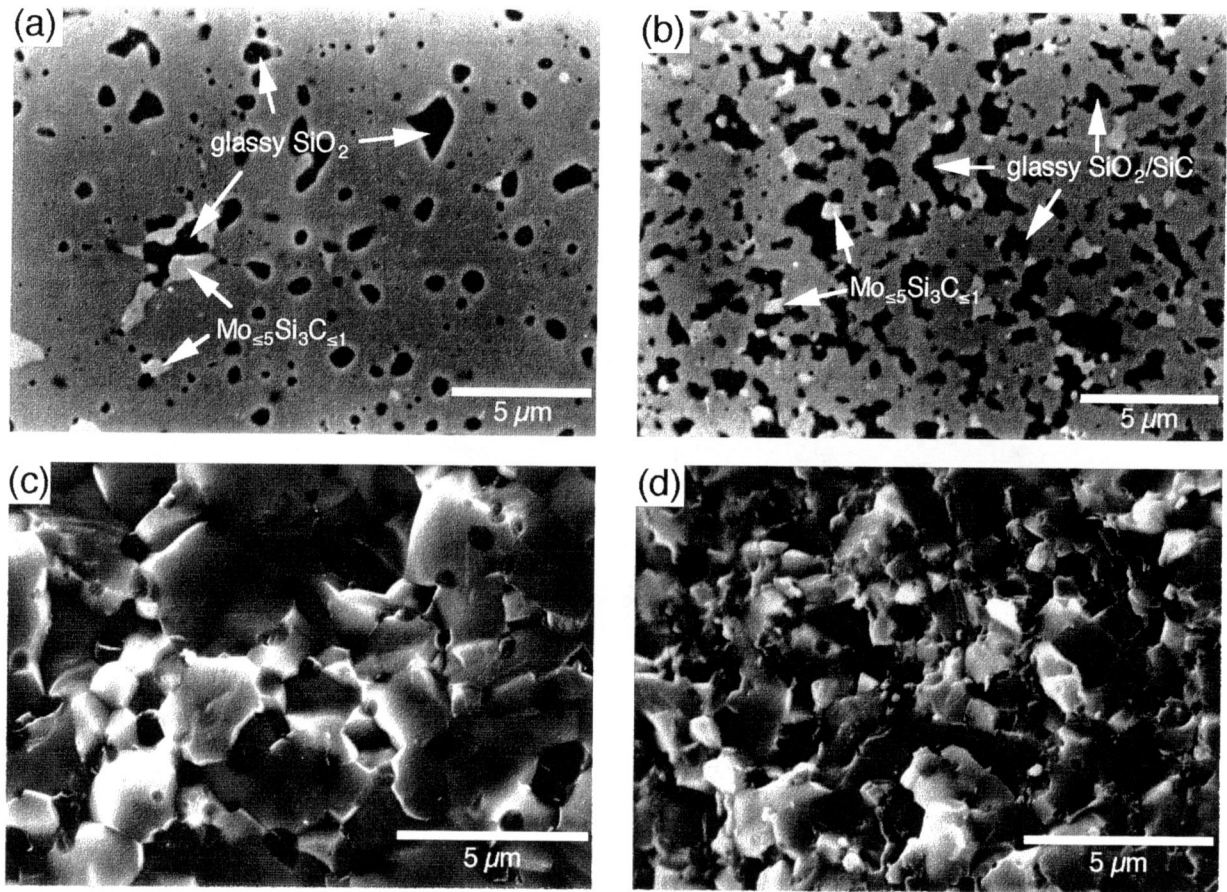|	$MoSi_2$	Mo_5Si_3	glassy SiO_2	Free-C	Fe_2O_3
content (mol%)	89.4	1.6	5.1	3.5	0.4
content (wt%)	91.1	6.2	2.0	0.3	0.4
density (g/cm³)	6.27	8.19	2.22	2.25	5.24

Fig. 3.3 Mo-Si binary phase diagram [20].

Fig. 3.4 SEM micrographs on polished surfaces for (a)$MoSi_2$ and (b)$MoSi_2$/15 vol% SiC composite hot-pressed at 1500°C; fracture surfaces images for (c)$MoSi_2$ and (d)$MoSi_2$/15 vol% SiC composite.

the grain growth of matrix was inhibited in $MoSi_2$/15 vol% SiC composite. As seen from these pictures, the fracture mode of $MoSi_2$/SiC composite differed from that of $MoSi_2$. $MoSi_2$ exhibited a mixture of inter- and intragranular fracture, whereas $MoSi_2$/SiC composite showed almost complete intergranular fracture. For the $MoSi_2$/15 vol% SiC composite system, while glassy SiO_2 at triple points was strengthened by the SiC dispersion, the composite included more grain boundary phase (about 20 vol%) than monolithic $MoSi_2$ (about 6 vol%). Since grain boundary phase is opt to contact each other (see. Fig. 3.4(b)), as was shown in Chap. 2, cracks propagate easier along the grain boundary. This is the main reason for the change of fracture mode. Moreover, it is considered that grain size refinement partially causes the change to the intergranular fracture [21].

TEM observation showed that some nano-sized SiC particles were within the $MoSi_2$ matrix grain. High-resolution TEM image revealed that the intragranular SiC particles directly bonded to $MoSi_2$ without impurity phases as shown in Fig. 3.5(a) and its enlargement (Fig. 3.5(b)). In
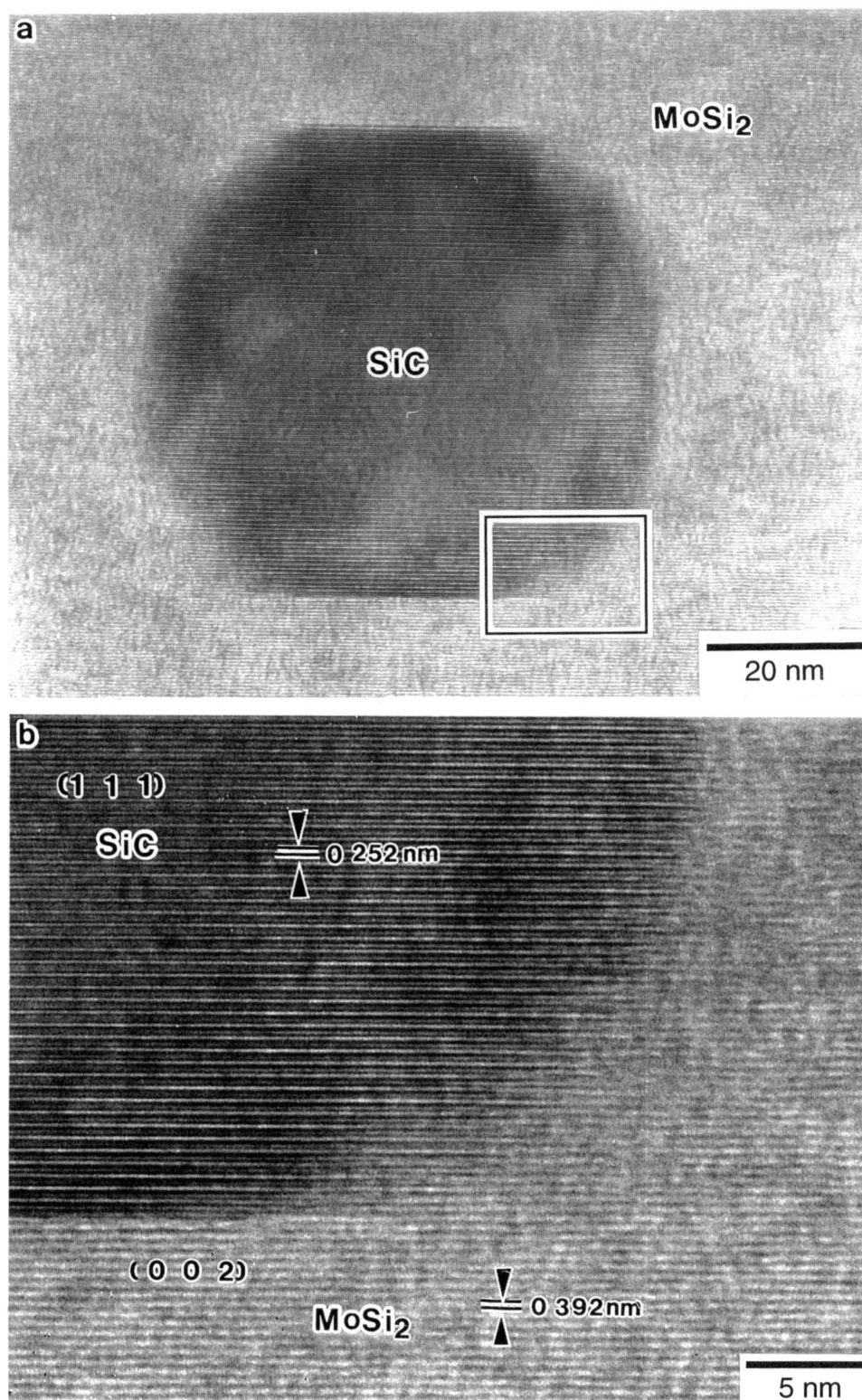
Fig.3.5 · High-resolution TEM images of (a) intragranular nano-sized SiC particle and (b) MoSi$_2$/SiC interface of MoSi$_2$/15 vol% SiC composite hot-pressed at 1500°C.

the vicinity of the interface between MoSi$_2$ and SiC, the interplaner spacing of SiC seemed to be changed. Such a change of the interplaner spacing relaxed the mismatch between MoSi$_2$ and intragranular SiC particles. Although the lattice matching between MoSi$_2$ and SiC does not seem to be good, simply judged the lattice spacing indicated, the matching should be actually better because there are two atomic layers in the {111} spacing of SiC and three layers in the (002) spacing of MoSi$_2$. This relation is discussed later in detail.

3.3.3 Mechanical Properties and Grain Size Refinement

The variation of Young's modulus with the SiC content is shown in Fig. 3.6. The Young's modulus of monolithic MoSi$_2$ was approximately 380 GPa. On the other hand, the Young's modulus of polycrystalline MoSi$_2$ calculated from the elastic moduli of single-crystal MoSi$_2$ is 440 GPa [22]. The difference between observed and calculated values is attributed to the existence of glassy SiO$_2$ which has small Young's modulus.

For composite system, although the Young's modulus of SiC is relatively high (450 GPa [23]), the MoSi$_2$/SiC composites possessed lower Young's modulus than those of the expected values from following equation, which shows the rule of mixture for particulate dispersed composites [24]:

$$\ln E_{\text{sintered body}} = V_{\text{SiC}} \ln E_{\text{SiC}} + V_{\text{Matrix}} \ln E_{\text{Matrix}} \tag{3.6}$$

Taking into account the microstructure, where a large portion of the SiC particles were trapped within glassy SiO$_2$, in particular for smaller additive content, it is considered that the elastic wave through the sintered bodies may be scattered by glassy SiO$_2$. In other words, apparent glassy phase content (actually glassy SiO$_2$ + SiC trapped in glassy SiO$_2$) increased with increasing SiC content. For higher SiC contents (10-15 mol%), however, the portion of SiC particles which directly connect with MoSi$_2$ increases. Hence, the almost constant Young's modulus observed for 5 to 15 % can be explained by the balanced effects of "decrease by apparent increase in glassy phase content" and "increase by actual SiC dispersion." Low Young's modulus observed for MoSi$_2$ with 10 vol% SiC hot-pressed at 1300-1400°C can be simply explained by the residual pores.

The variation of Vickers hardness with the SiC content is shown in Fig. 3.7. The hardness increased with an increase in the SiC content, and decreased with an increase in hot-pressing temperature. Although MoSi$_2$ is a brittle material, indentation test induces the microscopic plastic deformation and pumps the dislocations inside MoSi$_2$ grains. Thus, the hardening of the MoSi$_2$/SiC composites was caused by the inhibition of dislocation movement by the SiC dispersoid and corresponding fine grains. On the other hand, the dislocation moves more easier when the MoSi$_2$ grains become large. This was the main reason why the decrease in hardness was observed for samples hot-pressed at higher temperatures. The maximum value of 13.0 GPa was obtained for the MoSi$_2$/15 vol% SiC hot-pressed at 1400°C.
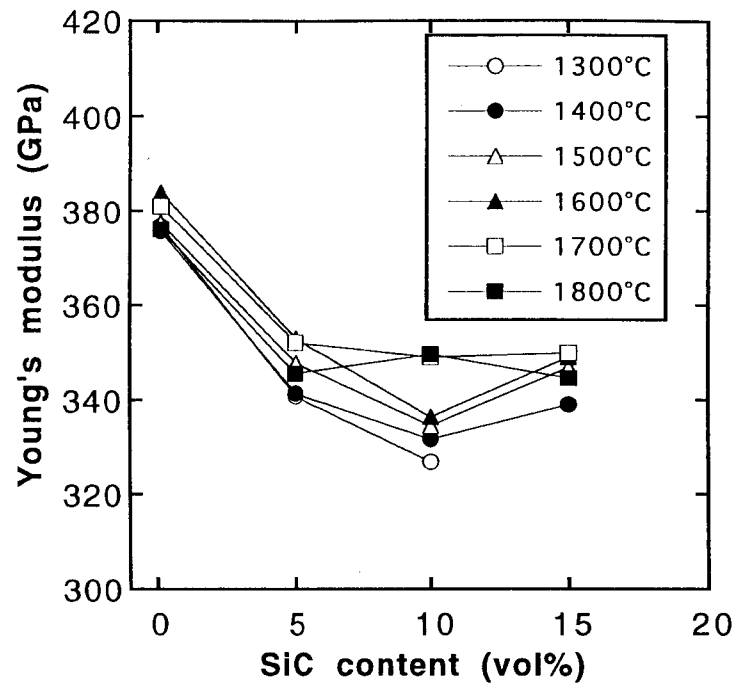
Fig. 3.6 Variation of Young's modulus with SiC content for $MoSi_2$ and $MoSi_2/SiC$ composites.
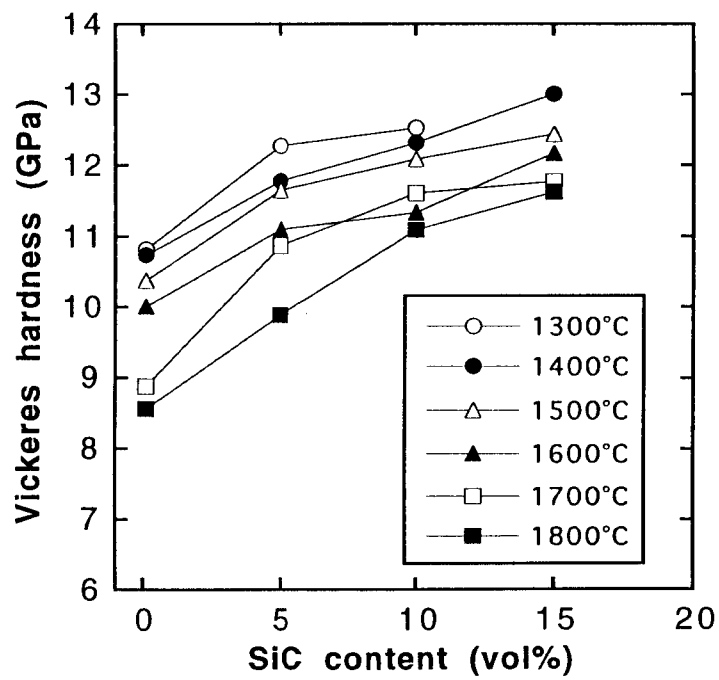

Fig. 3.7 Variation of Vickers hardness with SiC content for $MoSi_2$ and $MoSi_2/SiC$ composites.

The dependence of fracture toughness on the SiC content is shown in Fig. 3.8. The toughness increased with an increase in the SiC content. The influence of sintering temperature upon the fracture toughness was small for the 0-10% additions, because most of the added SiC particles trapped within the grain boundary SiO_2, and thus, the main toughening mechanism may be the crack bowing and deflection inside the brittle glassy SiO_2.

On the other hand, the higher hot-pressing temperature resulted in the higher toughness for the 15 vol% SiC composites. $MoSi_2$/15 vol% SiC composite hot-pressed at 1800°C gave the maximum toughness of about 3.3 MPa·m$^{1/2}$, which was approximately one and half times higher than that of monolithic $MoSi_2$. With higher volume fraction of SiC, the probability that SiC particles dispersed within $MoSi_2$ matrix grains became large. As was shown in the high-resolution TEM observation, intragranular SiC and $MoSi_2$ was directly connected each other. Hence, the residual stress, which was developed during the cooling process owing to the difference of thermal expansion coefficient between $MoSi_2$ and SiC, was also effectively enhanced fracture toughness.

The radial and tangential stresses σ_r and σ_θ are expressed as follows [25]:

$$\sigma_r = -\frac{(\alpha_m - \alpha_f)\Delta T}{\dfrac{1+v_m}{2E_m} + \dfrac{1-2v_f}{E_f}} \tag{3.7}$$

$$\sigma_\theta = \frac{1}{2} \cdot \frac{(\alpha_m - \alpha_f)\Delta T}{\dfrac{1+v_m}{2E_m} + \dfrac{1-2v_f}{E_f}} \tag{3.8}$$

where α is linear thermal expansion coefficient, v is Poisson's ratio, E is Young's modulus and ΔT is the cooling range; m and f express matrix ($MoSi_2$) and filler (SiC), and a negative sign means a compressive stress. Values for the material constants of $MoSi_2$ and SiC are $\alpha_m = 8.51 \times 10^{-6}$ K^{-1} (25–1000°C) [26], $\alpha_f = 4.51 \times 10^{-6}$ K^{-1}(20–1090°C) [26], $v_m = 0.150$ [22], $v_f = 0.192$ [26], $E_m = 440$ GPa [22] and $E_f = 450$ GPa [26]. ΔT is determined as 1000 K because the brittle to ductile transition temperature (BDTT) of $MoSi_2$ is about 1000°C. The calculated residual stresses are $\sigma_r = -1.49$ GPa and $\sigma_\theta = 0.75$ GPa, that is, 1.49 GPa compressive stress arises to the radius direction of the SiC particle located within the $MoSi_2$ matrix.

Fig. 3.9 shows the variation of average grain size of $MoSi_2$ matrix and fracture strength with SiC content for the $MoSi_2$/SiC composites prepared at 1500 and 1800°C. Relatively large grain growth was observed for $MoSi_2$ hot-pressed at 1800°C (15 μm), whereas it was inhibited for composite systems and the average grain size of matrix $MoSi_2$ decreased with SiC addition. These results suggested that added SiC particles reduced the matrix grain growth. The fracture strength increased with the SiC content, and thus SiC dispersion was found to be remarkably effective for $MoSi_2$-based materials with high strength. The $MoSi_2$/15 vol% SiC composite hot-
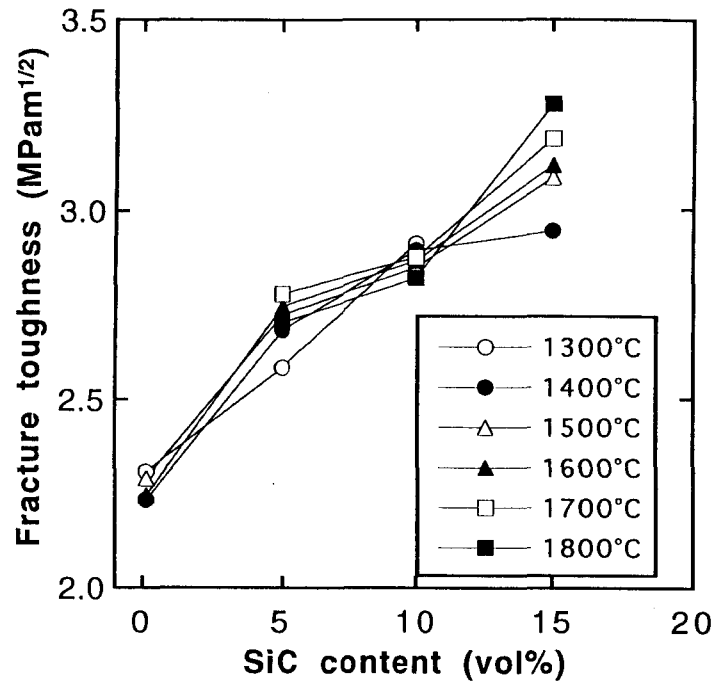
Fig. 3.8 Variation of fracture toughness with SiC content for MoSi$_2$ and MoSi$_2$/SiC composites.

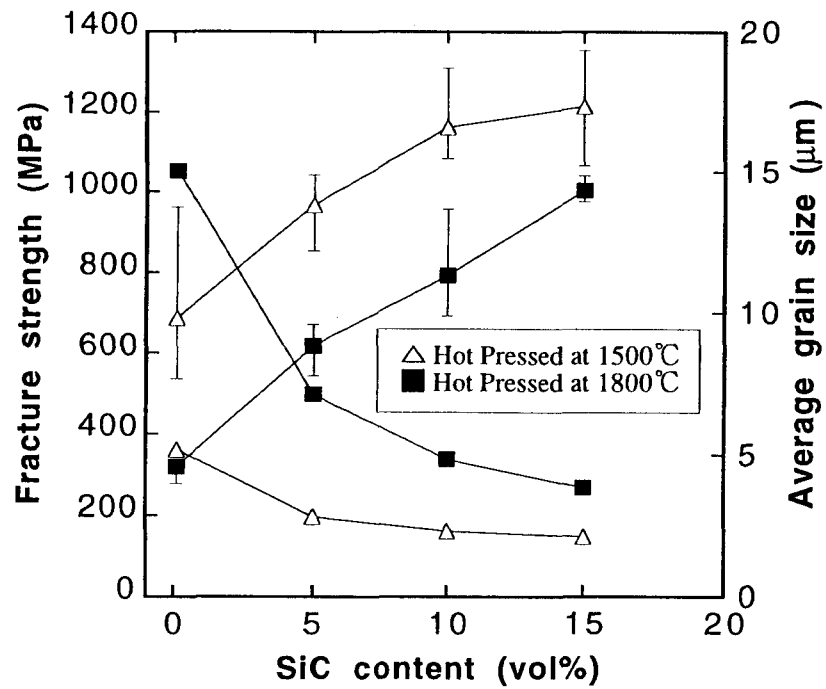**Fig. 3.9** Variation of fracture strenght and matrix grain size with SiC content for MoSi$_2$ and MoSi$_2$/SiC composites.

pressed at 1500°C gave the average strength of 1215 MPa, which was the maximum value in this work.

3.3.4 High-Temperature Properties

To clarify the deformation mechanism at high temperatures, internal friction (Q^{-1}) was measured for $MoSi_2$/15 vol% SiC composite. Shear modulus was simultaneously measured in this experiment. Fig. 3.10 shows the internal friction and shear modulus dependence on temperature. The internal friction continuously increased with an increase in temperature, and no clear peak was observed. The remarkable increase of internal friction and the decrease of shear modulus in vicinity of 1000°C indicate the softening of glassy SiO_2.

The internal friction dependence on strain is shown in Fig. 3.11. The internal friction did not depend on the strain, and it showed almost constant value at each temperature. This result suggests that the deformation mechanism at 1000-1200° C in this system should not be dislocation motion [27]. For $MoSi_2$-based materials with large amount of SiO_2, the deformation mechanism around 1100°C are attributed to grain boundary sliding [28,29].

Hardness at high temperatures is shown in Fig. 3.12. The hardness at room temperature was 10.5 GPa and 12.8 GPa for $MoSi_2$ and $MoSi_2$/15 vol% SiC composite, respectively. Up to 800° C, hardness decreased in a gentle slope. More than 1000° C, clear degradation of hardness was observed both for $MoSi_2$ and $MoSi_2$/SiC composite. This notable decrease in hardness was attributed to the grain boundary sliding, since the grain boundary glassy SiO_2-rich phase was softened in vicinity of 1000°C. However, the decrease in hardness for the composite was a little smaller than in $MoSi_2$. This is because intergranular SiC particles may prevented grain boundary sliding.

Fig. 3.13 shows strength dependence on temperature. Inspection of the graph, both $MoSi_2$ and $MoSi_2$/15 vol% SiC composite kept high strength revel up to 1000° C. Both materials showed brittle fracture up to 800° C. At 1000° C, both of them exhibited the slight plastic-deformation and then fractured (i.e. semibrittle fracture). More than 1100°C, both materials displayed plastic deformation without fracture. $MoSi_2$/SiC composites had higher strength than $MoSi_2$ at elevated temperatures. $MoSi_2$/15 vol% SiC composite showed 1030 MPa at 1000°C. It was extremely high value as a $MoSi_2$-based material. From these results, it is notable that $MoSi_2$/SiC composites may be useful as high-temperature structural materials. In spite of the fact that the $MoSi_2$/SiC composites included relatively much amount of SiO_2, the materials have much better mechanical properties than previous $MoSi_2$-based systems. Even $MoSi_2$ showed relatively high strength of 887 MPa. These results strongly suggested that it is very effective to use small starting powder, though they have somewhat large amount of SiO_2. SiO_2 reduction with keeping small grain size will result in much better improvement on mechanical properties.

Toughness and hardness were also improved by nano-sized SiC addition. The $MoSi_2$/15 vol% SiC composite hot-pressed at 1500°C exhibited 3.1 $MPa \cdot m^{1/2}$ in toughness and 10.4 GPa
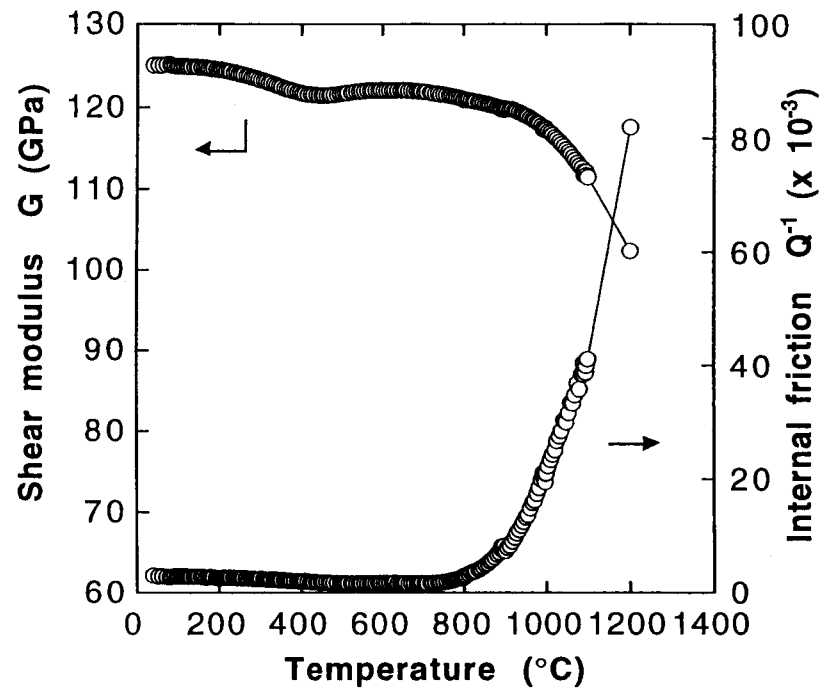
Fig. 3.10   Variation of shear modulus and internal friction with temperature for $MoSi_2/15$ vol% SiC composite.

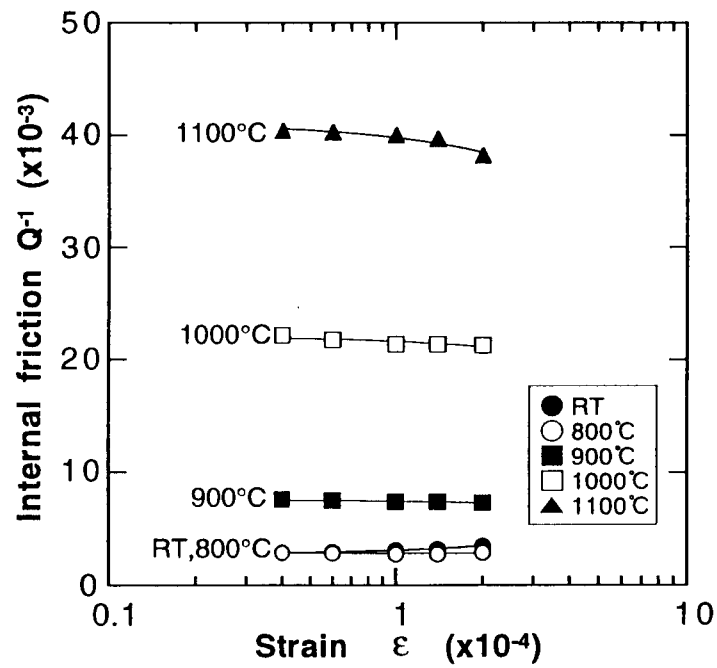**Fig. 3.11**   Variations of internal friction with strain for $MoSi_2/15$ vol% SiC composite.
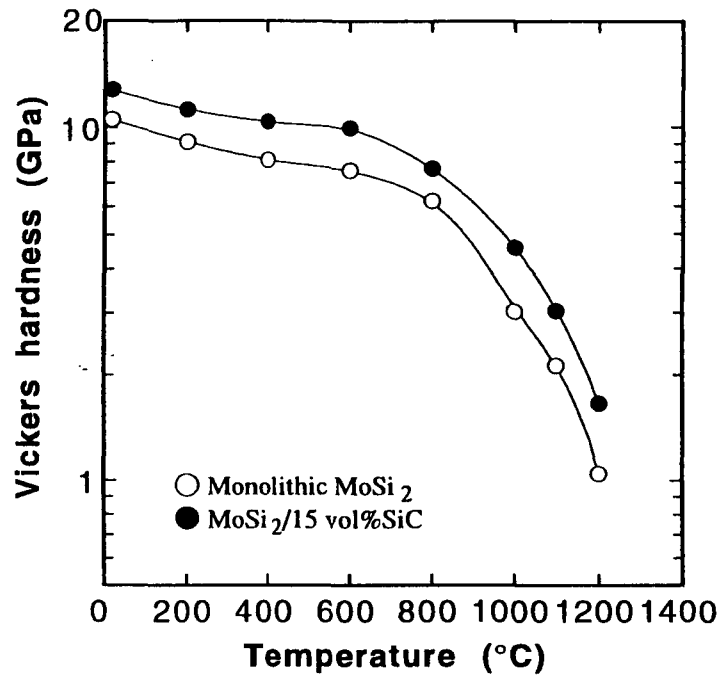
Fig. 3.12   Variations of Vickers hardness with temperature for MoSi$_2$ and MoSi$_2$/15 vol% SiC composites.
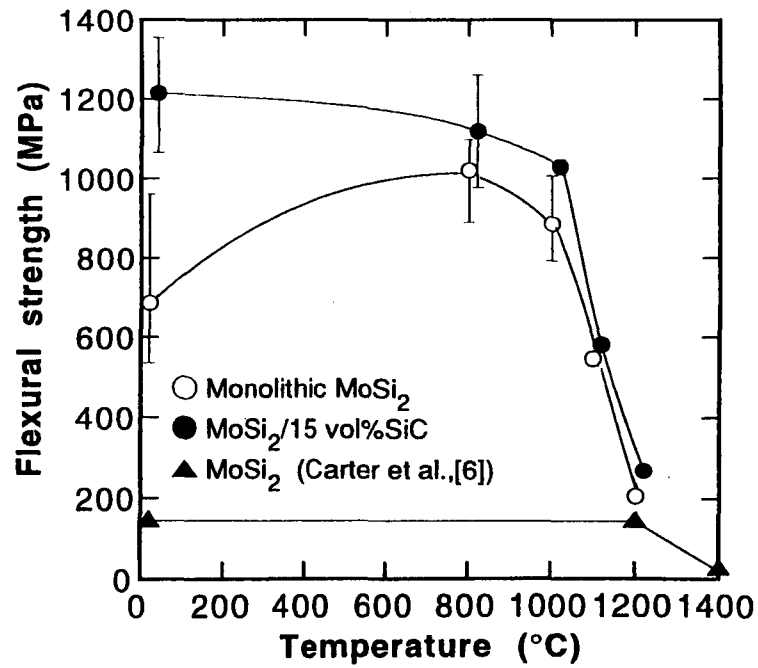

Fig. 3.13   Variations of flexural strength with temperature for MoSi$_2$ and MoSi$_2$/15 vol% SiC composites.

in hardness, while the $MoSi_2$ hot-pressed at 1500°C showed 2.3 $MPam^{1/2}$ and 10.4 GPa, respectively. It is concluded that nano-sized SiC reinforcement is effective to obtain high performance $MoSi_2$-based materials.

3.4 Discussion

3.4.1 Phase Relation and Microstructure Formation

In section 3.3.2, it was shown that monolithic $MoSi_2$ sintered bodies were composed of $MoSi_2$, $Mo_{\leq 5}Si_3C_{\leq 1}$ and glassy SiO_2, and that most of glassy SiO_2 located at triple points and $Mo_{\leq 5}Si_3C_{\leq 1}$ tended to neighbor with glassy SiO_2 (Fig. 3.4(a)). This microstructure formation is explained as follows; the $MoSi_2$ powder had the oxidized layer (i.e. glassy SiO_2) on the surfaces of each particle and a thin Mo_5Si_3 region below the SiO_2 layer [30,31]. During hot-pressing, glassy SiO_2 was concentrated mainly at triple points, and carbon impurities dissolved in Mo_5Si_3 to form $Mo_{\leq 5}Si_3C_{\leq 1}$. The microstructure formation behavior is schematically illustrated in Fig. 3.14.

In the composite system, glassy SiO_2 trapped a large portion of β-SiC (Fig. 3.4(b)). The microstructure formation for composite system is explained as follows; during hot-pressing, glassy SiO_2 did not wet $MoSi_2$ [32,33], similar to the monolithic $MoSi_2$ system as was demonstrated in Chap. 2. While smaller SiC particles (less than about 100 nm) could be incorporated into matrix grains during the matrix grain growth [34], larger ones (more than several hundred nm) could not be incorporated, and remained mainly at triple points. With the advance of hot-pressing, glassy SiO_2 and relatively larger SiC particles were also sintered at triple points. In other words, SiO_2/SiC composite could be formed at triple points as well as $MoSi_2$/nano-sized SiC composite at matrix. It is obvious from Figs. 3.4 (a) that the composite included more grain boundary phases compared to the monolithic $MoSi_2$. Image analyses of the SEM micrographs indicated that the total amount of grain boundary phases were about 6-8 and 20-22 vol% for monolithic $MoSi_2$ and $MoSi_2$/15 vol% SiC composite, respectively. Thus, in view of the volume fraction, most of SiC located not in the matrix but in the grain boundaries.

In section 3.3.2, it was also briefly described that $MoSi_2$ and SiC formed coherent interface. Fig. 3.15 illustrates the lattice structures and direction relationship indicated in Fig. 3.5(b). β-SiC has B3 structure, and along [111] direction, Si layer and C layer are stacking alternatively and these layers are equivalent in crystallography. $MoSi_2$ has $C11_b$ structure, and along [001] direction, one Mo layer and two Si layer are stacking. The diagonal distance of SiC unit cell (i.e. $\sqrt{3}\cdot a$) is 0.7551 nm and c-axis distance of $MoSi_2$ is 0.7845 nm. Suppose interfacial bonding is relaxed as schematically illustrated in Fig. 3.15, the mismatch is about 3.9%. Thus, as far as intragranular SiC, the interface between $MoSi_2$ and SiC was relatively coherent.
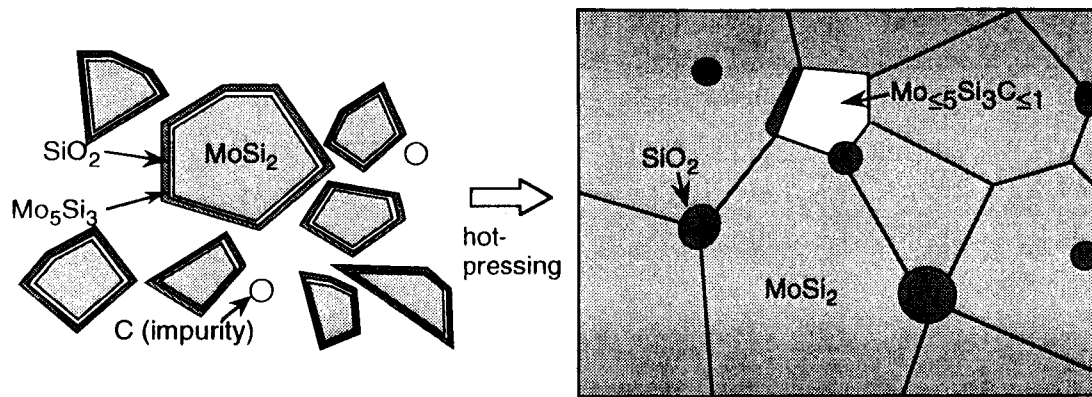
42

Fig. 3.14 Schematic illustration of the microstructure formation of MoSi$_2$ sintered bodies.
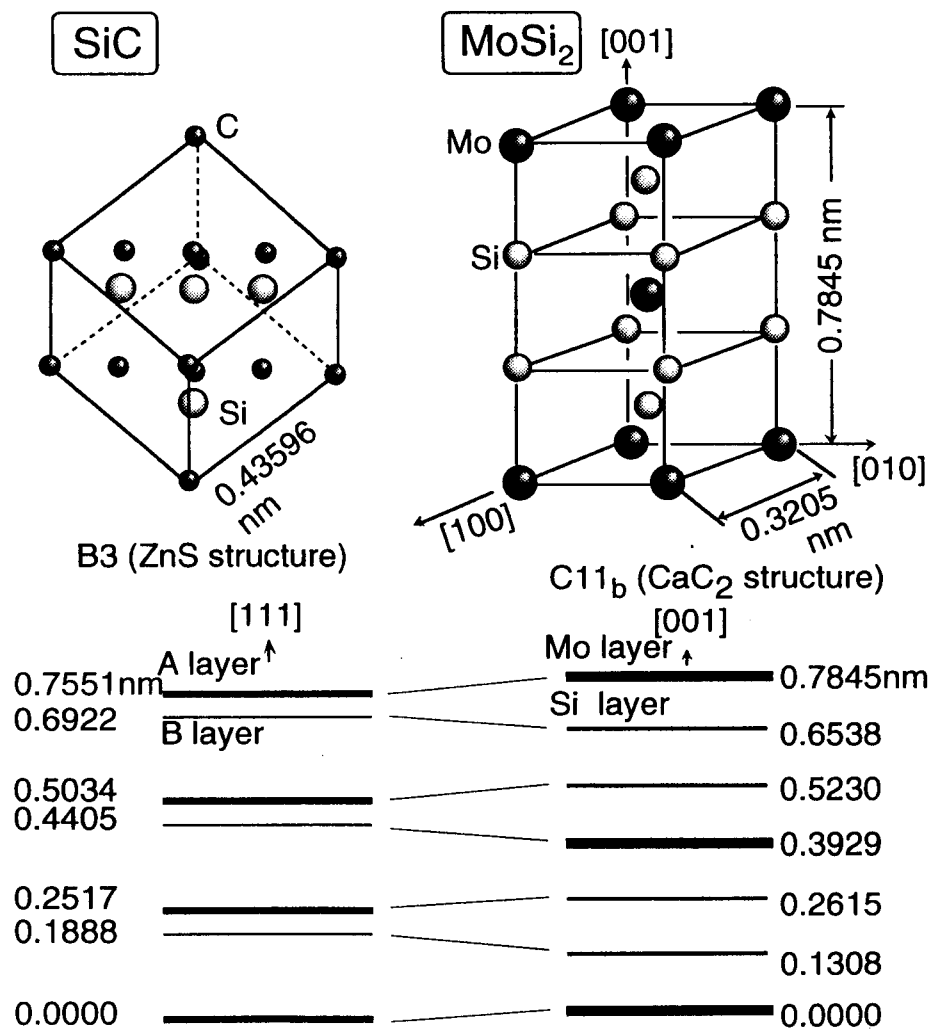

Fig. 3.15 Schematic illustration of cell structures and lattice matching between SiC (left) and MoSi$_2$ (right). A and B layers are crystallographically equivalent; one is a Si layer and the other is a C layer.

3.4.2 Young's Modulus Dependence

In section 3.3.3, an effective model to explain the decrease of Young's modulus was proposed, that is, "apparent" increase in glassy phase content. Monolithic $MoSi_2$ sintered body including about 8 vol% glassy SiO_2 confirmed by the image analysis. Supposing the sintered body does not include any $Mo_{\leq 5}Si_3C_{\leq 1}$ for the simplicity, the Young's modulus can be calculated by the following equation,

$$\ln E_{sintered\ body} = V_{SiO2} \ln E_{SiO2} + V_{MoSi2} \ln E_{MoSi2} \qquad (3.9)$$

where $V_{SiO2} = 8\ \%$, $V_{MoSi2} = 92\ \%$, $E_{SiO2} = 73$ GPa [35] and $V_{MoSi2} = 450$ GPa [22]. The calculated Young's modulus is 381 GPa, and this value is in good agreement with the experimental value of monolithic $MoSi_2$ in this study. (More detailed discussion for the monolithic $MoSi_2$ will be given in Chap. 4).

For 5 vol% SiC added system, if most of SiC particles are trapped in the glassy SiO_2, the "apparent" content of glassy SiO_2 will be about 13 vol%, and thus, the calculated Young's modulus is now 348 GPa, that is also in good agreement with the experimental value of $MoSi_2/5$ vol% SiC composites, as shown in Fig. 3.6. This model also suggests that a small amount of SiC additive (~ 5 vol%) is mainly incorporated within grain boundary glassy phase.

3.4.3 Correlation Between Grain Size of Matrix and Fracture Strength

In order to clarify the relationship between fracture strength (σ_f) and matrix grain size (d), σ_f - $d^{1/2}$ is plotted in Fig. 3.16. It is known that there are two typical σ_f - $d^{1/2}$ relationships for ceramic materials; Petch and Orowan relations [36,37]. For semibrittle materials and materials in which plastic deformation can take place only at high stress levels, stress builds up at the grain boundary until the strength of the solids is exceeded and fracture takes place. For this cases, it is well-known that the fracture strength is changed according to the relation as indicated by following Petch equation [36,37]:

$$\sigma_f = \sigma_0 + k_1 d^{-1/2} \qquad (3.10)$$

where σ_f is fracture strength, d is matrix grain size and σ_0 is constant. The k_1 is constant and given by Eq. 3.11:

$$k_1 = \{3\pi\gamma E/(1-v^2)\}^{1/2} \qquad (3.11)$$

where γ is surface energy, E is Young's modulus and v is Poisson's ratio. On the other hand, when the initial flaw size is limited by the grain size for materials which indicate the brittle fracture (i.e. fracture without plastic deformation) the strength may be expressed in following

44

Orowan relation [37]:

$$\sigma_f = k_2 \, d^{-1/2}$$

(3.12)

As shown in Fig. 3.16, the strength values lay on a straight line through the zero. The σ_f- $d^{1/2}$ relationship in this composite system seems to obey the above-mentioned Orowan equation. The observed load-displacement behavior and fracture surface morphology were consistent with this brittle fracture. Although some pores were observed both for monolithic $MoSi_2$ and $MoSi_2/SiC$ composites, theie size (sub-micron) was estimated to be 1/10 as small as initial flaw size calculated from Griffith equation. Thus these pores should not be fracture origins, and the initial flaw size is strongly depend on the matrix and SiO_2-rich grain sizes; largest SiO_2-rich grain had almost same grain size with average matrix grain size. It is concluded that the observed improvement of the fracture strength was mainly attributed to the grain growth inhibition of matrix and SiO_2-rich grain by SiC dispersion. In other words, SiC particles strengthened not only $MoSi_2$ matrix but glassy SiO_2 phase.
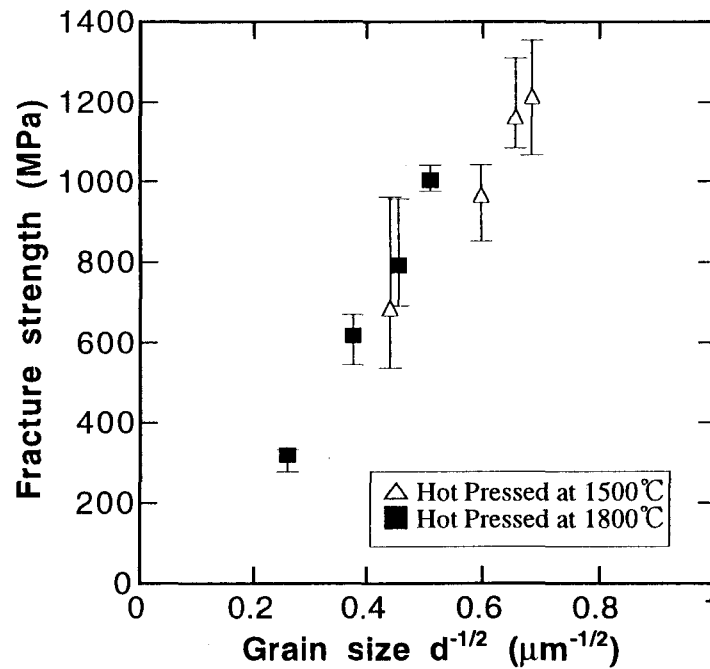

Fig. 3.16   Variations of fracture strength (σ_f) with matrix grain size ($d^{-1/2}$).

3.5 Conclusions

In this chapter, effects of nanometer-sized SiC dispersion on microstructure and mechanical properties of $MoSi_2$ were studied. In summary,

1. Fine SiC particle dispersed $MoSi_2$-based composites were fabricated by hot-pressing. The $MoSi_2$/ SiC composites were composed of $MoSi_2$, β-SiC, $Mo_{\leq5}Si_3C_{\leq1}$ and glassy SiO_2.

2. By optimizing hot-pressing conditions, the fracture strength was highly enhanced by the SiC addition. Maximum strength was observed for the $MoSi_2$/15 vol% SiC composite hot-pressed at 1500°C, 1215 MPa. The observed enhancement of fracture strength in this system was attributed mainly to the grain growth inhibition by SiC dispersoid.

3. Internal friction measurement suggested that the deformation mechanism at 1000-1200°C in $MoSi_2$/SiC composite system with some glassy SiO_2 should not be dislocation motion but grain boundary sliding. Although $MoSi_2$-based materials with much glassy SiO_2 generally do not show good mechanical properties, the composites in this study exhibited good mechanical properties in spite of relatively high SiO_2 level. This was because dispersed SiC particles strengthened not only matrix but also glassy SiO_2 phase effectively. The strength at 1000°C of $MoSi_2$/15 vol% SiC composite was extremely high, 1030 MPa.

References

1. F. W. Glaser, "A note on the metallic behavior of $MoSi_2$," *J. App. Phys.*, **22** [1] 103 (1951).

2. T. Kawaguchi, K. Kawasaki and T. Nakagawa, "$MoSi_2$ Infrared Light Source,"*J. Ceram. Soc. Jpn.*, **101** [2] 224-226 (1993) .

3. Y. L. Jeng and E. J. Lavernia, "Processing of Molybdenum Disilicide," *J. Mater. Sci.* **29**, 2557-2571 (1994).

4. F. D. Gac and J. J. Petrovic, "Feasibility of a Composite of SiC Whiskers in an $MoSi_2$ Matrix," *J. Am. Ceram. Soc.*, **68** [8] C200-C201 (1985).

5. K. Sadananda, H. Jones, J. Feng, J. J. Petrovic and A. K. Vasudevan, "Creep of Monolithic and SiC Whisker-Reinforced $MoSi_2$," *Ceram. Eng. Sci. Proc.*, **12** [9-10] 1671-1678 (1991).

6. D. H. Carter, W. S. Gibbs, and J. J. Petrovic, "Mechanical Characterization of SiC Whisker-Reinforced $MoSi_2$", in *Proc. the 3rd Int'l Symp. on Ceramics Materials & Components for Engines*, Nov. 1988, Las Vegas, NV. American Ceramic Society, Westerville, OH, 1989, pp977-986.

7. K. K. Richardson and D. W. Freitag, "Mechanical Properties of Hot Pressed SiC Platelet- Reinforced $MoSi_2$," *Ceram. Eng. Sci. Proc.*, **12** [9-10] 1679-1689 (1991).

8. R. M. Aikin, Jr., "Structure and Properties of In Situ Reinforced $MoSi_2$," *Ceram. Eng. Sci. Proc.*, **12** [9-10] 1643-1655 (1991).

9. R. M. Aikin, Jr.,"Strengthening of Discontinuously Reinfoced $MoSi_2$ Composites at High Temperatures," *Mater. Sci. Eng.*, **A155**, 121-133 (1992).

10. K. Niihara, A. Nakahira and T. Sekino, "New Nanocomposite Structural Ceramics," *Mater. Res. Soc. Symp. Proc.*, **286**, 405-412 (1993).

11. K. Niihara, "New Design Concept of Structural Ceramics - Ceramic Nanocomposites -," *J. Ceram. Soc. Jpn.*, **99** [10], 974-982 (1991).

12. K. Niihara, A. Nakahira, G. Sasaki and M. Hirabayashi, "Development of Strong Al_2O_3/SiC Composites," *Proc. MRS Int'l Mtg. on Adv. Composites*, (Plenum, New York, 1988) 129.

13. K. Niihara, A. Nakahira, "Structural Ceramic Nanocomposites by Sintering Method; Roles of Nano-size Particles", *Ceramics: Toward the 21st Century*, pp404, Japan, (1991).

14. F. Wakai, Y. Komada, S. Sakaguchi, K. Izaki, K. Niihara, "A Superplastic Covalent Crystal Composite," *Nature*, **344**, 421-423 (1990).

15. K. Niihara, K. Izaki, T. Kawakami, "Hot-Pressed Si_3N_4-32% SiC Nanocomposite from amorphous Si-C-N Powder with Improved Strength above 1200°C," *J. Mater. Sci. Lett.*, **10**, 112-114 (1990).

16. A. Nakahira, T. Sekino, Y. Suzuki, and K. Niihara, "High-Temperature Creep and Deformation Behavior of Al_2O_3/SiC Nanocomposite," *Ann. Chim. Fr.*, **18**, 403-408 (1993).

17. C. Herring, "Effect of Change of Scale on Sintering Phenomena," *J. Appl. Phys.*, **21** [4] 301-303 (1950).

18. K. Niihara, R. Morena and D. P. H. Hasselman, "Evaluation of K_{IC} of Brittle Solids by the Indentation Method with Low Crack-to-Indent Ratios," *J. Mater. Sci. Lett.*, **1** [1] 13-16 (1982).

19. E. Parthé and W. Jeitschko, "A Neutron Diffraction Study of the Nowotny Phase $Mo_{\leq 5}Si_3C_{\leq 1}$," *Acta Cryst.*, **19**, 1031-1037 (1965).

20. E. A. Brandes and G. B. Brook (Eds.), *Smithells Metals Reference Book, 7th edition*, Butterworth-Heinemann, Oxford, 1992.

21. R. W. Rice, "Strength and Fracture of Hot-Pressed MgO," *Proc. Br. Ceram. Soc.*, **20**, 329-63, (1972).

22. M. Nakamura, S. Matsumoto and T. Hirano, "Elastic Constants of $MoSi_2$ and WSi_2 SingleCrystals," *J. Mater. Sci.*, **25**, 3309-3313 (1990).

23. M. F. Ashby and D. R. H. Jones, *Engineering Materials*, Pergamon Press, (1980).

24. Y. Kagawa and H. Hatta,"Tailoring Ceramic Composites", Agune Shoufusya, Tokyo, pp.96-119, (1990).

25. J. Selsing, "Internal Stresses in Ceramics," *J. Am. Ceram. Soc.*, **44**, 419 (1961).

26. P. T. B. Shaffer, *Plenum Press Handbooks of High-Temperature Materials, No.1, Materials Index*, Plenum

Press, New York (1964).

27. D. -S. Sun, T. Yamane, J. Takahashi and K. Matsushita, "Amplitude Dependence of Internal Friction During Steady-State Creep of a 17Cr Ferritic Stainless Steel," *J. Mater. Sci. Lett.*, 1 2, 1185-87 (1993).

28. R. Gibala, A. K. Ghosh, D. C. Van Aken, D. J. Srolovitz, A. Basu, H. Chang, D. P. Mason and W. Yang, "Mechanical Behavior and Interface Design of $MoSi_2$-Based Alloys and Composites," *Mater. Sci. Eng.*, A 1 5 5, 147-158 (1992).

29. W. Jiang, K. Tsuji, T. Uchiyama and R. Watanabe, "Mechanical Properties of $MoSi_2$ Matrix Sintered Composites at Elevated Temperature," *Jap. Soc. Pow. & Pow. Metall.*, 4 3 [4] 444-449 (1996).

30. G. H. Meier and F. S. Pettit, "The Oxidation Behavior of Intermetallic Compounds," *Mater.Sci. Eng.*, A 1 5 3, 548-560 (1992).

31. D. A. Berztiss, R. R. Cerchiara, E. A. Gulbransen, F. S. Pettit and G. H. Meier, "Oxidation of $MoSi_2$ and Comparison with Other Silicide Materials," *Mater. Sci. Eng.*, A 1 5 5, 165-181, (1992).

32. T. E. Mitchell, R. G. Castro, J. J. Petrovic, S. A. Maloy, O. Unal and M. M. Chadwick, "Dislocations, Twins, Grain Boundaries and Precipitates in $MoSi_2$," *Mater. Sci. Eng.*, A 1 5 5, 241-249(1992).

33. K. Shobu, T. Watanabe and K. Tsuji, "Effects of Mo_2B_5 Addition to $MoSi_2$ Ceramics" (in Jpn.), *J. Ceram. Soc. Jap.* 9 7 [10] 1311-14 (1989).

34. M. Inoue, A. Nakahira and K. Niihara, "The Sintering Mechanism of Al_2O_3/SiC Nano-composites" (in Jpn.), *J. Jap. Soc. Pow. & Pow. Merall.*, 3 9 [6] 484-487 (1992).

35. Cyclopedia of Fine Ceramics, ed. by H. Yanagida et al., Gihodo Press, Tokyo, pp. 135- 153 (1987).

36. N. J. Petch, "Cleacvage Strength of Polycrystals," *J. Iron Steel Inst.*, 1 7 4 [1] 25-28 (1953).

37. W. D. Kingery, H. K. Bowen and D. R. Uhlmann, *Introduction to Ceramics, Second Edition*, New York, Chichester, Brisbane, Toronto, pp.768-815 (1976).

4

Microstructural Control by *In Situ* Crystallization of Grain Boundary Phase with Sc_2O_3 and Y_2O_3 Additions

In this chapter, the improvement in mechanical properties of powder processed $MoSi_2$ by the additions of Sc_2O_3 and Y_2O_3 will be discussed. The improvement is based on the microstructural control by *in situ* crystallization of grain boundary glassy SiO_2. Only 1 mol% Sc_2O_3 additions dramatically enhanced three-point bending strength from 521 to 1081 MPa. Vickers hardness, Young's modulus, fracture toughness and high-temperature strength were also improved by this low level of additive. The improvement of mechanical properties was attributed to the formation of several silicates: $Sc_2Si_2O_7$, $Y_2Si_2O_7$, Y_2SiO_5 and $Y_4Si_3O_{12}$, which were followed by X-ray diffraction, SEM-EDS, and TEM-EDS methods. Both ambient and high- temperature properties were successfully improved by this microstructural design.

4.1 Introduction

As was discussed before, $MoSi_2$ is an attractive candidate material for high temperature structural applications because of its high melting point ($2030°$ C), moderate density (6.27 g/cm^3) and excellent oxidation resistance [1,2]. Due to its intrinsically low ductility, powder processes are widely used for fabricating bulk $MoSi_2$ materials [3]. Since $MoSi_2$ powders, prepared by solid-state reaction and crushing processes, always contain a certain amount of oxygen, a "monolithic" $MoSi_2$ sintered body is actually composed of $MoSi_2$, Mo_5Si_3 and glassy SiO_2 phases; Mo_5Si_3, a low silicide phase, is formed by the deviation from the stoichiometry. With carbon impurity, the $Mo_{\leq5}Si_3C_{\leq1}$ Nowotny phase can also appear [4-6]. Such inclusions, low silicides and glassy SiO_2, affect various properties of $MoSi_2$ (here the author includes the $Mo_{\leq5}Si_3C_{\leq1}$ phase as a kind of low silicide); low silicides have less oxidation resistance than $MoSi_2$ [7], but they may strengthen $MoSi_2$ as the second phase reinforcement [8]. While dispersion of low silicides in $MoSi_2$ compacts has some advantages, glassy SiO_2 is always disadvantageous to mechanical properties [8]. As was menstioned in Chap. 2, the glassy SiO_2 phase forms discrete regions in $MoSi_2$ sintered bodies [5-6,8-9], which is opposite to Si_3N_4 where glassy SiO_2 wets two-grain boundaries and triple points as layers. Nevertheless, glassy

SiO_2 in $MoSi_2$ sintered bodies promotes creep by grain boundary sliding, as in Si_3N_4, because it softens at high temperatures. Thus, glassy SiO_2 degrades mechanical properties, not only at room temperature, but also at high temperatures.

The approaches to eliminate the siliceous grain boundary phase can be classified into five categories: (1) reducing oxygen content in starting $MoSi_2$ powders, e.g. in-flight treatment in an Ar-H_2 plasma treatment [3], and a hydrofluoric acid treatment [10]; (2) deoxidation during sintering process by, for example, carbothermal reduction [11-13] and hydrogen reduction [14]; (3) metathesis reaction during sintering, for example replacing silica by alumina through Al metal addition [15-17]; (4) double oxide formation during sintering [5]; (5) predominant oxidation of alloying element, e.g. aluminum, in starting powders [6,18]. The present authors developed the 4 th method (described in this chapter and next chapter), and the 5 th method (presented in Chap. 6).

In this chapter, *in situ* double oxide formation method was studied; namely, the grain boundary glassy SiO_2 reacted with oxide additives to form refractory double oxide during a hot-pressing process without another thermal treatment. Sc_2O_3 and Y_2O_3, with c-rare earth structure, are selected as additives because they have high melting point ($\sim 2400°C$) and high reactivity with SiO_2 to form very refractory double oxides. To clarify the effects of grain boundary phases, the author preferred to use a fine $MoSi_2$ powder (about 1 μ m) with rather high oxygen content (1.21 wt%). 1-20 mol% of R_2O_3 (R = Sc and Y) powders were added to the $MoSi_2$ powder for examining effects of double oxides formation and second phase dispersion of excess, unreacted, R_2O_3 in the $MoSi_2$ bodies.

Morgan et al. [19,20] previously studied effects of Sc_2O_3 addition on Si_3N_4, and reported that oxidation resistance and creep resistance were significantly improved by the easy crystallization of the $Sc_2Si_2O_7$ phase (also known as the mineral thortveitite). These observations were confirmed in later works [21,22]. We can imagine similar positive effects for the Mo-Si-Sc-O system because both Si_3N_4 and $MoSi_2$ have siliceous grain boundary phase, greatly affecting various mechanical properties. For Y_2O_3, Kulenko et al. [23] have reported on the $MoSi_2$-Y_2O_3 system prepared by pressureless sintering. The main purpose of their study was to increase the electrical resistivity of $MoSi_2$ bodies without consciously effecting the normal mechanical properties of $MoSi_2$. Hence, they examined relatively higher amounts of Y_2O_3 (10 to 50 %, presumably weight fraction as the authors did not clearly say), and mechanical properties were scarcely mentioned. Research on $MoSi_2/Y_2O_3$ composites was also carried out by Zalkind et al [24], who demonstrated that the $MoSi_2/Y_2O_3$ composites showed good corrosion resistance to melts of fuel slag, which encourages further study $MoSi_2/Y_2O_3$ system.

This study particularly emphasizes that a slight amount of Sc_2O_3 and Y_2O_3 additions are effective in greatly improving mechanical properties.

4.2 Experimental Procedure

4.2.1 Sample Preparation

Starting materials were $MoSi_2$ (1.01 μm, Japan New Metals Co., Ltd., almost identical powder used in Chap. 3), Sc_2O_3 and Y_2O_3 (about 2 μm, Kojundo Chemical Lab. Co. Ltd.). The R_2O_3 composition in this investigation was restricted to 1-20 mol% because certainly a larger amount of oxides might degrade the high-temperature mechanical properties. The chemical analysis of the starting $MoSi_2$ powder is shown in Table 4.1. Spectrochemical analysis revealed that the major impurities were 1.21 wt% oxygen, 0.20 wt% carbon and 0.21 wt% iron. The high oxygen level is associated with the fine particle size (1.01 μm) of the $MoSi_2$ powder. In addition, Table 4.2 shows the composition of the $MoSi_2$ starting powder calculated from Table 4.1, assuming that the phases in the powder were $MoSi_2$, Mo_5Si_3, glassy SiO_2, free carbon and Fe_2O_3. This result presumes that 1.21 wt% oxygen in the $MoSi_2$ powder is equivalent to about 6 vol% of glassy SiO_2. $MoSi_2$ and additive oxide powders were wet ball-milled with ZrO_2 balls for 24 h in n-hexane which was used to avoid the mechano-chemical oxidation by usual alcohol solvents as reported for Si_3N_4 [25]. Nominal compositions of the powder mixture are summarized in Table 4.3. The mixture was packed into carbon dies, coated with BN, and hot-pressed at 1600°C under an applied pressure of 30 MPa for 1 h in vacuum. The sintered disks, 44 mm in diameter and 5.0 mm in thickness, were cut, ground and polished into rectangular bars $4 \times 3 \times 36$ mm in size.

Table 4.1 Chemical analysis of the $MoSi_2$ starting powder.

	Mo*	Si	O	C	Fe
content (wt%)	62.18	36.20	1.21	0.20	0.21

*The content of Mo was calculated so that the total content was 100%.

Table 4.2 Calculated composition of the $MoSi_2$ starting powder.

	$MoSi_2$	Mo_5Si_3*	glassy SiO_2	Free-C**	Fe_2O_3
content (mol%)	91.2	0.9	5.1	2.5	0.3
content (wt%)	94.0	3.4	2.1	0.2	0.3
content (vol%)	90.9	2.5	5.7	0.5	0.4
density (g/cm³)	6.27	8.19	2.22	2.25	5.24

*Mo_5Si_3 increases with oxidation and reacts with carbon to form $Mo_{\le5}Si_3C_{\le1}$.
**Some carbon can dissolve in SiO_2 glass.

Table 4.3 Nominal* compositions of the powder mixtures.

No.	composition (mol%)			composition (wt%)**			composition (vol%)***		
	MoSi₂	Sc₂O₃	Y₂O₃	MoSi₂	Sc₂O₃	Y₂O₃	MoSi₂	Sc₂O₃	Y₂O₃
1	100	-	-	100	-	-	100	-	-
2	99	1	-	99.1	0.9	-	98.5	1.5	-
3	98	2	-	98.2	1.8	-	97.1	2.9	-
4	95	5	-	95.4	4.6	-	92.8	7.2	-
5	90	10	-	90.8	9.2	-	85.9	14.1	-
6	85	15	-	86.2	13.8	-	79.3	20.7	-
7	80	20	-	81.5	18.5	-	73.0	27.0	-
8	99	-	1	98.5	-	1.5	98.2	-	1.8
9	98	-	2	97.1	-	2.9	96.4	-	3.6
10	95	-	5	92.8	-	7.2	91.1	-	8.9
11	90	-	10	85.8	-	14.2	83.0	-	17.0
12	85	-	15	79.2	-	20.8	75.4	-	24.6
13	80	-	20	72.9	-	27.1	68.4	-	31.6

* supposing that the starting powders were pure $MoSi_2$, Sc_2O_3 and Y_2O_3.

** formula weight: $MoSi_2$ = 152.111, Sc_2O_3 = 137.91, and Y_2O_3 = 225.81

*** X-ray density: D_{MoSi2} = 6.27 g/cm³, D_{Sc2O3} = 3.840 g/cm³, and D_{Y2O3} = 5.032 g/cm³

4.2.2 Evaluation

Phase identification was carried out by X-ray diffraction (XRD) analysis. To minimize the anisotropic orientation effect, some liquid paraffin was mixed with the pulverized specimen. The microstructure was characterized by scanning electron microscopy (SEM, HITACHI S-5000) with energy dispersive X-ray spectrometry (EDS, HORIBA EMAX- 5770) with the samples pre-coated with carbon. Transmission electron microscopy (TEM, HITACHI H-8100) with EDS (Phillips PV9900) was also used for the microstructural characterization. The bulk density was measured by the Archimedes method in toluene at room temperature; temperature corrections were always carried out for the density measurements. Young's modulus was determined by the resonance vibration method adjusted to the thickness correction. More than five specimens in each case were subjected to three-point bending test (span: 30 mm, in air) to determine fracture strength up to 1300°C. The bending load was applied parallel to the hot-pressing axis with a crosshead speed of 0.5 mm/min. Hardness (H_v) was evaluated by Vickers indentation under a conditions of 98 N load with loading duration of 15 s in air. Fracture toughness (K_{IC}) at room temperature was determined simultaneously by the indentation fracture (IF) method [26]. K_{IC} values were calculated by using the empirical equation proposed by Niihara et al. [26] for a median crack, as mentioned in Chap. 3.

4.3 Results

4.3.1 Phase Analysis of the Sc_2O_3 Case

Fig. 4.1 shows the XRD patterns for (a)$MoSi_2$ with added Sc_2O_3 and (b)$MoSi_2$ with added Y_2O_3 hot-pressed bodies with increasing additive amounts. Since the XRD intensities of $MoSi_2$ were quite strong in comparison with those of other phases, the peak tops were truncated. The XRD analysis of the phases in the sintered bodies are summarized in Table 4.4. XRD analysis indicated that the monolithic $MoSi_2$ body was composed of $MoSi_2$ (tetragonal, $C11_b$), a small amount of $Mo_{\leq 5}Si_3C_{\leq 1}$(hexagonal, $D8_8$), and a trace of SiO_2 (cristobalite). The $Mo_{\leq 5}Si_3C_{\leq 1}$, Nowotny phase [27] is the only stable Mo-Si-C ternary phase. TEM selected area diffraction analysis revealed that most of the SiO_2 existed as glassy phase, however, the cristobalite observed by XRD must be attributed to partial crystallization of glassy SiO_2. In the $MoSi_2$/1-2 mol% Sc_2O_3 sintered bodies, $Sc_2Si_2O_7$, thortveitite, (Sc_2O_3 : SiO_2 = 1 : 2) was identified. $Sc_2Si_2O_7$ is a stable, refractory compound in the Sc_2O_3-SiO_2 binary system (M.P., $1860°$ C). $Sc_2Si_2O_7$ is reported to readily form also in the hot-pressed Si_3N_4-SiO_2-Sc_2O_3 system [19-22]. The cristobalite peak around 2θ = $22°$ decreased (as expected) with increasing Sc_2O_3 content (0-5 mol%) as $Sc_2Si_2O_7$ forms with the inevitable reaction with glassy SiO_2. For the $MoSi_2$ with 5 mol% Sc_2O_3, most of the silica in the sintered body was converted to the silicate, because the cristobalite peak disappeared and small peaks from unreacted Sc_2O_3 were observed. With higher Sc_2O_3 additions (10-20 mol%), the constituent phases were the same as in the $MoSi_2$/5mol% Sc_2O_3 case; the amount of unreacted Sc_2O_3 simply increased. In the Sc_2O_3-SiO_2 binary system [28], there should be another silicate, Sc_2SiO_5 (Sc_2O_3 : SiO_2 = 1 : 1) when Sc_2O_3 content becomes higher. However, the Sc_2SiO_5 phase was never observed in this experiment, as discussed later.

Table 4.4 Phase contents of the hot-pressed products in the $MoSi_2$/R_2O_3 (R =Sc and Y) systems.

| No.	Nominal starting composition (mol%)	Phases in product (identified by XRD)	
1	$MoSi_2$	$MoSi_2$, $Mo_{\leq 5}Si_3C_{\leq 1}$, SiO_2*	
2,3	+ 1,2% Sc_2O_3	$MoSi_2$, $Mo_{\leq 5}Si_3C_{\leq 1}$, SiO_2*, $Sc_2Si_2O_7$	
4	+ 5% Sc_2O_3	$MoSi_2$, $Mo_{\leq 5}Si_3C_{\leq 1}$,	$Sc_2Si_2O_7$, (trace Sc_2O_3)
5,6,7	+ 10,15,20% Sc_2O_3	$MoSi_2$, $Mo_{\leq 5}Si_3C_{\leq 1}$,	$Sc_2Si_2O_7$,Sc_2O_3
8,9	+ 1,2% Y_2O_3	$MoSi_2$, $Mo_{\leq 5}Si_3C_{\leq 1}$, SiO_2*, $Y_2Si_2O_7$, (trace Y_2O_3)	
10	+ 5% Y_2O_3	$MoSi_2$, $Mo_{\leq 5}Si_3C_{\leq 1}$, SiO_2*, $Y_2Si_2O_7$, $Y_4Si_3O_{12}$, (trace Y_2O_3)	
11,12,13	+ 10,15,20% Y_2O_3	$MoSi_2$, $Mo_{\leq 5}Si_3C_{\leq 1}$,	Y_2SiO_5, Y_2O_3

*cristobalite, partially crystallized from glassy SiO_2.
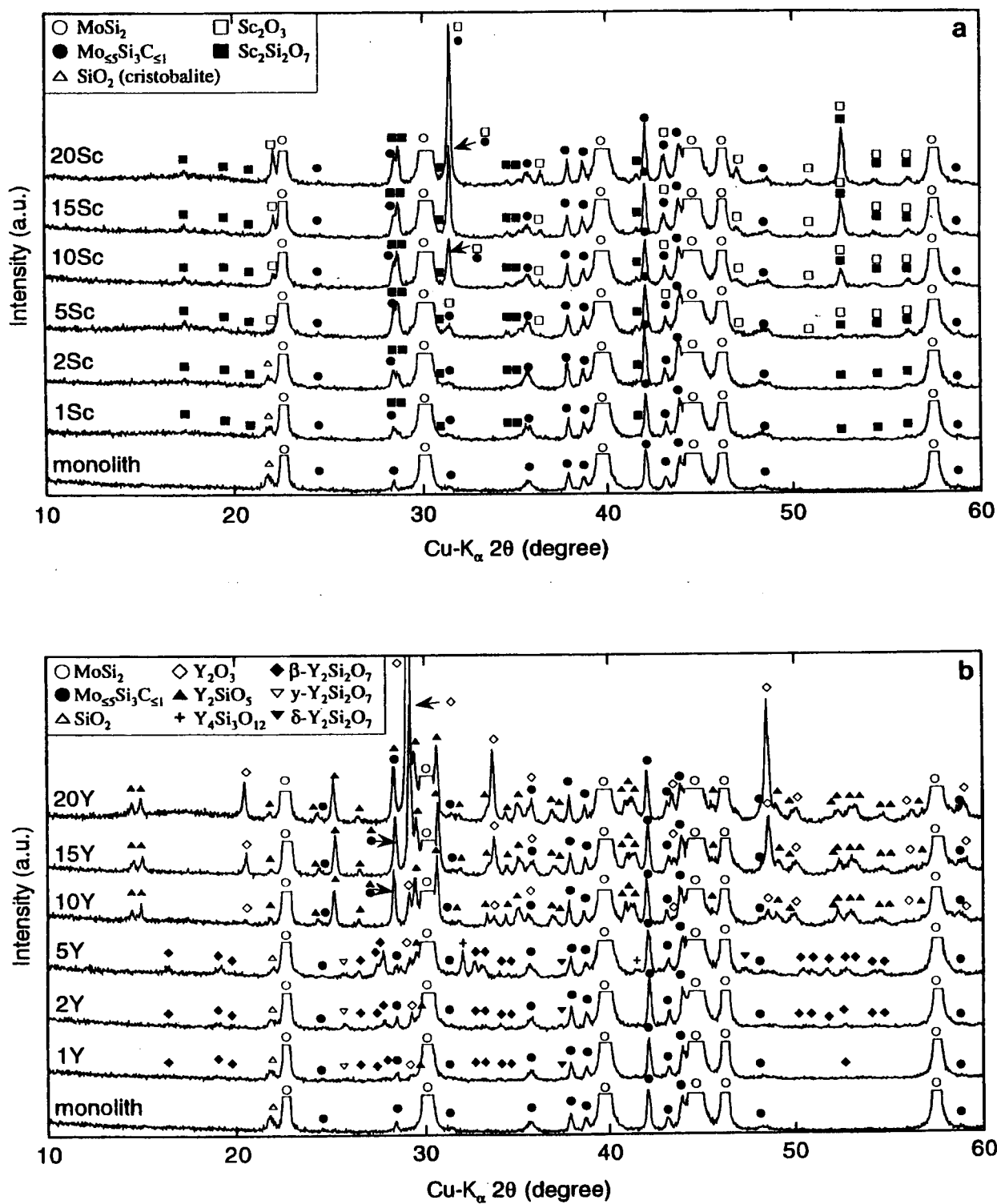
Fig. 4.1 X-ray diffraction patterns for (a) $MoSi_2$-SiO_2-Sc_2O_3 and (b) $MoSi_2$-SiO_2-Y_2O_3 systems.

4.3.2 Phase Analysis of the Y_2O_3 Case

For $MoSi_2$ with 1-2 mol% Y_2O_3, the formation of the 1:2 silicate, i.e. $Y_2Si_2O_7$, was confirmed similarly to the $Sc_2Si_2O_7$ formation in the $MoSi_2$-SiO_2-Sc_2O_3 system. Three polymorphs of $Y_2Si_2O_7$ phase were identified: β-phase (keiviite-(Y)), y-phase and δ-phase. β-$Y_2Si_2O_7$ has the thortveitite-type crystal structure and is stable at high temperatures around the hot-pressing temperature (1600°C) [29]. Dinger et al. [30] studied the crystallization behavior of glasses in the Y_2O_3-SiO_2-AlN system, and reported that y-$Y_2Si_2O_7$, δ-$Y_2Si_2O_7$ and β-$Y_2Si_2O_7$ phases were observed, with y-$Y_2Si_2O_7$ and δ-$Y_2Si_2O_7$ crystallizing about 1000°C and 1200°C, respectively, and β-$Y_2Si_2O_7$ crystallizing at higher temperatures. Since the hot-pressing time in this study was not long, it is perhaps not surprising that these polymorphs of $Y_2Si_2O_7$ remained in the sintered bodies. The intensity of the cristobalite peak at 2θ 22° also decreases with increasing Y_2O_3 content (0-5 mol%) similarly to the Sc_2O_3 case. A trace of Y_2O_3 was also identified in the $MoSi_2$/1-2 mol% Y_2O_3 in spite of the presence of free SiO_2; this may be because the reaction conditions were somewhat mild (1 h and 1600°C), and the reactants are separated by the majority $MoSi_2$ matrix. For $MoSi_2$ with 5 mol% Y_2O_3, $Y_2Si_2O_7$, unreacted SiO_2 and Y_2O_3 were observed in addition to $MoSi_2$ and $Mo_{\leq 5}Si_3C_{\leq 1}$. Furthermore, a notable peak at 2θ 32° was observed. This peak was never observed in the other specimens, and was identified as 2:3 silicate, $Y_4Si_3O_{12}$. According to the published phase diagram [29], this phase is not stable below 1650°C, nevertheless, it appears here. For compacts with higher Y_2O_3 additions (10-20 mol%), SiO_2 and $Y_4Si_3O_{12}$ disappear, and Y_2SiO_5 phase formed. The equivalent 1:1 silicate was not observed in the $MoSi_2$-SiO_2-Sc_2O_3 system.

4.3.3 Microstructure

Fig. 4.2 shows typical SEM photographs on the polished surfaces of monolithic $MoSi_2$ and $MoSi_2$ with R_2O_3 additives: (a) monolithic $MoSi_2$: (b) 1, (c) 5, (d) 10 and (e) 20 mol% Sc_2O_3: (f) 1, (g) 5, (h) 10 and (i) 20 mol%Y_2O_3. In these figures, the dark regions are oxide phases (not pores). The regions with light gray contrast are the $Mo_{\leq 5}Si_3C_{\leq 1}$ phase. In the monolithic $MoSi_2$ compacts, glassy SiO_2 particles with spherical or irregular shape were dispersed, this is unlike Si_3N_4 compacts where glassy SiO_2 distributes as films along grain boundaries. $Mo_{\leq 5}$ $Si_3C_{\leq 1}$ phase was usually found next to each glassy SiO_2. This microstructure may be explained as follows: the starting $MoSi_2$ powder had the oxidized layer (i.e. glassy SiO_2) on the surfaces and a thin Mo_5Si_3 region below the SiO_2 layer [31]. The glassy SiO_2 was concentrated mainly at triple points, and the $Mo_{\leq 5}Si_3C_{\leq 1}$ was formed by reactions between Mo_5Si_3 and impurity carbon during hot-pressing. SEM-EDS study revealed that Sc and Y elements predominantly appear in the silica pockets. Thus, it is inferred that the additives and silica react together at grain boundary pockets. The dark regions in the Figs. 4.2(a)-(i) were composed of the mixed oxides as mentioned in the phase analysis. With higher content of additives, oxide phases became continuous as seen in the pictures of Fig. 4.2 (d), (e), (h) and (i).
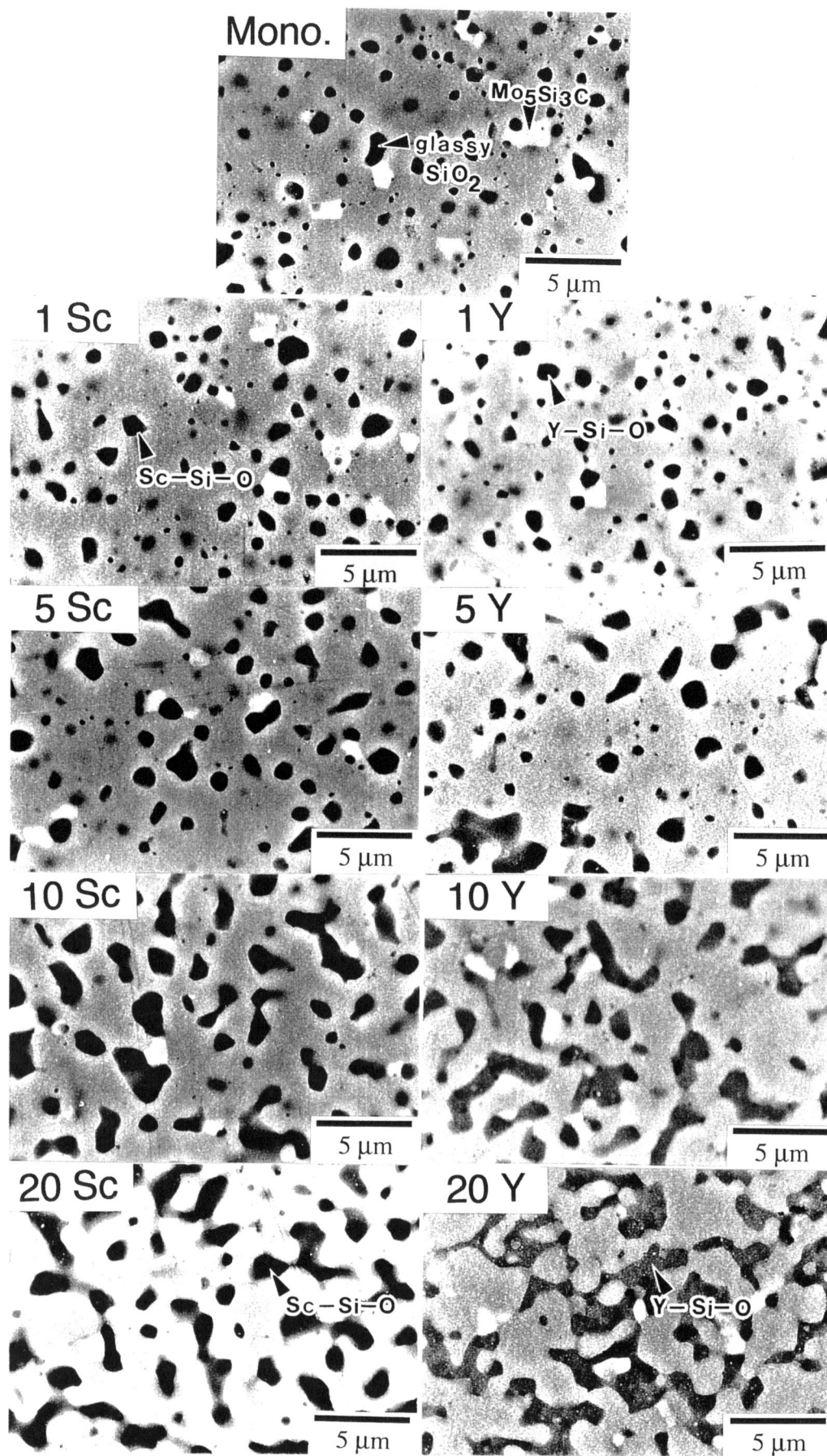
Fig. 4.2 SEM photographs of polished surfaces: (a) monolithic $MoSi_2$: (b) 1, (c) 5, (d) 10 and (e) 20 mol% Sc_2O_3: (f) 1, (g) 5, (h) 10 and (i) 20 mol% Y_2O_3.

4.3.4 Density

Fig. 4.3 shows the variation of density of hot-pressed $MoSi_2$ bodies with Sc_2O_3 and Y_2O_3 addition. The density of the monolithic $MoSi_2$ compact was 5.92 g/cm^3. This value was smaller than the theoretical density of the $MoSi_2$ phase determined by XRD, 6.27 g/cm^3. Since almost no pores were observed by SEM for the $MoSi_2$ sintered body, the decrement of density was attributed to the formation of glassy SiO_2 with its rather low density (2.20 g/cm^3). For the Y_2O_3 added system, the density increased and then decreased with Y_2O_3 content. This suggests the formation of a higher-density phase comparing to glassy SiO_2. With the Sc_2O_3 addition, the curve had a maximum at 5 mol%. It also suggests the formation of a higher-density phase. The density dependence will be discussed later in detail.

4.3.5 Mechanical Properties

Young's modulus dependence on Sc_2O_3 and Y_2O_3 content is shown in Fig. 4.4. The Young's modulus of the monolithic $MoSi_2$ compact is 372 GPa. This value is smaller than the theoretical Young's modulus of polycrystalline $MoSi_2$ calculated from the single crystal, 440 GPa [32]. In general, Young's modulus is strongly affected by the porosity. However, since almost no pores were observed in the sintered body as was mentioned above, the decrease in Young's modulus is also explained by the formation of glassy SiO_2 phase. For both Sc_2O_3 and Y_2O_3 addition, Young's modulus indicated the maximum values at 5 mol% addition. The 5 mol% addition is equivalent to the minimum additive composition to remove glassy SiO_2 in the sintered bodies. As Young's moduli of Sc_2O_3 and Y_2O_3 are smaller than $MoSi_2$, the 5 mol% addition resulted in the maximum values. The Young's modulus dependence will be discussed further in session 4.4.2.

Fig. 4.5 shows the variation of fracture strength with additive content. The strength value of the monolithic $MoSi_2$ was 521 MPa. Fracture strength increased and then decreased with increasing additive content. For both Sc_2O_3 and Y_2O_3 addition, maximum fracture strength was obtained for only 1 mol% addition. The strength values of $MoSi_2$ with 1 mol% Sc_2O_3 and Y_2O_3 were 1081 and 1028 MPa, respectively. These values were extremely high for $MoSi_2$ based materials [2]. Too much oxide phase decreases fracture strength when they are connected resulting in a larger potential flaw fracture origin. For 1 mol% addition, the total amount of oxide phase is still small, and oxide regions are discrete; the glassy SiO_2 sufficiently reacted with the additive to form 1:2 silicate, apparently causing strengthening. As only 1 mol% R_2O_3 additive is enough to greatly improve fracture strength, the use of expensive Sc_2O_3 may become cost-effective.

Fig. 4.6 shows the variation of Vickers hardness with additive content. The change of Vickers hardness with additive content resembled that of Young's modulus. Hardness showed its maximum value at 5 mol% for both Sc_2O_3 and Y_2O_3 additions. This is attributed to the approach to total crystallization of the glassy phase. The decrement of hardness for higher
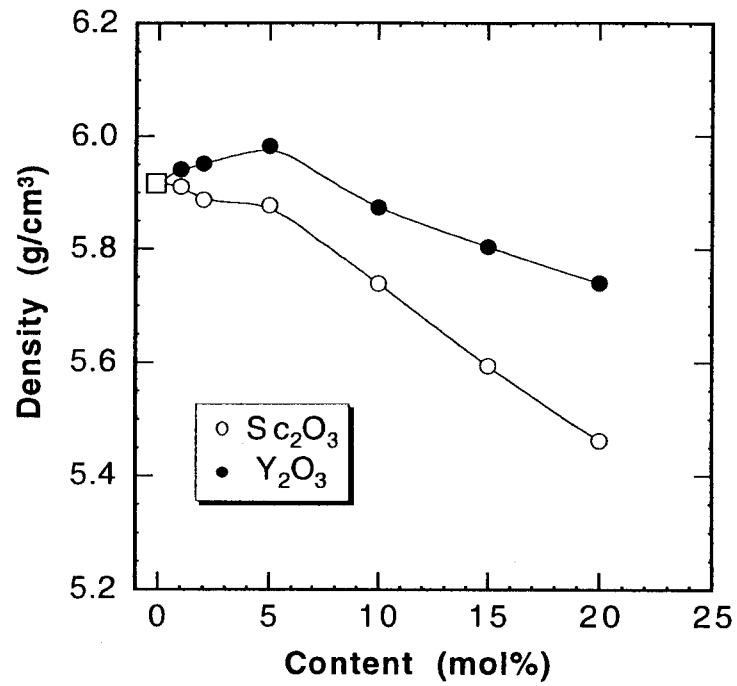
57

Fig. 4.3   Variation of density with R_2O_3 (R = Sc and Y) composition
for $MoSi_2$-SiO_2-R_2O_3 system.

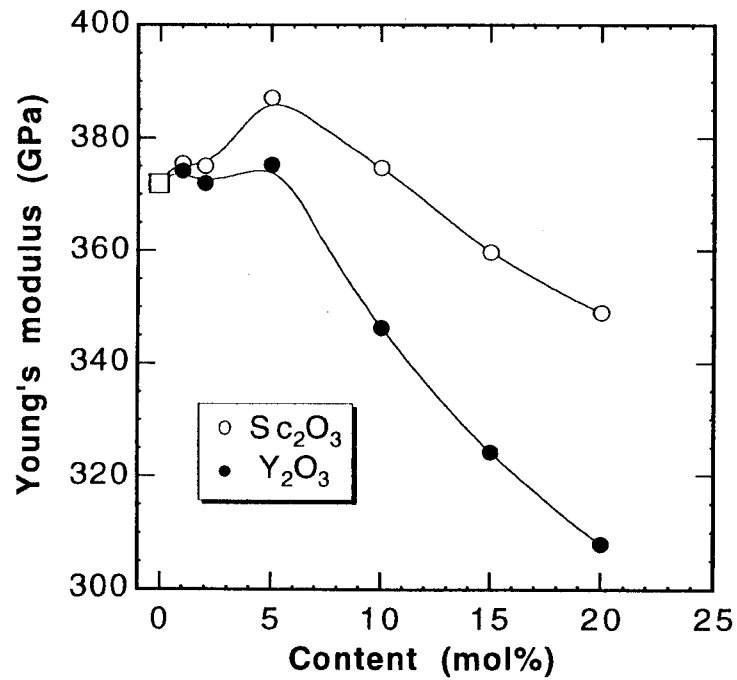**Fig. 4.4**   Variation of Young's modulus with R_2O_3 composition
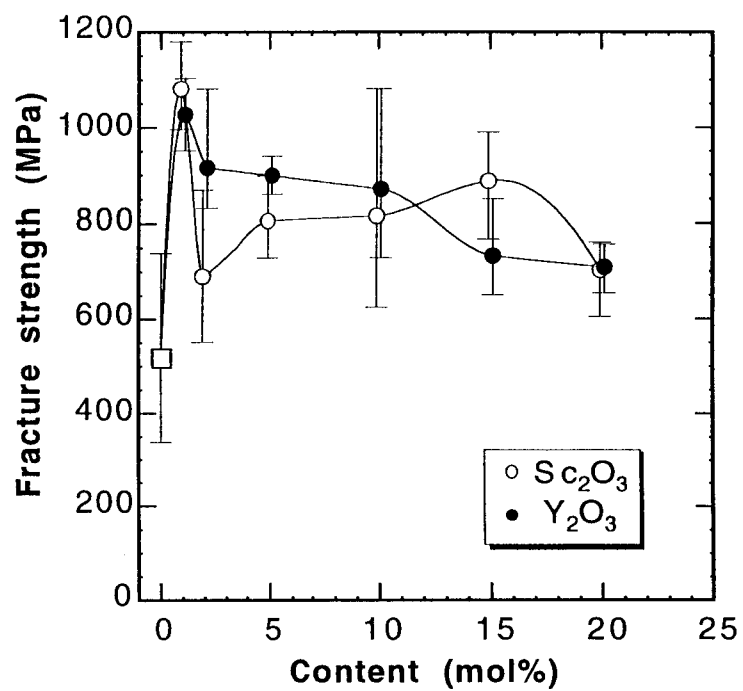for $MoSi_2$-SiO_2-R_2O_3 system.

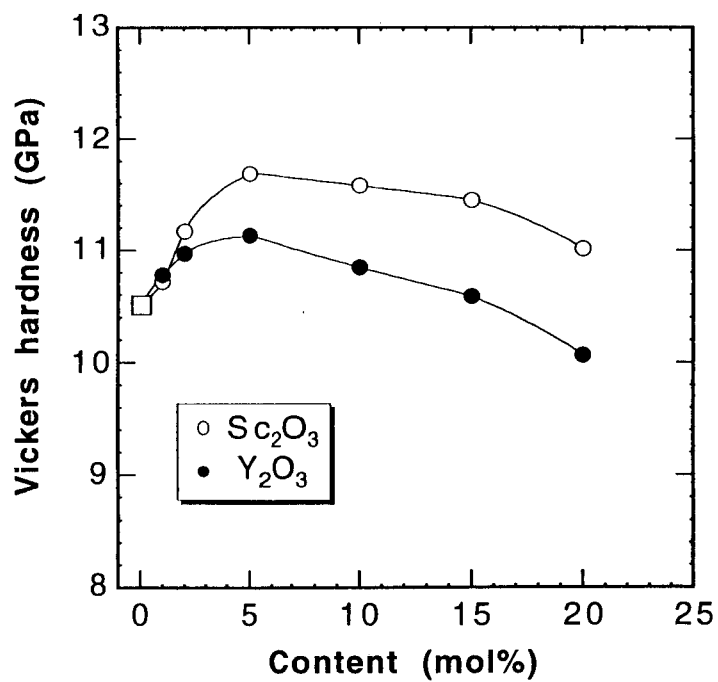**Fig. 4.5** Variation of fracture strength with R_2O_3 composition for $MoSi_2$-SiO_2-R_2O_3 system.

Fig. 4.6 Variation of Vickers hardness with R_2O_3 composition for $MoSi_2$-SiO_2-R_2O_3 system.

additive content was due to the softness of unreacted additive oxide.

Fracture toughness dependence on additive content is shown in Fig. 4.7. The change of fracture toughness with additive content was similar to that of Young's modulus and Vickers hardness for the same reasons. Too much additive also decreased fracture toughness, also for the same reasons.

Fig. 4.8 shows high-temperature strength of $MoSi_2$ with 1 mol% Sc_2O_3 and Y_2O_3. The values of two different monolithic $MoSi_2$ are also shown in the figure for reference; fine $MoSi_2$ was fabricated by hot-pressing a fine $MoSi_2$ powder (0.98 μm, as described in Chap. 3) at 1500°C, whose grain size was about 5 μm [33], and coarse $MoSi_2$ was made by hot-pressing a coarse powder (several tens of microns, typical values of conventional $MoSi_2$) at 1700°C [34]. Because coarse $MoSi_2$ contained less glassy phase, it maintained almost the same, albeit low, strength (~ 150 MPa) up to 1200°C. On the other hand, fine $MoSi_2$ showed improved strength for all the temperature range compared to coarse $MoSi_2$, although strength degradation was, indeed, observed above around 1000°C. The improvement of strength around 800°C was due to the healing effect of the glassy phase, and the drop down of strength about 1000°C was mainly due to the glassy phase allowing grain boundary sliding. $MoSi_2$ with additives showed much higher strength values (> 750 MPa) up to 1100°C. The strength of $MoSi_2$ with 1 mol% additives maintained higher values up to higher temperature. The fracture strength behavior tracks the removal of glassy SiO_2 by the addition of R_2O_3.

4.4 Discussion

4.4.1 Difference of Appeared Phases between Two Systems

Interesting differences between the formed silicates with Sc_2O_3 and Y_2O_3 additions were mentioned in section 4.3 (Fig. 4.1 and Table 4.4). Since there are limited thermodynamic data in the Sc_2O_3-SiO_2 and Y_2O_3-SiO_2 binary systems, the author basically used phase diagrams; Figs. 4.9(a) and (b) show the diagrams for Sc_2O_3-SiO_2 [28] and Y_2O_3-SiO_2 systems [29].

For 1-5 mol% Y_2O_3 addition, some silica remained in the sintered bodies and $Y_2Si_2O_7$ appeared as a crystalline phase. With more Y_2O_3 addition (10-20mol%), silica disappeared and Y_2SiO_5 phase was formed replacing $Y_2Si_2O_7$ phase as anticipated from Fig. 4.9(b) with some excess Y_2O_3 remaining. For Sc_2O_3 addition, the lower additive content (1-5 mol%) resulted in almost the same result as Y_2O_3 addition (i.e. formation of 1:2 silicate, $Sc_2Si_2O_7$), but, on the other hand, higher additive content (10-20 mol%) did not produce 1:1 silicate, Sc_2SiO_5. The hot-pressing temperature used in this study was 1600°C, and this temperature is evidently high enough for the following reaction:
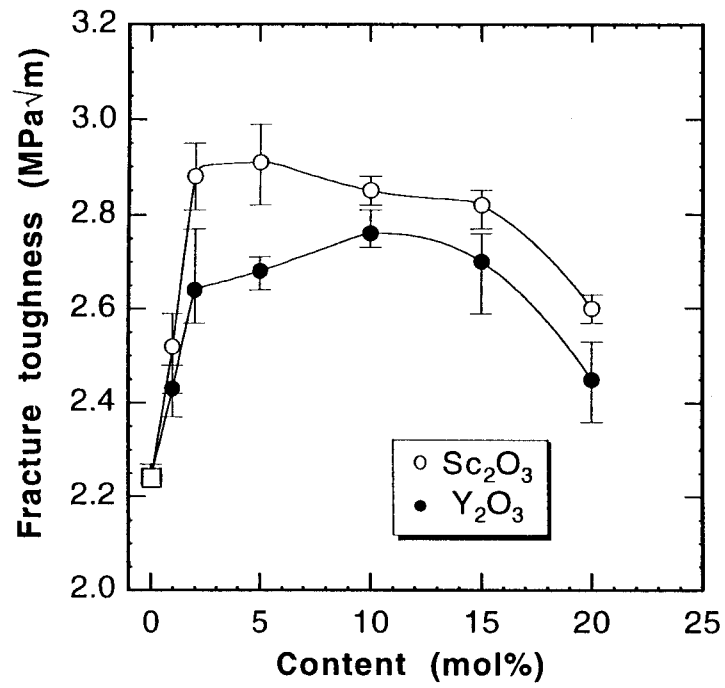
$$Sc_2O_3 + 2SiO_2 \rightarrow Sc_2Si_2O_7 \qquad (4.2)$$

Fig. 4.7 Variation of fracture toughness with R_2O_3 composition for $MoSi_2$-SiO_2-R_2O_3 system.

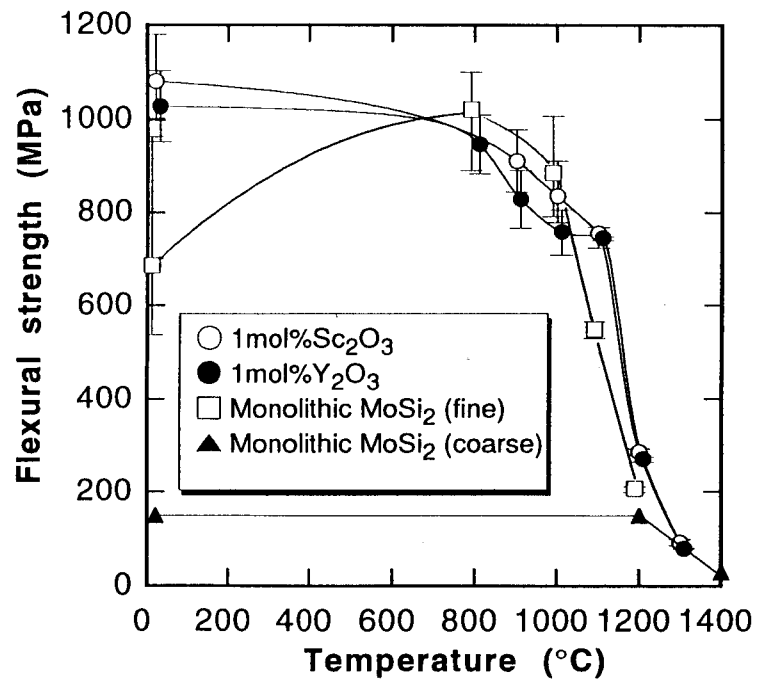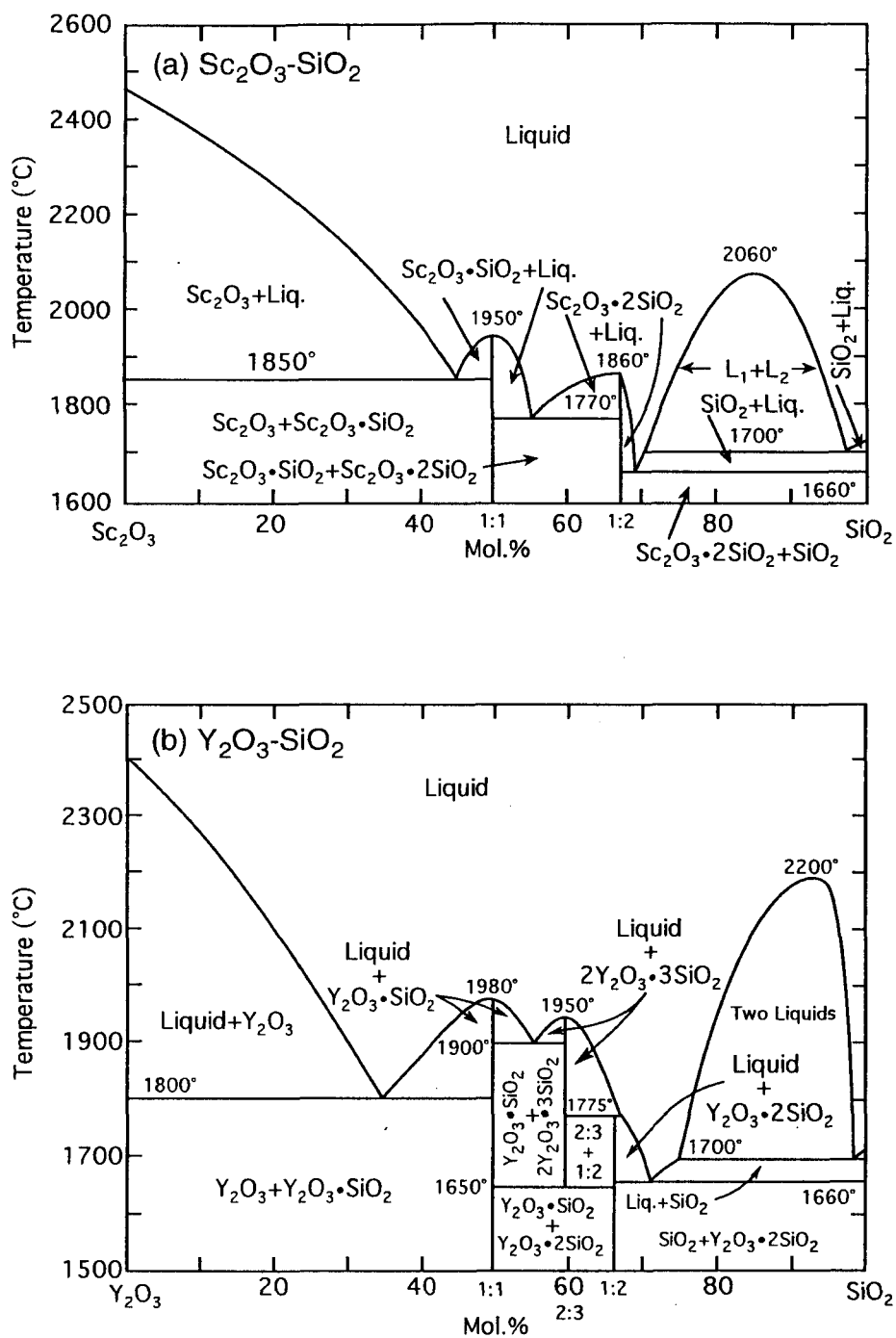**Fig. 4.8** Variation of flexural strength with temperature for $MoSi_2$-SiO_2-R_2O_3 system.

Fig. 4.9 Phase diagrams of (a) Sc$_2$O$_3$-SiO$_2$ and (b) Y$_2$O$_3$-SiO$_2$ binary systems [28,29].

expected because the eutectic temperature at 1660°C between $Sc_2Si_2O_7$ and SiO_2 is low enough for this reaction to easily take place. For more Sc_2O_3 content (10-20 mol%), where the eutectic temperature between Sc_2SiO_5 and $Sc_2Si_2O_7$, 1770°C, is much higher than the hot-pressing temperature, the following reactions evidently take place with more difficultly:

$$Sc_2O_3 + Sc_2Si_2O_7 \rightarrow 2Sc_2SiO_5 \tag{4.3}$$

$$\text{and/or} \quad Sc_2O_3 + SiO_2 \rightarrow Sc_2SiO_5 \tag{4.4}$$

For Y_2O_3-SiO_2 system, an eutectoid reaction exists between 1:1 and 1:2 silicates. The eutectoid transformation temperature is 1650° C, and it is 120° C lower than the eutectic temperature between Sc_2SiO_5 and $Sc_2Si_2O_7$. $MoSi_2$ with 5 mol% Y_2O_3 actually contained $Y_4Si_3O_{12}$ phase, and it demonstrated that the eutectoid reaction, indeed, took place in the $MoSi_2$-SiO_2-Y_2O_3 system. The fact that the 1:1 type silicate was formed for Y_2O_3 system, but was not observed for Sc_2O_3 added system is an intriguing difference.

4.4.2 Change of Density and Young's Modulus

As was shown in section 4.3, density and Young's modulus of sintered bodies increased and then decreased with additive content. To discuss such changes, densities and Young's moduli of constituent phases are listed in Table 4.5 [32,35-45]. The density of monolithic $MoSi_2$ sintered body was 5.92 g/cm³. This value is rather low comparing with the theoretical density calculated from XRD, 6.27 g/cm³[35]. Since almost no pores are observed by SEM for the $MoSi_2$ compact, the decrement of density must be attributed to the formation of low density (2.20 g/cm³) glassy SiO_2. As discussed in the phase analysis part, some cristobalite existed which spontaneously crystallized from glassy SiO_2. The density of cristobalite is 2.33 g/cm³[37], the difference of density between glassy SiO_2 and cristobalite is quite small. Although the density of $Mo_{\leq5}Si_3C_{\leq1}$ phase depends on its chemical composition, a typical value for $Mo_{4.8}Si_3C_{0.6}$ was reported as 7.891 g/cm³[36]. The density of monolithic $Mo_{\leq5}Si_3C_{\leq1}$ is slightly higher than that of $MoSi_2$. Since the content of $Mo_{\leq5}Si_3C_{\leq1}$ phase was small (about 3 vol% detected from an image analysis of SEM photographs), it can be neglected for the density calculation. Supposing that the $MoSi_2$ sintered body was composed of only $MoSi_2$ and glassy SiO_2, the density of sintered body is calculated by following equation:

$$D_{\text{sintered body}} = (1 - V_{SiO2}) D_{MoSi2} + V_{SiO2} D_{SiO2} \tag{4.5}$$

where V and D represent volume fraction and density: $D_{\text{sintered body}}$, D_{MoSi2} and D_{SiO2} are 5.92, 6.27 and 2.22 g/cm³, respectively. V_{SiO2} was calculated to be 8.6% by Eq. 4.5, in good agreement with the volume fraction from image analysis, about 8.5%. This value is somewhat

Table 4.5 Density and Young's modulus of phases present.

Phase	Density (g/cm^3)	Young's modulus (GPa)
MoSi$_2$	6.270 [35]	440 [32]
Mo$_{\leq5}$Si$_3$C$_{\leq1}$	7.891 [36]	285 [43]
SiO$_2$ (glass)	2.20 [37]	73 [37]
Sc$_2$O$_3$	3.840 [38]	227.6 [44]
Y$_2$O$_3$	5.032 [39]	171.5 [45]
Sc$_2$Si$_2$O$_7$	3.394 [40]	-
β-Y$_2$Si$_2$O$_7$	4.030 [41]	-
Y$_2$SiO$_5$	4.441 [42]	-

Y$_4$Si$_3$O$_{12}$ data was not available.

larger than the total oxide content in the starting MoSi$_2$ powder (about 6 vol%) as was listed in Table 4.2. It may be attributed to more oxidation of fresh surface by ball-milling.

Next, the density change with additive content is addressed. The volume change (ΔV) between before and after the following reactions,

$$Sc_2O_3 + 2SiO_2 \rightarrow Sc_2Si_2O_7 \tag{4.2}$$

$$Y_2O_3 + 2SiO_2 \rightarrow Y_2Si_2O_7 \tag{4.6}$$

were $\Delta V = -18\%$ and -15%, respectively. As almost no pores were observed by SEM, the progress of the reactions 4.2 or 4.6, i.e., removal of SiO$_2$, must result in an increase of density. For higher additive content (10-20 mol%), the densities become smaller as the densities of unreacted Sc$_2$O$_3$ and Y$_2$O$_3$ are smaller than that of MoSi$_2$.

Young's modulus showed its maximum at 5 mol% additions, as shown in Fig. 4.4. The Young's modulus of polycrystalline MoSi$_2$ has been calculated from the single crystal, 440 GPa [32]. On the other hand, that of glassy SiO$_2$ is much smaller, 73 GPa [37]. To a first approximation, the monolithic MoSi$_2$ sintered body was composed of 8.5 vol% of glassy SiO$_2$ phase and 91.5 vol% of MoSi$_2$ phase, the Young's modulus of the sintered body without pores was calculated to be 386 GPa, using the following equation [46]:

$$\ln E_{\text{sintered body}} = V_{\text{SiO2}} \ln E_{\text{SiO2}} + V_{\text{MoSi2}} \ln E_{\text{MoSi2}} \tag{4.7}$$

The value of 386 GPa, somewhat larger than the observed value of 372 GPa, is within a reasonable comparison. Then, on the second approximation, the effect of dispersion of the Mo$_{\leq5}$Si$_3$C$_{\leq1}$ phase was taken into account for the calculation. Recently, the authors investigated the

properties of polycrystalline $Mo_{\leq 5}Si_3C_{\leq 1}$ phase and its composites [43]. The measured Young's modulus of polycrystalline $Mo_{\leq 5}Si_3C_{\leq 1}$ was 285 GPa. In this experiment, about 3 vol% of Mo $_{\leq 5}Si_3C_{\leq 1}$ phase was dispersed in the monolithic $MoSi_2$ sintered body. The Young's modulus of the $MoSi_2$ sintered body without pores was calculated using a modified equation:

$$\ln E_{\text{sintered body}} = V_{SiO2} \ln E_{SiO2} + V_{Mo\leq5Si3C\leq1} \ln E_{Mo\leq5Si3C\leq1} + V_{MoSi2} \ln E_{MoSi2} \qquad (4.8)$$

where $V_{SiO2} = 8.5$ %, $V_{Mo\leq5Si3C\leq1} = 3.0$ %, and $V_{MoSi2} = 88.5$ %. The calculated Young's modulus was 373 GPa, and is in unreasonably excellent agreement with the observed value of 372 GPa.

The 5 mol% addition resulted in the maximum Young's modulus for both Sc_2O_3 and Y_2O_3 addition. As was discussed above, free silica disappeared around this composition. Although there was no available reported values of the Young's modulus for $Sc_2Si_2O_7$, $Y_2Si_2O_7$ and other silicate phases, it is considered that the Young's modulus of such crystalline phases is surely higher than that of glassy SiO_2. $Sc_2Si_2O_7$ should have higher Young's modulus than $Y_2Si_2O_7$, because Sc^{3+} ion is smaller than Y^{3+} ion, with inevitably stronger Sc-O-Si bonds than Y-O-Si (as also confirmed by the effectively higher high temperature stability). The Young's modulus of Sc_2O_3 and Y_2O_3 are 227.6 [44] and 171.5GPa [45], respectively, suggested again the stronger Sc-O bond than Y-O one (tracking the MP.s at 2460° C vs. 2400° C). Thus, the Young's modulus of Sc_2O_3 added system is always higher than that of Y_2O_3 added system.

4.4.3 Microstructural Dependence of Mechanical Properties

As detailed in section 4.3, only a small amount of rare earth oxide addition strongly improved various mechanical properties, e.g. 1 mol% additives significantly improved fracture strength. To illuminate the effect of crystallization on mechanical properties, TEM observation was performed on 1 mol% Sc_2O_3 added system, which showed the highest bending strength (Figs. 4.10(a) and (b)). Fig. 4.10(a) shows a siliceous pocket in the sintered body, in which a crystalline phase, $Sc_2Si_2O_7$, has formed. Dislocation networks were observed in the $MoSi_2$ around the oxide pockets (Fig. 4.10(b)). When glassy SiO_2 crystallizes, it should lose plastic deformability. Thus, thermal stress between matrix and oxides has not been fully relaxed by the plastic deformation of glassy SiO_2, leading to the numerous dislocations in the $MoSi_2$. For the 1-5 mol% addition, the amount of total oxide phase was not so large. Formed $R_2Si_2O_7$ crystals effectively toughened the glassy phase, and improved mechanical properties, perhaps by reducing the source flaw size in the glass. With more addition, however, the oxide phases become continuous, and may act as larger fracture origins; mechanical properties, especially strength, decline. In Fig. 4.5, error bars (5-6 specimen tests) become large at 10 mol% addition, which was equivalent to 14 and 17 vol% addition for Sc_2O_3 and Y_2O_3 addition, respectively (see Table 4.3). Thus, 10 mol% addition is at the threshold value of ~16 vol% for
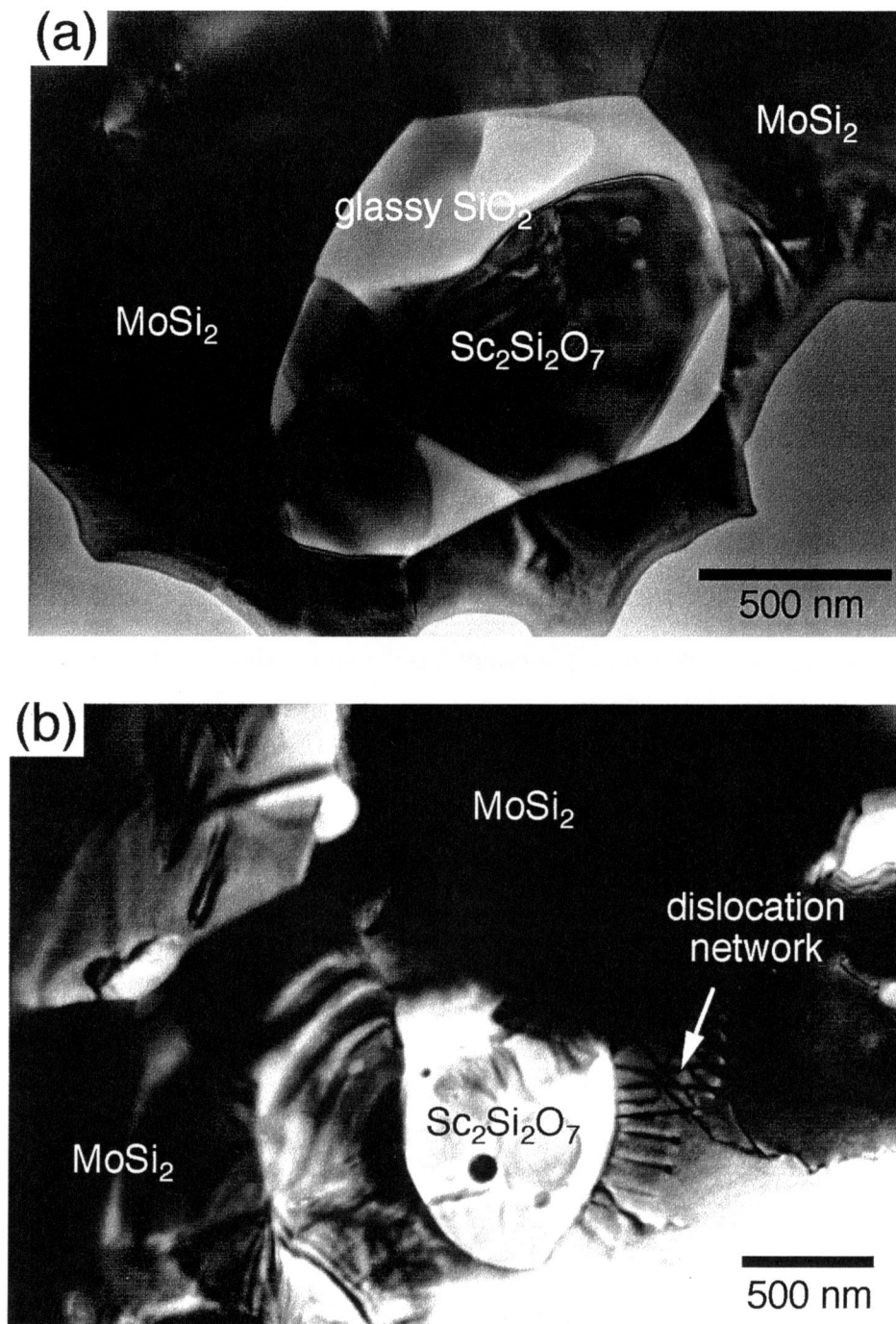
Fig. 4.10 TEM photographs of 1 mol% Sc_2O_3 added $MoSi_2$: (a) $Sc_2Si_2O_7$ formation inside the glassy SiO_2 pocket (by EDS), (b) dislocation networks around siliceous pockets.

percolation of oxide phases, and may well explain why the error bars increase at this level. At this stage, these reasonings should be considered preliminary and tentative.

4.4.4 Comparison with Other Techniques to Remove Glassy SiO_2

In the introduction section, SiO_2-removing techniques were classified into five categories. The present study on $MoSi_2$-SiO_2-Sc_2O_3 and $MoSi_2$-SiO_2-Y_2O_3 is basically equivalent to that done on Si_3N_4 based ceramics [19-22]. One difference, however, is that glassy SiO_2 in the $MoSi_2$ does not form films at grain boundaries. Here, glassy SiO_2 and additives concentrate at triple points, so that the bulk reaction seems to progress easily at relatively mild conditions (1600°C for 1 h).

4.5 Conclusions

In this study, the modification of the grain boundary phase in the $MoSi_2$ hot-pressed bodies by the addition of Sc_2O_3 and Y_2O_3 was studied. In summary:

1. The intergranular glassy SiO_2 phase was converted to the crystalline silicates.
2. Mechanical properties at room and high temperatures were enhanced by Sc_2O_3 and Y_2O_3 additions. Only 1 mol% additives highly improved various mechanical properties, bringing both technical and economical benefits.
3. These results indicate that *in situ* crystallization of the glassy SiO_2 phase by the addition of these refractory oxides has great advantages in fabricating $MoSi_2$-based composites with improved mechanical properties, and undoubtedly further optimization can be expected.

References

1. A. K. Vasudévan and J. J. Petrovic, "A Comparative Overview of Molybdenum Disilicide Composites," *Mater. Sci. Eng.*, A155, 1-17 (1992).

2. Y. L. Jeng and E. J. Lavernia, "Processing of molybdenum disilicide", *J. Mater. Sci.*, 29, 2557-2571 (1994).

3. X. Fan, T. Ishigaki and Y. Sato, "Phase Formation in Molybdenum Disilicide Powders during In-Flight Induction Plasma Treatment," *J. Mater. Res.*, 12 [5] 1315-1326 (1997).

4. A. Costa e Silva and M. J. Kaufman, "Phase Relations in the Mo-Si-C System Relevant to the Processing of MoSi₂-SiC Composites," *Matell. Mater. Trans.*, 25A, 5-15 (1994).

5. Y. Suzuki, T. Sekino and K. Niihara, "Effects of ZrO₂ Addition on Microstructure and Mechanical Properties of MoSi₂," *Scripta Metall. et Mater.*, 33 [1] 69-74 (1995).

6. Y. Suzuki, A. Nakahira, T. Sekino and K. Niihara, "Microstructure and Mechanical Properties of Mo-Si-Al Alloy and Mo-Si-Al/SiC Composite," *J. Jap. Soc. Pow. & Pow. Metall.*, 43 [3] 272-277 (1996).

7. E. Fitzer, in Ceramic Transactions, Vol. 10, *Corrosive and Erosive Degradation of Ceramics*, edited by R. B. Tressler and M. McNallan (American Ceramic Society, Westerville, OH, 1989) p.19.

8. R. Gibala, A. K. Ghosh, D. C. Van Aken, D. J. Srolovitz, A. Basu, H. Chang, D. P. Mason and W. Yang, "Mechanical Behavior and Interface Design of MoSi₂-Based Alloys and Composites," *Mater. Sci. Eng.*, A155, 147-158 (1992).

9. K. Shobu, T. Watanabe and K. Tsuji, "Effects of Mo₂B₅ Addition to MoSi₂ Ceramics", *J. Ceram. Soc. Jap.*, 97 [10] 1311-14 (1989).

10. J. Hojo, Y. Ishizaka, K. Kishi and S. Umebayashi, "Microstructure and Properties MoSi₂ and MoSi₂-SiC sintered bodies obtained from fine powders," *J. Jap. Soc. Pow. & Pow. Metall.*, 42 [11] 1295-1299 (1995).

11. W. A. Maxwell., NACA RME52 B06, (1952).

12. S. A. Maloy, A. H. Heuer, J. J. Lewandowski, and J. J. Petrovic, "Carbon Additions to Molybdenum Disilicide: Improved High-Temperature Mechanical Properties," *J. Am. Ceram. Soc.*, 74 [10] 2704-2706 (1991).

13. S. A. Maloy, J. J. Lewandowski, A. H. Heuer and J. J. Petrovic, "Effects of Carbon Additions on the High Temperature Mechanical Properties of Molybdenum Disilicide," *Mater. Sci. Eng.*, A155, 159-163 (1992).

14. E. Fitzer, K. Reinmuth and H. Schnabel., "Compacting and Sintering of Molybdenum Disilicide,"Arch. Eisenhüttenwesen, 40 [11] 895 - 900 (1969).

15. A. Costa e Silva and M. J. Kaufman, "Microstructural Modification of MoSi₂ through Aluminum Additions", *Scripta Metall. Mater.*, 29 [8] 1141-1145 (1993).

16. A. Costa e Silva and M. J. Kaufman, "Applications of *in situ* reactions to MoSi₂-based materials," *Mater. Sci. Eng.*, A195, 75-88 (1995).

17. A. Costa e Silva and M. J. Kaufman, "Synthesis of MoSi₂-Boride Composites through *In Situ* Displacement Reactions," *Intermetallics*, 5, 1-15 (1997).

18. Y. Suzuki, T. Sekino and K. Niihara, "Effects of Al Substitution and Nano-Sized SiC Dispersion on Microstructure and Mechanical Properties of MoSi₂," Proceedings of the 6th Tohwa University International Symposium: Frontier Nanostructured Ceramics, Fukuoka, October 1996, edited by Y. Nagano (Tohwa University Press, 1996) pp.189-194.

19. P. E. D. Morgan, F. F. Lange, D. R. Clarke and B. I. Davis, "A New Si₃N₄ Material: Phase Relations in the System Si-Sc-O-N and Preliminary Property Studies," *J. Am. Ceram. Soc.*, 64 [4] C-77-78 (1981).

20. P. E. D. Morgan, "Si₃N₄ Ceramic Densified Using Sc₂O₃ and SiO₂,"*US Patent*, No.4401768 (1983).

21. M. L. Mecartney, "Enhanced crystallization of a glassy phase in silicon nitride by the addition of scandia," *J. Am. Ceram. Soc.*, 70 [12] C380-382 (1987).

22. D.-S. Cheong, W. A. Sanders, "High-temperature deformation and microstructural analysis for silicon nitride-scandium(III) oxide," *J. Am. Ceram. Soc.*, **7 5** [12] 3331-36 (1992).

23. E. N. Kulenko and B. I. Polyak, "Sintering of the Ceramics Belonging to the $MoSi_2$-Y_2O_3 and $MoSi_2$-SiC Systems," *Refractories*, **3 0**, 418-425 (1990).

24. I. Ya. Zalkind, E. N. Kulenko, T. N. Morugova, A. I. Rekov and G. A. Fomina, "Interaction of the Granular-Laminar Material $MoSi_2$-Y_2O_3 with Fuel Slag," *Teplofiz. Vys. Temp.*, **1 9** [6] 1285-92 (1981).

25. S. Wada, "Increase of Oxygen Content in Si_3N_4 Powder During Ball Milling Using Alcohol as Solvent," *J. Ceram. Soc. Jpn.*, **1 0 4** [11] 1085-1087 (1996).

26. K. Niihara, R. Morena and D. P. H. Hasselman, "Evaluation of K_{IC} of Brittle Solids by the Indentation Method with Low Crack-to-Indent Ratios," *J. Mater. Sci. Lett.*, **1** [1] 13-16 (1982).

27. E. Parthé and W. Jeitschko, "A Neutron Diffraction Study of the Nowotny Phase $Mo_{\leq 5}Si_3C_{\leq 1}$," *Acta Cryst.*, **1 9**, 1031-1037 (1965).

28. E. M. Levin, C. R. Robbins and H. F. McMurdie, "Phase diagrams for ceramics, 1969 supplement", the American Ceramics Society, Ohio, U. S. A., p.105, No.2384, (1969).

29. E. M. Levin, C. R. Robbins and H. F. McMurdie, "Phase diagrams for ceramics, 1969 supplement", the American Ceramics Society, Ohio, U. S. A., p.107, No.2388, (1969).

30. T. R. Dinger, R. S. Rai and G. Thomas, "Crystallization Behavior of a Glass in the Y_2O_3-SiO_2-AlN System," *J. Am. Ceram. Soc.*, **7 1** [4] 236-244 (1988).

31. G. H. Meier and F. S. Pettit, "The oxidation behavior of intermetallic compounds," *Mater. Sci. Eng.*, **A 1 5 3**, 548-560 (1992).

32. M. Nakamura, S. Matsumoto and T. Hirano, "Elastic Constants of $MoSi_2$ and WSi_2 Single Crystals", *J. Mater. Sci.*, **2 5**, 3309-3313 (1990).

33. Y. Suzuki and K. Niihara, "Effect of SiC Reinforcement on Microstructure and Mechanical Properties of $MoSi_2$," *Sci. Eng. Comp. Mater.*, **6** [2] 85-94 (1997).

34. D. H. Carter, W. S. Gibbs, and J. J. Petrovic, "Mechanical Characterization of SiC Whisker-Reinforced $MoSi_2$," *Proceedings of Ceramics Materials & Components for Engines*, pp.977-986, (1988).

35. JCPDS Powder Diffraction File, No.41-0612 on $MoSi_2$.

36. JCPDS Powder Diffraction File, No.43-1199 on $Mo_{4.8}Si_3C_{0.6}$.

37. Cyclopedia of Fine Ceramics, ed. by H. Yanagida et al., Gihodo Press, Tokyo, pp. 135- 153 (1987).

38. JCPDS Powder Diffraction File, No.43-1028 on Sc_2O_3.

39. JCPDS Powder Diffraction File, No.43-1036 on Y_2O_3.

40. JCPDS Powder Diffraction File, No.20-1037 on $Sc_2Si_2O_7$.

41. JCPDS Powder Diffraction File, No.38-0440 on β-$Y_2Si_2O_7$.

42. JCPDS Powder Diffraction File, No.36-1476 on Y_2SiO_5.

43. Y. Suzuki and K. Niihara, "Synthesis and Mechanical Properties of $Mo_{\leq 5}Si_3C_{\leq 1}$ and $Mo_{\leq 5}Si_3C_{\leq 1}$-Based Composites," *Intermetallics* (in press)

44. S. L. Dole, O. Hunter Jr., and F. W. Calderwood, "Elastic Properties of Polycrystalline Scandium and Thulium Sesquioxides," *J. Am. Ceram. Soc.*, **6 0** [3-4] 167-168 (1977).

45. W. R. Manning, O. Hunter Jr., and B. R. Powell Jr., "Elastic Properties of Polycrystalline Yttrium Oxide, Dysprosium Oxide, Holmium Oxide, and Erbium Oxide: Room Temperature Measurements," *J. Amer. Ceram. Soc.*, **5 2** [8] 436-442 (1969).

46. Y. Kagawa and H. Hatta,"Tailoring Ceramic Composites," Agune Shoufusya, Tokyo, pp.96-119, (1990).

5

Combined Effects of *In Situ* Crystallization of Grain Boundary Phase and Transformation Toughening by ZrO_2 and HfO_2 Additions

In this chapter, the improvement in mechanical properties of powder processed $MoSi_2$ by the additions of 3 mol % Y_2O_3 stabilized ZrO_2 (3Y-ZrO_2) and HfO_2 were discussed, and the combined effects of *in situ* crystallization and transformation toughening were investigated. 3Y-ZrO_2 added $MoSi_2$ compacts were composed of matrix $MoSi_2$, $Mo_{\leq5}Si_3C_{\leq1}$, well-crystallized $ZrSiO_4$, and unreacted tetragonal ZrO_2; the glassy SiO_2 phase was successfully changed into the thermodynamically stable crystalline $ZrSiO_4$ by the 3Y-ZrO_2 addition, similarly to the rare earth oxide (R_2O_3) additives. $MoSi_2$ with only 1 mol % 3Y-ZrO_2 showed excellent fracture strength in analogy with $MoSi_2$ with R_2O_3 additives, and such strength enhancement was attributed to *in situ* crystallization of glassy SiO_2. $MoSi_2$ with higher content of 3Y-ZrO_2 additive showed well-balanced mechanical properties at room temperature, arisen from the combined effects of *in situ* crystallization and transformation toughening. 2 mol% HfO_2 addition also improved fracture strength via *in situ* crystallization of glassy SiO_2. $MoSi_2$ with 15-20 mol% HfO_2 exhibited obvious hardening, probably due to residual stress field formation arisen from the thermal expansion anisotropy.
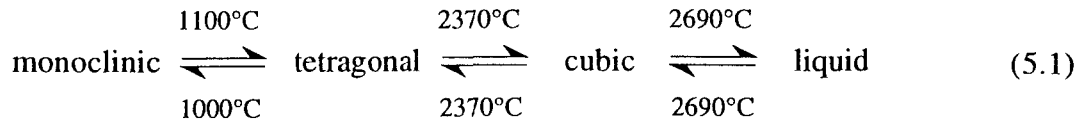
5.1 Introduction

In situ crystallization of glassy SiO_2 is a very useful method to improve mechanical properties of sintered $MoSi_2$, as was shown in Chap. 4. While only 1 mol% rare earth oxide additives markedly improved mechanical properties, higher content (15- 20 mol%) of additives did not appreciably improve mechanical properties. This was because intrinsic strength and toughness of rare earth oxides were not so high, and thus continuous oxide regions became fracture origin, or crack paths themselves.

Considerable research efforts have been devoted to zirconia (ZrO_2)-toughened ceramics (ZTCs), since the discovery of transformation toughening in the mid 1970s [1-4], when a dozen of years passed from the first suggestion by Wolten [5] that the tetragonal to monoclinic

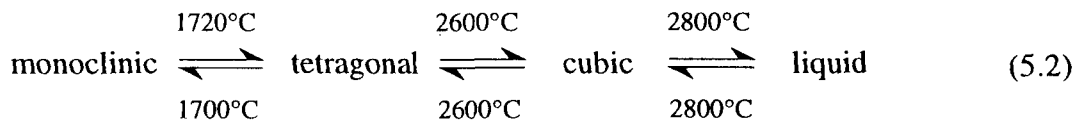transformation of ZrO_2 is martensitic, similarly to steel.

Both temperature and pressure affect the polymorphism of ZrO_2; ZrO_2 exhibits the following transformations with increasing temperature [6,7].

$$
\text{monoclinic} \underset{1000°C}{\overset{1100°C}{\rightleftharpoons}} \text{tetragonal} \underset{2370°C}{\overset{2370°C}{\rightleftharpoons}} \text{cubic} \underset{2690°C}{\overset{2690°C}{\rightleftharpoons}} \text{liquid} \tag{5.1}
$$

Adding another alloying oxide in ZrO_2 to form solid solution is the most common method to modify the tetragonal to monoclinic transformation temperature [1]. It is essential to form and retain the metastable tetragonal phase in sintered bodies to obtain excellent mechanical properties. Highly toughened tetragonal zirconia polycrystals are produced by doping Y_2O_3 or CeO_2, via a careful composition and processing control; 2.5 to 3 mol% Y_2O_3 doped ZrO_2 exhibits considerably high strength and toughness among oxide ceramics. Petrovic et al. [5-8] reported that ZrO_2 or partially-stabilized ZrO_2 (PSZ) additions were effective to improve the toughness of the brittle $MoSi_2$ matrix through transformation toughening, similarly to conventional ZTCs.

In addition to the transformation toughening effect, however, other important roles of ZrO_2 should be suggested because it easily forms many kinds of stable double oxides. ZrO_2 addition may decrease the glassy SiO_2 in $MoSi_2$ sintered bodies by forming a double oxide, $ZrSiO_4$, and hence improve various mechanical properties in a similar manner as rare earth oxide addition.

Hafnia (HfO_2) and hafnium-based materials are traditionally regarded as technologically important materials in the nuclear industry due to their exceptionally high neutron absorption coefficient [12]. HfO_2 has the same crystal structure as ZrO_2, but its tetragonal to monoclinic transformation temperature (approximately 1700°C) is approximately 700°C higher than that for ZrO_2, which is expressed as follows [5,13].

$$
\text{monoclinic} \underset{1700°C}{\overset{1720°C}{\rightleftharpoons}} \text{tetragonal} \underset{2600°C}{\overset{2600°C}{\rightleftharpoons}} \text{cubic} \underset{2800°C}{\overset{2800°C}{\rightleftharpoons}} \text{liquid} \tag{5.2}
$$

Thus, it has been suggested that high-temperature transformation toughening could be possible in HfO_2-toughened ceramics (HTCs) [12]. Although the concepts behind this suggestion are universally appreciated, only a limited success has been made of the fabrication and the microstructural and mechanical property evaluation of these materials [12]. Leaving the question that high-temperature transformation toughening in HTCs is effective or not, HfO_2 is still an attractive second phase reinforcement material due to its high melting point (~2800° C) and lowest vapor pressure among oxide ceramics.

In this chapter, the combined effects of in situ crystallization of glassy SiO_2 and transformation toughening on mechanical properties of $MoSi_2$ through the 3Y-ZrO_2 addition were

71

investigated by means of the comparison with HfO_2 and rare earth oxide additions. In particular, the dependence of fracture strength with additive contents was discussed in detail. Effects of processing conditions were also discussed for the $3Y$-ZrO_2 added $MoSi_2$ system.

5.2 Experimental Procedure

5.2.1 Sample Preparation

First, the composition dependence of additive oxides on mechanical properties was investigated by means of the same sample preparation methods as described in Chap. 4. Starting materials were $MoSi_2$ (1.01 μm, Japan New Metals Co., Ltd., the same powder used in Chap. 4), 3 mol% Y_2O_3 stabilized ZrO_2 ($3Y$-ZrO_2, specific surface area of 20 m^2/g, crystalline size measured by XRD of 35 nm, Sumitomo Osaka Cement Co. Ltd.) and HfO_2 (about 2 μm, 98%, unstabilized monoclinic structure, Kojundo Chemical Lab. Co. Ltd.). The $3Y$-ZrO_2 or HfO_2 composition in this investigation was restricted to 1-20 mol% because too much oxide additives might degrade the high-temperature mechanical properties. Nominal compositions of the powder mixture are summarized in Table 5.1. Oxide additives studied in Chaps. 4 and 5 have

Table 5.1 Nominal* compositions of the powder mixtures.

No.	composition (mol%)			composition (wt%)**			composition (vol%)***		
	$MoSi_2$	$3Y$-ZrO_2	HfO_2	$MoSi_2$	$3Y$-ZrO_2	HfO_2	$MoSi_2$	$3Y$-ZrO_2	HfO_2
1	100	-	-	100	-	-	100	-	-
2	99	1	-	99.2	0.8	-	99.1	0.9	-
3	98	2	-	98.3	1.7	-	98.3	1.7	-
4	95	5	-	95.8	4.2	-	95.7	4.3	-
5	90	10	-	91.6	8.4	-	91.3	8.7	-
6	85	15	-	87.2	12.8	-	86.8	13.2	-
7	80	20	-	82.8	17.2	-	82.3	17.7	-
8	99	-	1	98.6	-	1.4	99.1	-	0.9
9	98	-	2	97.2	-	2.8	98.3	-	1.7
10	95	-	5	93.2	-	6.8	95.7	-	4.3
11	90	-	10	86.6	-	13.4	91.3	-	8.7
12	85	-	15	80.3	-	19.7	86.8	-	13.2
13	80	-	20	74.3	-	25.7	82.3	-	17.7

* supposing that the starting powders were pure $MoSi_2$, Sc_2O_3 and Y_2O_3.
** formula weight: $MoSi_2$ = 152.111, $3Y$-ZrO_2 (0.97ZrO_2–0.03Y_2O_3)= 126.30 and HfO_2 = 210.49
*** X-ray density: D_{MoSi2} = 6.27 g/cm^3 , $D_{3Y-ZrO2}$ = 6.05 g/cm^3 , and D_{HfO2} = 10.111 g/cm^3.

different cationic valency (i.e. trivalent for Sc_2O_3 and Y_2O_3 (R_2O_3), and tetravalent for ZrO_2 and HfO_2 (MO_2)), but the same ranges of mole fractions were simply used (not as 1-20 mol% of R_2O_3 vs. 'M_2O_4') by following reason; formula weights of 3Y-ZrO_2 ($0.97ZrO_2$–$0.03Y_2O_3$) and HfO_2 are 126.30 and 210.49, respectively, which are close to those of Sc_2O_3 and Y_2O_3 (137.91 and 225.81). Thus, the weight fractions of $MoSi_2$/3Y-ZrO_2 and $MoSi_2$/Sc_2O_3 with same mole fractions are almost identical each other, and this relation is also applicable to $MoSi_2$/HfO_2 and $MoSi_2$/Y_2O_3 (see Tables 4.3 and 5.1). In addition, the volume fractions of $MoSi_2$/3Y-ZrO_2 and $MoSi_2$/HfO_2 with same mole fractions are almost identical each other, due to its similar lattice volume. $MoSi_2$ and additive oxide powders were wet ball-milled with ZrO_2 balls for 24 h in n-hexane which was used to avoid the mechano-chemical oxidation by usual alcohol solvents. The mixture was packed into carbon dies, coated with BN, and hot-pressed at 1600°C under an applied pressure of 30 MPa for 1 h in vacuum.

Second, effects of processing conditions were investigated for the 3Y-ZrO_2 added $MoSi_2$ system. Since 3Y-ZrO_2 powders are generally very fine, they can be nano-sized dispersoids in $MoSi_2$ matrix. To achieve more homogeneous and finer dispersion, polar solvents rather than nonpolar one for wet ball-milling are suitable for $MoSi_2$-based systems because a $MoSi_2$ powder has a surface SiO_2 layer accompanied with silanol groups. In addition, moderate viscosity is also favorable for wet ball-milling solvents. Hence, 1-butanol (1-BuOH) was used as a ball-milling solvent, although it may mechano-chemically oxidize $MoSi_2$ powders in some extent.

The sample preparation method was basically same in Chap. 3. Starting materials were $MoSi_2$ powder (0.98 μm, Japan New Metals Co., Ltd., identical one used in Chap. 3, and almost equivalent to the above mentioned powder) and 3 mol% Y_2O_3 doped ZrO_2 powder (3Y-ZrO_2, 0.3 μm, specific surface area of 18 m^2/g, crystalline size measured by XRD of 24 nm, Tosoh Co., Ltd.). 3Y-ZrO_2 was added 15 % by volume in order to compare with $MoSi_2$/15 vol%SiC nanocomposites in Chap. 3; the 15 vol% addition corresponded to 17.0 mol% or 14.6 wt% additions. $MoSi_2$ and 3Y-ZrO_2 powders were wet-ball-milled in 1-butanol with ZrO_2 balls for 24 h, and then the dried mixture was dry-ball-milled to crush the agglomeration. The mixture was hot-pressed at 1550°C under an applied pressure of 30 MPa for 1 h in an argon atmosphere.

The sintered disks were 44 mm in diameter and 5.0 mm in thickness. The hot-pressed bodies were cut, ground and polished into rectangular bars with 4×3×36 mm in size.

5.2.2 Evaluation

Evaluation was conducted in similar manners as described in Chap. 4, and shown here briefly. Phase identification was carried out by X-ray diffraction (XRD). The microstructure was characterized by scanning electron microscopy with energy dispersive X-ray spectrometry (SEM-EDS). Transmission electron microscopy (TEM) with EDS was also used for the

microstructural characterization. The bulk density was measured by the Archimedes method in toluene at room temperature. Young's modulus was determined by the resonance vibration method adjusted to the thickness correction. More than five specimens in each case were subjected to three-point bending test (span: 30 mm, crosshead speed of 0.5 mm/min, in air) to determine fracture strength up to 1300°C. Hardness (H_V) was evaluated by Vickers indentation under a conditions of 98 N load with loading duration of 15 s in air. Fracture toughness (K_{IC}) at room temperature was determined simultaneously by the indentation fracture (IF) method. High-temperature Vickers hardness was also evaluated under a conditions of 4.9 N load up to 1200°C for the $MoSi_2/17$ mol% (15 vol%) $3Y-ZrO_2$ composite, and compared with monolithic $MoSi_2$ hot-pressed at 1500°C.

5.3   Results

5.3.1   Phase Analysis

XRD analysis revealed that the $MoSi_2/3Y-ZrO_2$ composites consisted of $MoSi_2$, $Mo_{\leq 5}Si_3C_{\leq 1}$ Nowotny phase and well-crystallized $ZrSiO_4$ (probably a small quantity of Y_2O_3 was held in solid-solution); additionally, a trace of spontaneously crystallized SiO_2, cristobalite, was also observed for less additive contents, and unreacted tetragonal ZrO_2 ($t-ZrO_2$) was also identified for much additive contents, similarly to rare earth oxide additives as shown in Chap. 4. There was no observable difference of appeared phases between the two preparation methods. Fig. 5.1 shows a XRD pattern for the 17 mol% 3Y- ZrO_2 added $MoSi_2$ composite fabricated using 1-butanol. $ZrSiO_4$ was formed by a reaction between ZrO_2 and SiO_2 at the surfaces of starting $MoSi_2$ powder. The cristobalite peak around $2\theta = 22°$ decreased (as expected) with increasing ZrO_2 content as $ZrSiO_4$ forms with the inevitable reaction with glassy SiO_2. $ZrSiO_4$ has a low coefficient of thermal expansion (CTE) among most oxide ceramics ($4.1 \times 10^{-6}/K$ [14]), leading to a good thermal shock resistance, and possesses an excellent chemical corrosion resistance [15]. In addition, $ZrSiO_4$ is a compound thermodynamically stable up to about 1700°C [16,17]. Thus, the formation of $ZrSiO_4$ seems to be favorable to obtain good mechanical properties in the $MoSi_2-SiO_2-ZrO_2$ system.

Similar phase relationship was observed for $MoSi_2/HfO_2$ composites. They were composed of $MoSi_2$, $Mo_{\leq 5}Si_3C_{\leq 1}$ Nowotny phase and $HfSiO_4$, and a trace of cristobalite for less additives and unreacted monoclinic HfO_2 for much additive contents. $HfSiO_4$ was formed by a reaction between HfO_2 and SiO_2 similarly to $3Y-ZrO_2$ addition case. CTE of $HfSiO_4$ is rather small ($3.8 \times 10^{-6}/K$ [14]), leading to a good thermal shock resistance. $HfSiO_4$ is thermodynamically more stable than $ZrSiO_4$, up to 1750° C [18]. Thus, the formation of $HfSiO_4$, and hence, the dispersion of $HfSiO_4$ into the $MoSi_2$ matrix also seem to be favorable to improve mechanical properties in the $MoSi_2-SiO_2-HfO_2$ system.
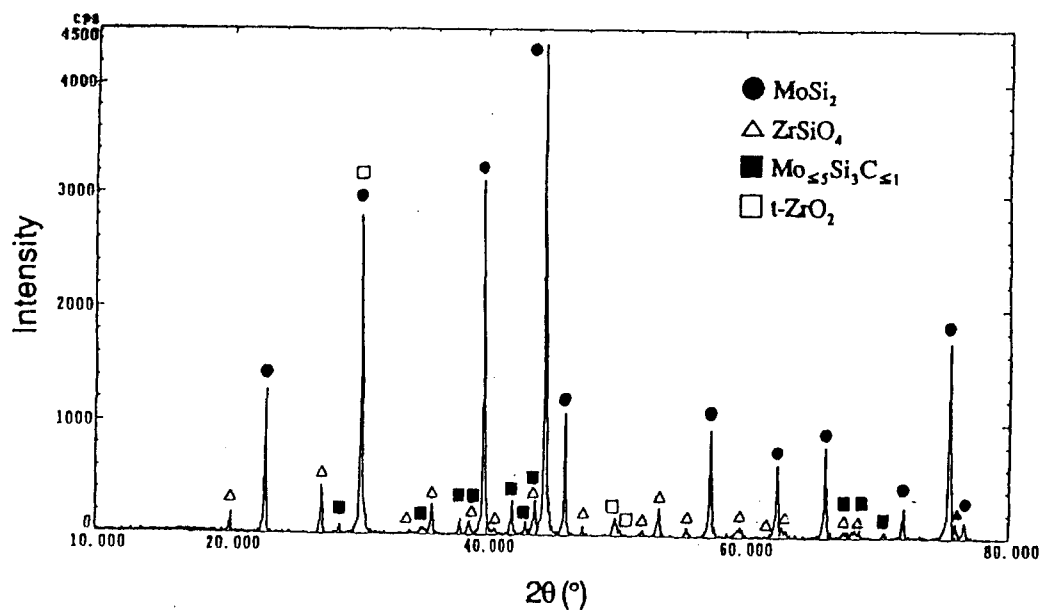
74

Fig. 5.1 X-ray diffraction pattern of the 17 mol% (15 vol%) 3Y-ZrO$_2$ added MoSi$_2$ composite.

5.3.2 Microstructure

Fig. 5.2 shows a SEM photograph of polished surface of the 17 mol% (15vol%) 3Y- ZrO$_2$ added MoSi$_2$ composite prepared using 1-BuOH. In this figure, the dark regions are oxide phases (not pores). As seen from Fig. 5.2, four regions were identified: MoSi$_2$, Mo$_{\leq5}$Si$_3$C$_{\leq1}$, ZrSiO$_4$/t-ZrO$_2$ mixed region and a trace of glassy SiO$_2$ residue. Thus, it is inferred that the additives and silica react together at grain boundary pockets. It is obvious that when compared to the hot-pressed MoSi$_2$ without oxide additives, the volume fraction of the glassy SiO$_2$ phase decreased with the ZrSiO$_4$ formation resulting from a reaction of SiO$_2$ with the added 3Y-ZrO$_2$. The ZrSiO$_4$ particles less than approximately 2 μm were homogeneously dispersed in the sintered bodies. The MoSi$_2$/1-20 mol% 3Y-ZrO$_2$ and HfO$_2$ composites prepared using hexane had similar microstructure with the MoSi$_2$/1-20 mol% Sc$_2$O$_3$ and Y$_2$O$_3$ composites. As far as the ability of homogeneous dispersion, 1-BuOH seemed to be better than n-hexane, although the difference was not so evident.

To make clear the *in situ* crystallization effect on microstructure, TEM observation was performed for the 17 mol% (15 vol%) 3Y-ZrO$_2$ added MoSi$_2$ composite. Fig. 5.3 shows a siliceous pocket in the sintered body, in which a crystalline phase, ZrSiO$_4$, was formed. Most of glassy SiO$_2$ was successfully crystallized, and unreacted t-ZrO$_2$ toughened oxide pockets. Furthermore, t-ZrO$_2$ particles simultaneously dispersed within MoSi$_2$ matrix grains (i.e. nano-
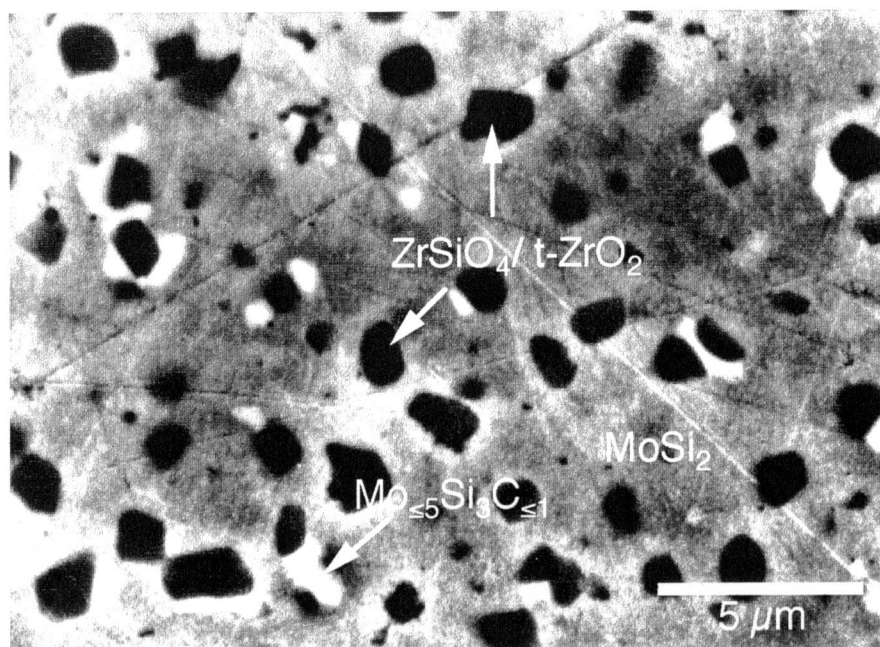
Fig. 5.2 SEM photograph of polished surfaces of the 17 mol% (15 vol%) 3Y-ZrO$_2$ added MoSi$_2$ composite.
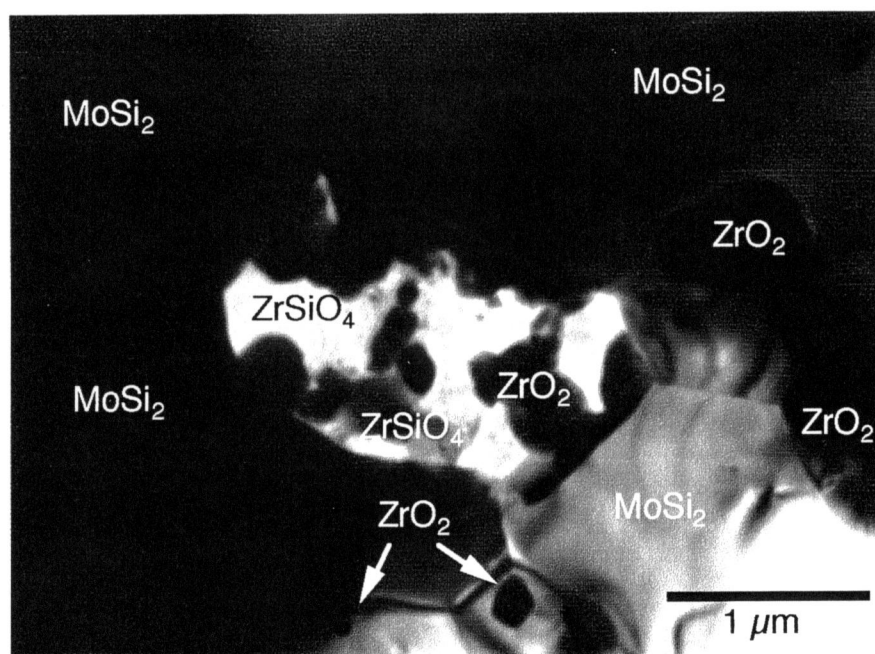
Fig. 5.3 TEM photograph of polished surfaces of the 17 mol% (15 vol%) 3Y-ZrO$_2$ added MoSi$_2$ composite.

dispersion). Such dispersion state can be achieved by the smallness of $3Y$-ZrO_2 powder used and the optimized ball-milling conditions. Less dislocations were observed in $MoSi_2/17$ mol% $3Y$-ZrO_2 composites than in $MoSi_2/Sc_2O_3$ and Y_2O_3 composites. This was probably because the CTE of t-ZrO_2 was close to that of $MoSi_2$.

5.3.3 Density

Fig. 5.4 shows the variation of density of hot-pressed samples with $3Y$-ZrO_2 and HfO_2 additions. The density of the monolithic $MoSi_2$ compact was 5.92 g/cm^3, and the deviation from the theoretical value (6.27 g/cm^3) was explained by the dispersion of glassy SiO_2 with low density (2.20 g/cm^3) as described in Chap. 4. For the $3Y$-ZrO_2 added system, the variation of density was small because the density of $3Y$-ZrO_2 (6.05 g/cm^3) was fairly close to $MoSi_2$. A slight decrease in density at 1 mol% addition can be explained by the slight decrease of sinterablity. The $MoSi_2/17$ mol% $3Y$-ZrO_2 composite using 1-BuOH (marked as $\triangle$) showed slightly smaller density than interpolated value from other $MoSi_2/3Y$-ZrO_2 composites. For the HfO_2 added system, the density monotonically increased with increasing HfO_2 content except a slight decrease at 1 mol%.

5.3.4 Mechanical Properties

Fig. 5.5 shows the variation of fracture strength with additive content. For the $3Y$-ZrO_2 added system, 1 mol % addition was considerably improved fracture strength. The strength value of this material was 1051 MPa, almost identical with $MoSi_2$ with 1 mol% Sc_2O_3 and Y_2O_3 additives. Above 2 mol% $3Y$-ZrO_2 addition, fracture strength was increased with increasing additive content.

For the HfO_2 added system, 2 mol % addition improved fracture strength, and the maximum strength was observed at 10 mol% addition. Improvement in fracture strength at a small amount of additives was mainly attributed to the *in situ* crystallization effect. Strength peak at small additive content was observed at 1 mol% for $3Y$-ZrO_2 and 2 mol% for HfO_2. While Sc_2O_3 and Y_2O_3 produced 1:2 silicates ($Sc_2Si_2O_7$ and $Y_2Si_2O_7$) with 1-2 mol% additives, ZrO_2 and HfO_2 formed 1:1 silicates ($ZrSiO_4$ and $HfSiO_4$). Thus, it was reasonable for HfO_2 case that the strength peak appeared at higher composition. It is considered for $3Y$-ZrO_2 case that the smallness of particles and dissolved Y_2O_3 may promoted the *in situ* crystallization. Somewhat complicated dependence of fracture strength is discussed later in detail. The $MoSi_2/17$ mol% $3Y$-ZrO_2 composite using 1-BuOH showed slightly higher strength than interpolated value from other $MoSi_2/3Y$-ZrO_2 composites. Presumably, nanometer-sized dispersoids and slightly lower hot-pressing temperature enabled to inhibit matrix grain growth more effectively.

Fig. 5.6 shows the variation of Vickers hardness with additive content. $MoSi_2/3Y$-ZrO_2 system showed a slight increase with increasing $3Y$-ZrO_2 content. Such a small increase in hardness is explained by the grain-size inhibition and a little higher hardness of polycrystalline
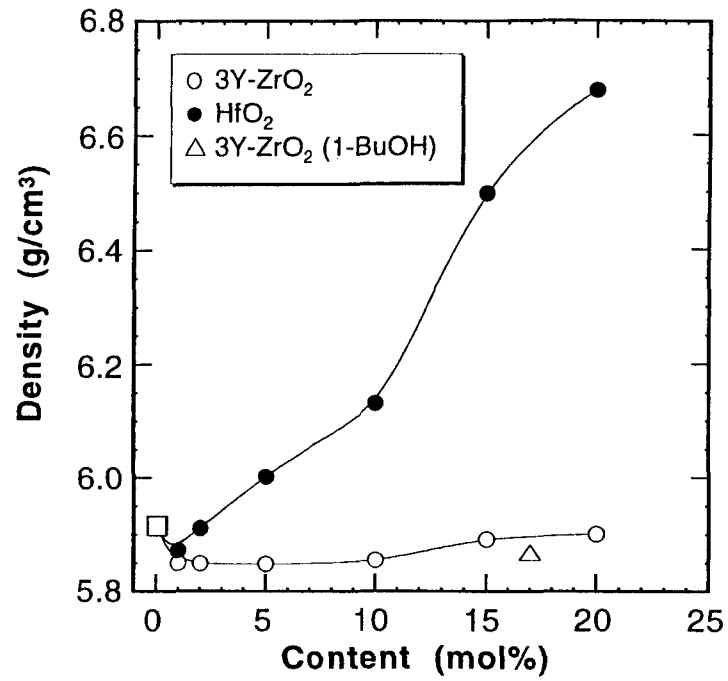
Fig. 5.4 Variation of density with MO_2 (M = Zr and Hf) composition
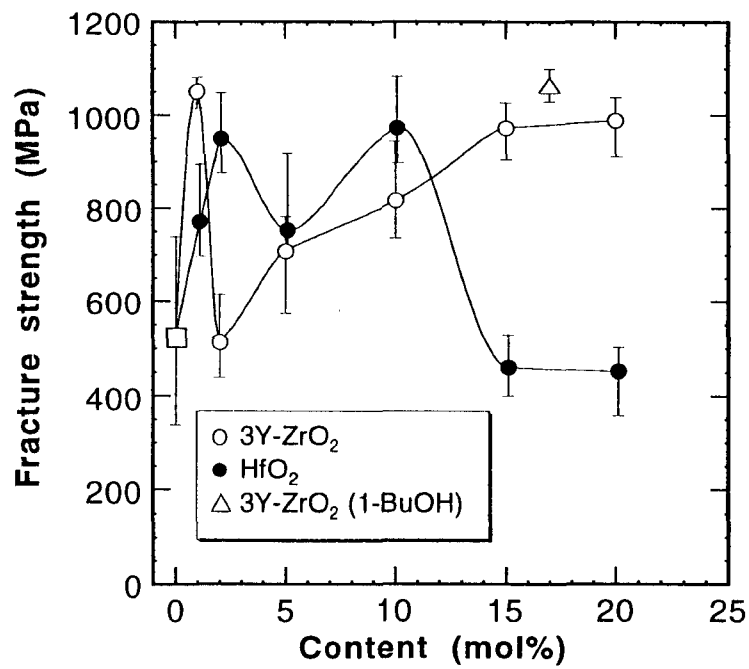for $MoSi_2$-SiO_2-MO_2 system.

Fig. 5.5 Variation of fracture strength with MO_2 composition
for $MoSi_2$-SiO_2-MO_2 system.

t-ZrO$_2$ (about 12 GPa for 3Y-ZrO$_2$ and about 10 GPa for MoSi$_2$). In good agreement with this consideration, the MoSi$_2$/17 mol% 3Y-ZrO$_2$ composite using 1-BuOH showed slightly higher hardness due to its a little finer microstructure.

On the other hand, MoSi$_2$/HfO$_2$ system exhibited a clear increase in hardness at 15 mol%. Since the hot-pressing temperature (i.e., 1600° C) is less than the monoclinic to tetragonal transformation temperature of unstabilized HfO$_2$ (i.e., 1720° C), there should not be severe microcrack formation via the volume expansion of tetragonal to monoclinic transformation during the cooling process; only the anisotropic thermal expansion of the monoclinic phase (α_a = ~ 7×10^{-6}, α_b = ~ 1.5×10^{-6} and α_c = ~ 12×10^{-6} [12]) may generate the residual stress field in the sintered bodies and probably pump in dislocations to MoSi$_2$ matrix. That is why the 15-20 mol% HfO$_2$ composites had higher hardness.

Fracture toughness dependence on additive content is shown in Fig. 5.7. Toughness of MoSi$_2$/3Y-ZrO$_2$ system was considerably increased with increasing additive content. The main toughening mechanism in this system, in particular for higher additive content, is transformation toughening of t-ZrO$_2$, while other mechanisms, such as residual stress fields, glassy phase removal and/or crack deflection may partially contribute to the observed toughening. A slightly smaller toughness observed for the MoSi$_2$/17 mol% 3Y-ZrO$_2$ composite using 1-BuOH can be explained by its smaller matrix grain size (2.4 μm), and probably by the more consumption of added 3Y-ZrO$_2$ for the reaction with SiO$_2$. Toughness of MoSi$_2$/1-10 mol% HfO$_2$ exhibited similar tendency to that of MoSi$_2$/1-10 mol% rare earth oxides (see. Fig, 4.7), probably due to the same toughening mechanism, that is, removal of brittle glassy SiO$_2$ by in situ crystallization. However, decrease of toughness was not observed for higher HfO$_2$ content (15-20 mol%) in contrast to the rare earth oxide additives; this phenomena can be explained by the same mechanism as described in Vickers hardness.

Preliminary results of high-temperature strength of the MoSi$_2$/17 mol% 3Y-ZrO$_2$ composite using 1-BuOH and the MoSi$_2$ with 1 mol% HfO$_2$ are shown in Fig. 5.8. The values of two different monolithic MoSi$_2$ are also shown in the figure for reference likewise in Chap. 4; the fine MoSi$_2$ compact was fabricated by hot-pressing a fine MoSi$_2$ powder (0.98 μm, as described in Chap. 3) at 1500° C, whose grain size was about 5 μm, and the coarse MoSi$_2$ compact was made by hot-pressing a coarse powder (several tens of microns, typical values of conventional MoSi$_2$) at 1700° C [19]. Because coarse MoSi$_2$ contained less glassy phase, it maintained almost the same (but low) strength (~ 150 MPa) up to 1200°C. On the other hand, fine MoSi$_2$ showed improved strength for all the temperature range compared to coarse MoSi$_2$, although strength degradation was, indeed, observed above around 1000°C. The improvement of strength around 800°C was due to the healing effect of the glassy phase, and the drop down of strength about 1000°C was mainly due to the glassy phase allowing grain boundary sliding.

The 17 mol% (15 vol%) 3Y-ZrO$_2$ added MoSi$_2$ showed less strength at high temperatures, because tetragonal phase was stabilized at high temperatures, and thus, the transformation
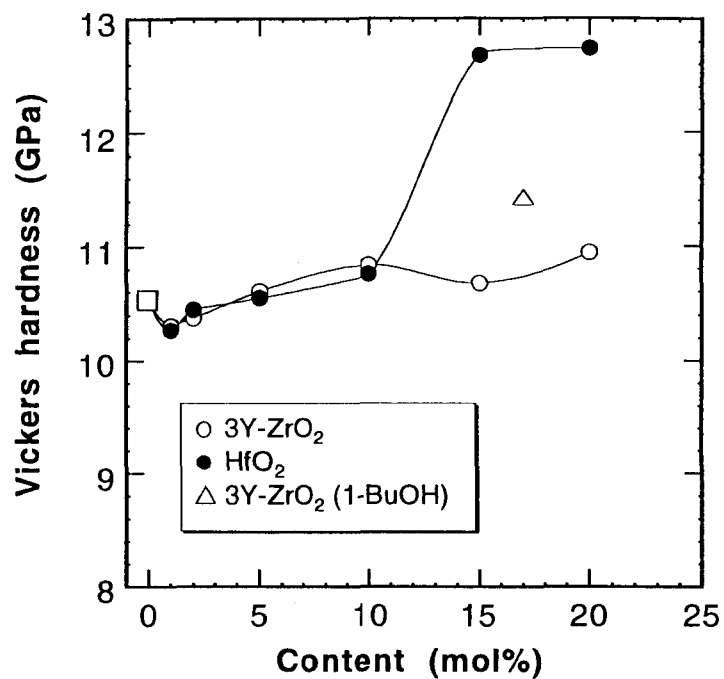
Fig. 5.6 Variation of Vickers Hardness with MO_2 composition for $MoSi_2$-SiO_2-MO_2 system.

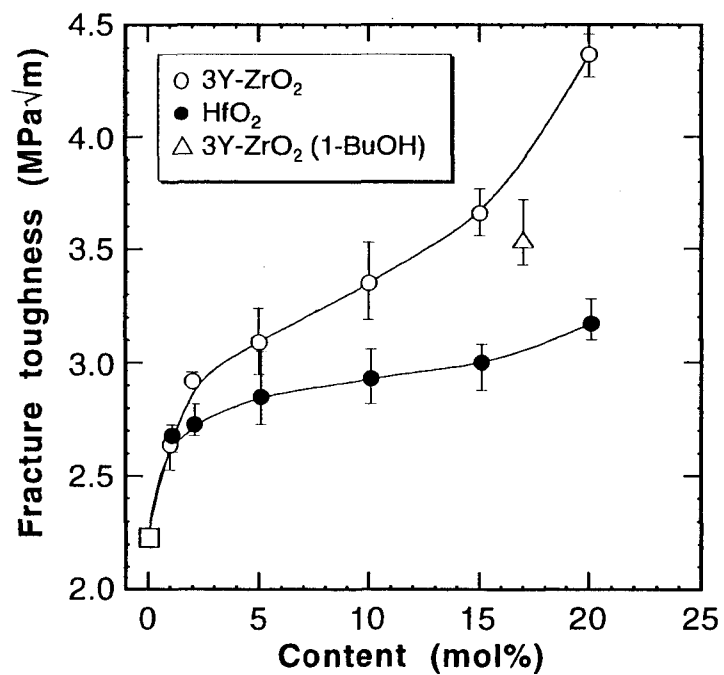**Fig. 5.7** Variation of fracture toughness with MO_2 composition for $MoSi_2$-SiO_2-MO_2 system.

toughening does not function. ZrO_2 ceramics intrinsically deform easily at high temperatures. The 1 mol% HfO_2 added $MoSi_2$ (actually, $MoSi_2$-$HfSiO_4$-glassy SiO_2 residue) showed almost same tendency as 1 mol% rare earth oxide. Although it has not been actually examined, 10-20 vol% of Y_2O_3 stabilized tetragonal HfO_2 addition may improve high-temperature strength, presumably by the transformation toughening at high temperatures.

Fig. 5.9 shows preliminary results of high-temperature hardness of the monolithic $MoSi_2$ hot-pressed at 1500°C and the 17 mol% 3Y-ZrO_2 added $MoSi_2$ hot-pressed at 1550° C. For monolithic $MoSi_2$, hardness was decreased in a gentle slope up to 800°C, and clear degradation was observed more than 1000°C. This notable decrease in hardness was attributed to the grain boundary sliding, since the grain boundary glassy SiO_2-rich phase was softened in vicinity of 1000° C. Hardness of the 17 mol% 3Y-ZrO_2 added $MoSi_2$ continuously decreased with increasing temperature, reflecting the easier deformability of ZrO_2 at high temperatures. These high-temperature tests suggest that the $MoSi_2$/ZrO_2 composites should be used for applications which do not require high strength at elevated temperatures, but need high toughness at room temperature, for example replacement of conventional $MoSi_2$ heating elements.

5.4 Discussion

5.4.1 Fracture Strength Dependence

As described in section 5.3, fracture strength of $MoSi_2$/3Y-ZrO_2 and $MoSi_2$/HfO_2 composites exhibited complex dependence with additive content. Fig. 5.10 shows observed fracture strength dependence and possible strengthening and anti-strengthening mechanisms for $MoSi_2$ with Sc_2O_3, Y_2O_3, 3Y-ZrO_2 and HfO_2 additives. In situ crystallization mechanism functioned in all 4 oxide additions. While Sc_2O_3 and Y_2O_3 form 1:2 silicates (i.e., $Sc_2Si_2O_7$ and $Y_2Si_2O_7$), 3Y-ZrO_2 and HfO_2 form 1:1 silicates (i.e., $ZrSiO_4$(ss) and $HfSiO_4$). Hence, more MO_2 additives should be required to fix glassy SiO_2 as silicates than R_2O_3 additives. However, the particle size of 3Y-ZrO_2 was considerably smaller than the others, and thus the 3Y-ZrO_2 has higher reactivity. Therefore, only $MoSi_2$/HfO_2 system showed the first maximum strength at 2 mol% addition.

Grain growth inhibition of $MoSi_2$ matrix generally restricts flaw size in sintered bodies, resulting improvement in fracture strength. Since the lattice volume increases in the order of $Y_2O_3 > Sc_2O_3 > 3Y$-$ZrO_2 \sim HfO_2$, Y_2O_3 becomes the largest volume fraction when all additives are the same mole fraction. However, 3Y-ZrO_2 should have the best ability to inhibit matrix grain growth due to its smallest particle size. As shown in Chap. 4, oxide additives tended to connect each other at higher contents, and became a large fracture origins, except 3Y-ZrO_2 which is strong itself by the transformation toughening. The complex strength dependence with additive contents can be explained by the combination of above-mentioned mechanisms.
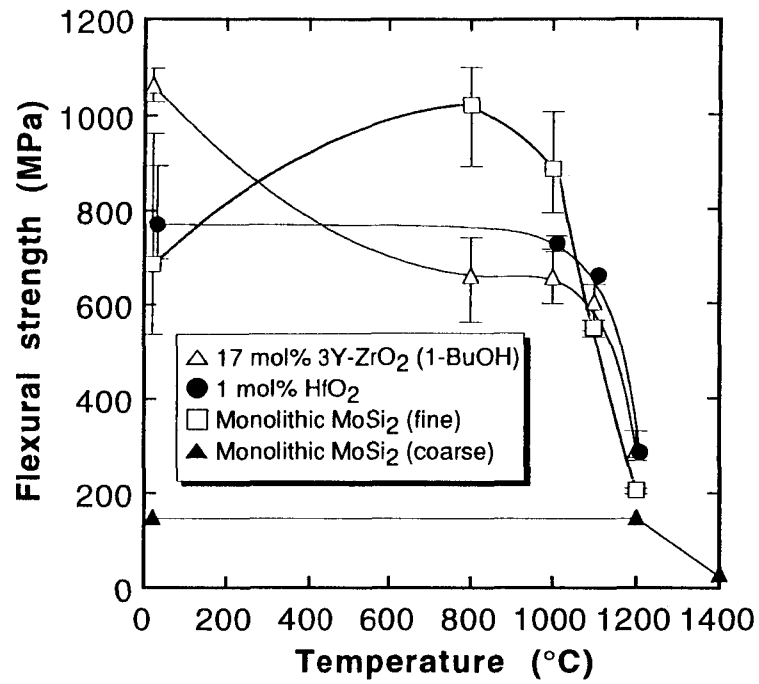
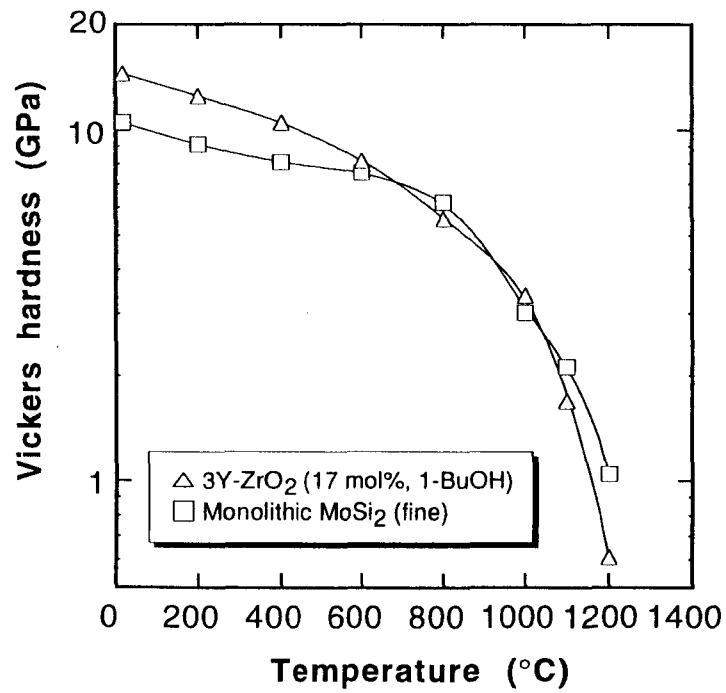Fig. 5.8   Variation of flexural strength with temperature for $MoSi_2$-SiO_2-MO_2 system.

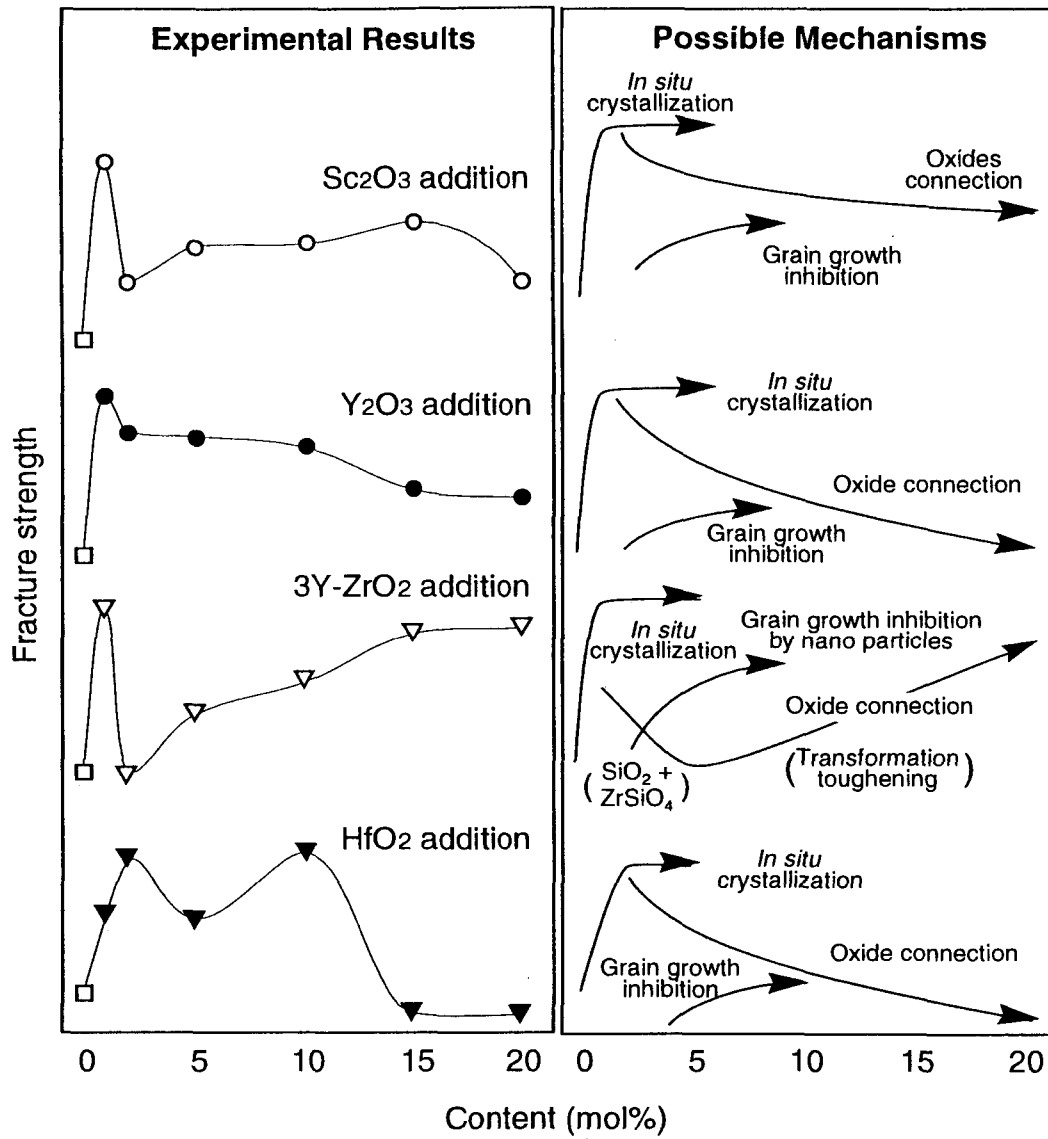Fig. 5.9   Variation of Vickers hardness with temperature for $MoSi_2$-SiO_2-MO_2 system.

Fig. 5.10 Comparison between obserbed fracture strength dependence with content of oxide additives (left) and possible strengthening mechanisms (right).

5.4.2 Comparison with Cordierite/ZrO$_2$ Composite

Oh et al. [20] reported that the m-ZrO$_2$ addition into cordierite (2MgO·2Al$_2$O$_3$·5SiO$_2$) resulted in the formation of ZrSiO$_4$ by a reaction of added monoclinic ZrO$_2$ (m-ZrO$_2$) with SiO$_2$, and the toughness was improved. For the cordierite/m-ZrO$_2$ system, the glassy phase was also formed together with the ZrSiO$_4$ at grain boundaries owing to the cordierite decomposition. On the contrary to their results, the formation of ZrSiO$_4$ in the present work was thought to be a direct reaction of ZrO$_2$ with glassy SiO$_2$ which located on the surface of MoSi$_2$ powder. This means that the amount of glassy SiO$_2$ was significantly decreased in the present system. Consistent with the decrement of the glassy phase, the mechanical properties were highly improved. It is worthy of note that the *in situ* crystallization method is effective to eliminate the siliceous grain boundary phase of MoSi$_2$ compacts, and this approach may be available to other silicides or silicon-based ceramics.

5.5 Conclusions

In this chapter, the improvement in mechanical properties of powder processed MoSi$_2$ by the additions of 3Y-ZrO$_2$ and HfO$_2$ were discussed. The combination effects of *in situ* crystallization and transformation toughening were examined via comparison with rare earth oxide (R$_2$O$_3$) additives. In summary:

1. 3Y-ZrO$_2$ added MoSi$_2$ compacts were composed of MoSi$_2$, Mo$_{\le 5}$Si$_3$C$_{\le 1}$, ZrSiO$_4$, and un-reacted t-ZrO$_2$. The intergranular glassy SiO$_2$ was successfully changed into the thermo-dynamically stable ZrSiO$_4$. MoSi$_2$/unstabilized HfO$_2$ compacts were composed of MoSi$_2$, Mo$_{\le 5}$Si$_3$C$_{\le 1}$, HfSiO$_4$, and unreacted monoclinic HfO$_2$.

2. 3Y-ZrO$_2$ and HfO$_2$ additions improved mechanical properties at room temperature. Only 1-2 mol% additives remarkably improved mechanical properties, similarly to R$_2$O$_3$ additive cases. MoSi$_2$ with higher content of 3Y-ZrO$_2$ additive exhibited fairly high toughness due to the combination of transformation toughening and *in situ* crystallization of brittle glassy SiO$_2$. However, 3Y-ZrO$_2$ addition resulted in the degradation of high-temperature strength and hardness due to its intrinsically poor high-temperature mechanical properties. The strength dependence with temperature of 1 mol% HfO$_2$ added MoSi$_2$ resembled that of R$_2$O$_3$ added MoSi$_2$ due to the similarity of crystallization of glassy SiO$_2$.

3. These results suggest that the MoSi$_2$/3Y-ZrO$_2$ composites should be used for applications which do not require high strength at elevated temperature, but need high toughness at room temperature, for example replacement of conventional MoSi$_2$ heating elements. Yttria-stabilized tetragonal HfO$_2$ addition may improve high-temperature properties of MoSi$_2$ via the possible transformation toughening at high temperatures.

References

1. R. C. Garvie, R. H. J. Hannink and R. T. Pascoe, "Ceramic Steel?," *Nature*, 2 5 8, 703 -704 (1975).

2. G. K. Bansal and A. H. Heuer, "Precipitation in Partially Stabilized Zirconia," *J. Am. Ceram. Soc.*, 5 8 [5-6] 235-238 (1975).

3. D. L. Porter and A. H. Heuer, "Mechanisms of Toughening Partially Stabilized Zirconia (PSZ)," *J. Am. Ceram. Soc.*, 6 0 [3-4] 183-184 (1977).

4. N. Claussen, "Comments on 'Precipitation in Partially Stabilized Zirconia'": D. L. Porter, G. K. Bansal and A. H. Heuer, "Reply to 'Precipitation in Partially Stabilized Zirconia'," *J. Am. Ceram. Soc.*, 5 9 [3-4] 179-182, (1976).

5. G. M. Wolten, "Diffusionless Phase Transformations in Zirconia and Hafnia," *J. Am. Ceram. Soc.*, 4 6, 418-422 (1963).

6. A. H. Heuer and M. Rühle, in *Advanced Ceramics, Vol.12, Science and Technology of Zirconia II*, eds. N. Claussen, M. Rühle, and A. H. Heuer, The American Ceramic Society, Columbus, OH, p.1 (1984).

7. J. E. Bailey, D. Lewis, Z. M.Librant and L. J. Porter, "Phase Transformations in Milled Zirconia," *Trans. & J. Br. Ceram. Soc.*, 7 1 [1] 25-30 (1972).

8. J. J. Petrovic and R. E. Honnell, "Partially Stabilized ZrO$_2$ Particle-MoSi$_2$ Matrix Composites," *J. Mater. Sci.*, 2 5, 4453-4456 (1990).

9. J. J. Petrovic, R. E. Honnell, T. E. Mitchell, R. K. Wade and K. J. McClellan, "ZrO$_2$- Reinforced MoSi$_2$ Matrix Composites," *Ceram. Eng. Sci. Proc.*, 1 2 [9-10] 1633-1642 (1991).

10. A. K. Bhattacharya and J. J. Petrovic, "R-Curve Behavior in Zirconia-Reinforced Molybdenum Disilicide Composites," *J. Am. Ceram. Soc.*, 7 5 (1992) 23-27.

11. J. J. Petrovic, A. K. Bhattacharya, R. E. Honnell, T. E. Mitchell, R. K. Wade and K. J. McClellan, "ZrO$_2$ and ZrO$_2$-SiC Particle Reinforced MoSi$_2$ Matrix Composites," *Mater. Sci. Eng.*, A 1 5 5, 259-266 (1992).

12. J. Wang, H. P. Li, R. Stevens, "Hafnia and Hafnia-Toughened Ceramics," *J. Mater. Sci.*, 2 7 [20] 5397-5430 (1992).

13. H. J. Garrett, "X-ray Studies of Tetragonal Monoclinic Inversion in ZrO$_2$," *Amer. Ceram. Soc. Bull.*, 4 2, 201 (1963).

14. E. C. Subbarao, D. K. Agrawal, H. A. McKinstry, C. W. Sallese and R. Roy, "Thermal Expansion of Compounds of zircon structure," *J. Am. Ceram. Soc.*, 7 3 [5] 1246-52 (1990).

15. I. Kondoh, T. Tanaka and N.Tamari, "Sintering of Zircon-Silicon Carbide Whisker Composites and Their Mechanical Properties," *J. Ceram. Soc. Jap.*, 1 0 1, 369-372 (1993).

16. P. T. B. Shaffer, *Plenum Press Handbooks of High-Temperature Materials*, Plenum, New York, p. 451, (1964).

17. W. C. Butterman and W. R. Foster, *Am. Mineralogist*, 5 2, 884, (1967).

18. V. N. Parfenenkov, R. G. Grebenshchikov and N. A. Toropov, *Dokl. Akad. SSSR*, 1 8 5 [4] 840 (1969).

19. D. H. Carter, W. S. Gibbs, and J. J. Petrovic, "Mechanical Characterization of SiC Whisker-Reinforced MoSi$_2$," *Proceedings of Ceramics Materials & Components for Engines*, pp.977-986, (1988).

20. Y. J. Oh, T. S. Oh, H. J. Jung, "Microstructure and Mechanical Properties of Cordierite Ceramics Toughened by Monoclinic ZrO$_2$," *J. Mater. Sci.*, 26, 6491-6495 (1991) .

6

Microstructural Control by Al Alloying and SiC Dispersion

The Mo-Si-Al alloys and Mo-Si-Al/SiC composites were fabricated by the powder metallurgical process from novel Mo-Si-Al pre-alloyed powders, and their microstructure and mechanical properties were evaluated. Nominal $MoSi_2$, $Mo(Si_{0.86},Al_{0.14})_2$ and $Mo(Si_{0.80},Al_{0.20})_2$ with and without 15 vol% SiC powders were hot-pressed in an argon atmosphere. While $MoSi_2$-based materials included some glassy SiO_2 phase, almost no glassy SiO_2 was found in Mo-Si-Al based materials. In Mo-Si-Al systems, α-Al_2O_3 was mainly dispersed instead of glassy SiO_2. The formation of α-Al_2O_3 was attributed to the predominant oxidation of aluminum at the surface of the Mo-Si-Al pre-alloyed powders. Mo-Si-Al sintered bodies were composed of hexagonal $Mo(Si,Al)_2$ (C40), tetragonal $MoSi_2$ (C11$_b$), $Mo_{\leq 5}Si_3C_{\leq 1}$ and α-Al_2O_3. The ratio and lattice parameters of C40 and C11$_b$ phases were quantitatively evaluated by the Rietveld analysis for X-ray powder diffraction profiles. For all systems, added nano-sized SiC particles effectively reduced the grain growth of the matrices. Combination of alloying and composite techniques were remarkably improved mechanical properties through microstructural modification.

6.1 Introduction

As was shown before, molybdenum disilicide ($MoSi_2$) is a promising material for various applications such as aerospace exposed to temperatures more than 1500°C, mainly because of its high melting point (2030°C) and fairly good oxidation resistance. However, its fracture toughness and strength are not high enough for high-temperature structural applications. Furthermore, glassy SiO_2 which is present in the metallurgically produced $MoSi_2$ powder strongly degrades the high-temperature mechanical properties [1]. Thus, many efforts have been made to improve mechanical properties of this material. In particular, "second phase dispersion [2-8]" and "SiO_2 elimination [9-14]" have been widely investigated.

Alloying with ternary elements is also a promising method to control various properties of $MoSi_2$. Although many transition metals can partially substitute the Mo sites in the $MoSi_2$

phase, only limited elements, such as aluminum and germanium, can replace the Si sites. After early works of the Mo-Si-Al ternary system, conducted by Nowotny et al. in 1950's - 1960's [15-18], several groups [19-29] studied on the Mo-Si-Al system and its constituent phases. In particular, the molybdenum alminosilicide, $Mo(Si,Al)_2$, has received much attention; Kisly et al. [19-20] reported that the $Mo(Si,Al)_2$ phase was more scale-resistant than $MoSi_2$ up to 1800°C. Maruyama et al. [21-23] pointed out that the oxidation rate was higher in $Mo(Si,Al)_2$ than in $MoSi_2$, but $Mo(Si,Al)_2$ showed better cyclic oxidation resistance even at 1750°C due to a good scale adherence. It is also reported that $Mo(Si,Al)_2$ has good pesting resistance at 500°C while $MoSi_2$ is severely oxidized around this temperature [24-25].

Aside from the oxidation properties of the $Mo(Si,Al)_2$ phase, alloying with Al brings other effects; added Al to $MoSi_2$ can act as deoxidant similarly to carbon addition to $MoSi_2$ [9-11]. Costa e Silva et al. [26-28] reported that elemental Al addition enabled to convert SiO_2 to α-Al_2O_3 in powder processed $MoSi_2$ as well as the crystallographical modification from tetragonal $C11_b$ structure of $MoSi_2$ to hexagonal C40 structure of $Mo(Si,Al)_2$; mixtures of $MoSi_2$ and Al metal powders were hot-pressed, and Al reacted with SiO_2 included in $MoSi_2$ powder. This "in situ displacement reaction" technique has an advantage of the ease of controlling Al content. This method, however, has some disadvantages: (1) flammability of a fine Al powder, (2) relatively high vapor pressure of Al during heating, causing the deviation from the desired composition, and (3) relatively large grain growth in final products (10-20 μm in Ref. 26), presumably by the formation of liquid phase during sintering.

To circumvent such problems, the authors [29,30] have produced Mo-Si-Al alloys and Mo-Si-Al based composites using fine pre-alloyed powders, and evaluated their microstructure and mechanical properties. In this chapter, the effects of Al substitution and nano-sized SiC dispersion on microstructure and mechanical properties of $MoSi_2$ were investigated in detail. The ratio of C40 and $C11_b$ phases was also analyzed quantitatively using the Rietveld analysis. Effects of di-phasic matrices on mechanical properties are also discussed.

6.2 Experimental Procedure

6.2.1 Starting Materials

Binary Mo-Si and ternary Mo-Si-Al pre-alloyed powders with different Al content were supplied by Japan New Metals Co., Ltd. The powders were fabricated from elemental powders of molybdenum (>99.9 wt.%), silicon (>99.75 wt.%) and aluminum (99.65 wt.%) by combustion synthesis and following crushing process. Initial compositions for the combustion synthesis were $Mo_{33.3}Si_{66.7}$, $Mo_{33.3}Si_{57.3}Al_{9.3}$ and $Mo_{33.3}Si_{53.3}Al_{13.3}$, which were corresponding to $MoSi_2$, $Mo(Si_{0.86}, Al_{0.14})_2$ and $Mo(Si_{0.80}, Al_{0.20})_2$, respectively. The result of chemical analysis and average particle size of the powders are listed in Table 6.1. As for $Mo(Si_{0.86}, Al_{0.14})_2$,

two powders with slightly different composition (powders B and C) were obtained. All powders had fine particle size (ca. 1.0-1.6 μm). Since aluminum and silicon have high vapor pressure, the obtained powder became Mo-rich compared with the stoichiometric composition. From the standpoint of mechanical properties, however, such deviation is rather favorable; if elemental Al and Si were remained in the materials, mechanical properties, especially high-temperature strength, will severely decrease. The pre-alloyed powders contained oxygen, carbon and iron impurities; they were contaminated by the crushing process. The compositions normalized by Mo, Si and Al elements were $Mo_{34.0}Si_{66.0}$, $Mo_{34.2}Si_{57.3}Al_{8.5}$, $Mo_{34.0}Si_{56.8}Al_{9.2}$, $Mo_{34.0}Si_{52.7}Al_{13.3}$, respectively.

For the composites, a commercial β-SiC powder (Mitsui Toatsu Chemical Co., Ltd.) was added 15 % by volume. The SiC starting powder contained less impurities than the Mo-Si-Al powders as indicated in Table 6.2; mean particle size of the β-SiC powder was 0.15 μm.

6.2.2 Specimen Preparation and Characterization

As received Mo-Si-Al powders were packed into graphite lined carbon dies with BN coating and then hot-pressed at 1500° C under an applied pressure of 30 MPa for 1 h in an argon atmosphere. As for composites, the β-SiC powder was added 15 vol% to the Mo-Si-Al pre-alloyed powders. They were mixed by wet ball-milling in 1-butanol with ZrO_2 balls for 24 h, and then the dried mixture was dry ball-milled for 24 h to crush the agglomerations. Mo-Si-Al/SiC mixed powders were hot-pressed at 1600°C. The hot-pressed disks were 44 mm in diameter and 5.0 mm in thickness. They were cut, ground and polished into rectangular bars with 4×3×36 mm in size.

Table 6.1 Composition and particle size of Mo-Si and Mo-Si-Al pre-alloyed powders.

Powder	Initial composition	Mo (at.%)	Si (at.%)	Al (at.%)	O (at.%)	C (at.%)	Fe (at.%)	d (μm)	Normalized composition*
A	$MoSi_2$	32.38	62.93	–	3.53	0.95	0.21	1.01	$Mo_{34.0}Si_{66.0}$
B	$Mo(Si_{0.86},Al_{0.14})_2$	33.14	55.64	8.20	2.57	0.38	0.07	1.61	$Mo_{34.2}Si_{57.3}Al_{8.5}$
C	$Mo(Si_{0.86},Al_{0.14})_2$	32.52	54.21	8.83	3.36	0.86	0.22	1.35	$Mo_{34.0}Si_{56.8}Al_{9.2}$
D	$Mo(Si_{0.80},Al_{0.20})_2$	32.62	50.59	12.74	2.91	0.95	0.20	1.40	$Mo_{34.0}Si_{52.7}Al_{13.3}$

*compositions were normalized by Mo, Si and Al.

Table 6.2 Chemical analyses of a SiC powder.

	SiC	SiO_2	free C	Fe	Al	Ca	Mg	Cr	Ni
content (wt%)	>99	0.15	0.10	0.012	0.0048	0.0040	0.0010	0.0030	0.0020

Phase identification and quantitative analysis were carried out by the X-ray diffraction (XRD) analysis. XRD profiles of the alloys and composites were measured on a RIGAKU RAD-B diffractometer with Cu-Kα radiation.

Bulk densities were measured by the Archimedes method in toluene. Microstructure was characterized by scanning electron microscopy (SEM, HITACHI S-5000) with an energy dispersive X-ray spectrometer (EDS, HORIBA EMAX-5770). Samples for SEM observations were pre-coated with gold or carbon. Average grain size was calculated by the linear intercept method for polarized optical micrographs. Five to six specimens were subjected to three-point bending tests (span: 30 mm) to determine the fracture strength. Bending load was applied parallel to hot-press axis with a crosshead speed of 0.5 mm/min. The hardness (H_v) was evaluated by Vickers indentation under a condition of 98 N load and loading duration of 15 s, and the fracture toughness (K_{IC}) was determined simultaneously by the indentation fracture (IF) method [31]. K_{IC} values were calculated by using the empirical equation proposed by Niihara et al. [31] for a median crack, as is mentioned in Chap. 3.

6.3 Quantitative Analysis by Rietveld Analysis

6.3.1 Outline of the Rietveld Method

In order to obtain weight fraction of matrices (i.e. $C11_b$: C40) and their lattice parameters, the X-ray diffraction profiles were analyzed by the Rietveld method using RIETAN-94 software [32,33].

The Rietveld method [34] is a technique for refining structure parameters (fractional coordinates, isotropic/anisotropic thermal parameters, occupation factors and magnetic moments, etc.) and lattice parameters directly from whole powder diffraction patterns without separating reflections [32,33]. It was originally devised for analysis of angle-dispersive neutron diffraction data [34]. After Malmros and Thomas [35] first applied the Rietveld method to XRD data, it has been widely used for structure refinements with conventional and synchrotron XRD data. It is now regarded as a fundamental technique of characterizing polycrystalline materials in the field of physics, chemistry, materials science, mineralogy, etc.

In the present calculation, the modified pseudo-Voigt function of Thompson, Cox and Hastings is used as the profile-shape function [36].

6.3.2 Quantitative Analysis of the Matrices Ratio ($C11_b$: C40)

The weight fraction of phases in a mixture can be determined by the Rietveld analysis as well as the structure parameters, as was reported by Hill and Howard [37]. The weight fraction is proportional to the product of scale factor, as derived in a multicomponent Rietveld analysis of the powder diffraction pattern, with the mass and volume of the unit cell.

When all phases are identical and crystalline, the weight fraction W of phase p is given by

$$W_p = S_p(ZMV)_p / \sum_i S_i(ZMV)_i \tag{6.2}$$

where S, Z, M and V are the Rietveld scale factor, the number of formula units per unit cell, the mass of the formula unit and the unit-cell volume, respectively. Although this method requires no standards, it provides extremely accurate phase analyses.

Crystal structures of $MoSi_2$ and $Mo(Si,Al)_2$ are shown in Figs. 6.1(a) and (b), respectively [38,39], and crystallographical data of tetragonal $MoSi_2$ ($C11_b$) and hexagonal $Mo(Si,Al)_2$ (C40) were summarized in Table 6.3 [40,41]. A similar pattern of stacking relationships exists for disilicide with the $C11_b$ and C40 structures. The atoms in the next layer in the silicides and alminosilicides occupy the saddle positions between two Si sites (Fig. 6.1(c)), while in the case of alminides, such as Ni_3Al, the atoms fit into the natural pockets between three contiguous atoms. The position coordinates of the Mo and (Si,Al) atoms in the C40 structure were derived from an isostructural compound, $CrSi_2$ [41]; ideal value ($x = 1/6$) was adapted to the position parameter of (Si,Al).

(a) C11_b (tetragonal)   (b) C40 (hexagonal)   (c) Geometry of stacking
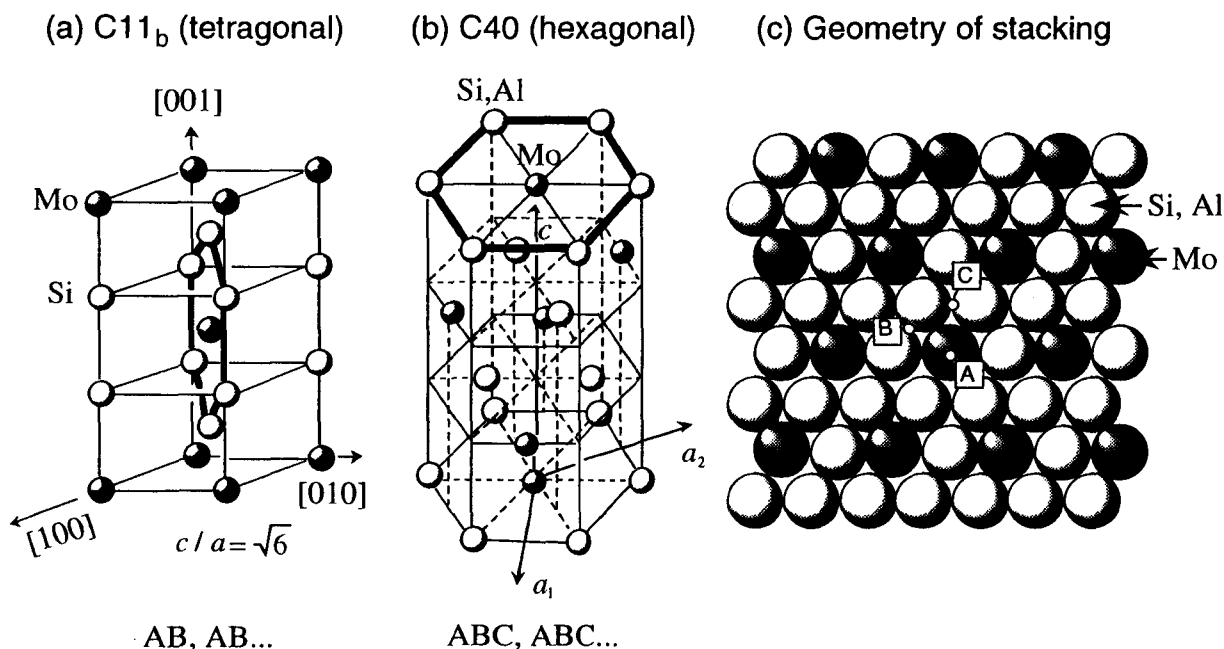
AB, AB...   ABC, ABC...

Fig. 6.1   Interrelationships between $C11_b$ and C40 structures in terms of the stacking sequence of the closed packed planes: (a) $C11_b$ with AB, AB... stacking, (b) C40 with ABC, ABC... stacking, and (c) stacking sequence of hexagonal planes.

Table 6.3 Crystallographical data of $MoSi_2$ ($C11_b$ [40]) and $Mo(Si,Al)_2$ (C40 [41]).

Parameter	molybdenum silicide		molybdenum alminosilicide	
Formula	$MoSi_2$		$Mo(Si,Al)_2$	
Space group	I4/mmm (No.139)		$P6_222$ (No.180)	
Strukturberichte	$C11_b$		C40	
Atom position	2 Mo in a	0, 0, 0	3 Mo in d	1/2, 0, 1/2
		1/2, 1/2, 1/2		0, 1/2, 1/6
	4 Si in e	0, 0, z		1/2, 1/2, -1/6
		0, 0, -z	6 (Si,Al) in j	x, 2x, 1/2
		1/2, 1/2, 1/2+z		-x, 2x, 1/2
		1/2, 1/2, 1/2-z		2x, x, 1/6
	z = 1/3 (ideal value)			-2x, -x, 1/6
				x, -x, -1/6
				-x, x, -1/6
			x = 1/6 (ideal value)	

6.4 Results and Discussion

6.4.1 Chemistry and Phase Identification

Phases of all the materials were characterized by XRD. Typical XRD patterns for Mo-Si-Al based system are shown in Fig. 6.2: (a) the $Mo_{34.2}Si_{57.3}Al_{8.5}$ pre-alloyed powder (powder B), (b) hot-pressed $Mo_{34.2}Si_{57.3}Al_{8.5}$ alloy and (c) $Mo_{34.2}Si_{57.3}Al_{8.5}$/SiC composite. XRD analysis indicated that the Mo-Si-Al powder was composed of $Mo(Si,Al)_2$ (hexagonal, C40), $MoSi_2$ (tetragonal, $C11_b$) and a small amount of Mo_5Si_3 (tetragonal $D8_m$). Since the XRD peaks of $Mo(Si,Al)_2$ and α-Al_2O_3 are overlapped and the atomic scattering factor of α-Al_2O_3 is smaller than $Mo(Si,Al)_2$, it is difficult to confirm the existence of α-Al_2O_3 by XRD for the pre-alloyed powder. However, the surface of the Mo-Si-Al powders must be covered by the Al_2O_3-rich oxide phases from the analogy to $MoSi_2$ powders with SiO_2-rich surface layer. The $Mo_{34.2}Si_{57.3}Al_{8.5}$ alloy was composed of hexagonal $Mo(Si,Al)_2$, tetragonal $MoSi_2$, $Mo_{\leq 5}Si_3C_{\leq 1}$ (hexagonal $D8_8$) and α-Al_2O_3. In this case, the existence of α-Al_2O_3 was followed by the SEM-EDS and TEM-EDS analyses. The $Mo_{34.2}Si_{57.3}Al_{8.5}$/SiC composite was composed of tetragonal $MoSi_2$, hexagonal $Mo(Si,Al)_2$, $Mo_{\leq 5}Si_3C_{\leq 1}$, α-Al_2O_3 and β-SiC. The formation of α-Al_2O_3 was attributed to predominant oxidation of aluminum [22] at surfaces of the Mo-Si-Al pre-alloyed powders. $Mo_{\leq 5}Si_3C_{\leq 1}$ Nowotny phase was derived by the reaction between Mo_5Si_3 and impurity carbon as was discussed before. Striking difference of $C11_b$/C40 ratio was observed for these three patterns (Fig. 6.2(a)-(c)). In the $Mo_{34.2}Si_{57.3}Al_{8.5}$ pre-alloyed powder, C40 phase was dominant (Fig. 6.2 (a)). On the other hand, $C11_b$ phase was increased and C40 phase was decreased after hot-pressing, even though C40 was still the major phase (Fig. 6.2 (b)). Furthermore, $C11_b$ became the major phase in the $Mo_{34.2}Si_{57.3}Al_{8.5}$/SiC composite. Such changes in the phase quantity will be discussed in detail in the next section.
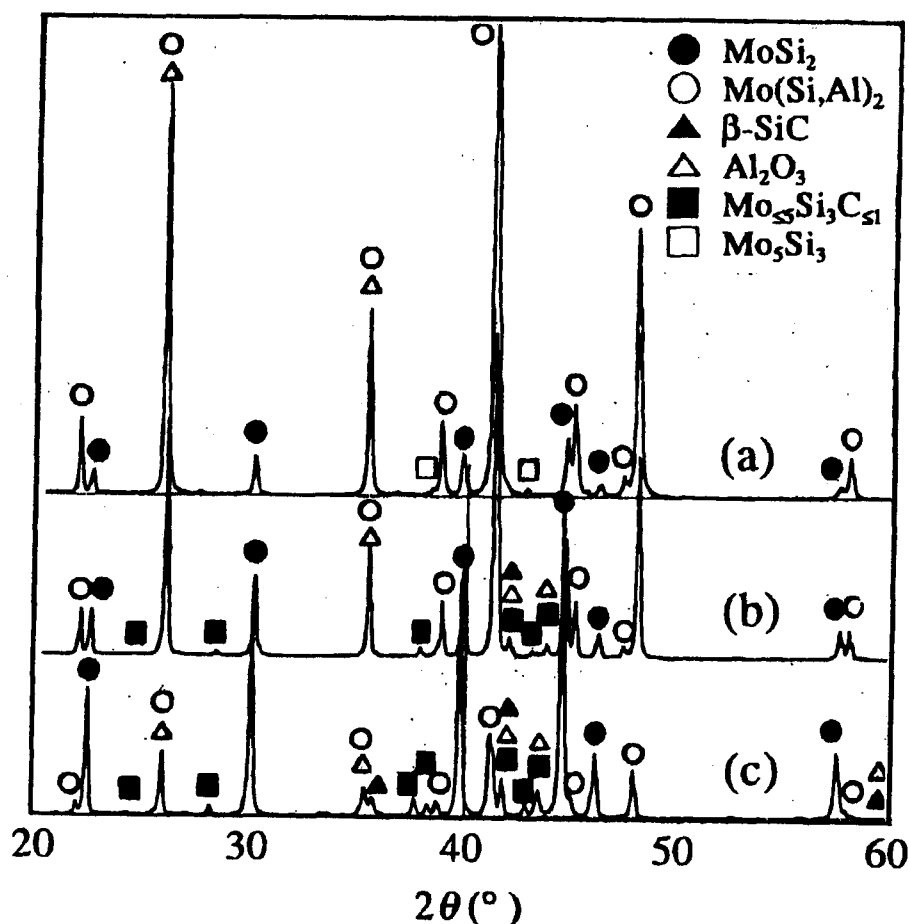
Fig. 6.2 X-ray diffraction patterns for (a) the $Mo_{34.2}Si_{57.3}Al_{8.5}$ pre-alloyed powder (powder B), (b) hot-pressed $Mo_{34.2}Si_{57.3}Al_{8.5}$ alloy and (c) $Mo_{34.2}Si_{57.3}Al_{8.5}/SiC$ composite.

6.4.2 Phasic Composition and Lattice Parameters

Fig. 6.3 shows XRD patterns of hot-pressed samples. Change of the phasic composition with Al content can be clearly seen in these patterns. Phasic composition and lattice parameters were quantitatively determined by the Rietveld analysis. Fig. 6.4 shows the typical result of the Rietveld refinement for $Mo_{34.0}Si_{56.8}Al_{9.2}/15$ vol% SiC composite from powder C. It shows the comparison between observed and calculated intensities of the XRD peaks, and the differential pattern for $Mo_{34.0}Si_{56.8}Al_{9.2}/15$ vol%SiC composite. Upper and lower tick marks are Bragg position for $C11_b$ and C40 phases, respectively. $Mo_{4.8}Si_3C_{0.6}$ (P6$_3$/mcm) was also taken into account for the calculation. Structural detail of the $Mo_{\leq 5}Si_3C_{\leq 1}$ phase will be given in Chap. 7. α-Al_2O_3 and SiC were disregarded in the calculation because of their weak intensities.

92
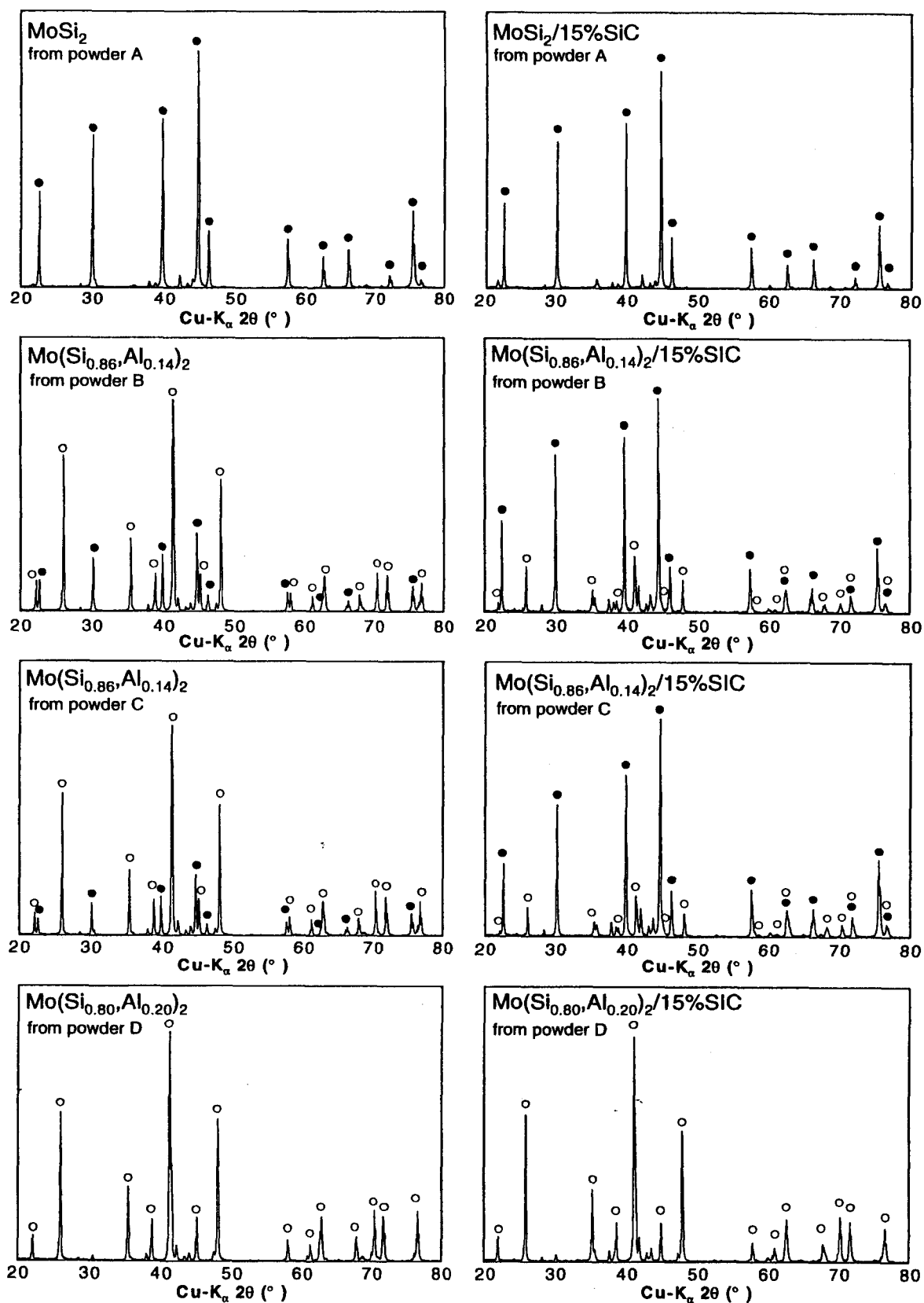
Fig. 6.3 XRD patterns for Mo-Si-Al based materials; $MoSi_2$ and $Mo(Si,Al)_2$ lines are marked as ● and ○, respectively. Other lines correspond to $Mo_{\leq5}Si_3C_{\leq1}$, SiC, α-Al_2O_3 as shown in Fig. 6.2.
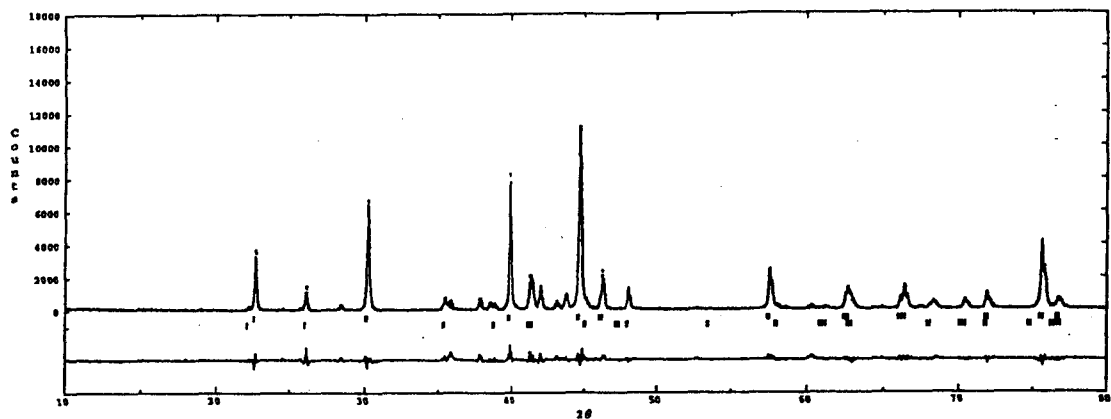
Fig. 6.4 Comparison between observed and calculated intensities of the X-ray diffraction peaks, and the differencial pattern for $Mo_{34.0}Si_{56.8}Al_{9.2}/15$ vol% SiC composite. Upper and lower tick marks are Bragg position for $C11_b$ and C40 phases, respectively. $Mo_{4.8}Si_3C_{0.6}$ (P6_3/mcm) was also taken into account for the calculation. $\alpha\text{-}Al_2O_3$ and SiC were disregarded because of their weak peaks.

Table 6.4 summarizes appeared phases, weight fractions of $C11_b$ and C40 phases and refined cell parameters for various materials. C40 content increased with Al content. On the other hand, the fraction of C40 phase was considerably decreased with the addition of nano-sized SiC particles. This will be due to (1) increase in oxygen content by the ball-mill process, resulting Al consumption as $\alpha\text{-}Al_2O_3$, and (2) increase in diffusion path by the grain growth inhibition caused by SiC dispersion. Effect of hot-pressing temperature on $C11_b$/C40 ratio was negligible in the range from 1500 to 1600° C. To discuss the phase relations, Mo-Si-Al ternary phase diagrams proposed by Maruyama et al.[22,24] are shown in Figs. 6.5 (a) and (b). In the Mo-Si-Al based materials fabricated in this study, Mo_5Si_3 drawn in the diagrams actually reacted with carbon impurity into $Mo_{\leq 5}Si_3C_{\leq 1}$. However, the phase relations of $Mo(Si,Al)_2$-$MoSi_2$-$Mo_{\leq 5}Si_3C_{\leq 1}$ pseudo ternary system can be easily expected similarly to the $Mo(Si,Al)_2$-$MoSi_2$-Mo_5Si_3 shown in the Figs. 6.5(a) and (b). The consumption of Al from the matrices resulted in the increase of $MoSi_2$ and $Mo_{\leq 5}Si_3C_{\leq 1}$ phases.

Lattice constants a and c of $C11_b$ were increased with increasing Al content. It suggests that Al atom substituted Si site of $C11_b$ structure. This agreed with the report by Harada et al. that $C11_b$ $MoSi_2$ dissolved Al up to about 3 at.% [42]. Lattice parameter a of C40 phase monotonously increased with increasing Al content. Lattice parameter c of C40 phase, however, was decreased at higher Al content. This phenomenon was also reported in the early work by Nowotny et al. [17]. It suggests that C40 structure is stabilized at higher Al content.

The ideal sixfold coordination at the Mo and Si-atomic sites in the tetragonal $C11_b$ structure is obtained when lattice parameter $c/a = 6^{1/2} = 2.449$, and the Si-atomic position parameter $z = 1/3$ [43]. That is, the $C11_b$ phase in the hot-pressed $MoSi_2$ compacts has almost identical

geometry as is shown in Table 6.4. On the other hand, $C11_b$ phase in the hot-pressed Mo-Si-Al alloy has elongated c axis. This means the crystallographical deviation of the ideal structures, and $C11_b$ phase cannot be stable with more Al content.

Table 6.4 Appeared phases and lattice parameters for Mo-Si-Al based materials.

Nomalized Composition (Nominal Composition)	Appeared phases†	Lattice parameters of matrices (nm)		
		a	c	c/a
$Mo_{34.0}Si_{66.0}$ ($MoSi_2$) (from powder A)	$C11_b$ (100) $Mo_{\leq5}Si_3C_{\leq1}$ SiO_2*	0.3204(3)	0.7845(5)	2.449
$Mo_{34.2}Si_{57.3}Al_{8.5}$ $(Mo(Si_{0.86},Al_{0.14})_2)$ (from powder B)	$C11_b$ (25.5) C40 (74.5) $Mo_{\leq5}Si_3C_{\leq1}$ α-Al_2O_3	0.3205(4) 0.4648(1)	0.7887(2) 0.6550(0)	2.461 1.409
$Mo_{34.0}Si_{56.8}Al_{9.2}$ $(Mo(Si_{0.86},Al_{0.14})_2)$ (from powder C)	$C11_b$ (21.5) C40 (78.5) $Mo_{\leq5}Si_3C_{\leq1}$ α-Al_2O_3	0.3206(3) 0.4649(2)	0.7889(3) 0.6550(9)	2.461 1.409
$Mo_{34.0}Si_{52.7}Al_{13.3}$ $(Mo(Si_{0.80},Al_{0.20})_2)$ (from powder D)	C40 (100) $Mo_{\leq5}Si_3C_{\leq1}$ α-Al_2O_3	0.4664(5)	0.6547(3)	1.404
$Mo_{34.0}Si_{66.0}$/15 vol% SiC ($MoSi_2$/15 vol% SiC) (from powder A)	$C11_b$ (100) $Mo_{\leq5}Si_3C_{\leq1}$ SiO_2* SiC	0.3205(5)	0.7849(4)	2.449
$Mo_{34.2}Si_{57.3}Al_{8.5}$/15 vol% SiC $(Mo(Si_{0.86},Al_{0.14})_2$/15 vol% SiC) (from powder B)	$C11_b$ (84.9) C40 (15.1) $Mo_{\leq5}Si_3C_{\leq1}$ α-Al_2O_3, SiC	0.3206(0) 0.465(0)	0.7889(0) 0.654(6)	2.461 1.408
$Mo_{34.0}Si_{56.8}Al_{9.2}$/15 vol% SiC $(Mo(Si_{0.86},Al_{0.14})_2$/15 vol% SiC) (from powder C)	$C11_b$ (84.4) C40 (15.6) $Mo_{\leq5}Si_3C_{\leq1}$ α-Al_2O_3 SiC	0.3206(9) 0.4652(2)	0.7891(0) 0.6550(6)	2.461 1.408
$Mo_{34.0}Si_{52.7}Al_{13.3}$/15 vol% SiC $(Mo(Si_{0.80},Al_{0.20})_2$/15vol%SiC) (from powder D)	C40 (100) $Mo_{\leq5}Si_3C_{\leq1}$ α-Al_2O_3 SiC	0.4655(1)	0.6548(0)	1.407

†values in parentheses show the weight fraction of matrices (in wt%).
*glassy SiO_2, and trace cristbalite.
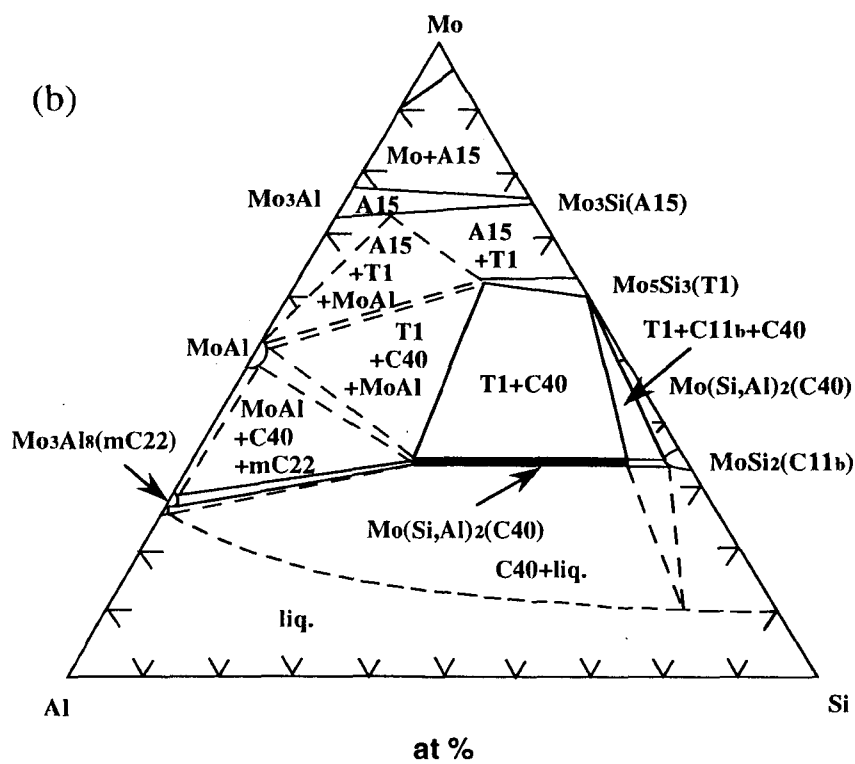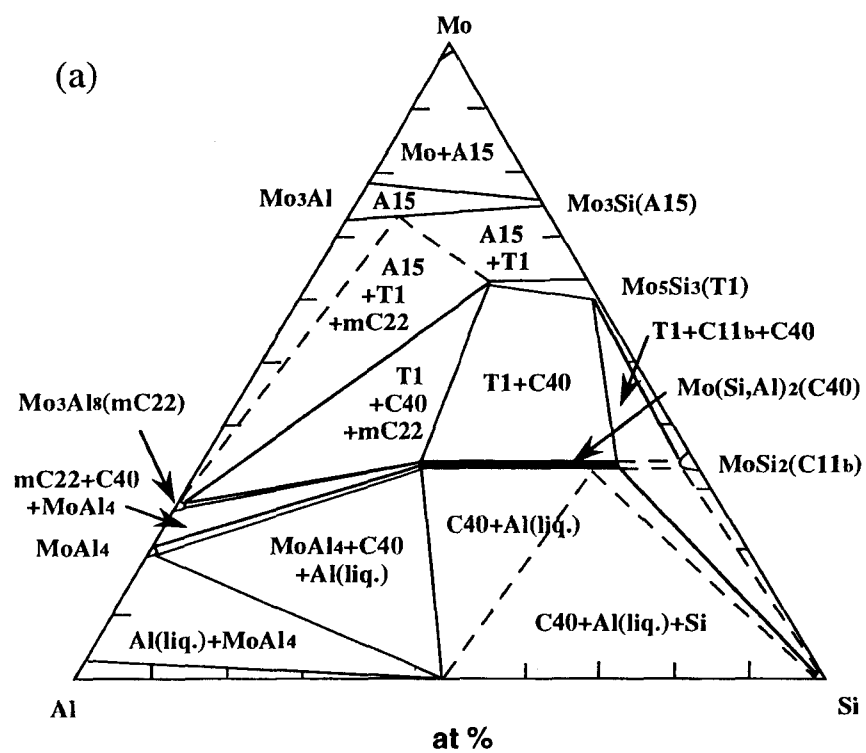
Fig. 6.5 Mo-Si-Al phase diagram proposed by Maruyama et al. at (a) 1050°C and (b) 1550°C.

The geometric "ideal" sixfold coordination at the Mo and (Si,Al)-atomic sites in the hexagonal C40 structure is obtained when lattice parameter $c/a = 1.5$, and the (Si,Al)-atomic position parameter $x = 1/6$ [43]. When the c/a becomes smaller than 1.5, the C40 structure is actually stabilized, and c/a is usually observed in the range of 1.39-1.44 [44]. In this study, c/a of C40 phase slightly decreased with increasing Al content. This probably means Al substitution stabilizes C40 structure.

6.4.3 Microstructure

Figs. 6.6(a) and 6.6(b) show typical backscattered electron images taken by SEM for the Mo-Si-Al alloy and the Mo-Si-Al/SiC composite prepared from powder B, respectively. Grain sizes of matrices were 6.5 μm for Mo-Si-Al and 2.2 μm for Mo-Si-Al/SiC composite, which were confirmed by the polarized optical microscopy. This suggests that added SiC particles effectively inhibited matrix grain growth. As seen from Fig. 6.6(a), four phases were clearly identified in the Mo-Si-Al alloy; EDS analysis revealed that phases which appear dark, relatively dark, relatively bright and bright were α-Al_2O_3, $MoSi_2$, $Mo(Si, Al)_2$ and $Mo_{\leq 5}Si_3C_{\leq 1}$, respectively. Combined with polarized optical microscopic observations, it was revealed that the smaller α-Al_2O_3 phase (~1 μm) had a nearly round shape and located within matrix grains and at grain boundaries, especially at triple points. This microstructure formation may be explained as follows; the Mo-Si-Al powder had the oxidized layer (i.e. α-Al_2O_3-rich oxides) on the surfaces and a thin Mo_5Si_3 region below the oxide layer [20,22]. The existence of Mo_5Si_3 phase was confirmed by XRD (see. Fig. 6.2(a)). During hot-pressing, α-Al_2O_3 was concentrated mainly at triple points similarly to glassy SiO_2 in Chap. 3, and carbon impurity dissolved in Mo_5Si_3 to form $Mo_{\leq 5}Si_3C_{\leq 1}$ (see Fig. 6.2(b)). In the Mo-Si-Al/SiC system, on the other hand, four regions were observed as shown in Fig. 6.6(b); regions appearing dark, relatively dark, relatively bright and bright were α-Al_2O_3/SiC mixed regions, $MoSi_2$, $Mo(Si,Al)_2$ and $Mo_{\leq 5}Si_3C_{\leq 1}$, respectively. It is considered that a large portion of SiC particles was trapped by Al_2O_3 during hot-pressing. That is to say, the composites can be thought as $MoSi_2$-$Mo(Si,Al)_2$ matrices composites with "Al_2O_3/SiC nanocomposite" dispersion was successfully fabricated.

Further SEM observation on fracture surfaces was performed to make clear the fracture mode for Mo-Si-Al alloys and its composite. Figs. 6.7(a) and (b) show SEM micrographs of the $Mo_{34.2}Si_{57.3}Al_{8.5}$ alloy and the $Mo_{34.2}Si_{57.3}Al_{8.5}$/15 vol% SiC composite, respectively. Comparing Figs. 6.7(a) and (b), the grain growth of matrix was inhibited in the composite. As seen from these pictures, the fracture mode of the composite differed from that of Mo-Si-Al alloy. Mo-Si-Al mainly exhibited intragranular fracture, whereas Mo-Si-Al/SiC composite showed both inter- and intragranular fracture. The C40 phase itself is more brittle than $C11_b$ phase due to less slip systems. Hence, the cracks tended to propagate through the matrix grains. This suggests too much C40 phase formation should be avoided to improve fracture toughness.
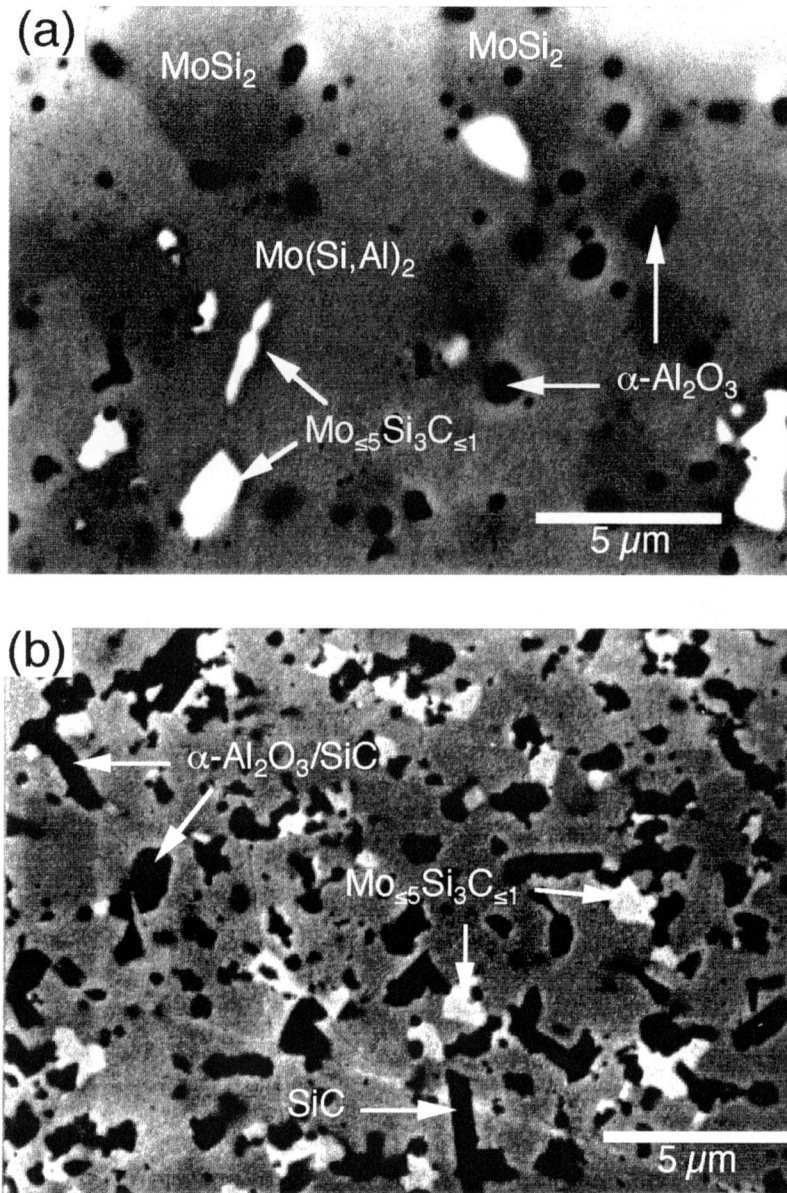
Fig. 6.6 Backscattered electron images for (a) hot-pressed $Mo_{34.2}Si_{57.3}Al_{8.5}$ alloy and (b) hot-pressed $Mo_{34.2}Si_{57.3}Al_{8.5}$ / 15 vol% SiC composite from powder B.

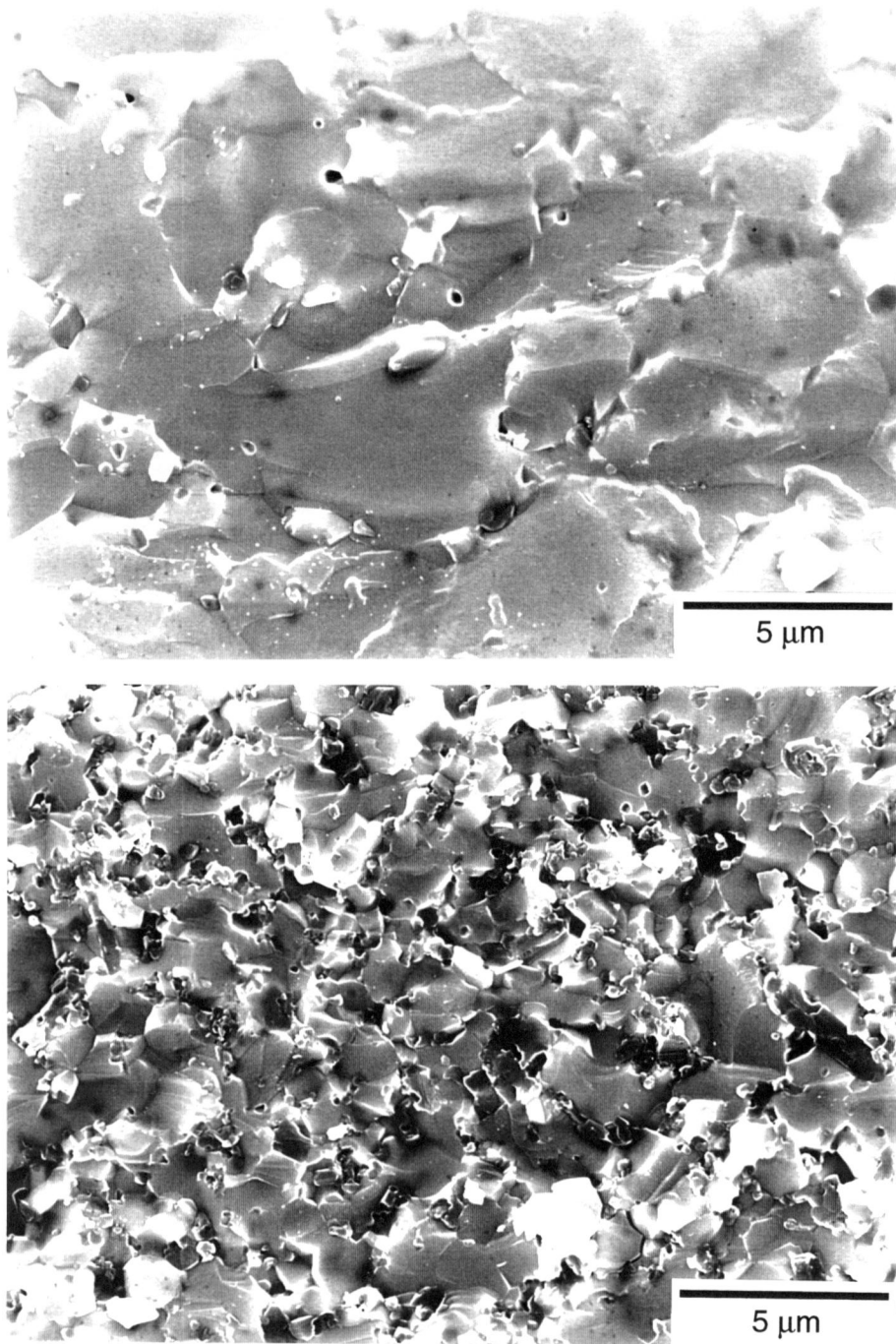**Fig. 6.7** SEM micrographs of fracture surfaces for (a) hot-pressed $Mo_{34.2}Si_{57.3}Al_{8.5}$ alloy and (b) hot-pressed $Mo_{34.2}Si_{57.3}Al_{8.5}$/ 15 vol% SiC composite from powder B.

For the Mo-Si-Al/15 vol% SiC composite system, while $\alpha\text{-}Al_2O_3$ at triple points was strengthened by the SiC dispersion, the composite included more grain boundary phase (about 20 vol%) than Mo-Si-Al alloy (about 6 vol%). Since grain boundary phase is opt to contact each other (Fig. 6.6(b)), cracks tend to propagate along the grain boundaries. $C11_b$-rich matrices must also affect the difference of fracture mode.

6.4.4 Room Temperature Properties

To clarify the effect of the microstructural modification on mechanical properties, fracture strength, hardness and fracture toughness were evaluated (Table 6.5).

Strength: For Mo-Si-Al alloy systems, fracture strength increased, and then decreased with increasing Al content. Strengthening in $Mo_{34.2}Si_{57.3}Al_{8.5}$ alloy fabricated from powder B (nominally $Mo(Si_{0.86},Al_{0.14})_2$) was mainly due to the $\alpha\text{-}Al_2O_3$ formation instead of glassy SiO_2. Comparing two nominal $Mo(Si_{0.86},Al_{0.14})_2$ alloys from powder B with from powder C, the latter includes much oxygen impurity. This resulted in a large agglomeration of $\alpha\text{-}Al_2O_3$, and it probably decreased fracture strength. In addition, the latter alloy also included more hexagonal C40 phase than that from powder B. The C40 phase has lower symmetry than $C11_b$, resulting in the less slip system and less deformability. On the other hand, the Mo-Si-Al alloy from powder B included small $\alpha\text{-}Al_2O_3$ particles as shown before. They effectively inhibited matrix grain growth, and they were much smaller than the expected critical flaw size. That is why there was serious difference between two alloys. The $Mo_{34.0}Si_{52.7}Al_{13.3}$ alloy (nominally $Mo(Si_{0.80}, Al_{0.20})_2$) also showed poor fracture strength; it is also attributed to the excess of C40 phase, with less deformability than $C11_b$ structure, decreasing fracture strength.

For the composite system, added SiC highly improved fracture strength. This was mainly due to the matrix grain growth inhibition, and toughening of dispersed $\alpha\text{-}Al_2O_3$ regions by SiC

Table 6.5 Phase ratio and room temperature mechanical properties of Mo-Si based materials.

Nomalized composition	Hot-pressing temperature (°C)	Matrices ratio tetra : hexa	Density (g/cm³)	Strength (MPa)	Hardness (GPa)	Toughness (MPa·m^{1/2})
$Mo_{34.0}Si_{66.0}$	1500	100 : 0	5.998	687	10.38	2.29
$Mo_{34.2}Si_{57.3}Al_{8.5}$*	1500	25.5 : 74.5	6.155	764	10.98	1.92
$Mo_{34.0}Si_{56.8}Al_{9.2}$**	1500	21.5 : 78.5	6.156	295	11.41	2.17
$Mo_{34.0}Si_{52.7}Al_{13.3}$	1500	0 :100	6.107	358	10.94	2.01
$Mo_{34.0}Si_{66.0}$/15 vol% SiC	1600	100 : 0	5.409	1101	11.77	3.79
$Mo_{34.2}Si_{57.3}Al_{8.5}$* /15 vol% SiC	1600	84.9 : 15.1	5.688	1107	14.21	3.00
$Mo_{34.0}Si_{56.8}Al_{9.2}$**/15 vol% SiC	1600	84.4 : 15.6	5.665	973	14.12	3.74
$Mo_{34.0}Si_{52.7}Al_{13.3}$/15 vol% SiC	1600	0 :100	5.626	636	13.75	3.14

*from 1.61 μm powder (2.57 at% oxygen), * from 1.35 μm powder (3.36 at% oxygen)

particles; for example, the grain size of matrices were 6.5 μm and 2.2 μm for $Mo_{34.2}Si_{57.3}Al_{8.5}$ alloy and $Mo_{34.2}Si_{57.3}Al_{8.5}$ /15 vol% SiC composites, respectively. Excess of C40 phase also decreased strength for composite system.

Hardness: Hardness increased, and then decreased with increasing Al content. Increment of hardness was attributed to the α-Al_2O_3 formation instead of glassy SiO_2. Decrement of hardness was probably related to the weakening of interatomic bond strength in C40 phase by the Al displacement. Mo-Si-Al/SiC composites showed very high hardness because of the hard SiC dispersion, the grain size refinement, and the increase of $C11_b$ phase with relatively high hardness.

Harada et. al [42] have briefly described the hardness of Al-alloyed $MoSi_2$ fabricated by using arc melting; the hardness decreased with increasing the Al content in the range of 0-10 at% (i.e. $MoSi_2$ to $MoSi_{1.7}Al_{0.3}$) and then increasing with increasing it in the range of 10-15 at% (i.e. $MoSi_{1.7}Al_{0.3}$ to $MoSi_{1.55}Al_{0.45}$). $C11_b$ dissolved Al up to 3 at.% and single phase C40 appeared more than 10 at% Al. They explained that the decrement of hardness was due to the solid solution "softening" (i.e. Al into Si-site of $C11_b$) and the increment was due to the crystallographical modification (i.e. $C11_b$ to C40). For powder metallurgically processed systems, however, other phases which are dispersing in alloys affect the hardness in addition to above mentioned mechanisms. Although $C11_b$ phase should be softened by dissolving Al (up to 3 at%) [42], Al_2O_3 and $Mo_{\leq5}Si_3C_{\leq1}$ dispersion should give hardening effect. Combination of these opposite effects, the hardness values of Mo-Si-Al alloys were a little higher than that of $MoSi_2$.

Toughness: Toughness of Mo-Si-Al alloy was slightly lower than that of $MoSi_2$. This was because the intragranular fracture was dominant for Mo-Si-Al owing to the brittle characteristics of C40 phase, while both inter- and intragranular fracture was observed for $MoSi_2$. Intrinsic bonding strength may also affect the fracture toughness. Toughening in composite systems was explained by residual stress via thermal expansion mismatch between matrix and dispersoids [29] and crack deflection by dispersed Al_2O_3-SiC composite regions

6.4.5 High-Temperature Strength

High-temperature strength was evaluated in order to examine the alloying and SiC dispersion effects and to confirm the usefulness of Mo-Si-Al. Fig. 6.8 shows the variation of strength with temperature for $MoSi_2$ from coarse powder [45], $MoSi_2$ from fine powder [4], $MoSi_2$/SiC composite [4], Mo-Si-Al alloy and Mo-Si-Al/15 vol% SiC composite from powder B. Although the strength values of fine $MoSi_2$ and $MoSi_2$/SiC composite were fall down more than 1000°C, Mo-Si-Al and Mo-Si-Al/SiC composite kept high strength values up to 1100°C. The strength values at 1100°C were 833 MPa for Mo-Si-Al and 954 MPa for Mo-Si-Al/SiC composite. The improvement on high-temperature strength was mainly due to the glassy SiO_2 elimination. It is concluded that alloying with Al was fairly effective to enhance mechanical properties not only at
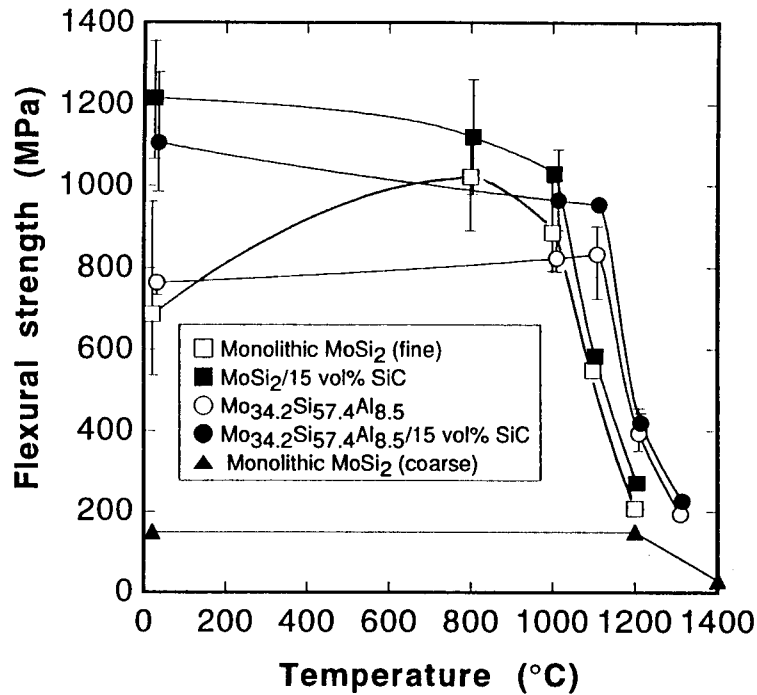
Fig. 6.8 Variation of strength with temperature for $MoSi_2$ based materials.

room temperature but also at high temperatures.

It is worthy of note that alloying with aluminum enables to control microstructure, i.e. elimination of glassy SiO_2 and crystallographical modification from $C11_b$ to C40. This approach may be available to other silicides.

6.6   Conclusions

The present work reveals microstructure and mechanical properties of the Mo-Si-Al alloy and the Mo-Si-Al/SiC composite. Alloying and composite techniques were simultaneously adapted to obtain better mechanical properties. The results are summarized as follows;

1. Mo-Si-Al alloy and Mo-Si-Al/SiC composite were fabricated by the powder metallurgical process from a novel pre-alloyed powder. The alloy was composed of $MoSi_2$, $Mo(Si,Al)_2$, α-Al_2O_3 and $Mo_{\leq 5}Si_3C_{\leq 1}$. The composite was composed of these four phases and β-SiC. The intergranular glassy SiO_2 phase could be changed into thermodynamically stable α-Al_2O_3 by the alloying.

2. Mechanical properties such as hardness and strength were enhanced by alloying unless excess of C40 phase was formed. Combination of alloying and composite techniques, hardness, strength, toughness and high-temperature strength were simultaneously improved.

3. These results indicate that the combination of alloying and composite techniques has great advantages to fabricate $MoSi_2$-based materials with well-balanced mechanical properties. Further optimization of fabrication conditions will enable to improve the mechanical properties of $MoSi_2$-based system.

References

1. R. B. Schwarz, S. R. Srinivasan, J. J. Petrovic and C. J. Maggiore, "Synthesis of Molybdenum Disilicide by Mechanical Alloying," *Mater. Sci. Eng.*, A 1 5 5, 75-83 (1992).

2. F. D. Gac and J. J. Petrovic, "Feasibility of a Composite of SiC Whiskers in an $MoSi_2$ Matrix," *J. Am. Ceram. Soc.*, 6 8 [8] C200-C201 (1985).

3. K. K. Richardson and D. W. Freitag, "Mechanical Properties of Hot Pressed SiC Platelet-Reinforced $MoSi_2$," *Ceram. Eng. Sci. Proc.*, 1 2, 1679-1689 (1991).

4. Y. Suzuki and K. Niihara, "Effect of SiC Reinforcement on Microstructure and Mechanical Properties of $MoSi_2$," *Sci. & Eng. Comp. Mater.*, 6 [2] 85-94 (1997).

5. J. J. Petrovic and R. E. Honnell, "Partially Stabilized ZrO_2 Particle-$MoSi_2$ Matrix Composites," *J. Mater. Sci.*, 2 5, 4453-4456 (1990).

6. J. J. Petrovic, R. E. Honnell, T. E. Mitchell, R. K. Wade and K. J. McClellan, "ZrO_2- Reinforced $MoSi_2$ Matrix Composites," *Ceram. Eng. Sci. Proc.*, 1 2, 1633-1642 (1991).

7. R. G. Castro, R. W. Smith, A. D. Rollett and P. W. Stanec, "Toughness of Dense $MoSi_2$ and $MoSi_2$/Tantalum Composites Produced by Low Pressure Plasma Deposition," *Scripta. Metall. Mater.*, 2 6 [2] 207-212 (1992).

8. L. Shaw and R. Abbaschian "Toughening $MoSi_2$ with Niobium Metal - Effects of Size and Orientation of Ductile Laminae," *Acta Metall. Mater.*, 4 2 [1] 213-223 (1994).

9. S. A. Maloy, A. H. Heuer, J. J. Lewandowski, and J. J. Petrovic, "Carbon Addtions to Molybdenum Disilicide: Improved High-Temperature Mechanical Properties," *J. Am. Ceram. Soc.*, 7 4 [10] 2704-2706 (1991).

10. S. A. Maloy, J. J. Lewandowski, A. H. Heuer and J. J. Petrovic, "Effects of Carbon Additions on the High Temperature Mechanical Properties of Molybdenum Disilicide," *Mater. Sci. Eng.*, A 1 5 5, 159-163 (1992).

11. N. S. Jacobson, K. N. Lee, S. A. Maloy and A. H. Heuer, "Chemical Reactions in the Processing of $MoSi_2$+Carbon Compacts," *J. Am. Ceram. Soc.*, 7 6 [8] 2005-2009 (1993).

12. D. K. Patrick and D. C. Van Aken, "Microstructural Analysis and High-Temperature Strength of a Directionally Solified $Er_2Mo_3Si_4$-$MoSi_2$ Eutectic", *Scripta Metall. et Mater.*, 3 0 [8] 981-985 (1994).

13. R. Gibala, A. K. Ghosh, D. C. Van Aken, D. J. Srolovitz, A. Basu, H. Chang, D. P. Mason and W. Yang, "Mechanical Behavior and Interface Design of $MoSi_2$-Based Alloys and Composites," *Mater. Sci. Eng.*, A 1 5 5, 147-158 (1992).

14. Y. Suzuki, T. Sekino and K. Niihara, "Effects of ZrO_2 Addition on Microstructure and Mechanical Properties of $MoSi_2$," *Scripta Metall. et Mater.*, 3 3 [1] 69-74 (1995).

15. H. Kudielka and H. Nowotny, "Disilizidsysteme," *Mh. Chem.*, 8 7 [3] 471-482(1956).

16. H. Nowotny and H. Huschka, "Untersuchungen der Teilsysteme Aluminium-$TiSi_2$, -$ZrSi_2$, -$MoSi_2$ und -WSi_2," *Mh. Chem.*, 8 8 [4] 494-501 (1957).

17. H. Nowotny and C. Brukl, "Ein Beitrag zum Dreistoff: Molybdän-Aluminium-Silizium," *Mh. Chem.*, 9 1 [2] (1960) 313-318.

18. C. Brukl, H. Nowotny and F. Benesovsky, "Untersuchungen in den Dreistoffsystemen: V-Al-Si, Nb-Al-Si, Mo-Al-Si bsw. Cr(Mo)-Al-Si," *Mh. Chem.*, 9 2 [5] 967-980 (1961).

19. P. S. Kisly and V. Yu. Kodash, "The Mullite Coatings on Heaters Made of Molybdenum Disilicide," *Ceram. Int'l.*, 1 5, 189-191 (1989).

20. V. Yu. Kodash, P. S. Kisly and V. J. Shemet, "High Temperature Oxidation of Molybdenum Alumino-silicides," *High. Temp. Sci.*, 2 9, 143-152 (1990).

21. T. Maruyama, K. Yanagihara and K. Nagata, "High Temperature Oxidation of Intermetallic Compounds of $Mo(Si_{1-x}Al_x)_2$," *Corrosion Science*, 3 5 [5-8] 939-944 (1993).

22. K. Yanagihara, T. Maruyama and K. Nagata, "Isothermal and Cyclic Oxidation of $Mo(Si_{1-x}Al_x)_2$ up to 2048K," *Mater. Trans. JIM*, 3 4 [12] 1200-1206 (1993).

23. K. Yanagihara, T. Maruyama and K. Nagata, "High Temperature Oxidation of Mo-Si-X Intermetallics (X =

Al, Ti, Ta, Zr and Y)," *Intermetallics*, 3, 243-251 (1995).

24. K. Yanagihara, T. Maruyama and K. Nagata, "Effect of Third Elements on the Pesting Suppression of Mo-Si-X Intermetallics (X = Al, Ta, Ti, Zr and Y)," *Intermetallics*, 4, S133-S139 (1996).

25. A. Stergiou, P. Tsakiropoulos and A. Brown, "The Intermediate and High-Temperature Oxidation Behavior of Mo(Si$_{1-x}$,Al$_x$)$_2$ Intermetallis Alloys," *Intermetallics*, 5, 69-81 (1997).

26. A. Costa e Silva and M. J. Kaufman, "Microstructural Modification of MoSi$_2$ through Aluminum Additions," *Scripta Metall. Mater.*, 2 9 [8] 1141-1145 (1993).

27. A. Costa e Silva and M. J. Kaufman, "In-Situ Formation of Alumina Coatings in Niobium Toughened Mo(Si,Al)$_2$," *Scripta Metall. Mater.*, 3 1 [7] 853-858 (1994).

28. A. Costa e Silva and M. J. Kaufman, "Applications of In Situ Reactions to MoSi$_2$-Based Materials," *Mater. Sci. Eng.*, A1 9 5, 75-88 (1995).

29. Y. Suzuki, A. Nakahira, T. Sekino and K. Niihara, "Microstructure and Mechanical Properties of Mo-Si-Al Alloy and Mo-Si-Al/SiC Composite," *J. Jap. Soc. Pow. & Pow. Metall.*, 4 3 [3] 272-277 (1996).

30. Y. Suzuki, T. Sekino and K. Niihara, "Effects of Al Substitution and Nano-Sized SiC Dispersion on Microstructure and Mechanical Properties of MoSi$_2$," *Proc. of the 6th Tohwa University Int'l Symp.:* Fukuoka, Oct. 1996, ed. by Y. Nagano, Tohwa University Press, Japan, (1996), pp.189-194.

31. K. Niihara, R. Morena and D. P. H. Hasselman, "Evaluation of K$_{IC}$ of Brittle Solids by the Indentation Method with Low Crack-to-Indent Ratios," *J. Mater. Sci. Lett.*, 1 [1] 13-16 (1982).

32. F. Izumi, "Rietveld Analysis Programs RIETAN and PREMOS and special applications", *The Rietveld Method*, ed. by R. A. Young, Oxford University Press, Oxford (1993), Chap. 13.

33. Y. -I. Kim and F. Izumi, "Structure Refinements with a New Version of the Rietveld-Refinement Program RIETAN," *J. Ceram. Soc. Jpn.*, 1 0 2 [4] 401-404 (1994).

34. H. M. Rietveld, "Line Profiles of Neutron Powder-Diffraction Peaks for Structure Refinement," *Acta Crystallogr.*, 2 2, 151-152 (1967).

35. G. Malmros and J. O. Thomas, "Least-Squares Structure Refinement Based on Profile Analysis of Powder Film Intensity Data Measured on an Automatic Microdensitometer," *J. Appl. Crystallogr.*, 1 0, 7-11 (1977).

36. P. Thompson, D. E. Cox and J. B. Hastings, "Rietveld Refinement of Debye-Scherrer Synchrotron X-Ray Data from Al$_2$O$_3$," *J. Appl. Crystallogr.*, 2 0 [2] 79-83 (1987).

37. R. J. Hill and C. J. Howard, "Quantitative Phase Analysis from Neutron Powder Diffraction Data Using the Rietveld Method," *J. Appl. Crystallogr.*, 2 0 [6] 467-474 (1987).

38. D. M. Shah, D. Berczic, D. L. Anton and R. Hecht, "Appraisal of Other Silicides as Structural Materials," *Mater. Sci. Eng.*, A1 5 5, 45-57 (1992).

39. J. Maas, G. Bastin, F. van Loo and R. Metselaar, "The Texture in Diffusion-Grown Layers of Disilicides MeSi$_2$ (Me = Mo, W, Ti, V, Nb, Ta) and Compounds with Related Structures(NbGe$_2$, TaGe$_2$, TiGe$_2$, TiNiCu)," *Z. Metallkde*, 7 5 [2] 140-145 (1984).

40. T. A. Adler and C. R. Houska, "Integrated Intensities and Lattice Parameters for MoSi$_2$," *J. Am. Ceram. Soc.*, 6 1 [3-4] 182-183 (1978).

41. L. F. Mattheiss, "Electronic Structure of CrSi$_2$ and Related Refractory Disilicide," *Phys. Rev. B*, 4 3 [15] 12549-12555 (1991).

42. Y. Harada, Y. Funato, M. Morinaga, A. Ito and Y. Sugita "Solid Solubilities of Ternary Elements and Their Effects on Microstructure of MoSi$_2$," *J. Japan Inst. Metals*, 58 [11] 1239-1247 (1994).

43. L. F. Mattheiss, "Calculated structural properties of CrSi$_2$, MoSi$_2$, and WSi$_2$," *Phys. Rev. B*, 4 5 [7] 3252-3259 (1992).

44. M. -A. Nicolet and S. S. Lau, "Formation and Characterization of Transitio-Metal Silicides", *VLSI Electronics: Microstructure Science, Vol.6*: eds. N. G. Einsprush and G. B. Larrabee (Academic Press, New York, 1983), pp.329-464 (1983).

45. D. H. Carter, W. S. Gibbs, and J. J. Petrovic, "Mechanical Characterization of SiC Whisker-Reinforced MoSi$_2$," *Proc. 3rd Int'l Symp. on Ceram. Mater. & Comp. for Engines*, Nov. 1988, Las Vegas, NV. American Ceramic Sosiety, Westerville, OH, (1989) pp.977-986.

Synthesis and Mechanical Properties of $Mo_{\leq5}Si_3C_{\leq1}$ and $Mo_{\leq5}Si_3C_{\leq1}$-Based Composites

In this chapter, the first systematic study of $Mo_{\leq5}Si_3C_{\leq1}$ and $Mo_{\leq5}Si_3C_{\leq1}$-based composites was conducted. The $Mo_{\leq5}Si_3C_{\leq1}$ phase was synthesized by the reactive hot-pressing (RHP) from elemental molybdenum, silicon, and carbon powders at 30 MPa and 1500° C for 1-2 h. The products were characterized using chemical and X-ray fluorescence analyses, X-ray diffraction and scanning electron microscopy. Although a small amount of SiO_2-rich glassy phase (about 1 wt%) was contained, sintered compacts consisting of only the crystalline $Mo_{\leq5}Si_3C_{\leq1}$ phase were produced from Mo, Si and C powders via a hot-pressing process. Phase relations in the Mo-Si-C system and lattice parameters of the $Mo_{\leq5}Si_3C_{\leq1}$ phase were examined. Fracture strength, Vickers hardness and fracture toughness of $Mo_{\leq5}Si_3C_{\leq1}$ hot-pressed at 1500°C for 2 h were 485 MPa, 12.1 GPa and 3.3 MPa·m$^{1/2}$, respectively. These results suggest the potential of $Mo_{\leq5}Si_3C_{\leq1}$ not only as a new reinforcement second phase but also as a new matrix material of composites of Mo-Si compounds. $Mo_{\leq5}Si_3C_{\leq1}/Mo_2C$ and $Mo_{\leq5}Si_3C_{\leq1}/MoSi_2$ in-situ composites were also prepared by controlling Si content. The surface of $Mo_{\leq5}Si_3C_{\leq1}/Mo_2C$ composite was easily corroded particularly in the presence of moisture. On the other hand, $Mo_{\leq5}Si_3C_{\leq1}/MoSi_2$ composite showed better corrosion resistance, and well-balanced mechanical properties. The $Mo_{\leq5}Si_3C_{\leq1}$-$MoSi_2$ pseudo-binary system may be of importance for new high-temperature structural materials.

7.1 Introduction

Various advanced structural material systems have been extensively investigated for applications under severe environments such as at temperatures higher than 1500°C or in corrosive atmospheres. Of such advanced structural materials, composites based on the Mo-Si-C system are of interest since they contain $MoSi_2$ and/or SiC with a high melting temperature and good oxidation resistance as constituent phases.

The molybdenum carbosilicide ($Mo_{\leq5}Si_3C_{\leq1}$) is the only stable ternary Mo-Si-C phase which is called as the Nowotny phase [1]. $Mo_{\leq5}Si_3C_{\leq1}$ is a nonstoichiometric compound which has

the hexagonal $D8_8$ structure. It has been reported that $Mo_{\leq5}Si_3C_{\leq1}$ is found in $MoSi_2$ compacts containing some amount of carbon [2-8]; Maloy et al. [2-4] reported that carbon (added to $MoSi_2$ as a deoxidant) removed SiO_2 at grain boundaries and formed $Mo_{\leq5}Si_3C_{\leq1}$ and SiC. Costa e Silva et al. [5] pointed out that the third phase in silicon-lean $MoSi_2$/SiC composites should be $Mo_{\leq5}Si_3C_{\leq1}$ instead of Mo_5Si_3 through thermodynamical calculations. Since $Mo_{\leq5}Si_3C_{\leq1}$ is likely to coexist with $MoSi_2$, it is interesting to clarify the role of $Mo_{\leq5}Si_3C_{\leq1}$ in composites based on the Mo-Si-C system. There is a great possibility for $Mo_{\leq5}Si_3C_{\leq1}$ to be not only a reinforcement second phase but also a new matrix phase of composites based on the Mo-Si-C system, because of (1) its high melting point which is about 2100° C and (2) its relatively complex structure that may lead to good creep resistance. However, most of its physical and mechanical properties are still unknown, except some crystallographical parameters. Clarifying the properties of $Mo_{\leq5}Si_3C_{\leq1}$ is thus indispensable for studying composites based on the Mo-Si-C system.

In this investigation, monolithic $Mo_{\leq5}Si_3C_{\leq1}$ was synthesized using reactive hot-pressing (RHP) from elemental molybdenum, silicon and graphite powders. $Mo_{\leq5}Si_3C_{\leq1}$ based in situ composites were also fabricated by controlling silicon content. Constituent phases and composition of composites were quantitatively analyzed by X-ray diffraction (XRD), X-ray fluorescence spectrometry (XRF) and scanning electron microscopy combined with energy dispersive X-ray spectrometry (SEM-EDS). Some mechanical properties were evaluated.

7.2 Experimental procedure

7.2.1 Sample Preparation

High purity powders of elemental molybdenum (ca. 1.5 μm, >99.9 %), silicon (<10 μm, >99.9 %) and graphite (about 5 μm, 99.7 %) were used for preparations of sintered compacts. All powders used in this experiment were commercial powders, supplied from Kojundo Chemical Lab. Co. Ltd. The average particle size and purity of powders used are shown in Table 7.1. Mo, Si and C powders were weighed, and they were mixed by wet ball-milling in acetone with SiC balls for 48 h. Wet ball-milled mixture was dried and then dry ball-milled to crush large agglomerates. The mixed powder was packed into carbon dies coated with BN and then reactively hot-pressed at 1600° C under an applied pressure of 30 MPa for 2 h. Hot-pressing was conducted in a pressurized argon atmosphere (0.5 MPa) to minimize silicon vaporization. Hot-pressed disks were 44 mm in diameter and 5.0 mm in thickness. Sintered compacts were cut, ground and polished into rectangular bars with $4 \times 3 \times 36$ mm in size. Their bulk density was measured by the Archimedes method in toluene. Experimental procedures are schematically summarized in Fig.7.1.

Table 7.1 Size and purity of powders used

Powder[†]	Average size (μm)	Purity (wt%)[††]	Impurities (wt%)
Mo	1.5	> 99.9	W (0.01), Si (0.01), Fe (0.004)
Si	<10	> 99.9	Fe (0.05), Cr (0.01), Ni (0.007), Ca (0.001), Mn (0.001)
C (graphite)	5	99.7	Fe (0.1), Si (0.04), Ca (0.02), Al (0.008), Mg (0.005)

[†] All powders were purchased fromKojundo Chemical Laboratory Co., Ltd.
[††] Catalogue vcalues measured by ICP. Light elements such as C, N and O were not counted.
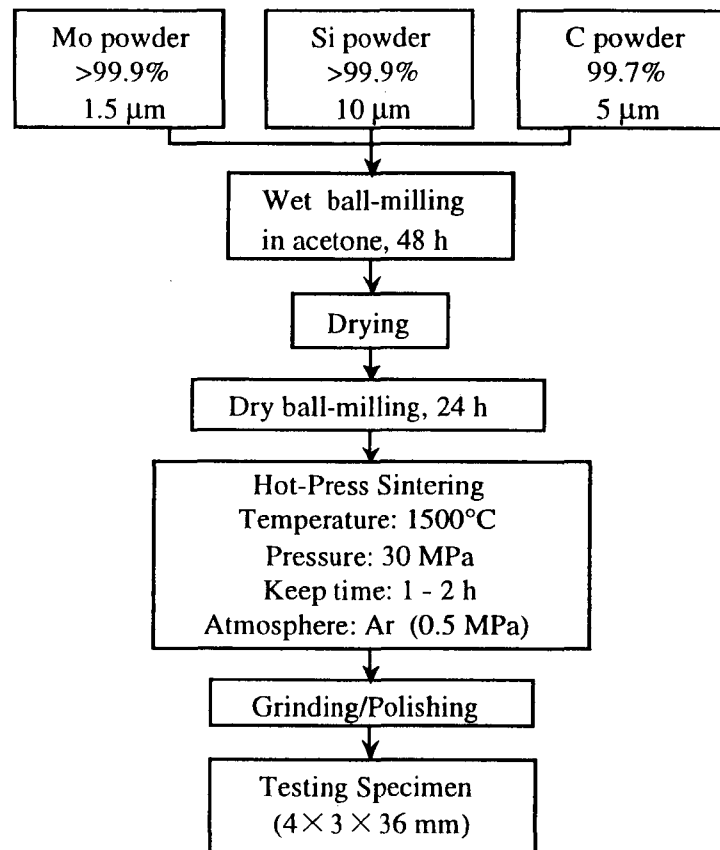
Fig. 7.1   Schematic illustration of experimental procedure.

7.2.2   Evaluation

X-ray diffraction profiles of the sintered materials were measured on a RIGAKU RAD-B diffractometer with Cu-Kα radiation; the tube voltage and current were 150 kV and 50 mA, respectively. The diffraction profiles were analyzed by the Rietveld method using $RIETAN$-94 software by Izumi et. al. [9,10]. Crystallographical parameters of $Mo_{\leq 5}Si_3C_{\leq 1}$ in Table 7.2 [1,11] were used for the Rietveld analysis.

Formula	$Mo_3Mo_{\leq 2}Si_3C_{\leq 1} = Mo_{\leq 5}Si_3C_{\leq 1}$			(Ideal formula : $T_3^I T_2^{II} M_3 X$)		
Space group	$P6_3/mcm$, hexagonal, $c/a \sim 0.69$					
Point positions	T^I in 6(g)	x,0,1/4	0,x,1/4	$\bar{x},\bar{x},1/4$	$\bar{x},0,3/4$	$0,\bar{x},3/4$	x,x,3/4	(x ~ 0.24)
	T^{II} in 4(d)	1/3,2/3,0	2/3,1/3,0	1/3,2/3,1/2	2/3,1/3,1/2	
	M in 6(g)	x,0,1/4	0,x,1/4	$\bar{x},\bar{x},1/4$	$\bar{x},0,3/4$	$0,\bar{x},3/4$	x,x,3/4	(x ~ 0.61)
	X in 2(b)	0,0,0	0,0,1/2			

[†]Nowotny phases are quaternary or ternary metallic phases of composition $T_3^I T_{\leq 2}^{II} M_3 X_{\leq 1}$ where T; transition metal (group 3A to 8A), M; metamatal (group 3B to 5B, mostly Si and Ge) and X; nonmetal (like C,N, also B and O) [1].

Composition analyses of sintered compacts were carried out by XRF (Philips, PW 2400) for Mo and Si, by a thermal conductivity method for carbon (LECO, WR12) and by an infrared absorption method for oxygen (LECO, TC436). The determination of Mo and Si content was also performed by gravimetric analysis. Mo and Si contents determined by these two methods were in good agreement with each other (within 0.5 wt%).

Microstructures of compacts were characterized by SEM (Hitachi S-5000) with EDS (Horiba EMAX-5770). Samples for SEM observations were pre-coated with Au. Mechanical properties were evaluated at room temperature. Five or six specimens were subjected to three-point bending test (span: 30 mm) to determine fracture strength. Bending load was applied parallel to the hot-pressing axis with a cross-head speed of 0.5 mm/min. Hardness (H_v) was evaluated by Vickers indentation under a conditions of 98 N load with loading duration of 15 s. Fracture toughness (K_{IC}) was determined simultaneously by the indentation fracture (IF) method [12]. K_{IC} values were calculated by the Niihara's equation [12].

7.3 Results and Discussion

7.3.1 Synthesis of Monolithic $Mo_{\leq 5}Si_3C_{\leq 1}$

$Mo_{56.1}Si_{36.9}C_{7.0}$ (corresponding to $Mo_{4.57}Si_3C_{0.57}$) was chosen for the initial composition to synthesize monolithic $Mo_{\leq 5}Si_3C_{\leq 1}$. X-ray diffraction analyses of powdered samples made from sintered compacts indicated that they consist of only $Mo_{\leq 5}Si_3C_{\leq 1}$ (Fig.7.2(a)). Unreacted components and other intermetallic phases were not observed. Composition analyses revealed that the composition of sintered compacts was $Mo_{56.6\pm 0.5}Si_{35.9\pm 0.5}C_{7.5\pm 0.5}$ ($Mo_{4.7}Si_3C_{0.6}$). The difference between the composition of powder mixture and that of sintered compacts was not so large. Strictly speaking, small amounts of carbon gain and silicon loss were observed. A small amount of carbon is thought to be picked up from organic solvent, carbon die and hot-pressing atmosphere (CO molecule must be in the furnace because a carbon die and a carbon heating

element were used). A small amount of silicon loss may be due to the vaporization during the hot-pressing. Rietveld analyses of the obtained XRD profile gave a hexagonal unit cell with lattice parameters $a = 0.72903$, $c = 0.50434$ nm, and $c/a = 0.6918$ (Fig. 7.2(b)). Taking into account the non-stoichiometric character, they are in good agreement with the parameters in the Powder Diffraction File (PDF) 43-1199 for $Mo_{4.8}Si_3C_{0.6}$, $a = 0.729260$ nm, $c = 0.50439$ nm, and $c/a = 0.6916$.

Fig. 7.3 shows a typical SEM micrograph of the polished surface of a compact. Although some spherical glassy SiO_2 particles existed in the hot-pressed compact, neither unreacted components nor binary intermetallic phases were observed. The presence of SiO_2 may be attributed to the oxidation of silicon powder. The amount of SiO_2 was estimated to be about 1 wt% from oxygen analysis.

7.3.2 Synthesis of $Mo_{\leq5}Si_3C_{\leq1}$-Based Composites

$Mo_{\leq5}Si_3C_{\leq1}$-based composites were fabricated by controlling the initial Si content. First, a $Mo_{\leq5}Si_3C_{\leq1}/Mo_2C$ composite was produced using an initial composition such as $Mo_{57.1}Si_{35.7}C_{7.1}$ (corresponding to $Mo_{4.80}Si_3C_{0.60}$) containing less silicon than the initial composition used for producing the monolithic $Mo_{\leq5}Si_3C_{\leq1}$ phase. The Mo : C atomic ratio is the same as that of the monolithic $Mo_{\leq5}Si_3C_{\leq1}$ phase (i.e. 8:1). X-ray diffraction analyses of the compact show that it consists of $Mo_{\leq5}Si_3C_{\leq1}$ and hexagonal Mo_2C (Fig. 7.4(a)). The compositional change during hot-press sintering was almost identical to the case of monolithic $Mo_{\leq5}$ $Si_3C_{\leq1}$ compacts. This will be discussed in the next section. Fractions of constituent phases were determined by Rietveld analyses of the XRD profile. The sintered compact was found to be composed of 97 wt% of $Mo_{\leq5}Si_3C_{\leq1}$ and 3 wt% of Mo_2C. Lattice parameters of the $Mo_{\leq5}$ $Si_3C_{\leq1}$ phase were $a = 0.72878$, $c = 0.50569$ nm, and $c/a = 0.6939$. The c/a ratio of the $Mo_{\leq5}Si_3C_{\leq1}$ phase in the $Mo_{\leq5}$ $Si_3C_{\leq1}/Mo_2C$ composite was larger than that of monolithic $Mo_{\leq5}Si_3C_{\leq1}$ compact. The reason for this will be discussed in section 7.3.4. SEM-EDS study clearly showed the existence of $Mo_{\leq5}$ $Si_3C_{\leq1}$, Mo_2C and SiO_2-rich glassy phase (Fig.7.5(a)).

Secondly, a $Mo_{\leq5}Si_3C_{\leq1}/MoSi_2$ composite was produced using an initial composition of $Mo_{53.7}Si_{39.6}C_{6.7}$ (corresponding to $Mo_{4.07}Si_3C_{0.51}$) containing more silicon than the initial composition for $Mo_{\leq5}Si_3C_{\leq1}$ monolithic compacts. The Mo : C atomic ratio was the same as that for the former two types of compacts. XRD showed the presence of only $Mo_{\leq5}Si_3C_{\leq1}$ and tetragonal $MoSi_2$ phases (Fig. 7.4(b)). The composition of sintered compact was slightly different from the initial one, similarly to the case of monolithic $Mo_{\leq5}Si_3C_{\leq1}$ compact (i.e., small increment of Si and decrement of C). The hot-pressed compact was composed of 94 wt% of the $Mo_{\leq5}Si_3C_{\leq1}$ phase and 6 wt% of $MoSi_2$. Lattice parameters of the $Mo_{\leq5}Si_3C_{\leq1}$ phase were $a = 0.72884$, $c = 0.50164$ nm, and $c/a = 0.6883$. The c/a of the $Mo_{\leq5}Si_3C_{\leq1}$ phase in the $Mo_{\leq5}$ $Si_3C_{\leq1}/MoSi_2$ composite was smaller than that of monolithic $Mo_{\leq5}Si_3C_{\leq1}$. SEM-EDS analyses indicated the existence of $Mo_{\leq5}Si_3C_{\leq1}$, $MoSi_2$ and SiO_2-rich glassy phase (Fig. 7.5(b)).
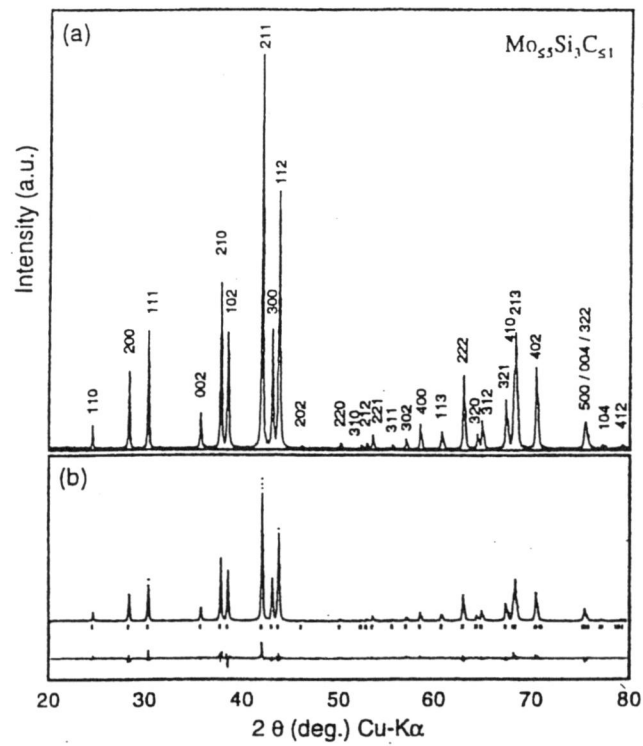
Fig. 7.2 (a) XRD pattern for a $Mo_{\leq 5}Si_3C_{\leq 1}$ compact hot-pressed at 1500°C for 2 h, (b) comparison between observed and calculated intensities of the XRD peaks for the $Mo_{\leq 5}Si_3C_{\leq 1}$ phase. The difference in intensity between observed and cal-culated peaks is also shown. Tick marks are Bragg positions.

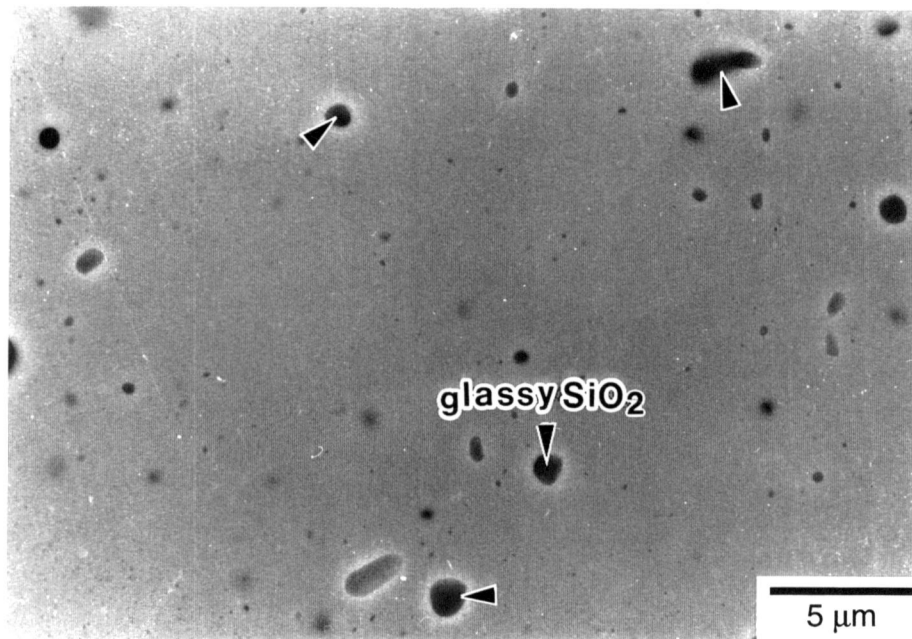**Fig. 7.3** SEM micrograph on the polished surface of a $Mo_{\leq 5}Si_3C_{\leq 1}$ compact hot-pressed at 1500°C for 2 h.
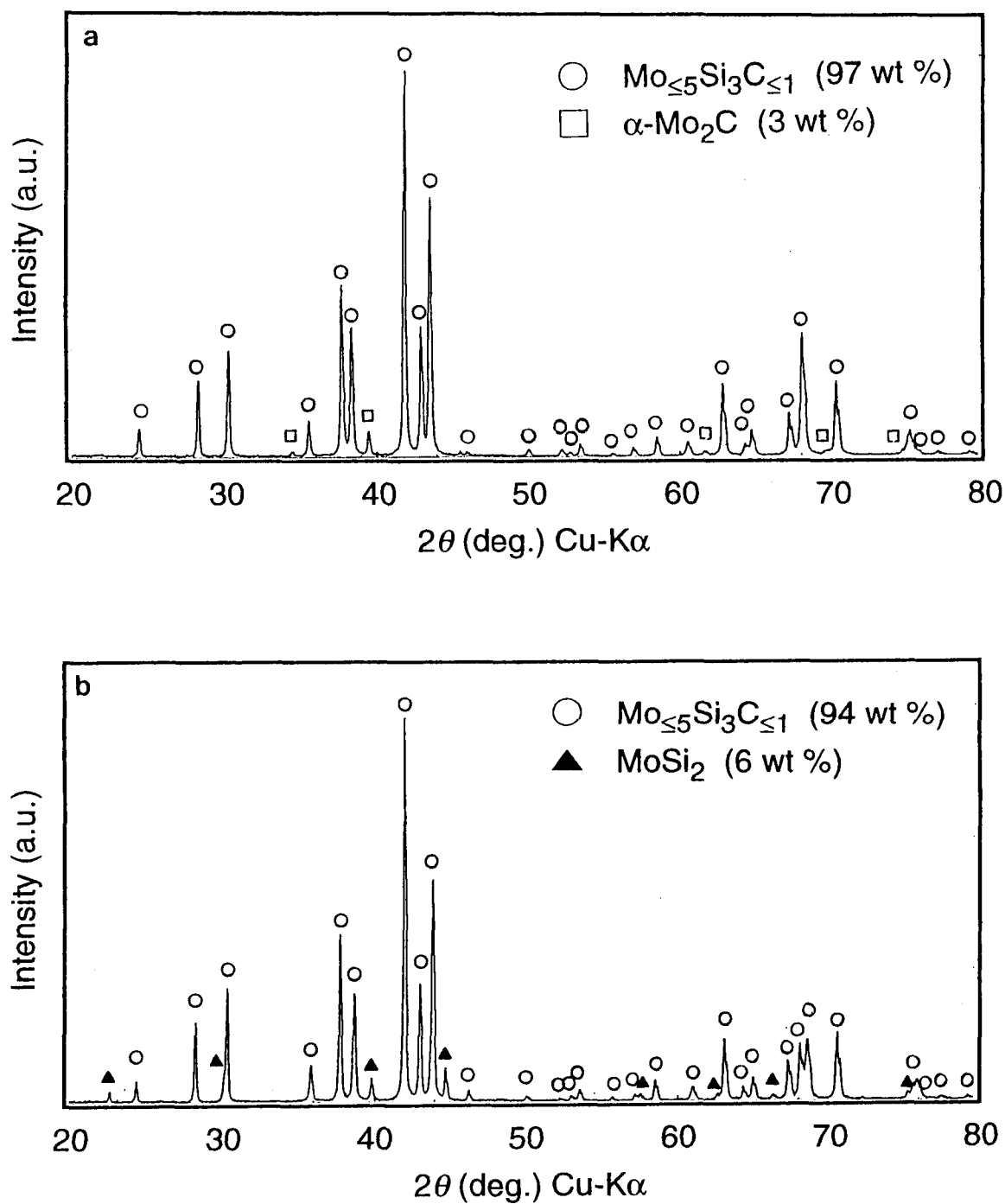
111

Fig. 7.4 X-ray diffraction pattern for (a) a $Mo_{\leq 5}Si_3C_{\leq 1}/Mo_2C$ composite from the initial composition of $Mo_{57.1}Si_{35.7}C_{7.1}$ and (b) a $Mo_{\leq 5}Si_3C_{\leq 1}/MoSi_2$ composite from $Mo_{53.7}Si_{39.6}C_{6.7}$.
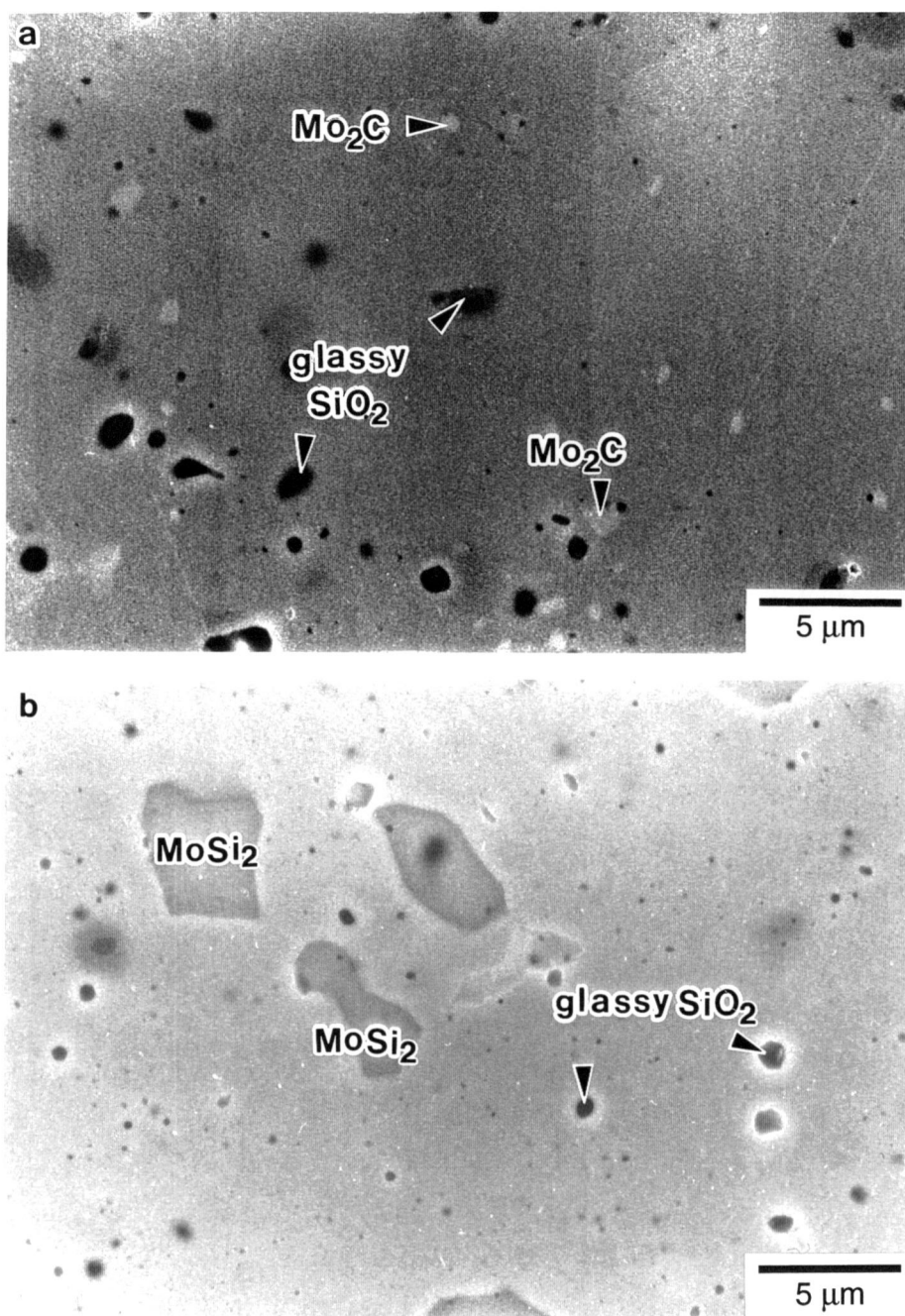
Fig. 7.5 SEM images of (a) a $Mo_{\leq5}Si_3C_{\leq1}/Mo_2C$ composite from the initial composition of $Mo_{57.1}Si_{35.7}C_{7.1}$ and (b) a $Mo_{\leq5}Si_3C_{\leq1}/MoSi_2$ composite from $Mo_{53.7}Si_{39.6}C_{6.7}$.

113

7.3.3 Synthesis Conditions and Phase Relations

Since the first research on the ternary Mo-Si-C system by Nowotny et al. [13], several groups have been studied on the Mo-Si-C system and the $Mo_{\leq 5}Si_3C_{\leq 1}$ phase; the phase equilibria in the Mo-Si-C system by Brewer et al. [14], Loo et al. [15], and Costa e Silva et al. [5]; crystal structural studies using neutron diffraction by Parthé et al. [1] and X-ray diffraction by Garin et al. [16].

When single phase $Mo_{\leq 5}Si_3C_{\leq 1}$ was synthesized by reactive hot-pressing [1] or combustion synthesis [16], a small amount of Mo_2C usually coexisted with the $Mo_{\leq 5}Si_3C_{\leq 1}$ phase. The reaction temperature and time seem to be high and long enough ($1600°C$, 12 h for Ref. 1, and $1450°C$, 0.5 h followed by $1550°C$, 8 h for Ref. 16) for samples to be equilibrated at high temperatures. Thus, the coexistence of Mo_2C should be attributed to the slight deviation from the composition which was aimed at. In the present investigation, the initial composition was determined by taking into account the variations of Si and C contents during sintering. This was because single phase $Mo_{\leq 5}Si_3C_{\leq 1}$ compacts (strictly, with a small amount of glassy phase) were successfully obtained by a simple reactive hot-pressing. The reactive sintering condition in this experiment was $1500°C$ for 2 h. Although only 1 h hot-pressing was enough to obtain the same single phase $Mo_{\leq 5}Si_3C_{\leq 1}$, the consition was not enough for densification.

The isothermal section of the Mo-Si-C phase diagram at $1600°C$ reported by Nowotny et al. [13] and its enlargement around $Mo_{\leq 5}Si_3C_{\leq 1}$ are shown in Fig. 7.6 (a) and (b), respectively. The $Mo_{\leq 5}Si_3C_{\leq 1}$ phase is marked as N in the figures. Although the original diagram [13] included MoC, it is not stable at high temperatures [5,14]; thus, MoC is removed in Fig. 7.6. In Fig. 7.6(b), A, B and C are corresponding to the initial composition for monolithic $Mo_{\leq 5}Si_3C_{\leq 1}$, $Mo_{\leq 5}Si_3C_{\leq 1}$ /Mo_2C and $Mo_{\leq 5}Si_3C_{\leq 1}$/$MoSi_2$ composites. Arrows indicate how these compositions tend to change during hot-press sintering, and hatched area represents the homogeneous region of $Mo_{\leq 5}Si_3C_{\leq 1}$ at $1200°C$ reported by Loo et al. [15]. Although our results are in conflict with the Loo's phase diagram where the $Mo_{\leq 5}Si_3C_{\leq 1}$ phase is not equilibrium with $MoSi_2$ but SiC is in equilibrium with Mo_5Si_3, the single-phase region of $Mo_{\leq 5}Si_3C_{\leq 1}$ seems to be consistent with our result. The difference among Nowotny's, Loo's and our results with respect to the $Mo_{\leq 5}Si_3C_{\leq 1}$ single-phase region may be explained in terms of the difference in equilibrating temperature, that is $1600°C$ for Nowotny's [13], $1200°C$ for Loo's [15] and $1500°C$ for our results.

7.3.4 Lattice Parameters

In section 7.3.1 and 7.3.2, variations of lattice parameters during sintering were briefly described. Table 7.3 shows a comparison of lattice parameters in the literatures with those obtained in the present work. Except Brewer's work, all data show that the $Mo_{\leq 5}Si_3C_{\leq 1}$ phase in typical monolithic $Mo_{\leq 5}Si_3C_{\leq 1}$ compacts has a unit cell of $a \approx 0.729$ nm, $c \approx 0.504$ nm, and $c/a \approx 0.692$. The lattice parameter c increased in the Mo-rich region and decreased in the

Mo-poor region. This may be related to the occupancy of the T^{II} sites in the Table 7.2.

The carbon content did not affect the lattice parameters so much as Nowotny et al. [13] pointed out. The relationship between lattice parameter c/a and atomic ratio Mo/Si is shown in Fig.7.7.
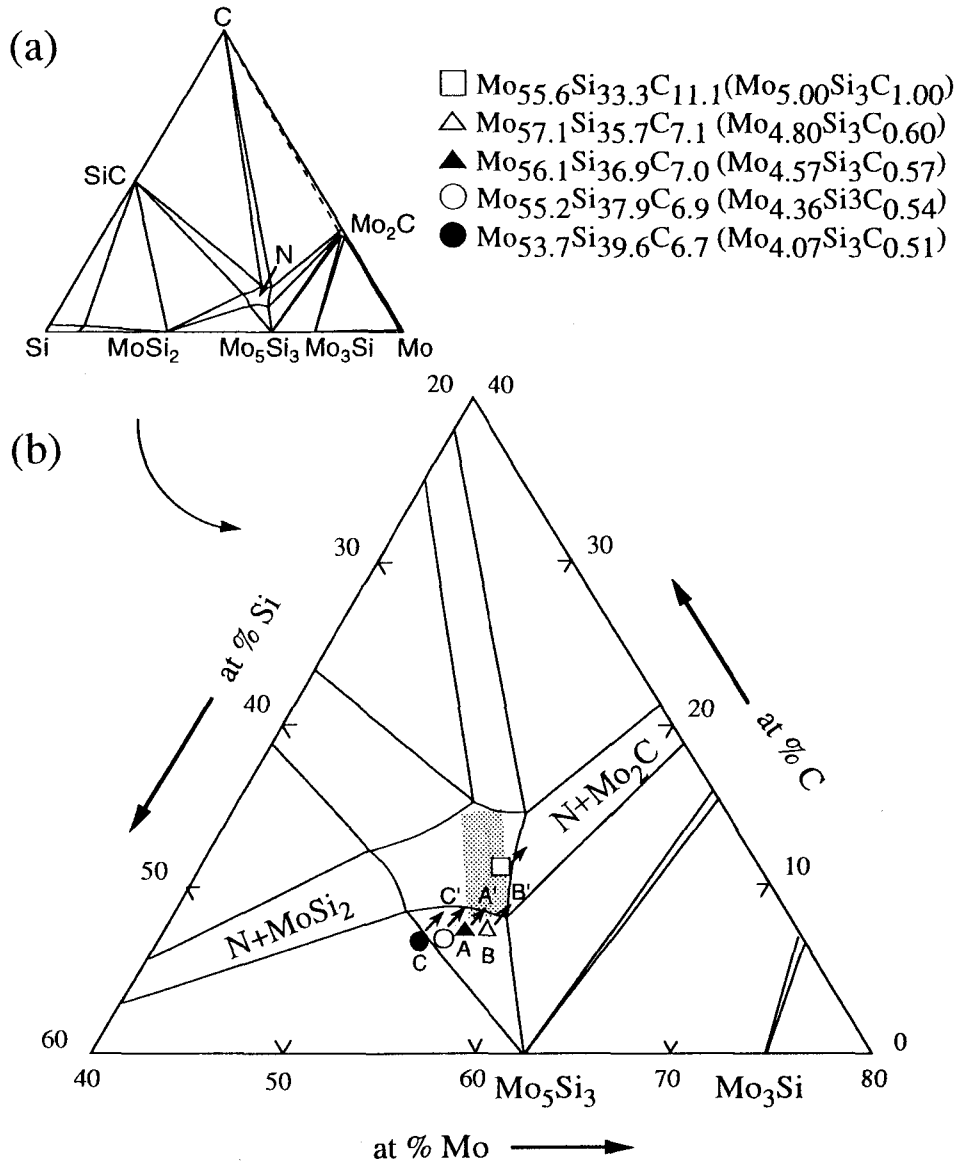

Fig. 7.6 (a) Isothermal section of the Mo-Si-C phase diagram at 1600°C based on Nowotny's report [13], and (b) enlargement around $Mo_{\leq 5}Si_3C_{\leq 1}$, marked as N.

Table 7.3 Lattice parameters of $Mo_{\leq 5}Si_3C_{\leq 1}$ phase in literatures and this work

Reference	Composition	a (nm)	c (nm)	c/a	Remarks
Nowotny et al. [13]	Mo-rich limit	0.728	0.506	0.695	
	Mo-poor limit	0.728	0.500	0.687	
Brewer et al. [14]	"Mo_4Si_3C"	0.728(5)	0.524(2)	0.7196	"Mo_4Si_3C" was an estimated formula
Parthé et al. [1]	$Mo_{4.8}Si_3C_{0.6}$	0.7286	0.5046	0.6926	Neutron diffraction
Garin et al. [16]	$Mo_{4.8}Si_3C_{0.6}$	0.72866(2)	0.50405(3)	0.6918	Reference data of PDF 43-1199
PDF 43-1199	$Mo_{4.8}Si_3C_{0.6}$	0.729260(13)	0.50439(2)	0.6916	Re-calculation of Garin's data
This work	$Mo_{4.7}Si_3C_{0.6}$	0.72903	0.50434	0.6918	monolithic $Mo_{\leq 5}Si_3C_{\leq 1}$
	Mo-rich region	0.72878	0.50569	0.6939	$Mo_{\leq 5}Si_3C_{\leq 1}$/3 wt%$Mo_2C$ composite
	Mo-poor region	0.72884	0.50164	0.6883	$Mo_{\leq 5}Si_3C_{\leq 1}$/6 wt%$MoSi_2$ composite
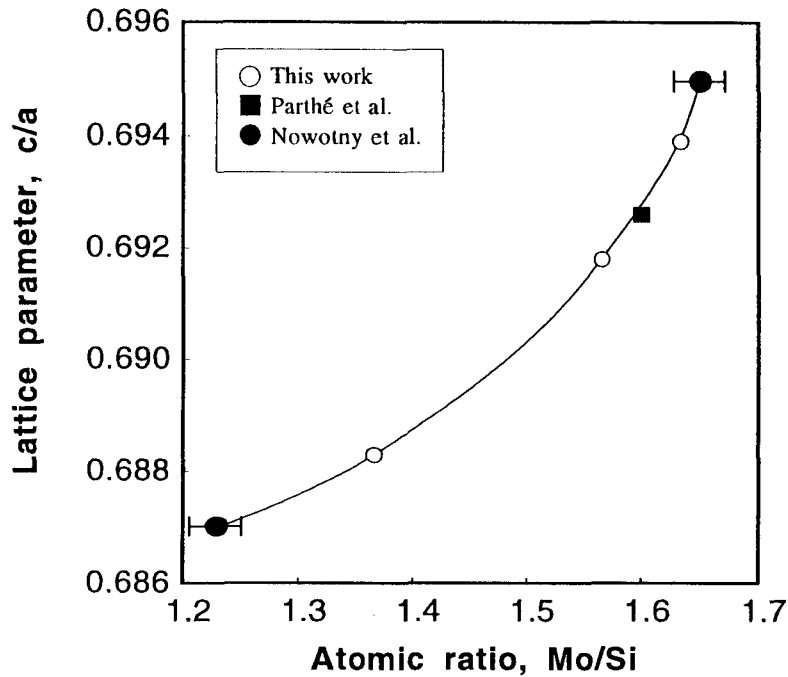
Fig. 7.7 Relationship between c/a and Mo/Si.

7.3.5 Mechanical properties

Table 7.4 summarizes densities and mechanical properties of $Mo_{\leq 5}Si_3C_{\leq 1}$-based materials. Monolithic $Mo_{\leq 5}Si_3C_{\leq 1}$ sintered compacts showed relatively good mechanical properties; fracture strength (σ_f), Vickers hardness (H_V) and fracture toughness (K_{IC}) of $Mo_{\leq 5}Si_3C_{\leq 1}$ hot-pressed at 1500°C for 2 h were 440 MPa, 12.1 GPa and 3.3 MPa·m$^{1/2}$, respectively.

Table 7.4 Mechanical properties of $Mo_{\leq5}Si_3C_{\leq1}$-based materials

Samples	Hot-pressing conditions	Density d (g/cm^3)	Strength σ_f (MPa)	Hardness H_V (GPa)	Toughness K_{IC} (MPa·m$^{1/2}$)
$Mo_{\leq5}Si_3C_{\leq1}$	1500°C, 1 h	7.45	462	11.0	3.2
$Mo_{\leq5}Si_3C_{\leq1}$	1500°C, 2 h	7.61	485	12.1	3.3
$Mo_{\leq5}Si_3C_{\leq1}$	1600°C, 2 h	7.68	440	12.6	3.7
$Mo_{\leq5}Si_3C_{\leq1}$/3 wt% Mo_2C	1500°C, 1 h	7.55	439	11.2	3.1
$Mo_{\leq5}Si_3C_{\leq1}$/3 wt% Mo_2C	1500°C, 2 h	7.66	423	11.9	3.1
$Mo_{\leq5}Si_3C_{\leq1}$/6 wt% $MoSi_2$	1500°C, 1 h	7.48	383	12.4	4.3
$Mo_{\leq5}Si_3C_{\leq1}$/6 wt% $MoSi_2$	1500°C, 2 h	7.49	393	12.4	4.3

Young's modulus (E) of $Mo_{\leq5}Si_3C_{\leq1}$ was 285 GPa (measured by a vibration method). These values are moderate or relatively high in comparison to those of other monolithic silicides, and suggest the possibility for $Mo_{\leq5}Si_3C_{\leq1}$ as a new matrix material as well as a reinforcement second phase material. *In situ* $Mo_{\leq5}Si_3C_{\leq1}$-base composites with Mo_2C did not show any superiority in mechanical properties to monolithic $Mo_{\leq5}Si_3C_{\leq1}$ compacts. However, $Mo_{\leq5}Si_3C_{\leq1}$ /$MoSi_2$ composites showed a higher toughness than monolithic $Mo_{\leq5}Si_3C_{\leq1}$ compacts. Further microstructural control will be needed to enhance their mechanical properties.

Preliminary oxidation tests at room temperature were performed for each samples. After one month, $Mo_{\leq5}Si_3C_{\leq1}$/Mo_2C composites lost the metallic appearance on their surface. However, $Mo_{\leq5}Si_3C_{\leq1}$ and $Mo_{\leq5}Si_3C_{\leq1}$/$MoSi_2$ composites kept metallic luster. This was in agreement with the fact that oxidation resistance of silicides generally increases with increasing silicon content. Thus, considering good oxidation resistance and good mechanical properties of $Mo_{\leq5}Si_3C_{\leq1}$/ $MoSi_2$ composites, they can be candidates of high-temperature structural materials.

7.4 Conclusions

To the best of our knowledge, this is the first systematic study of $Mo_{\leq5}Si_3C_{\leq1}$-based materials. The results are summarized as follows;

1. The monolithic $Mo_{\leq5}Si_3C_{\leq1}$ phase was successfully synthesized by reactive hot-pressing of elemental molybdenum, silicon and carbon powders. $Mo_{\leq5}Si_3C_{\leq1}$ based *in situ* composites were also fabricated by a simple RHP method.

2. The relationship between the axial c/a and Mo/Si atomic ratio was revealed. The c/a increased with increasing the Mo/Si ratio.

3. Mechanical properties such as fracture strength, Vickers hardness, and fracture toughness of $Mo_{\leq5}Si_3C_{\leq1}$ and $Mo_{\leq5}Si_3C_{\leq1}$-based composites were first evaluated. Fracture strength,

Vickers hardness and fracture toughness of $Mo_{\leq 5}Si_3C_{\leq 1}$ hot-pressed at 1500°C for 2 h were 440 MPa, 12.1 GPa and 3.3 MPa·m$^{1/2}$, respectively. Young's modulus of $Mo_{\leq 5}Si_3C_{\leq 1}$ was 285 GPa.

4. Mechanical and oxidation tests suggest that $Mo_{\leq 5}Si_3C_{\leq 1}/MoSi_2$ composites can be candidates for high temperature structural materials. Optimizing process conditions will lead to improvements in the mechanical properties.

References

1. E. Parthé and W. Jeitschko, "A Neutron Diffraction Study of the Nowotny Phase $Mo_{\leq 5}Si_3 C_{\leq 1}$," *Acta Cryst.*, **1 9**, 1031-1037 (1965).

2. S. A. Maloy, A. H. Heuer, J. J. Lewandowski and J. J. Petrovic, "Carbon Additions to Molybdenum Disilicide: Improved High-Temperature Mechanical Properties," *J. Am. Ceram. Soc.*, **7 4** [10] 2704-2706 (1991).

3. S. A. Maloy, J. J. Lewandowski, A. H. Heuer and J. J. Petrovic, "Effects of Carbon Additions on the High Temperature Mechanical Properties of Molybdenum Disilicide," *Mater. Sci. Eng.*, **A 1 5 5**, 159-163 (1992).

4. N. S. Jacobson, K. N. Lee, S. A. Maloy and A. H. Heuer, "Chemical Reactions in the Processing of $MoSi_2$ + Carbon Compacts," *J. Am. Ceram. Soc.*, **7 6** [8] 2005-2009 (1993).

5. A. Costa e Silva and M. J. Kaufman, "Phase Relations in the Mo-Si-C System Relevant to the Processing of $MoSi_2$-SiC Composites," *Matell. Mater. Trans. A*, **2 5 A**, 5-15 (1994).

6. Y. Suzuki, T. Sekino and K. Niihara, "Effects of ZrO_2 Addition on Microstructure and Mechanical Properties of $MoSi_2$," *Scripta Metall. et Mater.*, **3 3** [1] 69-74 (1995).

7. Y. Suzuki, A. Nakahira, T. Sekino and K. Niihara, "Microstructure and Mechanical Properties of Mo-Si-Al Alloy and Mo-Si-Al/SiC Composite," *J. Jap. Soc. Pow. & Pow. Metall.*, **4 3** [3] 272-277 (1996).

8. Y. Suzuki and K. Niihara, "Effect of SiC Reinforcement on Microstructure and Mechanical Properties of $MoSi_2$," *Science and Engineering of Composite Materials*, 6 [2] 85-94 (1997).

9. F. Izumi, in The Rietveld Method, ed. by R. A. Young, Oxford University Press, Oxford, 1993, Chap. 13.

10. Y. -I. Kim and F. Izumi, "Structure Refinements with a New Version of the Rietveld-Refinement Program RIETAN," *J. Ceram. Soc. Jpn.*, **1 0 2** [4] 401-404 (1994).

11. The Int'l Union of Crystall., in International tables for X-ray crystallography, Kynoch Press, Birmingham, 1969, vol.1, p.302.

12. K. Niihara, R. Morena and D. P. H. Hasselman, "Evaluation of K_{IC} of Brittle Solids by the Indentation Method with Low Crack-to-Indent Ratios," *J. Mater. Sci. Lett.*, 1 [1] 13-16 (1982).

13. H. Nowotny, E. Parthé, R. Kieffer and F. Benesovsky, "Das Dreistoffsystem: Molybdän-Silizium-Kohlenstoff," *Mh. Chem.*, 85, 255-272 (1954).

14. L. Brewer and O. Krikorian, "Reaction of Refractory Silicides with Carbon and Nitrogen," *J. Electrochem. Soc.*, **1 0 3** [1] 38-51 (1956).

15. F. J. J. van Loo, F. M. Smet, G. D. Rieck and G. Verspui, "Phase relations and diffusion paths in the Mo-Si-C system at 1200°C", *High Temp.-High Press.*, **1 4**, 25-31 (1982).

16. J. L. Garin and R. L. Mannheim, "X-ray Powder Diffraction of $Mo_{4.8}Si_3C_{0.6}$," *Powder diffraction* 8 [1] 65-67 (1993).

8

Summary and Conclusions

Development of innovative high-temperature structural materials is strongly desired for high-performance gas turbines and spacecraft airframes. Advanced materials for high-temperature applications based on refractory intermetallic compounds are gaining importance as attractive alternatives to conventional high-temperature materials, such as Ni based superalloys, carbon/carbon composites, and some ceramics based composites.

In this study, the author proposed a new material design concept for $MoSi_2$ based materials, "simultaneous strengthening and toughening both of $MoSi_2$ matrix and SiO_2 grain boundary phase," to overcome above mentioned problems. Strong and tough $MoSi_2$ based composites up to high temperatures were successfully developed along with the concept; the mechanisms of the strengthening and toughening were also clarified. The relationship between microstructure and mechanical properties of $MoSi_2$ based composites was studied in detail. The strategy to fabricate excellent and promising $MoSi_2$ based materials was established via this study. The main conclusions in this study are summarized as follows.

In Chapter 2, the formation mechanism of discrete glassy SiO_2 in $MoSi_2$, and sintering mechanism of a $MoSi_2$ powder were clarified on the basis of observation from an *in situ* SEM. It was revealed that the discrete glassy SiO_2 in $MoSi_2$ sintered bodies was formed by softening of surface oxide layer of a $MoSi_2$ powder, and following condensation due to the poor wettability between $MoSi_2$ and glassy SiO_2. The *in situ* observation also exhibited that the sintering mechanism of a $MoSi_2$ powder was solid state sintering.

Furthermore, a quantitative evaluation of glassy SiO_2 in sintered $MoSi_2$ was successfully conducted by applying the cryogenic specific heat measurement which was originally developed for Si_3N_4 based materials. Combination of these two methods enabled more precise evaluation of sintered $MoSi_2$ based materials.

In Chapter 3, $MoSi_2$ matrix composites reinforced by nano-sized β-SiC particles were fabricated by hot-pressing, and the relationship between microstructure and mechanical properties was investigated. The $MoSi_2$/SiC composites were composed of $MoSi_2$, $Mo_{\leq 5}Si_3C_{\leq 1}$, β-SiC

and glassy SiO_2. SiC particles were dispersed mainly at the grain boundaries SiO_2 and partially within the $MoSi_2$ matrix grains. That is to say, simultaneous strengthening and toughening of $MoSi_2$ and glassy SiO_2 were observed. TEM observation showed that the interface between $MoSi_2$ and SiC within $MoSi_2$ matrix grain was directly bonded without any reaction phases. Fracture strength was remarkably enhanced by the SiC addition. The observed enhancement of fracture strength in this system was mainly attributed to the grain growth inhibition by SiC dispersoid. The high-temperature deformation mechanism in the $MoSi_2$/SiC composite system with some glassy SiO_2 should be grain boundary sliding rather than dislocation motion, suggested by internal friction measurement. Although $MoSi_2$-based materials with much glassy SiO_2 generally do not show good mechanical properties, the present composites exhibited good mechanical properties in spite of relatively high SiO_2 level. This was because dispersed SiC particles strengthened not only matrix but also glassy SiO_2 phase effectively.

In Chapter 4, the modification of the grain boundary phase in the $MoSi_2$ compacts by the additions of Sc_2O_3 and Y_2O_3 was studied. With rare earth oxide additives, mechanical properties were considerably improved, which was based on the microstructural control by *in situ* crystallization of glassy SiO_2 to form several refractory silicates: $Sc_2Si_2O_7$, $Y_2Si_2O_7$, Y_2SiO_5 and $Y_4Si_3O_{12}$. Only 1 mol% Sc_2O_3 addition dramatically enhanced fracture strength from 521 to 1081 MPa. Vickers hardness, Young's modulus, fracture toughness and high-temperature strength were also improved by this low level of additive. Both ambient and high-temperature properties were successfully improved by this microstructural design. These results indicate that *in situ* crystallization of the glassy SiO_2 phase by the addition of these refractory oxides has great advantages in fabricating $MoSi_2$-based composites with improved mechanical properties.

In Chapter 5, the improvement in mechanical properties by the additions of $3Y$-ZrO_2 and HfO_2 was discussed. The combination effects of *in situ* crystallization and transformation toughening were examined via comparison with rare earth oxide additives. $3Y$-ZrO_2 added $MoSi_2$ compacts were composed of $MoSi_2$, $Mo_{\leq 5}Si_3C_{\leq 1}$, $ZrSiO_4$, and unreacted tetragonal ZrO_2. The intergranular glassy SiO_2 was changed into the refractory $ZrSiO_4$ crystalline phase. $MoSi_2$/ unstabilized HfO_2 compacts were composed of $MoSi_2$, $Mo_{\leq 5}Si_3C_{\leq 1}$, $HfSiO_4$, and unreacted monoclinic HfO_2. $3Y$-ZrO_2 and HfO_2 additions improved mechanical properties, in particular at room temperature. Only 1-2 mol% additives remarkably improved various mechanical properties, similarly to rare earth oxide additive cases. $3Y$-ZrO_2 added $MoSi_2$ also exhibited fairly high toughness due to the combination of transformation toughening and *in situ* crystallization of brittle glassy SiO_2. However, $3Y$-ZrO_2 addition resulted in the degradation of high-temperature strength and hardness. The strength dependence with temperature of 1 mol% HfO_2 added $MoSi_2$ resembled that of R_2O_3 added $MoSi_2$ due to the similarity of crystallization of glassy SiO_2. These results suggest that the $MoSi_2$/$3Y$-ZrO_2 composites should be used for

applications that do not require high strength at elevated temperature, but need high toughness at room temperature, for example replacement of conventional $MoSi_2$ heating elements. Yttria-stabilized tetragonal HfO_2 addition may improve high-temperature properties of $MoSi_2$.

In Chapter 6, alloying and composite techniques were simultaneously adapted to obtain better mechanical properties of $MoSi_2$ based materials. The Mo-Si-Al alloys and Mo-Si-Al/SiC composites were fabricated by the powder metallurgical process from novel Mo-Si-Al pre-alloyed powders, and the relationship between microstructure and mechanical properties was clarified. While $MoSi_2$ based materials included some glassy SiO_2 phase, almost no glassy SiO_2 was found in Mo-Si-Al based materials. In Mo-Si-Al systems, $\alpha\text{-}Al_2O_3$ was mainly dispersed instead of glassy SiO_2. The formation of $\alpha\text{-}Al_2O_3$ was attributed to the predominant oxidation of aluminum at the surface of the Mo-Si-Al pre-alloyed powders. Mo-Si-Al sintered bodies were composed of hexagonal $Mo(Si,Al)_2$ (C40), tetragonal $MoSi_2$ (C11$_b$), $Mo_{\leq 5}Si_3C_{\leq 1}$ and $\alpha\text{-}Al_2O_3$. For all systems, added nano-sized SiC particles effectively reduced the grain growth of the matrices. Combination of alloying and composite techniques markedly improved mechanical properties via microstructural modification.

In Chapter 7, the first systematic study of $Mo_{\leq 5}Si_3C_{\leq 1}$ and $Mo_{\leq 5}Si_3C_{\leq 1}$-based composites was conducted. The monolithic $Mo_{\leq 5}Si_3C_{\leq 1}$ phase was successfully synthesized by reactive hot- pressing of elemental molybdenum, silicon and carbon powders. $Mo_{\leq 5}Si_3C_{\leq 1}$-based in situ composites were also fabricated by a simple RHP method. The relationship between the axial c/a and Mo/Si atomic ratio was revealed. The c/a increased with increasing the Mo/Si ratio. Mechanical properties such as fracture strength, Vickers hardness, and fracture toughness of $Mo_{\leq 5}Si_3C_{\leq 1}$ and $Mo_{\leq 5}Si_3C_{\leq 1}$-based composites were first evaluated. Preliminary mechanical and oxidation tests suggest that $Mo_{\leq 5}Si_3C_{\leq 1}/MoSi_2$ composites can be candidates for high temperature structural materials. Informative basic data of $Mo_{\leq 5}Si_3C_{\leq 1}$ phase were obtained, and they will be useful for future development of $MoSi_2$ based materials.

As a whole, the new material design concept for $MoSi_2$ based materials, "simultaneous strengthening and toughening both of $MoSi_2$ matrix and SiO_2 grain boundary phase," was confirmed to be very effective to produce excellent and promising $MoSi_2$ based materials. The new material design strategy, i.e., the utilization of fine $MoSi_2$ powders and proper alloy and composite technologies, enables to produce such $MoSi_2$ based materials

Finally, the author hopes that the concepts, findings, and strategies obtained in this study will contribute to the progress in science and engineering.

Molecular Dynamics Computer Simulation of Single Crystal MoSi$_2$

Molecular dynamics (MD) simulation of single crystal MoSi$_2$ was attempted to reproduce its crystal structure, and the preliminary results were demonstrated. Possibility of computer simulation method for this material was discussed. The interatomic potential model consisted of two-body interactions of Stillinger-Weber type potentials. Complex C11$_b$ crystal structure was successfully reproduced in some extent. To the best of the author's knowledge, this is the first application of MD method for MoSi$_2$.

A1.1 Introduction

As described in Chap. 1, MoSi$_2$ intermetallic compound has a relatively complex crystal structure and strong covalent interatomic bonds; the poor deformability of MoSi$_2$ based materials is partially explained by such a complex crystal structure and chemical-bond states. To understand the various properties of MoSi$_2$ and to develop more excellent MoSi$_2$-based materials, it is indispensable to investigate the atomic-level properties of MoSi$_2$.

In order to clarify the relationship between atomic/molecular level structure and macro level physical properties of materials, various computer simulations were conducted [1]. In particular, a very promising way to construct theoretical models for solid state materials is to use molecular dynamics (MD) computer simulation method based on the establishment of proper interatomic potentials, because the method enables to investigate local structures, auto- and cross-correlations in both space and time [2]. A lot of MD simulations were conducted for amorphous or glassy materials [2-5], crystalline pure metals [6-7], oxide-based ceramics [8-14] and polymers [15,16]. On the other hand, only limited studies have been conducted for intermetallic compounds due to their complex interatomic bonds and crystal structures; most of the reported MD simulations for intermetallics have focused cubic-structured compounds with high symmetry, such as NiAl with B2 structure [17,18], RuAl with B2 structure [19], Ni$_3$Al with L1$_2$ structure [17,18], Mo$_3$Si with A15 structure [20,21] and so on. As far as the author

knows, MD simulations of more complex intermetallic compounds have been scarcely performed. Several MD studies associated with the Mo-Si binary system can be found in the literatures: above mentioned cubic Mo_3Si by Chudinov et al. [20,21], Mo-Si bilayer by Mazzone [22], Mo-Si multilayer by Morgan et al. [23], and amorphous Mo-Ge alloys by Ding et al. [24]. However, it may be particularly difficult to make MD simulations for transition metal disilicides, such as $MoSi_2$, due to their low crystal symmetry and strong covalent bonds.

In this chapter, the preliminary MD simulation of single crystal $MoSi_2$ was attempted to reproduce its crystal structure, and the preliminary results were demonstrated. To the best of the author's knowledge, this is the first application of MD method for $MoSi_2$, and even for transition metal disilicides.

A1.2   Interatomic Potentials

There are two types of interatomic potential functions used in MD simulations, that is *ab initio* quantum-mechanical potentials and empirical potentials [24]. *Ab initio* potentials are obtained by fitting a functional form to the results of quantum-mechanical calculations of the total energy of an assembly of atoms as a function of their nuclear positions. Although such potentials have been applied for more than two decades for MD simulations, too much calculations are generally required for the *ab initio* calculations. On the other hand, empirical potentials are obtained by assuming a functional form that describes the physical features believed to be important in the correct potential and then obtaining values for parameters in the function by using experimental data [24]. The empirical potentials were used in the present study.

In the Mo-Si binary system, three types of atomic interactions should be considered: (1) interactions among Si atoms, (2) those among Mo atoms, and (3) those among Si atoms and Mo atoms. The adopted potentials in this study were determined in terms of the reproduction of the crystal structure of $MoSi_2$, rather than the thermodynamic and elastic properties

A1.2.1   Si-Si Interactions

Several sets of Si-Si potentials reproducing pure diamond-structured silicon have been proposed by Keating [25], by Stillinger and Weber (SW) [26] and by Tersoff [27] and so on. These potentials consists of two-body term representing the tendency for silicon atoms to form chemical bonds each other, and three-body term promoting the formation of 109.47° bond angles between the various bonds made by silicon atoms. Cowley [28] examined the validity of these empirical potentials by using lattice dynamics, and suggested that the SW potential gave the best overall description of the lattice dynamics for silicon, although it was not so complete. Hence, Jian et al. [29] proposed a set of modified potential parameters for the SW potential.

The two-body interaction of the SW potential consists of following term:

$$V_2(r_{ij}) = \varepsilon f_2(r_{ij} / \sigma) \qquad \text{(A1.1)}$$

$$f_2(r) = \begin{cases} A(Br^{-p} - r^{-q})\exp[\delta / (r - b)] & (r < b) \\ 0 & (r \geq b) \end{cases} \qquad \text{(A1.2)}$$

where A, B, p, q, d, b are the intrinsic potential parameters, $r_{ij} = |r_i - r_j|$, ε and σ are normalizing constants for energy and distance, chosen to give f_2 depth as -1 and to make f_2 a minimum at $r = 2^{1/6}$, respectively. The subscript '2' means a two-body term. It is obvious that f_2 must be a function only of scaler distance. This generic form automatically cuts off at $r = b$ without discontinuities in any r derivatives, which is a distinct advantage in any molecular dynamics simulations [26].

The three-body interaction of the SW potential consists of following term:

$$V_3(r_i, r_j, r_k) = \sum f_3(r_i / \sigma, r_j / \sigma, r_k / \sigma) \qquad \text{(A1.3)}$$

$$f_3(r_i, r_j, r_k) = h(r_{ij}, r_{ik}, \theta_{jik}) + h(r_{ji}, r_{jk}, \theta_{ijk}) + h(r_{ki}, r_{kj}, \theta_{ikj}) \qquad \text{(A1.4)}$$

$$h(r_{ij}, r_{ik}, \theta_{jik}) = \lambda \exp[\gamma(r_{ij} - b)^{-1} + \gamma(r_{ik} - b)^{-1}] \times [\cos\theta_{jik} + 1/3]^2 \qquad \text{(A1.5)}$$

where θ_{ijk} is the angle subtended by r_{ij} and r_{jk} with the vertex at i. The function h belongs to a two-parameter family (λ, $\gamma > 0$). The three-body interaction obviously becomes zero at the perfect tetrahedral angle $\theta_t = 109.47°$ and is positive otherwise. Thus, the trigonometric part of Eq. A1.5 clearly discriminates in favor of pairs of bonds emanating from vertex i with the desired geometry [26]. Table A1.1 shows several sets of the SW potential parameters for diamond structured silicon and germanium in the literatures [26, 29, 30].

Table A1.1 SW potential parameters for diamond-structured Si and Ge

	Si		Ge	
	Ref. 26	Ref. 29	Ref. 30	Ref. 29
A	7.049 556 277	6.865 464 121	7.049 556 277	6.768 571 075
B	0.602 224 558 4	0.611 445 848	0.602 224 558 4	0.616 574 299
ε (eV)	2.17	2.17	1.93	1.93
σ (Å)	2.0951	2.0951	2.181	2.181
λ	21.0	9.11	31.0	8.37
δ	1.0	0.9757	1.0	0.9625
	$p = 4$,	$q = 0$,	$\gamma = 1.2$,	$b = 1.8$

Due to the reproductivity of physical properties and the flexibility of function shapes, the two-body term of SW potential was basically applied to molecular dynamics simulations for $MoSi_2$. The scale energy (ε) was determine to reproduce the cohesive energy of $MoSi_2$. For the Si-Si interaction, the scale energy (ε) was reduced to 70 % of the original ε. This assumption may be reasonable to explain the difference in bonding strength between pure Si and $C11_b$ $MoSi_2$. The three-body term should be modified if it is applied for the MD simulations of $MoSi_2$ because the bond angles in $MoSi_2$ are quite different from those in pure silicon. Thus, the only two-body term was taken into account for this preliminary study.

A1.2.2 Mo-Mo Interactions

Empirical potentials for interactions among molybdenum atoms were proposed by van Heugten [31] and by Miller [32], and these were assessed by Ding et al. [24]. Both are pairwise additive two-body interactions; the former was obtained from analysis of phonon dispersion curves for crystalline molybdenum, and the latter was obtained from elastic constants and the vacancy formation energy. Ding et al.[24] indicated that the Miller potential was better than the Heugten potential, but that the Miller potential should be modified due to the lack of sufficient repulsive force. They multiplied the Miller potential by a factor of 3.5 and were able to get satisfactory results. The rescaled Miller potential kept a desirable feature of the original Miller potential predicting that bcc structure as the most stable structure of pure Mo metal. The Mo-Mo two-body potential is given by the following polynomial equation [24,32],

$$\varphi(r) = \begin{cases} c\exp(-dr) & 0 < r < r_1 \\ A_k r^3 + B_k r^2 + C_k r + D_k & r_k < r \le r_{k+1}, (k = 1-7) \\ 0 & r > r_8 \end{cases} \tag{A1.7}$$

where A_k, B_k, C_k and D_k are the actual potential parameters with φ in eV and r in Å. Original parameters of the Miller potentials are listed in Table A1.2. The rescaled Miller potential by Ding et al. was simply obtained by multiplying all parameters in Table A1.2 by a factor of 3.5.

Table A1.2 The coefficients of the eight-spline molybdenum potential [32].

k	r_k (Å)	A_k	B_k	C_k	D_k
1	1.57	−164.545 411	834.204 102	−1 455.743 492	889.882 814
2	1.727	105.241 308	−563.560 890	958.196 649	−499.742 060
3	2.041	−84.699 215	599.444 934	−1 415.498 239	1 115.161 695
4	2.355	0.163 385	−0.109 336	3.547 931	6.780 704
5	3.2185	−4.222 760	42.241 089	−139.852 783	153.013 092
6	3.454	−0.682 693	5.558 915	−13.152 236	7.138 892
7	3.611	3.899 581	−44.080 856	166.096 680	−208.617 432
8	3.768	0.0	0.0	0.0	0.0

In this study, a SW-type potential function was used for describing the Mo-Mo two-body interactions. The potential was obtained by the curve fitting for the rescaled Miller potential using nonlinear least-square algorithm, and multiplied by a factor of 0.7 for the coincidence to the Si-Si interactions as mentioned before. That is, the Mo-Mo potential is based on the 245% ($= 3.5 \times 0.7$) of the original Miller potential.

A1.2.3 Mo-Si Interactions

For interactions among Mo and Si atoms, a Mo-Ge SW-type potential [24] was basically adapted. The potential allows the formation of a chemical bond between the metal and metalloid. The scale length (σ) was determined to reproduce the $MoSi_2$ structure, by the trials of MD calculations using more than 100 sets of the potential parameters.

The scale energy (ε) for the Mo-Si two-body interaction was determined to reproduce the cohesive energy of $MoSi_2$. The potential depth of the Mo-Si interaction was about 70 % of that of the Mo-Ge interaction [24].

A1.3 Calculational Methods

MD simulation under constant (N, V, E) was carried out using the simulation program, MASPHYC-2 (Fijitsu Co. Ltd.). A rectangular basic cell and 3-dimensional periodic boundary conditions were adopted. The basic cell consisted of $6a \times 6b \times 3c$ which contained 648 atoms. The cut-off radius of 0.5 nm was applied to the two-body interactions throughout the simulations. The simulation of a time period of 20 ps (2×10^{-11}s) was performed with a time step of 2 fs, after 2 ps of relaxation. Fig. A1.1 shows the $MoSi_2$ basic cell in this study.
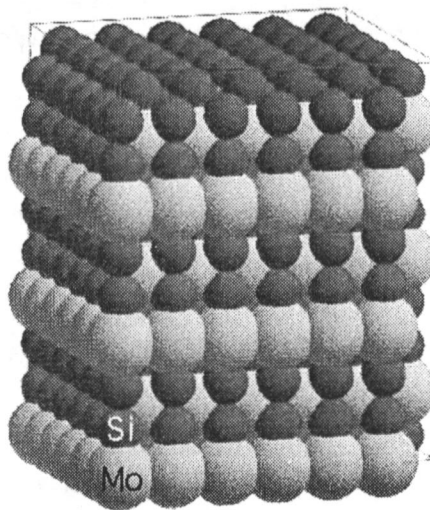
Fig. A1.1 The $MoSi_2$ basic cell consisted of $6a \times 6b \times 3c$ containing 648 atoms.

A1.4 Results and Discussion

Table A1.3 shows a set of tentative SW potential parameters reproducing C11$_b$ MoSi$_2$. The lattice energy par 3 atoms (i.e. 1 Mo and 2 Si atoms) obtained by the MD calculation using the potential parameters listed in Table A1.3 was 19.8 eV, which was in good agreement with the reported cohesive energy, 19.6944 eV obtained by the band calculation [33]. Fig. A1.2 shows the variation of temperature with simulation time for MoSi$_2$. Although the intended temperature was 300 K, the resultant temperature became about 700 K. This means the repulsive force of the potentials was somewhat weak, compared to the real MoSi$_2$ crystal. However, such a stable

Table A1.3 A set of tentative SW potential parameters (two-body term) obtained for MoSi$_2$.

	Si-Si	Mo-Si	Mo-Mo
A	7.049 556 277	10.016 22	7.448 9*
B	0.602 224 558 4	0.978 233 1	1.490*
ε (eV)	1.519*	1.351*	1.579*
σ (Å)	2.0951	1.98*	2.35*
δ	1.0	1.0	1.0
p	4	4	6*
q	0	0	0
b	1.8	1.8	1.74*

* determined in this study.
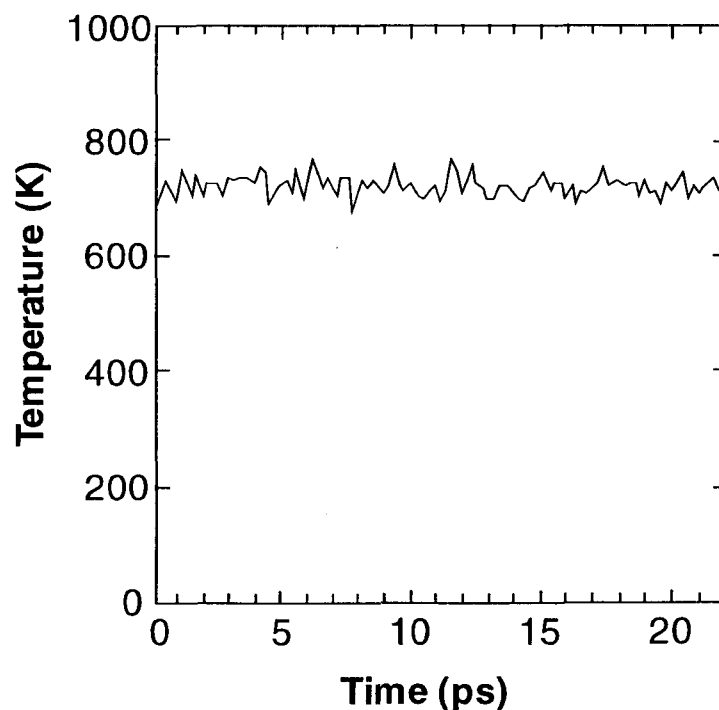
Fig. A1.2 Variation of temperature with simulation time for MoSi$_2$.

temperature dependence means that the $MoSi_2$ structure was reproduced by the MD calculation in some extent. Fig. A1.3 shows trajectories of atoms observed from [100] direction during 20 ps (10^4 steps). As seen this figure, all atoms migrated around their positions, showing the stable MD simulation. However, the atomic vibration along with the [001] direction seems to be restricted in this calculation. A preliminary MD simulation under (N, T, P) ensemble using the potential parameters in Table A1.3 revealed that the reproduced lattice tended to transform into quasi-bcc structure. More precise interatomic potentials are required to simulate various properties of $MoSi_2$, and such potentials can be constructed using many-body terms.

A1.5 Conclusions

In this chapter, molecular dynamics (MD) simulation of single crystal $MoSi_2$ was conducted to reproduce its crystal structure, and the preliminary results were demonstrated. Complex $C11_b$ crystal structure was successfully reproduced in some extent using two-body interactions of Stillinger-Weber type potentials. To the best of the author's knowledge, this is the first application of MD method for $MoSi_2$. Future development of many-body interatomic potentials enables to reproduce more precise $MoSi_2$ structure, and to help the atomic level analyses.
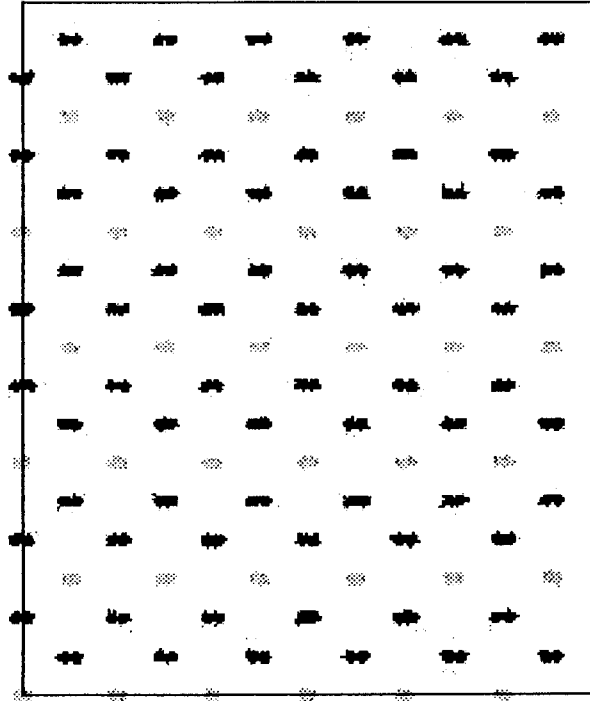
Fig. A1.3   Side view of the trajectory of atoms: Mo (gray) and Si (black).

References

1. A. M.Mazzone, "Recent Developments of Molecular Dynamics Simulations in Ion Implantation and in Material Processing," *Diffus. Defect Data, Solid State Data B, Solid State Phenom.*, 2 7, 51-66, (1992).

2. K. V. Damodaran, V. S. Nagarajan and K. J. Rao, "A Molecular Dynamics Study of ZrO_2-SiO_2 System," *J. Non-Cryst. Solids*, 124, 233-241 (1990).

3. Y. Matsui and K. Kawamura, "Instantaneous Structure of an $MgSiO_3$ melt simulated by Molecular Dynamics," *Nature*, 285, 648-649 (1980).

4. A. B. Rosenthal and S. H. Garofalini, "Molecular Dynamics Simulation of Amorphous Zinc Silicate," *J. Non-Cryst. Solids*, 8 7, 254-262 (1986).

5. R. Ochoa, T. P. Swiler and J. H. Simmons, "Molecular Dynamics Studies of Brittle Failure in Silica: Effect of Thermal Vibrations," *J. Non-Cryst. Solids*, 128, 57-68 (1991).

6. D. D. Koleske and S. J. Sibener, "Molecular Dynamics Simulations of the Basal Planes of Ni and Cu Using Finnis-Sinclair Potentials," *Surface Science*, 290 [1-2] 179-194 (1993).

7. M. Murata and Y. Murai, "Application of Meso-Fracture Mechanics to Behavior of Micro-Surface Crack via Molecular Dynamic Method," (in Jpn.) *Tetsu-to-Hagane*, 8 0 [2] 84-89 (1994).

8. F. Shimojo, T. Okabe, F. Tachibana, M. Kobayashi and H. Okazaki, "Molecular Dynamics Studies of Yttria Stabilized Zirconia. I. Structure and Oxygen Diffusion," *J. Phys. Soc. Jpn.*, 6 1 [8] 2848-2857 (1992).

9. F. Shimojo and H. Okazaki, "Molecular Dynamics Studies of Yttria Stabilized Zirconia. II. Microscopic Mechanism of Oxygen Diffusion," *J. Phys. Soc. Jpn.*, 6 1 [11] 4106-4018 (1992).

10. K. Fukuda, I.Fujii, R. Kitoh and I. Awai, "Molecular Dynamics Study of the TiO_2 (Rutile) and TiO_2-ZrO_2 Systems," *Acta Crystallogr.*, B49, 781-783 (1993).

11. X. Li and B. Hafskjold, "Molecular Dynamics Simulations of Yttrium-Stabilized Zirconia," *J. Phys., Condens. Matter.*, 7, 1255-1271 (1995).

12. H. W. Brinkman, W. J. Briels and H. Verweij, "Molecular Dynamics Simulations of Yttria-Stabilized Zirconia," *Chem. Phys. Lett.*, 247, 386-390 (1995).

13. D. -W. Kim, N. Enomoto, Z. Nakagawa and K. Kawamura, "Molecular Dynamic Simulation in Titanium Dioxide Polymorphs: Rutile, Brookite, and Anatase," *J. Am. Ceram. Soc.*, 7 4 [4] 1095-1099 (1996).

14. S. Blonski and S. H. Garofalini, "Atomic Structure of Calcium Silicate Intergranular Films in Alumina Studied by Molecular Dinamics Simulations," *J. Am. Ceram. Soc.*, 8 0 [8] 1997-2004 (1997).

15. J. H. R. Clarke and D. Brown, "Molecular Dynamics Modelling of Polymer Materials," *Mol. Simul.*, 3 [1-3] 27-47 (1989).

16. J. Gao and J. H. Weiner, "Molecular Dynamics Simulations of Chain Relaxation and Crack Propergation in Polimer Liquid Crystals," *J. Chem. Phys.*, 9 5 [4] 2890-2896 (1991).

17. A. Voter and S. F. Chen, "Accurate Interatomic Potentials for Ni, Al and Ni_3Al," *MRS Symp. Proc.*, 8 2, 175-180 (1987).

18. S. Charpenay, P. C. Clapp, J. A. Rifkin, Z. Z. Yu and Voter, "Molecular Dynamics Study of Crack Propagation in Ni-Al," *MRS Symp. Proc.*, 141, 323-329 (1989).

19. C. S. Becquart, P. C. Clapp and J. A.Rifkin, "Molecular Dynamics Simulation of Fracture in RuAl," *MRS Symp. Proc.*, 288, 519-524 (1993).

20. V. G. Chudinov, N. V. Moseev, B. N. Goshchitskii and V. I. Protasov, "Possible Amorphisation and Phase Separation of Intermetallic Mo_3Si Compound under Radiation. Molecular dynamics study," *Phys. Status Solidi*, A 85 [2], 435-40 (1984).

21. N. V. Moseev, V. G. Chudinov, B. N. Goshchitskii and V. I. Protasov, "Molecular Dynamics Study of Atomic Configuration of Point Defects in Intermetallic Compound Mo_3Si," *Phys. Status Solidi*, A 9 4 [1] 147-152 (1986).

22. A.M. Mazzone, "Molecular Dynamics Simulations of Ion Beam Mixing of Mo-on-Si Bilayers," *Phys.*

Status Solidi, **A142** [2] K73-77 (1994).

23. W. L. Morgan and D. B. Boercker, "Simulating Growth of Mo/Si Multilayers," *Appl. Phys. Lett.*, **59** [10] 1176-8 (1991).

24. K. Ding and H. C. Andersen, "Molecular-Dynamics Computer Simulation of Amorphous Molybdenum-Germanium Alloys," *Phys. Rev. B*, **36** [5] 2675-2686 (1987).

25. P. N. Keating, "Effect of Invariance Requirements on the Elastic Strain Energy of Crystals with Application to the Diamond Structure," *Phys. Rev.*, **145** [3] 637-645.

26. F. H. Stillinger and T. A. Weber, "Computer Simulation of Local Order in Condensed Phases of Silicon," *Phys. Rev.*, **B31** [8] 5262-5271 (1985).

27. J. Tersoff, *Phys. Rev. Lett.*, **56**, 632 (1986).

28. E. R. Cowley, *Phys. Rev. Lett.*, **60**, 2379 (1988).

29. Z. Jian, Z. Kaiming and X. Xide, "Modification of Stillinger-Weber Potentials for Si and Ge," *Phys. Rev.*, **B41** [18] 12915-12918 (1990).

30. K. Ding and H. C. Andersen, *Phys. Rev. B*, **34**, 6987 (1986).

31. W. F. W. M. van Heutgen, *Phys. Status Solidi*, **B82**, 501 (1977).

32. K. M. Miller, "Point defect-dislocation interactions in molybdenum," *J. Phys*, **F11**, 1175-89 (1981).

33. B. K. Bhattacharyya, D. M. Bylander and Leonard Kleinman, "Comparison of Fully Relativistic Energy Bands and Cohesive Energies of $MoSi_2$ and WSi_2," *Phys. Rev. B*, **32** [12] 7973-7978 (1985) .

List of Publications

Papers

1) Manufacturing Nano-Diphasic Materials from Natural Dolomite: *In Situ* Observation on Nano-Phase Formation Behavior
Y. Suzuki, P. E. D. Morgan, T. Sekino and K. Niihara
J. Am. Ceram. Soc., 80 [11] 2949-2953 (1997).

2) Microstructure and Mechanical Properties of $MoSi_2$/SiC Composites
Y. Suzuki, A. Nakahira, T. Sekino and K. Niihara
Ceramic Transactions, 44, 427-434 (1994).

3) Effect of SiC Reinforcement on Microstructure and Mechanical Properties of $MoSi_2$
Y. Suzuki and K. Niihara
Science and Engineering of Composite Materials, 6 [2] 85-94 (1997).

4) Effects of ZrO_2 Addition on Microstructure and Mechanical Properties of $MoSi_2$
Y. Suzuki, T. Sekino and K. Niihara
Scripta Metallurgica et Materialia, 33 [1] 69-74 (1995).

5) Microstructure and Mechanical Properties of Mo-Si-Al Alloy and Mo-Si-Al/SiC Composite
Y. Suzuki, A. Nakahira, T. Sekino and K. Niihara
J. Jap. Soc. Powder Powder Metall., 43 [3] 272-277 (1996).

6) Synthesis and Mechanical Properties of $Mo_{\leq5}Si_3C_{\leq1}$ and $Mo_{\leq5}Si_3C_{\leq1}$-Based Composites
Y. Suzuki and K. Niihara
Intermetallics, 6 [1] 7-13 (1998).

7) The Improvement in Mechanical Properties of Powder Processed $MoSi_2$ by the Addition of Sc_2O_3 and Y_2O_3
Y. Suzuki, P. E. D. Morgan and K. Niihara
J. Am. Ceram. Soc., (in contribution).

8) X-Ray Powder Diffraction Pattern of $CaMg(CO_3)_2$
Y. Suzuki, P. E. D. Morgan and K. Niihara
Powder diffraction, (in contribution).

9) *In Situ* Observation of Discrete Glassy SiO_2 Formation and Quantitative Evaluation of Glassy SiO_2 in $MoSi_2$ Compacts
Y. Suzuki, T. Sekino, T. Hamasaki, K. Ishizaki and K. Niihara
Materials Letters, (in contribution).

10) The Improvement in Mechanical Properties of Powder Processed $MoSi_2$ by the Addition of $3Y$-ZrO_2 and HfO_2
   Y. Suzuki, P. E. D. Morgan and K. Niihara
   J. Am. Ceram. Soc., (in preparation).

11) Microstructure and Mechanical Properties of SiC Particulate Reinforced Mo-Si-Al Alloy Matrix Composites
   Y. Suzuki and K. Niihara
   J. Eur. Ceram. Soc., (in preparation).

Proceedings

12) Effects of Al Substitution and Nano-Sized SiC Dispersion on Microstructure and Mechanical Properties of $MoSi_2$
   Y. Suzuki and K. Niihara
   Proc. 6th Tohwa Univ. Int'l Symp.; Frontier Nanostructured Ceramics, 189-194 (1996).

13) Effect of SiC Reinforcement on Microstructure and Mechanical Properties of $MoSi_2$
   Y. Suzuki and K. Niihara
   Design and Manufacturing of Composites, Technomic Pub., PA, 179-182 (1997).

14) Development of Strong $MoSi_2$-Based Composites
   Y. Suzuki, P. E. D. Morgan and K. Niihara
   Proc. 6th Int'l Symp. Ceramic Materials & Components for Engines, (in press).

15) *In Situ* Observation of Nanophase Formation Behavior from Dolomite Using SEM and XRD Hot Stages
   Y. Suzuki, P. E. D. Morgan, T. Sekino and K. Niihara
   Proc. 6th Int'l Symp. Ceramic Materials & Components for Engines, (in press).

List of Supplementary Publications

Papers

1) High-Temperature Creep and Deformation Behavior of Al_2O_3/SiC Nanocomposite
   A. Nakahira, T. Sekino, **Y. Suzuki** and K. Niihara
   Ann. Chim. Fr., **18**, 403-408 (1993).

2) A Novel Unidirectionally Solidified Al_2O_3/$Er_3Al_5O_{12}$ Composite with Excellent High-Temperature Properties
   K. Niihara, **Y. Suzuki**, Y. Waku and N. Nakagawa
   Materials Research Innovations, (in preparation).

3) Molecular Dynamics Study of Molybdenum Disilicide
   Y. Suzuki, M. Takeuchi and K. Niihara
   Chem. Phys. Lett., (in preparation).

Patent Pending

4) Molybdenum Disilicide Based Composites and Their Fabrication Processes
   K. Niihara, **Y. Suzuki** and N. Kuroishi
   Japanese Patent, Toku-Gan-Hei 8-292645.

Translation

5) Creating Nanophase Materials, by R. W. Siegel, *Scientific American*, Dec., (1996).
   K. Niihara and **Y. Suzuki**
   Nikkei Science, 88-95, March, (1997).

Acknowledgements

Yoshikazu Suzuki

January, 1998
Osaka, Japan